Centre for CO_2 Technology

UCL

Electrochemical Treatment of Stainless Steel for Application in Polymer Electrolyte Fuel Cell Bipolar Plates

Ebrahim Mohammed Gabreab

UCL

A thesis for the degree of Doctor of Philosophy of the University College London

NPL National Physical Laboratory

EPSRC Engineering and Physical Sciences Research Council

Electrochemical Innovation Lab

Department of Chemical Engineering

University College London (UCL)

Torrington Place, London, WC1E 7JE, United Kingdom

Carbon Management • Power Systems • Sustainability

I Ebrahim M Gabreab, confirm that the work presented in the thesis is my own. Where information has been derived from other sources, I confirm that this has been indicated in the thesis.

_____

Signature

_____

Date

i. Acknowledgements

I would like to express immense gratitude to my principal supervisor Dr. Dan Brett, who has been a remarkable mentor. His encouragements, support, patience, motivation, enthusiasm, immense knowledge, guidance and friendship have helped me in all the time of research and writing of this thesis.

I would also like to especially thank my secondary supervisor Dr. Gareth Hinds (NPL), for his insightful knowledge, support and friendship. Your advice has been invaluable on both an academic and a personal level.

I would like to thank Dr. Paulo Lattieri for her suggestion on the undertaking of this PhD, your advice and encouragement has been invaluable. I am most grateful to the technical team; Mike, Simon, Martyn, Dave and Mark for their assistance and guidance in setting up experimental equipment, the workshop team; Erich, John and Graham for their technical assistance and guidance in the build of the electrochemical cells and the compression rig. Thanks to the departmental office staff, Anna, Pattie, Mae and Agata for their assistance, guidance and patience with all technical proceeding.

I would also like to thank my colleagues and friends at the CO_2 Centre, as well as those in the Department, for their assistance throughout this project, for promoting a stimulating academic and social environment. I would particularly like to thank Jason, Flora, Ishanka, Toby, Mithilla, Tom, Luigi, Miguel and Silo for their support and encouragement throughout. I'm also particularly gratefully for the input from Emma Farndon (Intelligent Energy) for her expertise in stainless steel electrochemistry, Sarah Fearn (Imperial College) for her assistance with FIB SIMS, Leyla Wickstrom (NPL) for her assistance with SEM imaging, Laurie Winkless (NPL) for her assistance with AFM imaging, and Kirk R. Weisbrod (LANL) for his assistance with current efficiency calculations.

I would also like to acknowledge the financial, academic and technical support of the University College of London and NPL, particularly in the award of a Postgraduate Research Studentship that provided the necessary financial support for this research.

Above all, I would like to thank my parents and aunt, for their love and support, for helping me be the best I can, for which my mere expression of thanks does not suffice. Thank you to my siblings who have given me their unequivocal support throughout. To my children, Anisah and Aidan for being a source of inspiration, I hope my achievements will inspire you just as much. Amongst my friends; Ariam, Makda, Edward, Degen, Abiel, Mehary, Brook, Alex, Samson, Simon, and Betiel, thank you for the enthusiasm, optimism all the great moments of joy. Amongst my fellow postgraduate students in the Department of BioChem, I would like to thank you all for the great footie sessions and social outings.

ii. Abstract

Polymer electrolyte fuel cell (PEFC) performance is typically considered to have reached the targets required for most applications; however, maintaining this performance throughout the operational lifetime of the fuel cell, or restricting its degradation to an acceptable level, is still a challenge. One of the most important yet understudied areas identified as a source of fuel cell performance degradation is the bipolar plate (BPP). The BPP typically accounts for more than 80% of the weight of a stack and almost all of the volume. Thus BPP weight and size reduction, while maintaining the desired properties is crucial in increasing the performance, making fuel cells more commercially viable.

Stainless steels BPPs are a popular choice, with the advantage of low cost, high strength and good corrosion resistance as well as ease of incorporating a flow field via stamping or embossing. The main criterion for material suitability with regards to stainless steel in particular, is large voltage drops at the interface; a consequence of corrosion protective insulating surface oxides. Surface modification / treatment techniques of inexpensive and widely available metals are capable of improving the performance of metals in fuel cell environments and are an alternative to the use of costly precious metal coatings. Electrochemical surface treatments involve modification of the oxide layer by enriching its chromium content, leading to higher corrosion resistance and lower interfacial contact resistance (ICR).

This project explores the use of electrochemical surface treatment to improve the corrosion and contact resistance of 316 stainless steel (316 SS). The process is an anodic treatment, whereby the material is polarised positive of the transpassive region, under process conditions of H_2SO_4-to-glycerol ratio at varying treatment times. The surface treatment demonstrates an increase in the corrosion resistance, enhanced durability of the passive film and significantly reduces ICR (interfacial contact resistance), to values well below the DoE 2017 targets at a compression of

200 psi (138 N cm^{-2}). While ex-situ near-surface characterisation suggests the improved properties of the electrochemically treated 316 SS are primarily as a consequence of Cr enrichment at the near-surface of the material. AFM analysis of surface roughness and morphology demonstrated increased Ra values of treated samples; which although has been previously associated with improved ICR, was not significant enough in this study to affect the ICR. The addition of glycerol as a viscosity-enhancing agent did not demonstrate a significant improvement of the process, while shorter treatment times demonstrated greater process current efficiencies, which consequently impact the economic costs. The process demonstrates that the use of anodized treated 316 SS to improve low ICR and satisfactory corrosion resistance of low cost metallic bipolar plate PEFCs is feasible.

iii. Publications

Primary journal articles

Ebrahim M. Gabreab, Gareth Hinds, Sarah Fearn, David Hodgson, Jason Millichamp, Paul R. Shearing, Daniel J.L. Brett, “An electrochemical treatment to improve corrosion and contact resistance of stainless steel bipolar plates used in polymer electrolyte fuel cells”, Journal of Power Sources, Volume 245 (2014), pages 1014-1026

Additional journal articles

J. Millichamp, E. M Gabreab, N.P. Brandon, R.J.C. Brown, D. Hodgson, C. Kalyvas, G. Manos, D.J.L. Brett, “Application of a $GaPO_4$ Crystal Microbalance for the Detection of Coke Formation in High-Temperature Reactors and Solid Oxide Fuel Cells”, Ind Eng Chem Res, Volume 50 (2011), pages 8371-8375.

Conference presentations and proceedings

Ebrahim M Gabreab, “Anodization treatment for stainless steel to improve corrosion resistance and interfacial contact resistance for use as bipolar plates in PEM fuel cells”, Industrial Advisory Group meeting, NPL, Teddington, UK. May 2012

Ebrahim M Gabreab, “Application of electropolishing techniques to stainless steel bipolar plate to improve corrosion resistance for use as bipolar plates in PEM fuel cells”, Industrial Advisory Group meeting, NPL, Teddington, UK. Nov 2012

Ebrahim M Gabreab, “Investigating corrosion and ion leaching of stainless steel bipolar plates used in polymer electrolyte fuel cells”, Industrial Advisory Group meeting, NPL, Teddington, UK. May 2011

Ebrahim M Gabreab, “Investigating corrosion and ion leaching from metallic bipolar plates used in polymer electrolyte fuel cells”, Industrial Advisory Group meeting, NPL, Teddington, UK. Sept 2009

Ebrahim M Gabreab, “Investigating corrosion and ion leaching from metallic bipolar plates used in polymer electrolyte fuel cells”, Electrochem Conference, Manchester, UK. Sept 2009

iv. Contents

1 Introduction and Literature review 23

1.1 Fuel Cells 23

1.2 Proton exchange membrane fuel cell (PEMFC) 24

1.3 PEMFC performance & operating principles 25

1.4 PEMFC Challenges 29

1.5 Role of the Bipolar Plate 31

1.6 Bipolar plate materials 32

1.6.1 Graphite 32

1.6.2 Composites 33

1.6.3 Metallic 37

1.6.4 Coated metals 41

1.6.5 Surface treated metals 44

1.7 Cost of Bipolar Plates 45

1.8 Materials, Machining and Forming 50

1.9 Bipolar Plate Characterization and Materials Testing 55

1.9.1 Bulk Electrical conductivity 56

1.9.2 Contact Resistance 57

1.9.3 Corrosion Resistance 60

1.10 Corrosion rate methodologies 61

1.10.1 Pourbaix diagrams 62

1.10.2 Potentials and polarization 63

1.10.3 Polarization behaviour of corroding metals 65

1.10.4 Passivation 71

1.10.5 Corrosion of Stainless Steel Bipolar Plates 76

1.11 Interfacial Contact Resistance (ICR) 80
1.11.1 Factors Influencing ICR 81
1.11.2 Theory of contact resistance 84
1.12 Surface treatment of Stainless steel 86
1.12.1 Electropolishing 86
1.12.2 Electropolishing mechanisms 89
1.13 The anode potential and current density relationship 92
1.14 Effects of electropolishing parameters 94
1.14.1 Bath temperature 94
1.14.2 Time of treatment 95
1.14.3 Acid concentration 96
1.14.4 Agitation of the electrolyte 96
1.14.5 Surface finish 97
1.15 Project objectives 98
2 Methodology and Experimental 101
2.1 DC Electrochemical methods 101
2.1.1 Potential measurements 102
2.1.2 Linear Polarization 102
2.1.3 Polarization resistance 103
2.2 AC Methods 104
2.3 Electrochemical Test Equipment 105
2.3.1 Potentiostat 105
2.3.2 Electrochemical cells 105
2.4 Corrosion in simulated fuel cell environment 109
2.4.1 Specimen preparation 109
2.4.2 Aqueous solutions 110

2.4.3 Aeration and Deaeration 111
2.5 Materials 112
2.6 Interfacial Contact Resistance 113
2.6.1 Surface characterisation post treatment 116
2.6.2 Focused Ion Beam Secondary Ion Mass Spectrometry (FIB-SIMS) 117
2.6.3 SEM 117
2.6.4 AFM 117
2.7 Calculations 117
2.7.1 Tafel line (Extrapolation) 117
2.7.2 Current Efficiency calculations 120
3 Results 123
3.1 Characterization of untreated stainless steel 123
3.1.1 Thermodynamic modelling 123
3.2 Corrosion behaviour of stainless steels 128
3.2.2 Electrical Contact Resistance 144
3.2.3 Discussion 145
3.3 Anodization surface treatment 150
3.3.1 Process electrochemistry 151
3.3.2 Surface analysis 163
3.3.3 Interfacial contact resistance 170
3.3.4 Corrosion in simulated PEFC environment 174
3.3.5 Durability 184
3.3.6 Discussion 191
4 Conclusion 197
5 Future work 200

6 Nomenclature 202

7 Appendix A1 204

8 Appendix A2 210

9 References 221

v. List of Figures

Figure 1: PEMFC, with end plates for drawing current from all over the face of the electrodes and also supplying gas to the electrodes [5]. 24
Figure 2: Typical fuel cell polarization curve and breakdown of cell voltages loses for an acid electrolyte [7]..... 28
Figure 3: Weight structure of a fuel cell stack [12] 30
Figure 4: Classification of bipolar plate materials [17] 32
Figure 5: Fuel cell stack cost structure at the beginning of the learning curve analysis (2000) [12]. 47
Figure 6: Fuel cell stack cost structure at 5 million cumulative vehicles (2020) [12]. 47
Figure 7: Cost drivers for polymer fuel cell stacks [63] 49
Figure 8: Bipolar plate image with incorporated flow field, manifold, gasket grooves and positioning holes [11]. 50
Figure 9: Classification of bipolar plate manufacturing alternatives [17]. .. 51
Figure 10: Bipolar plate stamping process diagram [62]. 53
Figure 11: Ex-situ method of measuring interfacial contact resistance of a bipolar plate and GDL material using (a) two bipolar plate samples, (b) a single bipolar plate sample [11]. 58
Figure 12: Schematic polarization curve for a corroding metal [89]..... 64
Figure 13: Development of corrosion potential (E_{corr}) and corrosion current (i_{corr}) from the combination of the two equilibrium electrodes [89]. 69
Figure 14: A schematic anodic polarization curve for a metal showing polarization behaviour [89]. 73
Figure 15: Schematic polarization curve for corrosion, passivation and passive film breakdown for stainless steels in dilute acid solutions [89]. .. 74
Figure 16: Surface roughness vs. contact resistance values obtained from ASTM316L stainless steel surface (treated with different grades of emery paper) in contract with TORAY paper [102]. 83

Figure 17: Interfacial contact resistance measured after various chemical treatments for 446M [108]. 84
Figure 18: Schematic of real contact spots in case of normal contact surfaces (top and right) and a current restriction (left) [102]. 85
Figure 19: Schematic model for the anodic dissolution with arrows (1) moving in the direction of the acceptor and (2) the moving direction of metal ions [123]. 90
Figure 20: Schematic diagram of the microstructure transformation of an adsorbed shielding molecule layer on SS anodized at a constant current density; (1) weak and (2) strong molecular aggregates and clusters of the adsorbed molecules on the electrode surface [123]. 91
Figure 21: An ideal characteristic *I-V* curve for the determination of the process current and association voltage [126] 93
Figure 22: Galvanostatic transients in saturated $LiNO_3$ electrolyte at 0.2, 0.4, 0.63 and 0.75 A cm^{-2} [132]. 97
Figure 23: Nyquist plot for the impedance spectra simulated in the frequency range from 10 mHz to 10kHz [139]. 104
Figure 24: Schematic diagram of the Avesta electrochemical cell used for corrosion studies. 107
Figure 25: Schematic diagram of electropolishing cell. 108
Figure 26: Illustration of rig used to perform interfacial contact resistance measurements. (Top) arrangement for measuring contact resistance with steel sample, and (Bottom) arrangement to determine contact resistance between GDL and gold plated copper 115
Figure 27: Computer aided design (CAD) image of ICR compression rig. . 116
Figure 28: Potential-pH equilibrium diagram for the iron-water system at 70 °C (solid substances considered are only; Fe, Fe_3O_4 and Fe_2O_3)..... 125
Figure 29: Potential-pH equilibrium diagram for the chromium-water system at 70 °C, considering anhydrous Cr_2O_3 (in chloride free solution) 127
Figure 30: Potential-pH equilibrium diagram for the nickel-water system at 70 °C 128

Figure 31: Tafel plots of 904L SS in 0.5M H_2SO_4, de-aerated with N_2 in the PEM fuel cell operating temperature range at a scan rate of 1 mV s^{-1}. 130
Figure 32: Tafel plots of 310 SS in 0.5M H_2SO_4, de-aerated with N_2 in the PEM Fuel cell operating temperature range at a scan rate of 1 mV s^{-1}. ... 130
Figure 33: Tafel plots of 316 SS in 0.5M H_2SO_4, de-aerated with N_2 in the PEM Fuel cell operating temperature range at a scan rate of 1 mV s^{-1}. ... 131
Figure 34: Tafel plots of 316 SS in 0.5M H_2SO_4, de-aerated with N_2 in the PEM Fuel cell operating temperature range at a scan rate of 1 mV s^{-1}. ... 131
Figure 35: Dependence of E_{corr} of 904, 304 & 316 SS, alloys on temperature in 0.5M H_2SO_4, de-aerated with N_2. 132
Figure 36: Tafel plot extrapolation of 904L SS in 0.5M H_2SO_4 at 60°C, de-aerated with N_2 at a scan rate of 1 mV s^{-1}. 132
Figure 37: Tafel plot extrapolation of 904L SS in 0.5M H_2SO_4 at 70°C, de-aerated with N_2 at a scan rate of 1 mV s^{-1}. 133
Figure 38: Tafel plot extrapolation of 904L SS in 0.5M H_2SO_4 at 80°C, de-aerated with N_2 at a scan rate of 1 mV s^{-1}. 133
Figure 39: Tafel plot extrapolation of 310 SS in 0.5M H_2SO_4 at 60°C, de-aerated with N_2 at a scan rate of 1 mV s^{-1}. 134
Figure 40: Tafel plot extrapolation of 310 SS in 0.5M H_2SO_4 at 70°C, de-aerated with N_2 at a scan rate of 1 mV s^{-1}. 134
Figure 41: Tafel plot extrapolation of 310 SS in 0.5M H_2SO_4 at 80°C, de-aerated with N_2 at a scan rate of 1 mV s^{-1}. 135
Figure 42: Tafel plot extrapolation of 316 SS in 0.5M H_2SO_4 at 60 °C, de-aerated with N_2 at a scan rate of 1 mV s^{-1}. 135
Figure 43: Tafel plot extrapolation of 316 SS in 0.5M H_2SO_4 at 70°C, de-aerated with N_2 at a scan rate of 1 mV s^{-1}. 136
Figure 44: Tafel plot extrapolation of 316 SS in 0.5M H_2SO_4 at 80°C, de-aerated with N_2 at a scan rate of 1 mV s^{-1}. 136
Figure 45: Tafel plot extrapolation of 304 SS in 0.5M H_2SO_4 at 60°C, de-aerated with N_2 at a scan rate of 1 mV s^{-1}. 137

Figure 46: Tafel plot extrapolation of 304 SS in 0.5M H_2SO_4 at 70°C, de-aerated with N_2 at a scan rate of 1 mV s^{-1}. 137
Figure 47: Tafel plot extrapolation of 304 SS in 0.5M H_2SO_4 at 80°C, de-aerated with N_2 at a scan rate of 1 mV s^{-1}. 138
Figure 48: LPR Polarization curve obtained by potentiodynamic polarization (± 10 mV/*E*corr, 0.1 mV/s) for 904L SS in 0.5 M H_2SO_4 at (a) 60 ° C (b) 70 ° C and (c) 80 ° C..... 140
Figure 49: LPR Polarization curve obtained by potentiodynamic polarization (±10 mV/Ecorr, 0.1 mV/s) for 310 SS in 0.5 M H_2SO_4 at (a) 60 ° C (b) 70 ° C and (c) 80 ° C..... 141
Figure 50: LPR Polarization curve obtained by potentiodynamic polarization (± 10 mV/Ecorr, 0.1 mV/s) for 304 SS in 0.5 M H_2SO_4 at (a) 60 ° C (b) 70 ° C and (c) 80 ° C..... 142
Figure 51: LPR Polarization curve obtained by potentiodynamic polarization (±10 mV/Ecorr, 0.1 mV/s) for 304 SS in 0.5 M H_2SO_4 at (a) 60 ° C (b) 70 ° C and (c) 80 ° C..... 143
Figure 52: Comparison of ICR as a function of compaction force for 310 SS, 904L SS, 304 SS & 316 SS 144
Figure 53: Interfacial contact resistance for 310 SS, 904L SS, 304 SS and 316 SS at the DOE recommended compaction force of 140 N cm^{-2} 145
Figure 54: Polarization characteristics (E_{corr} – 2600 mV_{HRE} at 1 mV s^{-1}) obtained on 316 SS showing current profile for passive, active and pitting regimes as a function of sulphuric acid concentration at 25 ° C and 1 atm. 152
Figure 55: Weight loss for anodization process of 316 SS as a function of Current density (C.D) and H_2SO_4 concentration at 25 ° C and 1 atm, at treatment time of 5 min. 156
Figure 56: Current efficiency for anodization process of 316 SS as a function of current density and H_2SO_4 concentration at 25 ° C and 1 atm, at treatment time of 5 min. 156

Figure 57: Current efficiency for anodization process of 316 SS as a function of treatment time and current density at room temperature in 0.5 M H_2SO_4 157
Figure 58: Polarization characteristics (1 mV s^{-1}) obtained on 316SS in 0.5M H_2SO_4 electrolyte showing current profile for passive, active and pitting regimes as a function of v/v% of glycerol 158
Figure 59: Electropolishing polarization characteristics obtained on 316 SS dependent on convection/stirring conditions in 0.5 M H_2S0_4 with no glycerol additive at temperature of 25 ˚C..... 160
Figure 60: Electropolishing polarization characteristics obtained on 316 SS additive dependent on convection/stirring conditions in 0.5 M H_2S0_4 with 10% v/v glycerol additive at temperature of 25 ˚C..... 160
Figure 61: Electropolishing polarization characteristics obtained on 316 SS additive dependent on convection/stirring conditions in 0.5 M H_2S0_4 with 30% v/v glycerol additive at temperature of 25 ˚C..... 161
Figure 62: Potential transient of 316 SS in 0.5 M H_2SO_5 with 0%, 10% and 30% glycerol additive at 12.5 mA cm^{-2} at 25 ° C for 1800 s 162
Figure 63: ToF SIMS isotope count (Fe, Cr, Ni and Mo) of untreated 316 SS (1) and treated samples of 316 SS in 0.5 M H_2SO_5 with 0%, 10% and 30% glycerol additive at 12.5 mA cm^{-2} at 25 165
Figure 64: SEM image of untreated 316 SS (left) alongside inverted image (right) at magnification ×900. 166
Figure 65: SEM image of treated 316 SS in 0.5 M H_2SO_5 with 0% glycerol additive, 12.5 mA cm^{-2}, 25 ° C, treatment time of 5 min, at magnification ×900, 0% (10 min) at magnification ×900 and 0% (30 min) magnification ×1500, showing general dissolution at grain boundary. 167
Figure 66: SEM image of treated 316 SS in 0.5 M H_2SO_5 with 10% glycerol additive, 12.5 mA cm^{-2}, 25 ° C, treatment time of 5 min, at magnification ×900, 10% (10 min) at magnification ×900 and 10% (30 min) magnification ×1500, showing general dissolution at grain boundary. 168

Figure 67: SEM image of treated 316 SS in 0.5 M H_2SO_5 with 30% glycerol additive, 12.5 mA cm^{-2}, 25 ° C, treatment time of 5 min, at magnification ×900, 30% (10 min) at magnification ×900 and 30% (30 min) magnification ×1500, showing general dissolution at grain boundary. 169
Figure 68: ICR as a function of compaction force for electrochemically treated 316 SS with 100:0 v/v glycerol additive (0%), 12.5 mA cm^{-2}, 25 ° C, at treatment times of 5, 10 and 30 min. 171
Figure 69: ICR as a function of compaction force for electrochemically treated 316 SS with 90:10 v/v glycerol additive (10%), 12.5 mA cm^{-2}, 25 ° C, at treatment times of 5, 10 and 30 min. 172
Figure 70: ICR as a function of compaction force for electrochemically treated 316 SS with 70:30 v/v glycerol additive (30%), 12.5 mA cm^{-2}, 25 ° C, at treatment times of 5, 10 and 30 min. 172
Figure 71: Close up of ICR as a function of compaction force for electrochemically treated 316 SS with 100:0 v/v glycerol additive (0%), 12.5 mA cm^{-2}, 25 ° C, at treatment times of 5, 10 and 30 min. 173
Figure 72: Close up of ICR as a function of compaction force for electrochemically treated 316 SS with 90:10 v/v glycerol additive (10%), 12.5 mA cm^{-2}, 25 ° C, at treatment times of 5, 10 and 30 min. 173
Figure 73: Close up of ICR as a function of compaction force for electrochemically treated 316 SS with 70:30 v/v glycerol additive (30%), 12.5 mA cm^{-2}, 25 ° C, at treatment times of 5, 10 and 30 min. 174
Figure 74: Polarization curves of 0% samples in comparison with 316 SS, in simulated PEFC anode environment (1 M H_2SO_4 +2 ppm F^- ions at 70 ˚C) purged with H_2 gas. 177
Figure 75: Polarization curves of 10% samples in comparison with 316 SS, in simulated PEFC anode environment (1 M H_2SO_4 +2 ppm F^- ions at 70 ˚C) purged with H_2 gas. 177
Figure 76: Polarization curve of 0% samples in comparison with 316 SS, showing potential range in simulated PEFC anode environment (1 M H_2SO_4 + 2 ppm F^- ions at 70˚C) purged with H_2. 179

Figure 77: Polarization curve of 10% samples in comparison with 316 SS, showing potential range in simulated PEFC anode environment (1 M H_2SO_4 + 2 ppm F^- ions at 70 ˚C) purged with H_2. 179
Figure 78: Tafel plots showing OCP shifts of 0% samples in comparison with 316 SS, in simulated PEFC anode environment (1 M H_2SO_4 + 2 ppm F^- ions at 70 ˚C) purged with H_2. 180
Figure 79: Tafel plots showing OCP shifts of 10% samples in comparison with 316 SS, in simulated PEFC anode environment (1 M H_2SO_4 + 2 ppm F^- ions at 70 ˚C) purged with H_2. 180
Figure 80: Polarization curve of 0% samples in comparison with 316 SS, in simulated PEFC cathode environment (1 M H_2SO_4 + 2 ppm F^- ions at 70˚C) purged with air..... 182
Figure 81: Polarization curve of 10% samples in comparison with 316 SS, in simulated PEFC cathode environment (1 M H_2SO_4 + 2 ppm F^- ions at 70˚C) purged with air..... 182
Figure 82: Close up of Cathodic range (800-1200 mV_{HRE}) of the polarization curve of 0% samples in comparison with 316 SS, in simulated PEFC cathode environment (1 M H_2SO_4 + 2 ppm F^- ions at 70˚C) purged with air. 183
Figure 83: Close up of Cathodic range (800-1200 mV_{HRE}) of the polarization curve of 10% samples in comparison with 316 SS, in simulated PEFC cathode environment (1 M H_2SO_4 + 2 ppm F^- ions at 70˚C) purged with air. 183
Figure 84: Potentiostatic data at anode operating potential of 100 mV_{HRE} in simulated fuel cell anode conditions (1 M H_2SO_4 + 2 ppm F^- ions), at 70 ˚C purged with H_2. 187
Figure 85: Potentiostatic data at cathode operating potential of 800 mV_{HRE} in simulated fuel cell cathode conditions (1 M H_2SO_4 + 2 ppm F^- ions), at 70 ˚C purged with Air. 188
Figure 86: Current density values over 200 scans (scan rate of 1mV cm^{-2}) at anode operating potentials; cyclic scans between OCP – 100 mV_{HRE} in

simulated fuel cell anode conditions (1 M H_2SO_4 + 2 ppm F^- ions), at 70 ˚C purged with H_2. 189
Figure 87: Current density values over 200 scans (scan rate of 1mV cm^{-2}) at cathode operating potentials: cyclic scans between 600-1500 mV_{HRE} in simulated fuel cell cathode conditions of (1M H_2SO_4 + 2 ppm F^- ions), at 70 ˚C purged with air. 190
Figure 88: SEM image of untreated 316 SS (left) alongside inverted image (right) at magnification ×900. 205
Figure 89: SEM image of 0% (5min) (left) alongside inverted image (right), showing general dissolution at grain boundary at magnification ×900. ... 205
Figure 90: SEM image of 0% (10 min) (left) alongside inverted image (right), showing general dissolution at grain boundary at magnification ×900. ... 206
Figure 91: SEM image of 0% (30 min) (left) alongside inverted image (right), showing general etching and some shallow pits at magnification ×1500. 206
Figure 92: SEM image of 10% (5 min) (left) alongside inverted image (right), showing general dissolution at grain boundary at magnification ×900. ... 207
Figure 93: SEM image of 10% (10 min) (left) alongside inverted image (right), showing general dissolution at grain boundary at magnification ×900. 207
Figure 94: SEM image of 10% (30 min) (left) alongside inverted image (right), showing general dissolution at grain boundary at magnification ×1500. 208
Figure 95: SEM image of 30% (5 min) (left) alongside inverted image (right), showing general dissolution at grain boundary at magnification ×900. ... 208
Figure 96: SEM image of 30% (10 min) (left) alongside inverted image (right), showing general dissolution at grain boundary at magnification ×900. 209
Figure 97: SEM image of 30% (30 min) (left) alongside inverted image (right), showing general dissolution at grain boundary at magnification ×1500. 209

Figure 98: Screen image of Ra measurement scan for untreated 316 SS, using AFM contact mode topography line scan at scan size of 90 µm. 211
Figure 99: Screen image of Ra measurement scan for 0% (5 min), using AFM contact mode topography line scan at scan size of 90 µm. 212
Figure 100: Screen image of Ra measurement scan for 0% (10 min), using AFM contact mode topography line scan at scan size of 90 µm..... 213
Figure 101: Screen image of Ra measurement scan for 0% (30 min), using AFM contact mode topography line scan at scan size of 90 µm..... 214
Figure 102: Screen image of Ra measurement scan for 10% (5 min), using AFM contact mode topography line scan at scan size of 90 µm..... 215
Figure 103: Screen image of Ra measurement scan for 10% (10 min), using AFM contact mode topography line scan at scan size of 90 µm..... 216
Figure 104: Screen image of Ra measurement scan for 10% (30 min), using AFM contact mode topography line scan at scan size of 90 µm..... 217
Figure 105: Screen image of Ra measurement scan for 30% (5 min), using AFM contact mode topography line scan at scan size of 90 µm..... 218
Figure 106: Screen image of Ra measurement scan for 30% (10 min), using AFM contact mode topography line scan at scan size of 90 µm..... 219
Figure 107: Screen image of Ra measurement scan for 30% (30 min), using AFM contact mode topography line scan at scan size of 90 µm..... 220

vi. List of Tables

Table 1: Representative physical properties of different carbon-carbon composites. 34
Table 2: Coating processes for metallic plates [62] 54
Table 3: Target values for different BPP performances characteristics 56
Table 4: Contact resistance between different BBP materials under varying compaction pressures. 59
Table 5: Simulated fuel cell environments used for corrosion studies of different BPP materials 61
Table 6: Bulk elemental composition (w.t %) of stainless steel (Supplier data) 113
Table 7: Stainless steel sample supplier details and dimensions 113
Table 8: Calculation of the charge required to dissolve 1g of 3166,assuming valency of Fe=3, Cr=6 and Ni=2. 120
Table 9: Corrosion current densities of tested stainless steel alloys determined by Tafel plot extrapolation method at 60, 70 and 80 °C. 138
Table 10: Comparison of corrosion current densities of 910L, 310, 304 and 316 stainless steel alloys determined by Tafel plot extrapolation method and LPR method at 60, 70 and 80 °C in 0.5 M H_2S0_4 139
Table 11: Current efficiencies and the associated data for the anodization process of 316 SS under different conditions. All measurements were performed at 25 °C 154
Table 12: Current efficiencies as a function of treatment time and current densities 0.5M H_2SO_4 and the associated data for anodization process of 316 SS under different conditions. All measurements were performed at 25 °C 155
Table 13: ToF SIMS isotope count (Fe, Cr, Ni and Mo) of untreated 316 SS and treated 316 SS in 0.5 M H_2SO_5 with 0%, 10% and 30% glycerol additive at 12.5 mA cm^{-2} at 25 ° C 164

Table 14: Ra measurements of 316 SS and treated 316 SS in 0.5 M H_2SO_5 with 0,10 and 30% glycerol additive, 12.5 mA cm^{-2}, 25 ° C at treatment times of 5, 10 and 30 min 170
Table 15: ICR values of 316 SS and treated 316 SS in 0.5 M H_2SO_5 with 0,10 and 30% glycerol additive, 12.5 mA cm^{-2}, 25 ° C, treatment times of 5, 10 and 30 min, at the DoE target compression force at 140 N cm^{-2}..... 174
Table 16: Comparison of corrosion current densities at E_{corr}, 0.1 mV_{HRE}, peak (i_{crit}) and passivation (i_p) of anodised treated and untreated 316 stainless steel determined by Tafel plot extrapolation method and LPR method at 70 °C in Anodic PEM fuel cell simulated environment..... 178
Table 17: Comparison of corrosion current densities of 316 SS and treated 316 SS (Treatment condition: H_2S0_4 + v/v glycerol additive of 0 and 10%, 12.5 mA cm^{-2}, 25 ° C, at 5 and 10 min) in the PEM fuel cell cathode operating potential range (800 mV_{HRE} and 1200 mV_{HRE}) at 70 °C in simulated PEM fuel cell cathode environment. 184

1 Introduction and Literature review

1.1 Fuel Cells

The industrialization of developing nations as well as an increase in world population has created a dramatic increase in the consumption of energy. The majority of the energy required worldwide is met through the combustion of fossil fuels; resources that have become an integral part of modern life. However, the excessive consumption of these energy sources has a significant adverse impact on the environment, resulting in health risks to all life forms as well as the threat of global climate change. Furthermore, the diminishing fossil fuel reserves are also intensifying international tensions, affecting national security and contributing to high inflation rates.

Fuel cells are a promising energy conversion technology which can help meet the requirements for energy security, economic growth, and environmental sustainability [1]. This is mainly due to the technical and environmental advantages offered by fuel cells such as high efficiency, reliability and clean power.

A fuel cell is an electrochemical device that converts chemical energy of reactants (fuel and oxidant) directly into electrical energy. In this sense it is similar to batteries; although in a battery the active ingredients are built into it during its manufacture, whereas in a fuel cell as they get consumed they are injected continuously from an external source. Whilst, although fuel cells and heat engines are both energy conversion devices with reactants stored externally; fuel cells operate isothermally at a given temperature and electrical energy is generated directly in a single step through electrochemical reaction [2]. Moreover, as there are fewer moving mechanical parts in the fuel cell itself, fuel cells can potentially deliver more reliable long term operation; therefore, it is expected that fuel cells will have a higher electrical efficiency than heat engines as there is no

Carnot limitation and the efficiency increases to about twice that of an internal combustion engine [3].

Fuel cells have technical challenges as well as practical issues such as manufacturing and material costs. In order to solve these issues, different fuel cell types have been tried and tested for various applications. There are approximately six classes of fuel cell that have emerged as viable systems and are usually distinguished by the electrolyte used; although there are other important differences such as operating temperatures [4]. The proton exchange membrane fuel cell (PEMFC) is the focus of this research.

1.2 Proton exchange membrane fuel cell (PEMFC)

The PEMFC is so named as it uses an ion conducting polymer electrolyte onto each side of which is bonded to a porous catalyst electrode. Thus the anode-electrolyte-cathode assembly is a single component usually referred to as the membrane electrode assembly (MEA), which are connected in series using bipolar plates, as shown in Figure 1.

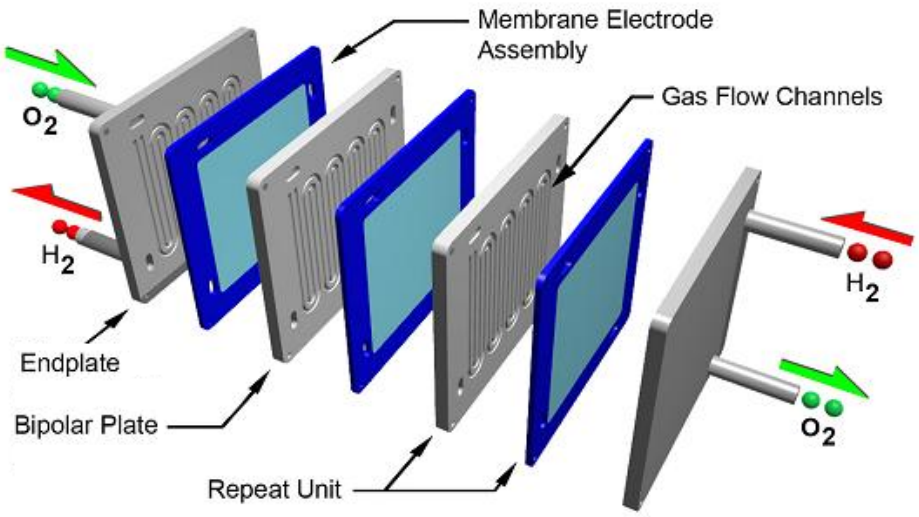

Figure 1: PEMFC, with end plates for drawing current from all over the face of the electrodes and also supplying gas to the electrodes [5].

The bipolar plates (BPPs) on either side of the cell serve the function of current collection and gas reactant distribution, with the latter

accomplished by flow distribution channels formed in the bipolar plate. The MEA is composed of the electrolyte membrane sandwiched between two thin catalyst layers and gas diffusion layers (GDLs). This unit cell is then connected in electrical series to form a stack.

The polymer electrolytes work at low temperatures (~80 °C), which has the advantage that PEMFCs can start-up quickly, and allows for compact design. Further advantages are that there are no corrosive fluid hazards and that the cell can operate in any orientation [4]. These factors make the PEMFC particularly suitable for use in automotive and portable applications.

1.3 PEMFC performance & operating principles

A fuel cell is composed of three active components; an anode (fuel electrode), a cathode (oxidant electrode) and an electrolyte. The fuel (hydrogen) is oxidised at the anode/electrode interface into hydrogen ions (proton) and electrons. The proton then migrates through the electrolyte, while the electrons are conducted around an external circuit; both arriving at the other electrode (the cathode) where the protons and electrons react with oxygen supplied, forming water. The two half-cell reactions that occur at the anode and cathode are:

Anodic half-cell reaction $H_2 \rightarrow 2H^+ + 2e^-$

Equation 1

Cathodic half-cell reaction $\frac{1}{2}O_2 + 2H^+ + 2e^- \rightarrow H_2O$

Equation 2

Thus, at the anode the hydrogen has been oxidised to form protons while on the cathode the oxygen is reduced to water by combining with the hydrogen ions and electrons. As a result, the overall cell reaction can be obtained by summing the above two half-cell reactions to yield

Overall cell reaction $H_2 + \frac{1}{2}O_2 \rightarrow H_2O + Electric\ energy$

Equation 3

In fuel cell operation, an electric potential difference exists between the anode, which has a lower electrical potential and the cathode, which has a higher electrical potential. This potential difference is known as the cell potential, E_r and has a thermodynamic value of 1.229 V when the fuel is pure hydrogen and the oxidant is pure oxygen at standard state of 25 °C and 1 atm [4]. It is often referred to as the reversible cell potential as it can only be achieved when the cell is operated under thermodynamically reversible conditions. Applying fundamental thermodynamic principles allows the reversible cell potential can be derived. The ideal potential for the PEMFC is given by the Gibb's free energy (Δ*G*), which is given by Equation 4.

$$\Delta G = \Delta G^{\circ} - RT\ln\left(\frac{a_{H_2} \cdot a_{O_2}{}^{1/2}}{a_{H_2O}}\right)$$

Equation 4

Where:

Δ*G*°	Standard free energy for the overall reaction
a_{H2}, a_{O2}, a_{H2O}	Activities of hydrogen, oxygen and water respectively.
R	Gas constant, 8.314 J mol^{-1} K^{-1}
T	Temperature, K

The electrical work done through Equation 1 & Equation 2, for the reaction at a unit activity of both reactants is equal to the Gibbs free energy release, as shown in Equation 5.

$$E_r = -\Delta G^{\circ} / n.F$$

Equation 5

Where:

n number of electrons transferred

F Faradays constant

The change in Gibbs free energy at standard conditions for the overall reaction is either -237.3 KJ mol^{-1} or -228.1 KJ mol^{-1}, depending on whether liquid water or water vapour respectively is produced [6]. Hence Equation 5 yields a reversible cell potential of 1.23 V and 1.18 V for the two products respectively, as shown by Copper *et al.* [6]. In order to calculate the theoretical cell potential under non-standard conditions, Equation 4 and Equation 5 can be combined and modified to form the Nernst Equation (Equation 7), assuming an ideal gas, activities can be replaced with partial pressures (Equation 6). Since for a mix of gas at low pressure; the activity is equal to the ratio of the partial pressure of the gas over the standard pressure [4].

$$a_i = \frac{P_i}{P^{\theta}}$$

Equation 6

$$E = E_r + \frac{RT}{n.F} ln\left(\frac{P_{H_2} P_{H_2O}^{0.5}}{P_{H_2O}}\right)$$

Equation 7

Where:

E Theoretical cell voltage under standard conditions

P_{H2}, P_{O2}, P_{H2O} Partial pressures of hydrogen, oxygen and water respectively.

The Nernst equation takes into account the Gibbs free energy of reaction and the partial pressures of reactants and products to determine the equilibrium reduction potential of a half-cell in an electrochemical cell or the total voltage (electromotive force) for a full electrochemical cell. It describes the measured electrode potentials measured (which is reversible

and reflects the maximum driving force for the reaction) for zero current flow between a reference electrode and the electrode.

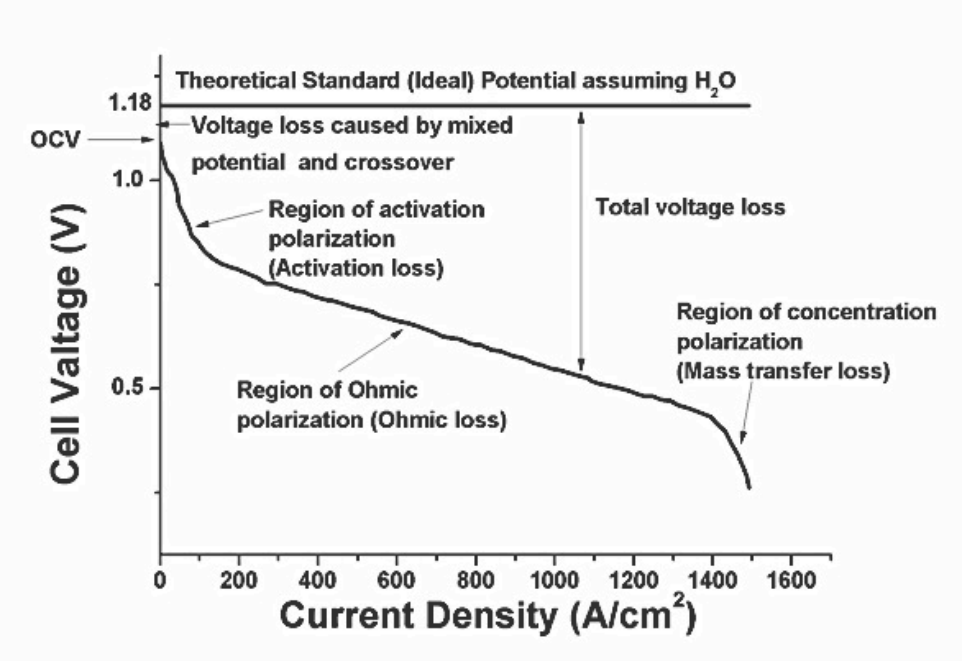

Figure 2: Typical fuel cell polarization curve and breakdown of cell voltages loses for an acid electrolyte [7].

In practice however, there are always energy losses (electrical potential losses) within the system due to irreversible losses which reduce the cell potential *E* to around 0.7 - 0.8 V [1] at typical operational current densities. As more current is drawn from the fuel cell (i.e. more power output from the cell), the cell potential difference decreases. The voltage losses within a fuel cell are more commonly referred to as overpotentials and are a consequence of a phenomenon known as polarization. Figure 2 shows a typical polarization curve that depicts the various losses associated with the fuel cell at various overpotentials, where: [8]

- A steep initial decrease at large load resistances where the voltage drops rapidly with increasing current, is attributed to the barrier for the electron transfer reactions occurring at the electrodes.
- A further decrease of the load resistance into the ohmic polarization region, the voltage decreases almost linearly with

the current, as the current is limited by the internal resistance of the electrolyte to ion flow

- Even further decrease of the external resistance, into the region know as the concentration, or mass transfer, polarization region, the current reaches a limiting value where the mass transfer of reactants to the electrode/electrolyte interface limits the reaction.

The output voltages of a fuel cell, can thus be expressed empirically by taking the thermodynamically predicted voltage output of the fuel cell and then subtracting the voltage drops due to the various losses:

$$V = E_r - \eta_{act} - \eta_{ohmic} - \eta_{conc}$$

Equation 8

Where:

V real output voltage of the fuel cell (V)

E_r thermodynamically predicted fuel cell output (V)

η_{act} / η_{ohmic}/ η_{conc} activation, ohmic, mass transport losses

1.4 PEMFC Challenges

Despite over 170 years of history, fuel cells are still not ready for widespread commercialization [9]. Factors limiting commercialization include excessive capital costs and limited durability. In order for PEFCs to appeal in the general market, and compete with current technologies, substantial cost reductions of both materials and their processing has to transpire. The DoE has projected the cost of automotive fuel cells to reduce from $106/kW in 2006 to $55/kW when manufactured a volume of 500,00 units/year ($67/kW at 100,000 units/year) in 2013 and is targeting a cost of $30/kW [10]. The estimates are based on a 80 kW_{net} automotive polymer electrolyte membrane (PEM) fuel cell system operating on direct hydrogen [10]. Therefore, factors such as material performance, cell lifetime and lower production costs that continue to retard development of fuel cells will require further development in order to reduce capital costs. The

bipolar plate (BPP) is an example of a component that still requires significant improvement in order to optimise fuel cell performance and realize operating targets [11].

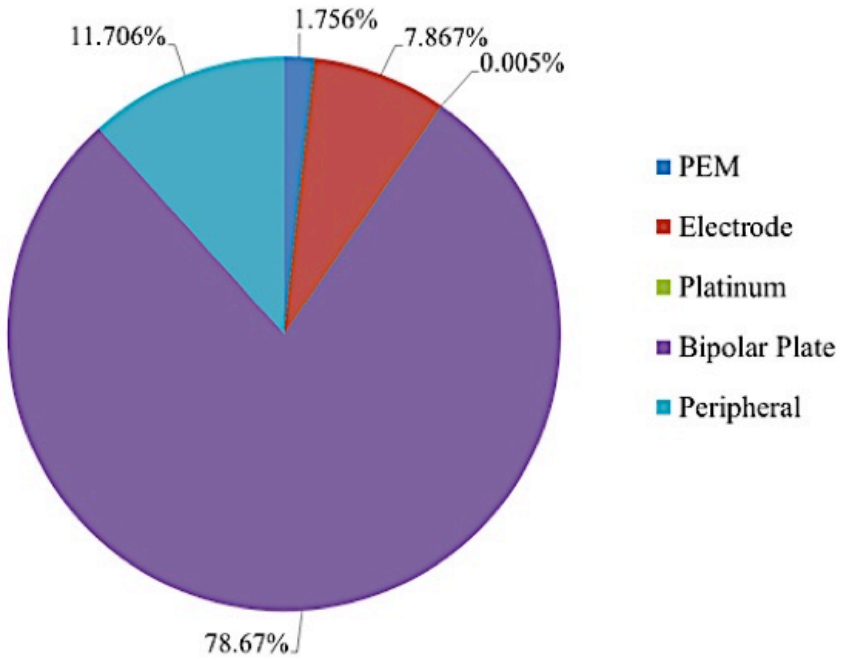

Figure 3: Weight structure of a fuel cell stack [12]

The price of raw materials and often complex processing during the manufacturing of BPPs makes it one of the most expensive parts of the fuel cell. Considering that the industry standard Graphite bipolar plate typically accounts for nearly 80% of the weight (Figure 3) and most of the volume of fuel cell stacks; the volume and weight specific cost per unit power is highly sensitive to the material and physical properties of the BPP [12]. Although estimates of the cost of BPPs vary widely depending on, cost evaluation methodology, differences in material, processing costs, operating conditions and improvements in the technology. The cost evaluation models can be instructive when assessing the relevant costs of BPP and have shown agreement with those published in literature within 10% [13].

1.5 Role of the Bipolar Plate

The bipolar plate constitutes the mechanical 'backbone; of the PEFC, and had multiple roles within a fuel cell [14], these include:

1. Carry fuel and oxidant to the respective electrodes and disperse them in an even manner.

- Physically separate the fuel and oxidant
- Conduct electronic current from each electrode.
- Provide mechanical support and strength to the membrane electrode assembly (MEA).
- Handle transmission of seal stress.
- Incorporate internal manifolds and help moderate the stack temperature by acting as a heat source/sink.

The multiple roles of the bipolar plate and the challenging environment in which it operates mean that the ideal material should be able to operate in an acidic environment of *p*H 3 - 5 in the presence of SO_4^{2-}, NO_3^-, Cl^-, F^- ions as well as potentials of 0 - 1000 mV versus HRE (Hydrogen Reference Electrode) by contact with the electrodes [15] and an operating temperature range of (60 - 120 °C) [16]. The ideal bipolar plate should incorporate excellent corrosion resistance, resistance to ion leaching, minimum electrical resistivity, be thermally stable as well as have good thermal conductivity, good mechanical strength and have a low contact resistance with the gas diffusion layer (GDL). Furthermore, they need to be thin and lightweight to increase the power density ratio, be inexpensive and easy to manufacture as well as being environmentally benign [14]. Thus the weight and size reduction, while maintaining the desired properties, is crucial in increasing the performance of a fuel cell and making it more commercially viable.

1.6 Bipolar plate materials

Materials used in PEFC as bipolar plates fall mainly into three categories with subgroups, which are grouped depending on what the material is based on, as demonstrated in Figure 4 [11];

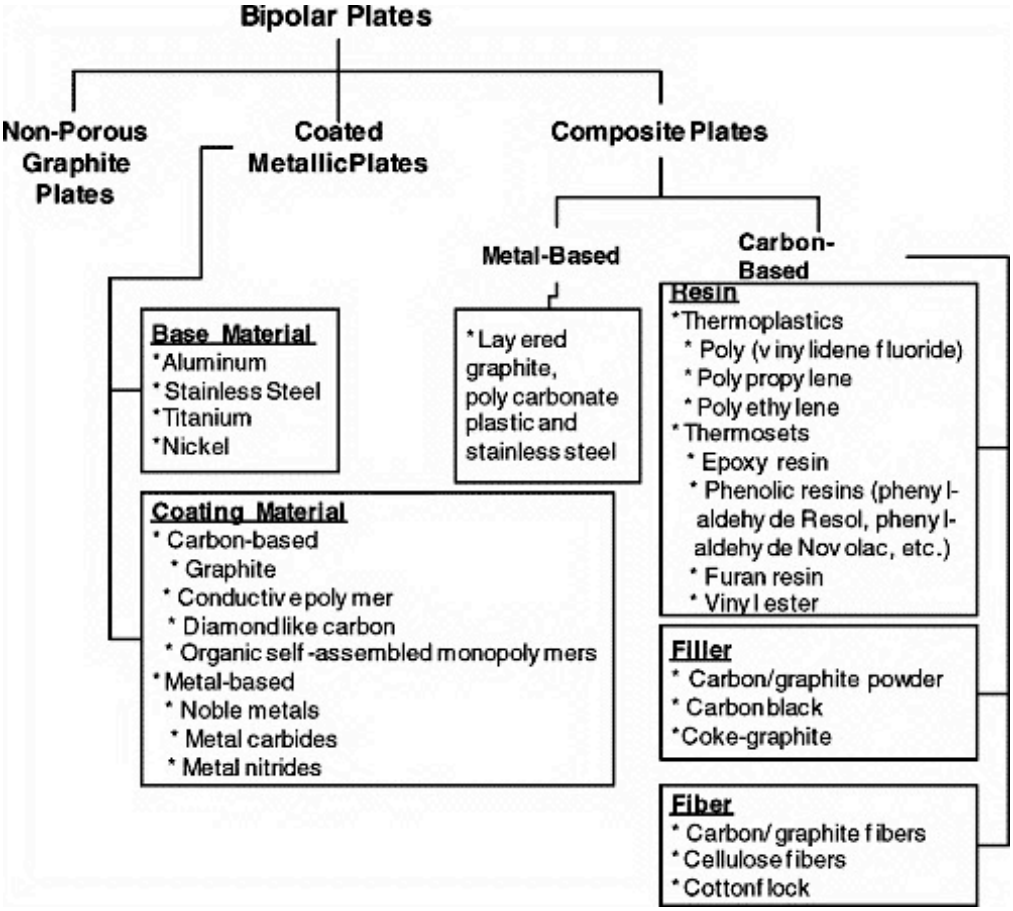

Figure 4: Classification of bipolar plate materials [17]

1.6.1 Graphite

Bipolar plates made from graphite, both natural and synthetic, have been considered the industry standard for PEFCs because of its excellent corrosion resistance, surface energy and contact angles [1]. However, its brittleness and lack of mechanical strength means it requires expensive machining. It is also relatively porous, which means thick bipolar plates must be used, reducing the specific volumetric and gravimetric power density of the stack. POCO Graphite (TX, USA) and SGL (Germany) provide

pyrolitic impregnation (a thermal treatment that seals the pores to a depth of ~7 mm into the surface of the graphite) to render them gas impermeable [18]. Such materials have demonstrated high electronic and thermal conductivity, low contact resistance, are corrosion resistant, easily machined and can operate at temperatures as high as 450 ˚C, unlike resin impregnated graphite which is limited to ~150 ˚C [11]. However, its relatively poor cost effectiveness for large volume of manufacture makes it unsuitable for commercialisation.

The current challenge is being overcome by use of various metallic and carbon composite materials that are more robust, thinner and less expensive to manufacture. GraphTec (OH, USA) have developed a flexible graphite bipolar plate material (GRAFCELL) made by expanding natural graphite [19]. This has the advantage of very low contact resistance and density as well as having excellent sealing characteristics and meeting basic costs targets. Grafoil, another form of expanded graphite, has also been considered as a bipolar plate. The soft and compressible nature of the materials means low contact resistance as its malleable attribute means it can mould itself around asperities on the surface, leading to greater surface contact [20]. The only disadvantages are that flexible graphite materials are mechanically weaker, therefore mechanical support will usually be required and that they tend to have relatively high gas permeability compared to other plate materials [11].

1.6.2 Composites

These are an alternative to graphite, offering a reduction in weight, manufacturing time and costs as they can be moulded or extruded into the desired shapes. Composite materials can be categorised as either carbon-carbon or carbon-polymer composites.

Carbon-carbon composites

Carbon–carbon composites, which consist of a carbon matrix reinforced with carbon fibres [21], are being applied to BPPs as a result of their

attractive characteristics: flexure strength, low density, chemical stability, high electrical and thermal conductivity as well as their ability to operate at high temperatures (in excess of 400 °C) [22]. Table 1 list the representative physical properties of different carbon-carbon composites.

Table 1: Representative physical properties of different carbon-carbon composites.

Property	Value	Reference
Electrical conductivity (S cm^{-1})	200 – 300	[22]
	500 - 700	[23]
Bulk resistivity (Ω cm)	151.6 - 131.1	[24]
	12.2 ± 4.2	[22]
	8 - 10	[23]
Flexural strength (kg_f cm^{-2})	394 - 209	[24]
	178.4 ± 26.5	[22]
	316 - 422	[23]
Density (g cm^{-3})	1.82 - 1.69	[24]
	0.96	[22]
	1.15 – 1.25	[23]
Water absorption (%)	0.133 - 0.287	[24]

Besmann et al. [22] proposed carbon-carbon polymer plates prepared by slurry moulding of carbon fibres suspended in water/phenolic resin mixture perform. This is followed by a chemical vapour infiltration (CVI) process which involves treating the component with a gaseous mixture containing methane at a temperature of 1500 °C, depositing carbon at the near-surface of the material, making the plate impermeable to reactant and significantly enhancing the conductivity [22].

A limitation of the process is the loss of dimensional tolerance as a result of shrinkage in the mould. This affects the accuracy of the plate thickness, which is particularly important as it can lead to seal leakage when the tolerance accumulates, as the plates are stacked. Advances in the moulding process accuracy have been made by Porvair Fuel Cells, who have

improved the thickness uniformity in length and width. However, currently the main disadvantage is considered to be the long processing time in comparison to carbon-polymer moulded plates, along with the high temperature CVI process associated costs, making the product expensive.

It has been claimed that the processing costs are not prohibitive in manufacturing, expecting that the material could be produced using a continuous process analogous to paper-making, and that penetrations, channels, and other features could be directly applied. Moreover, estimates of total costs indicate a 23 × 23 cm plate could be produced in high volume for <$2 / unit. This includes current materials cost (fibber, phenolic resin) of $0.12 / plate, estimate of batch preform processing cost of $0.26 / plate and CVI cost of $1 / plate (B.F. Goodrich Corp. quote for batch processing of 30,000 plates) [22]. Manufacturing in quantities exceeding 10^6 units per annum have been estimated at a cost of $10 kW^{-1} [23].

Carbon-polymer composites

Carbon-polymer composite materials have been developed as an alternative to carbon-carbon composites, made by incorporating carbonaceous material such as graphite, metal-coated graphite or low melting metal alloys into a polymer resin (thermosetting or thermoplastic) binder. The main advantages of these plates are that they are low cost, lightweight and amenable to rapid processing by means of compression or injection moulding, thereby reducing the cost as the machining process is removed. This approach has been developed further by SGL Technologies GmbH, who have developed a composite comprised of polypropylene and phenol bonded graphite which could be injection moulded [25].

However, until recently the performance of these composite as BPPs have been substandard to other materials as a result of low electrical conductivity. A high loading of graphite into the composite is required in order to increase the electrical conductivity without compromising too much on the mechanical properties and mouldability. Typical electrical

conductivity ranges from as low as 2.36 (2.14 at 70 °C) S cm^{-1} for 60 / 40 wt.% of polyvinylidende (PVDF) - carbon black (CB) composites [26] to 300 S cm^{-1} for composites with loadings as high as 93%.

The choice and proportion of carbonaceous material, polymer binding, other mechanical and conducting enhancing components are therefore vital in achieving the desired properties as well as determining the cost and processing conditions. *Kuan et al.* [16] have systematically studied the effect of graphite content and powder size on the physical, thermal, mechanical and electrical properties of a vinyl ester binder based composite and found that over a specific range of graphite loading (60 - 80% w.t) and graphite particle size (53 - 117 μm) to have a pronounced effect on the key properties and ease of processing.

Furthermore the choice of polymer binder also plays a significant role and is largely governed by the chemical resistance to the fuel cell environment, creep resistance, thermal stability, viscosity (when loaded with conductive filler) and the cost depending on the composition of the resin. Thermoset resins such as phenolics, epoxies, polyester and vinyl esters are currently most commonly used in carbon polymer composites as its low viscosity can accommodated a higher proportion of conductive filler, increasing the conductivity of the composite as well as facilitating the moulding process, allowing more elaborate designs.

On the other hand, thermoplastics such as PVDF, polypropylene and polyethylene have been applied to a lesser extent since they are generally less chemically stable than thermosets and have to operate at lower temperatures (typically 200 - 250 °C) to avoid melting [11]. Their higher viscosities limit the amount of graphite that can be loaded while maintaining the desired mould properties and temperatures, and as a consequence of this they suffer from lower electronic conductivity than their counterparts.

Liquid crystal polymer (LCP) with carbon content 85% have been developed by Thermotropic LC co-polyesters sold under the trade name Vectra®

(Ticona, Germany) and moulded by SGL Carbon. They have the advantage of accommodating higher carbon content due to the viscosity of the polymer. These materials have the advantage that they can be injection moulded while the higher carbon content improves the electrical and thermal conductivity. The structure of this material also has the added advantage of making the material stronger, stiffer, and more chemically resistant due to its molecular structure [27]. Furthermore, the material has also demonstrated very low hydrogen permeability of only 78 $cm^3\ m^{-2}\ d^{-1}\ bar^{-1}$ (Vectra® A 950) at room temperature [28], while still capable of operating at higher temperatures of up to 200 °C [11].

1.6.3 Metallic

The main advantage of using metallic BPPs is that they have a high electrical conductivity, lower gas permeation rate (in the order of 10^{-12} $cm^3\ s^{-1}\ cm^{-2}$ for 316 SS plates) [29], and are generally less expensive (material and processing cost) than carbon based BPPs [2]. Metals also are much denser than graphite or composites, and therefore a substantial reduction in their thickness is attainable [30]. Hence, they can be manufactured in thin sheets, realizing a reduction in weight and density compared to materials such as graphite. This in turn means increased volumetric and gravimetric power density.

Corrosion within the fuel cell environment is the main disadvantage of using metallic BPPs without use of costly precious metal coatings. It can take place both at the anode and the cathode of an operating PEMFC. At the anode, the surface oxide formation, which may act to prevent further corrosion, can be retarded as a result of the presence of a reducing environment, leading to unwanted hydride formation and dissolution of the metal in water [31]. At the cathode, the oxidizing environment can substantially increase the corrosion rate of metallic bipolar plates, leading to performance losses and even premature failure of the whole stack [31].

The surface oxide may also change the physical morphology (i.e. surface roughness) of the surface, potentially reducing the contact area with the

GDL [32] and consequently increasing the contact resistance between the bipolar plate and the GDL [33].

Moreover, the durability of PEM fuel cell can be adversely affected by contaminants such as corrosion products that increase the risk of contamination of the membrane electrode assembly (MEA). As the dissolution of the passive film occurs leached ions diffuse into the MEA leading to:[34]

- Kinetic effect due to a decrease in the catalyst activity involving poisoning of the catalyst
- Conductivity effect due to an increase in the solid electrolyte resistance
- Mass transport effect, hindering the mass transport of hydrogen and/or oxygen, caused by changes in the catalyst layer structure, interface properties and hydrophobicity

The main metallic suitability properties are determined by key factors such as weight, cost, corrosion resistance, ease of manufacture / processing and contact resistance. Bulk resistance of metallic BPPs is not usually considered as a factor as these values are very low for metallic BPPs, especially since they are made very thin [11]. Of all the issues mentioned above, cost is the most defining one and although various metals have been assessed and many qualify in terms of materials properties only a few meet cost targets [11].

Stainless steel, aluminium alloys, titanium alloys, nickel alloys, copper alloys, and metal-based composites have been used to fabricate plates. Research has mainly been focused on iron-based alloys, such as stainless steels, because of their low cost; however, more recently, considerable efforts have been expended to investigate noble metals, aluminium, and titanium as the material of choice for fabricating bipolar plates.

Surface modification or coatings have also been proposed and corrosion-resistant coatings have been developed to improve the corrosion and contact resistance, however, the cost of surface modification or applying a

coating are limited by the cost of candidate substrate SSs if cost targets are to be meet [35].

Stainless steels

Stainless steels have the advantage of low cost, high strength, good corrosion resistance and ease of incorporating a flow field via stamping or embossing [36]. The performance of stainless steel is however limited due to its inherent characteristics; in particular the formation of passive films in PEMFC environments, composed mainly of chromium oxide, which although it prevents the SS from further corrosion, it also increases the contact resistance due to the high electrical resistance of chromium oxide [35]. This can become particularly significant at the cathode of the fuel cell due to the oxidising environment [37].

There are three types of stainless steel, which contain varying quantities of Cr: Austenitic (18 - 20% Cr), Ferritic (17% Cr) and Matensitic (≥ 11.5% Cr). Chromium acts to form a thin oxide layer (Cr_2O_3), which protects the surface and inhibits corrosion and the formation of thick oxide films and ion leaching. However, the passive layer increases contact resistance between the plates and the GDL, which is accountable for the vast majority of the voltage drop. Due to this reason most studies of metallic BBPs use contact resistance measurements as the main criteria of material suitability.

Austenitic, or 300 series, stainless steels represent compositional modifications of the classic 18/8 (18% Cr - 8% Ni) stainless steel. The austenitic class offers the most resistance to corrosion in the stainless group, owing to its substantial nickel content and higher levels of chromium that give it an austenitic structure at all temperatures from the cryogenic region to the melting point of the alloy. They are the largest category of stainless steel, accounting for about 70% of all production [38]. To utilize inexpensive bipolar plates, commercialized steels such as types 316, 304 and 310 SS have received increasing attention as a replacement for nonporous graphite bipolar plates [39].

Some important compositional modifications of the 300 series of austenitic steels that improve corrosion resistance include [40]:

- Addition of molybdenum/ molybdenum plus nitrogen to improve pitting and crevice corrosion resistance.
- Addition of nickel and chromium to improve high temperature oxidation resistance and strength.

Ferritic stainless steels have been considered as bipolar plate materials as the low Ni content reduces the cost of the material and eliminates the potential problem of Ni ions contaminating the membrane. The performance of some ferritic steels was evaluated by *Wang and Turner* [37]. Studies of the nature of the passive film in ferritic stainless steel have demonstrated that nickel is not a major component in the oxide film [37], indicating that perhaps nickel could be eliminated without changing the performance. In addition, recent work has shown that nickel from 316L stainless steel can be a major contaminant in the membrane, reducing overall conductivity, chemical analysis after 100 h cell operation revealed an amount of 76 μ g cm^{-2} Nickel and almost no iron and chromium in the MEA [41].

Titanium

Titanium, because of its relatively low density, adequate mechanical strength and high corrosion resistance (due to an insulating oxide film) has been investigated as a material for bipolar plates. However, *Davies et al.* [39] found that the surface passive film on titanium plates in a PEMFC significantly increases ohmic loses within the stack, offering a much lower fuel cell performance compared to uncoated 316 SS.

Titanium alloys with Nb and Ta were studied as possible bipolar plate materials and it was found that the resistivity of surface oxides was lower than that of pure Ti [42]. Titanium coated with PEMcoat^{TM} FC5, a proprietary coating developed by INEOS Chlor, has been described as having a contact resistance similar to graphite [43].

Aluminium

Aluminium has the advantage of low density and cost compared to other bipolar plates materials. However, it has the same tendency as stainless steel and titanium to develop an oxide film that reduces the surface conductivity. This disqualifies it as a viable bipolar plate material except when used in combination with other metals or suitably coated.

The use of an inter-metallic coating formed by FeAl deposited on 316L SS plates for PEMFC has been proposed by *Frangini and Masci* [44]. Gold-coated aluminium was reported to operate similarly to graphite by *Woodman et al.* [45]; however, defects in the layer resulted in performance degradation, a problem associated with the coating procedure and more importantly use of precious metals significantly elevates the cost of the BPP.

Nickel

Nickel is a widely available material that is relatively inexpensive and exhibits ductility and manufacturability. However, pure nickel does not form a protective oxide layer and this means it is susceptible to severe corrosion (corrosion rate >1000 $\mu m\ cm^{-2}$) [45]. Therefore, it must be alloyed with e.g. chromium. *Shanian and Savadogo* [46] showed a Ni-50Cr alloy to be very stable with minimum corrosion rates and low electrical resistivity compared to stainless steel alloys.

Copper

The main advantages of copper alloys over conventional materials are that it has superior electrical and thermal conductivity. Studies of the copper beryllium alloy C-17200 in simulated PEMFC environment conclude a corrosion rate of ~0.28 $\mu m\ year^{-1}$ at 70 °C [47].

1.6.4 Coated metals

Oxide formation and ion dissolution due to corrosion of metal bipolar plates can be avoided by employing various coatings. The coatings should be conductive and adhere to the base metal without exposing the substrate to corrosive media while aiming to be impermeable to the

reactant gases, be chemically inert and provide low contact resistance. Another key issue is the integrity of the coating, as it has to be resistant to cracking, blistering and pinhole formation since these can accelerate corrosion of the substrate.

The main types of coatings commonly used are:

- Carbon-based coatings - graphite, conductive polymer, diamond-like carbon and organic self-assembled monopolymers.
- Metal-based coatings – noble metals, metal nitrides, metal carbides and chromium coatings.

Graphite coatings

Graphite protective coatings that are deposited directly onto stainless steel have been developed [48]. The coating is composed of three layers, the middle being spray coated graphite while the top and bottom layers are made from a high carbon content polymer, which upon pyrolysis forms a thick dense coating. These coatings are claimed to be strongly adherent to the substrate with high electrical conductivity and corrosion resistance.

Conducting polymers

Conductive polymers, such as polypyrrole (PPY) and polyaniline (PANI), have been deposited onto 316L [49] or Al alloy [50], both demonstrated very good corrosion resistance in comparison to the substrate. However, the immersion time was not accompanied with evolution of the electrochemical behaviour. Coating degradation was however considered for PPy-coated 304 SS which although demonstrated current densities as low as 0.2 µm cm^{-2}, current density increased with time as a consequence of the disappearance of the coating layer [51]. Despite the suitable corrosion properties for short immersion times, it is clear PPy and PANI coatings lack stability for a well-succeeded commercial use as protective layers on stainless steel bipolar plates.

Diamond-like Carbon (DLC)

DLC deposited onto stainless steel 316L substrate has been described as offering a combination of wear resistance, chemical inertness and good

metal adhesion properties [52]. *Lee et al.* [53] investigated the influence of DLC coating for as bipolar plate materials by studying the performance of aluminium 5052 alloy, PVD coated with a DLC film in a single cell PEMFC and concluded that such plates performed better than graphite, but the cell life was shorter.

Noble Metals

A thin coating of gold on a low cost substrate has been claimed to be an economical feasible alternative to graphite. *Lu and Wang* [54] used stainless steel bipolar plates with a gold coating of 0.5 µm in direct methanol fuel cells and reported a decrease in the contact resistance [45]. However, the main problem with this approach is that difference in thermal expansion coefficients (TEC) can lead to cracking as well as delamination of the coating. Furthermore imperfections in the coating (pinholes or cracks) can lead to the metals further down the electrochemical series being oxidised and dissolving with corresponding increase in the corrosion current, while the coating is reduced.

Metal Nitrides

The formation of a protective nitride layer directly onto titanium, chromium and alloys thereof, can impart high electrical conductivity and corrosion resistance. *Hentall et al.* [55], confirmed that coating 316L steel with titanium nitride reduces the long-term voltage decay rate almost to that of graphite. *Brady et al.* [56], studied the nitration of several nickel chromium alloys such as NI-50Cr and NI-30Cr with results indicating that CrN / Cr_2N based surfaces hold promise to meet U.S. DoE performance goals for automotive applications. However, these alloys are very expensive for PEMFC application and lower Cr alloys do not benefit from the same degree of corrosion protection.

Metal Carbides

Transition metal carbides and borides are metallic ceramics that offer excellent electric conductivity, low rates of diffusion of impurities, hardness, good resistance to mechanical wear and low rates of corrosion

[57]. *LaConti et al*. [58] described the use of moulded titanium carbides bipolar plates for use in PEMFC with suggestions that long term mechanical and thermodynamic stability could be achieved in acidic media at high anodic potentials.

Chromium coatings

Chromium - nitrogen films as a coating material for stainless steel plates have received some attention. *Fu et al*. [59] states that 316L SS plates coated with $Cr_{0.49}$ $N_{0.51}$ delivered good performance in terms of interfacial conductivity and corrosion resistance and exhibited high surface energy. *Wu et al*. [60] also examined the corrosion resistance and interfacial contact resistance of chromium-containing carbon films on unpolished 316L SS and concluded that the film with the highest chromium content; that is, 23 wt% Cr, exhibited the best corrosion resistance in the PEMFC simulated environment at 70 °C. However, it is imperative to note that although CrN-coated stainless steel plates exhibit higher corrosion resistance in reducing and oxidizing environments, the presence of any pinholes or micro cracks in the CrN film will initiate and enhance local corrosion, leading to performance loss and cell degradation.

1.6.5 Surface treated metals

The search for surface treatments of inexpensive and widely available metals that are capable of enhancing their performance in fuel cell environments is well established. Surface modification techniques, including electrochemical surface treatment, carburization, thermal nitriding, low temperature plasma nitriding and ion implantation, have been extensively investigated. Most electrochemical surface treatments involve the modification of the oxide layer by decreasing its thickness or enriching its chromium content, leading to higher corrosion resistance and lower ICR.

One of the promising techniques in surface treatment of austenitic stainless steels is carburization. Low-temperature carburization (between 450 – 470 °C) is preferred to enhance the corrosion resistance of austenitic

stainless steels while maintaining an acceptable hardness. Plasma carburization has been increasingly used to improve the surface properties of many metals, including stainless steels, owing to its environmentally friendly characteristics as well as the fact that it can readily penetrate micro gaps to give an even surface treatment [31].

1.7 Cost of Bipolar Plates

The predicted costs of a fuel cell vary widely among studies and with improvements to the technology are constantly being adjusted. Some of the key factors that have a significant effect on the predicted cost are: evaluation methodology, design hypothesis, fuel cell size, application and operating conditions [11]. However, a complete cost analysis should also take into account product lifetime, disposal cost, cooling plate numbers, technology licencing cost and manufacturing volume [12]. On this basis, cost evaluation models can be instructive particularly when they agree with published results.

Through the application of high-capacity manufacturing processes, the cost of fuel cells is expected to reduce significantly; therefore making PEFCs commercially viable. The expected costs for production of 500,000 units per year as estimated by several models; by *Lomax* et al. of Direct Technologies Inc. (DTI) in 1998 [61], update by *Arthur D. Little* (ADL) [62], for the Department of Energy and Transportation Fuel Cell program in 2000 (later by *Bar-On et al*. in 2002 [13]), by *Jeong and Oh* in 2002 [3], by *Tsuchiya et al*. in 2004 [12], and more recently in 2011 by The Office of Naval Research (ONR) [63]. These studies provided a sense of relative component cost and also demonstrate the effect each has on the cost evaluation and future predictions.

The ADL study calculations assume a stack net power of 50 kW, fuelled by reformate, in a system operating at a typical cell current of 310 mA cm^{-2} and cell voltage of 0.8 V. The stack consists of 376 cells each with an active area of 600 cm^{-2} and the BPP material is carbon composite. The total cost

of CA. $140 /kW is based on; ~75% due to raw materials, ~15% due to the BPP with smaller fractions attributed to the cost of energy, labour, tooling, and fixed overheads.

The Gas Technology Institute, through US DoE sponsored program (DoE # DEFC02- 92EE50477) in 2000 [64], set a cost target of $10 /kW as a production price for mouldable composite graphite BPPs. The report predicts raw materials costs of the order of $4 /kW or less, (running at 0.6 W cm^{-2}) and within $6 /kW for the manufacturing costs (for an annual production quantity of 100 M of fuel cells or 20,000 vehicles). However, this analysis assumes that the BPPs used are of a simple geometry; as with other types of BBP technology, the carbon composite moulding technique manufacturing cost is highly dependent on the level of complexity of the BBP features and overall cell design. This costing also assumes that no post-machining is required (i.e., all forming is achieved in the moulding process).

Jeong and Oh [3] apply simulation results of a developed power-efficiency curve used in modelling fuel cell systems to analyse the cost and the life-cycle cost of the fuel cell hybrid vehicle. They conclude that the main contributor to the high capital cost is the material cost ~68% (based on 2002 PEM fuel cell cost range of 1000 - 2000 $/kW), for the BPP in a fuel cell stack intended for automotive applications. Although they illustrate the significant cost of the BBP, the fuel cell model adopted does not consider the characteristics of current-potential and the auxiliary system in detail, which means such cost estimates are innately speculative.

Moreover, studies by *Tsuchiya et al*. in 2004 [12] describe the cost structure of the fuel cell stack ($/kW) and the possibility of reducing cost by learning curve analysis (a macro-scope model that describes human activity of accumulating knowledge or experience by cumulative production, and adapted to an industrial production processes). The cost structure assumes a 50 kW fuel cell for an average sized automobile production system. The assembly costs are based on the assumption of the typical performance of

single fuel cell of 0.6 - 0.7 V and 0.3 - 0.6 A cm^{-2} cell current density which equates to power density of 2 kW m^{-2} or more and a cell area estimate of 25 m^2; that is 278 layers with 30 × 30 cm cell area.

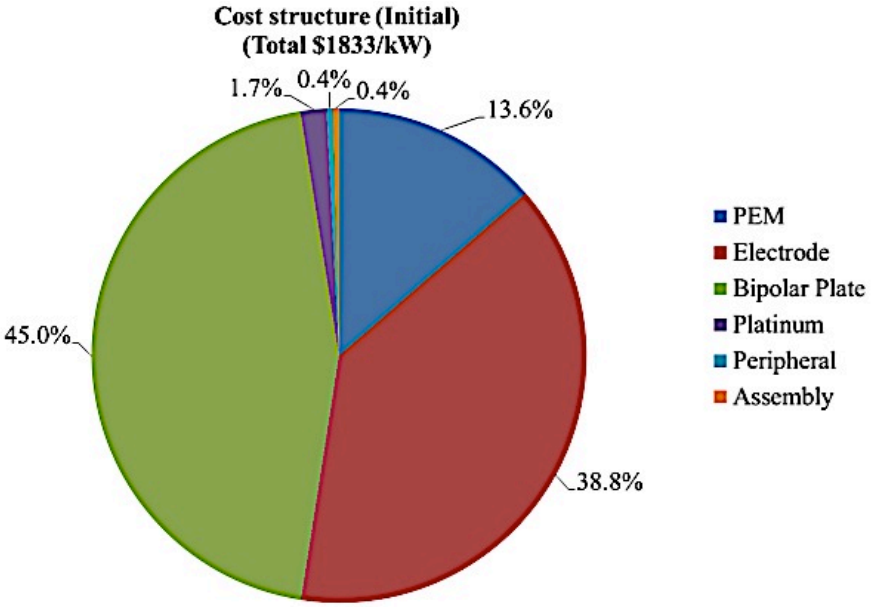

Figure 5: Fuel cell stack cost structure at the beginning of the learning curve analysis (2000) [12].

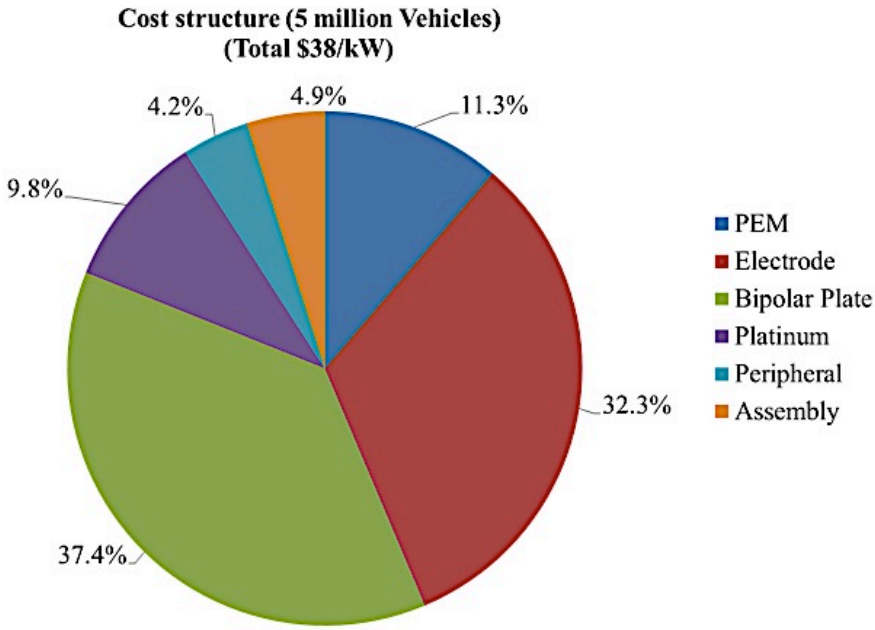

Figure 6: Fuel cell stack cost structure at 5 million cumulative vehicles (2020) [12].

The model predicts a reduction of the overall cost of a fuel cell stack from $1833 /kW to just $38 /kW, largely due to the fact BPPs and electrodes

dominate the cost share at the beginning (Figure 5 and Figure 6), but they become less dominated by a gradual increase in cost shares of platinum, peripherals and assembly. This is because; mass production (5 million vehicles) will decrease the total fuel cell stack cost ($/kW) and at the same time gradually increase the share of the elements with relatively large progress ratio that would remain with fewer learning effects.

The cost estimates for BPPs reported by Directed Technologies Inc. (2008) reflect advances made in technology, improvements / corrections made in the cost analysis, and alterations on anticipated 2010 and 2015 systems to be developed [62]. The report indicates that the choice of bipolar plate material / construction is purely a cost decision with the stamped metal plates appearing to be the most promising, with costs ranging from $3.17 /$kW_{gross}$ (2015 technology, 500,000 systems / year) to $6.75 /$kW_{gross}$ (2007 technology, 1,000 systems / year), compared to $3.45 /$kW_{gross}$ and $6.32 /$kW_{gross}$ for the injection moulded version. Here injection moulding machine cost is the main contributor accounting for ~75% of bipolar plate cost, with materials and tooling contributing to ~15% and ~10% respectively.

More recently studies (2011) conducted by ORN [63], sponsored and completed the Manufacturing Fuel cell Manhattan Project (MFCMP), aimed to determine the major fuel cell cost drivers, gaps and best practices. The study focused in on the affordability and manufacturability of fuel cells under 10 kW, along with their complementary balance-of-plant (BoP) and fuel processing (FP) subsystems with the aim of improving practices within the industry to meet the DoE's 2015 10 kW PEFC stack cost target of ~ $500 /kW. The balance-of-stack (BOS) is considered here to constitute the BPP as either a low temperature (LTPEM) or high temperature (HTPEM) PEFC component, which comprises of about 25% and 35% (Figure 7), of the total cost of the stack, respectively. The 10 kW stack model is representative of current commercial stack deliveries. Volumes were considered to be equivalent to low rate production runs (i.e. 10,000 stacks per year), a

realistic total platinum loading of 0.5 mg cm^{-2} and moulded graphite resin BPPs were assumed.

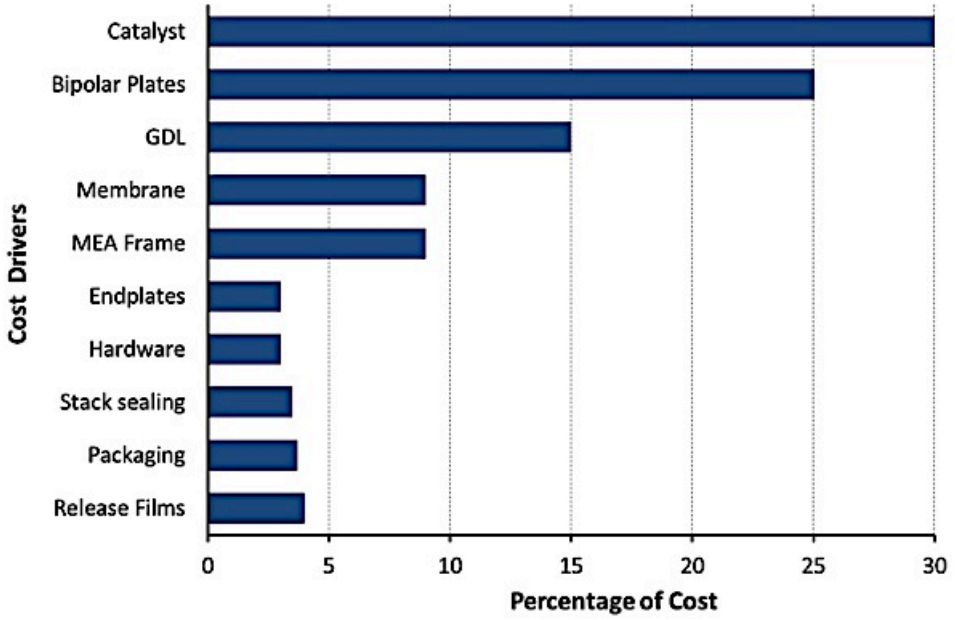

Figure 7: Cost drivers for polymer fuel cell stacks [63]

These descriptions are based on summing up all cell areas and there is no explicit expression of the number of cells. The cost of materials such as electrodes, bipolar plates and peripherals are assumed to be independent of power density. Furthermore, it should be noted that the performance of the membrane and the amount of platinum sometimes have a strong relationship with power density and these are not always considered. However, the cost structures discussed here all agree that estimates of bipolar plates (~29% for a carbon composite material [61] and up to 90% for stainless steel [13]) and electrodes have a large share of stack cost and this would still be very significant even at the mass production stage. And since the primary expense is always the material cost, for any particular material the most direct way to reduce the cost is to use less; this can be done by reducing the surface area and / or the thickness of the plate. In practice, a reduction of the geometric surface area necessitates an increase in power density, so as to maintain the overall specific power of the device, while consequently decreasing the resource use of other materials per unit power output [12] and optimising fuel cell performance [11].

1.8 Materials, Machining and Forming

The cost of BPP is mainly determined by the material, method of manufacture and in particular the forming of the flow-field geometry. As well as designing the flow-field, the production of a BPP has also to incorporate cooling channels along with features such manifolds and gasket grooves as seen in Figure 8.

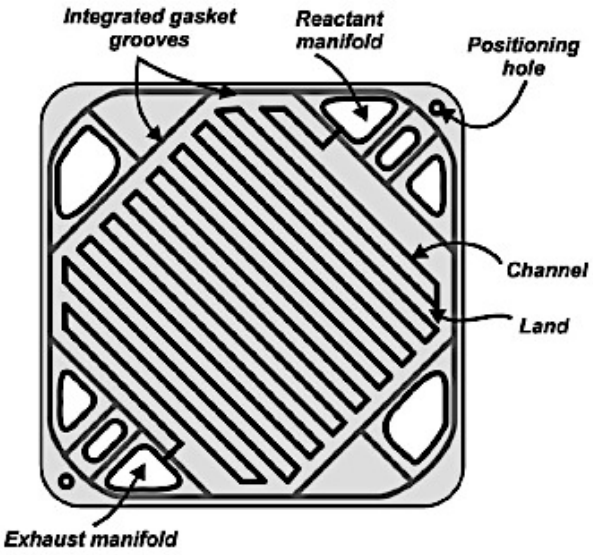

Figure 8: Bipolar plate image with incorporated flow field, manifold, gasket grooves and positioning holes [11].

Factors such as quantity, level of detail, dimension tolerance, and the range of materials that can be processed play a vital role in the aggregate cost [11]. Since each processing step required for a given part adds cost, with added operations directly resulting in increased cost per piece, it would be desirable to produce fuel cell repeat parts such as BPPs through a net repeat process. The suitability of a given material to the PEM fuel cell operating requirements then become the central issue [62]. Figure 9 provides the classifications of the bipolar plate materials and the manufacturing alternatives.

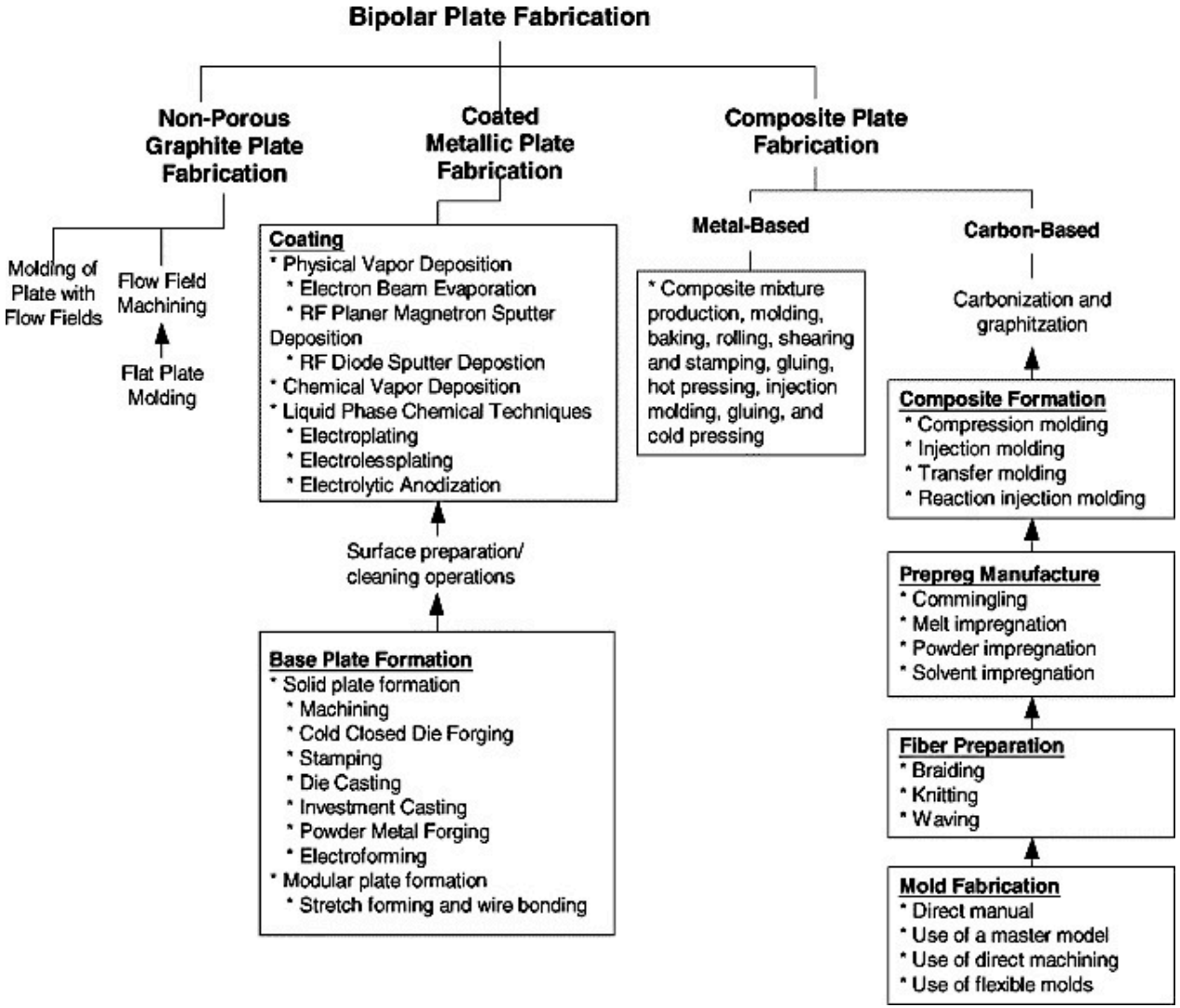

Figure 9: Classification of bipolar plate manufacturing alternatives [17].

The most common way in which prototypes are produced (particularly graphite plates) is manual or computerized numerical control (CNC) routing. The machining tolerance is high and although individual changes to flow-channel designs can be easily accommodated, the machining time for each plate is too long for large-scale manufacturing purposes, i.e. a single 200 cm^2 plate could take as long as 15 min [11]. The long cycle time, high capital cost of CNC machines and tool wear make machining of this sort an expensive forming method.

ElectroEtch™ is an etching technique developed by Morgan Fuel Cells (UK) for low-cost and rapid BBP feature fabrication. The process involves using a high-precision grit blasting technique to produce a plate in a matter of minutes. This offers a rapid prototyping capability, produce a plate in a matter of minutes; while allowing complicated flow-fields to be formed (down to 150 µm feature size with tolerance within ±25 µm) at a fraction of the cost as it takes the same time to etch any pattern [65].

Metallic plates have been demonstrated in the past, normally using costly metals such as titanium (Ti) or nickel (Ni), or coatings of noble metals such as gold (Au) on less noble structural materials. Recent evidence suggests that less expensive raw materials may suffice in the PEM automotive fuel cell operated on hydrogen and air [36]. This therefore suggests that a close examination of the cost implications of mass-produced, less expensive raw materials is warranted.

The most common means of manufacturing sheet metal articles at high rate is stamping [45], from a continuous coil of material which is pre-slit to width. This usually entails the use of a progressive die-set which completes all of the required operations on the metal fed from the coil in progression, with a completed part being ejected once per cycle of the stamping press, as shown in Figure 10 [62]. The machine rate for stamping equipment, which represents the levelized operating cost per unit production time including capital amortization, operator labour, and other costs, depends critically upon the total force developed by the machine.

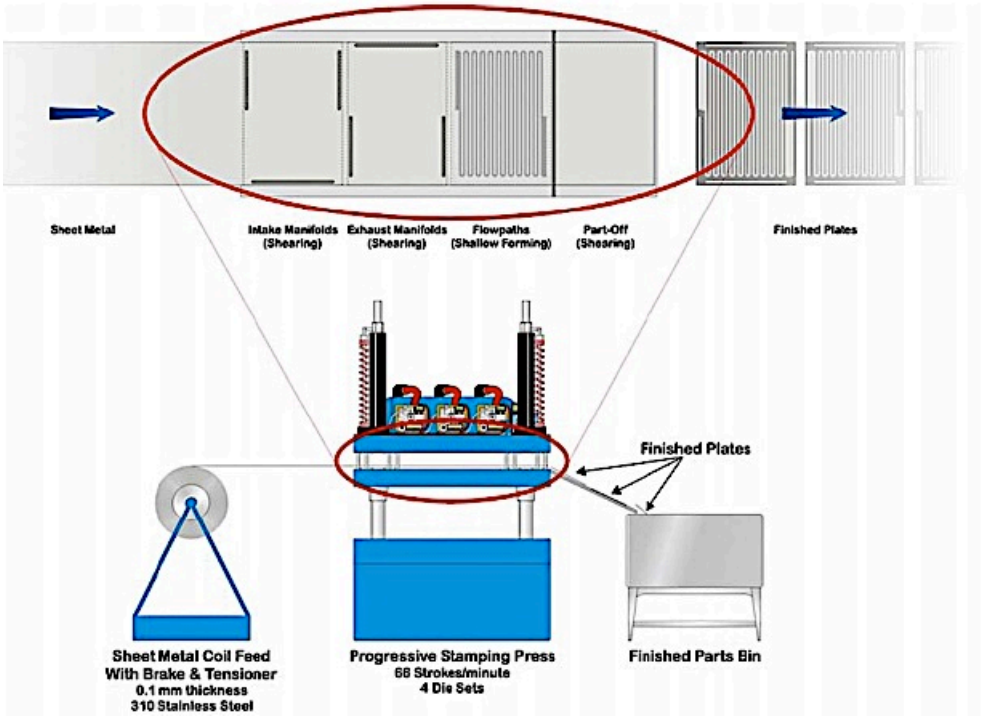

Figure 10: Bipolar plate stamping process diagram [62].

A wide variety of coatings and processes have been developed to address the concerns associated with bare metallic bipolar plates The process for fabricating coated metallic bipolar plates once the formation of the base plate is complete, includes: surface preparation and cleaning operations, and more importantly the coating processes. Coating processes for solid or modular metallic bipolar plates include a variety of deposition processes as listed in Table 2. Processes include physical vapour deposition techniques like electron beam evaporation, sputtering and glow discharge decomposition, chemical vapour deposition technique, and liquid phase chemical techniques like electro- and electro-less deposition, chemical anodization /oxidation over-coating, and painting.

The process brings significant benefits to metallic bipolar plate performance, but also incorporates an added cost to the manufacturing process. However, it has also been noted that using base metallic materials is far less costly and will help reduce the overall cost of metallic plate

coatings. Current costs of ceramic coatings developed by Impact Coatings (SWE) are current estimated at $5 /kW and are expected to reach below the US Department of Energy's 2017 target of $1 /kW [66].

Table 2: Coating processes for metallic plates [62]

Coating method	Coating processes
Gold topcoat layering	Pulse current electrodeposition
Stainless steel layering	Physical vapour deposition (PVD) (e.g. magnetron sputtering), or chemical vapour deposition (CVD) and electroless deposition for Ni-Ph alloy
Graphite topcoat layering	PVD (closed-field, unbalanced, magnetron sputter ion plating) and chemical anodization/oxidation over-coating
Graphite foil layering	Painting OR pressing
Titanium nitride layering	RF-diode sputtering
Indium doped tin oxide layering	Electron beam evaporation
Lead oxide layering	Vapour deposition and sputtering
Silicon carbide layering	Glow discharge decomposition and vapour deposition
Titanium aluminium nitride layering	RF-planar magnetron (sputtering)

Carbon composite bipolar plates have been made using thermoplastic (polypropylene, polyethylene, poly(vinylidene fluoride)) or thermosetting resins (phenolics, epoxies and vinyl esters) with fillers and with or without fibre reinforcement [67]. Carbon composites have the key advantage of introducing flow-field design during the moulding process, which is performed by compression or injection moulding. The primary advantage of injection moulding over compression moulding is a shorter cycle time, resulting in lower labour and machine costs.

Successful injection moulding requires that the thermoplastic (or less preferably, thermoset) polymer or filled polymer composite have an

adequate combination of material properties for the given application. Injection moulding also has the advantage of short processing times, i.e. as little as 30 s per plate [11], with very tight tolerances in one or more axes, fine surface details and with substantial variations in thickness. As a result of sophisticated injection moulding machines, the manufacturing automation and mass production process is made easier. Their cost estimate of production of injection moulded bipolar plates (assuming high purity carbon black as the conductive filler) stated costs between $3 /kW and $6 /kW to be fairly level across manufacturing rate. *Heinzel et al*. [68] have demonstrated injection moulded BBPs using a thermoplastic binder and conductivity-enhancing additives that affords process times between 30 and 60 s per plate with materials cost estimates in the region of 0.8 to 4 € /kW.

Although the injection moulding process in general offers many advantages, its drawbacks are excessive mould wear and limited size-to-thickness ratio due to high loads of graphite required to achieve conductivity targets [69]. The key factor in cost reduction for each of the advanced technology cases is that higher power density leads to smaller plate area. The main contributor to material cost was the electrically conductive carbon powder filler, considering relative resins are relatively inexpensive [62].

1.9 Bipolar Plate Characterization and Materials Testing

The suitability of a material to be used as a bipolar plate can only be made by a comprehensive range of tests (most of which are ex-situ) that characterise properties that meet proposed targets, as shown in Table 3.

Table 3: Target values for different BPP performances characteristics

Property	Value	Reference
Electronic conductivity	**>10 S cm^{-1}**	**[67, 70]**
	>100 S cm^{-1}	**[71]**
Contact resistance	**<50 mΩ cm^2 (Metallic after 5000 h)**	**[72]**
Thermal conductivity	**>20 W m^{-1} K^{-1}**	**[70]**
Gas Permeability	**<2.0×10^{-6} cm^3 cm^{-2} s^{-1}**	**[71]**
Mechanical strength	**>260 kg cm^{-2} (flexural)**	**[70]**
	>43 kg cm^{-2} (crush)	**[71]**
	>1.5 kg cm^{-2} (compressive)	**[67]**
Corrosion rate	**<1 µA cm^{-2}**	**[73]**
Dimensional tolerance	**>0.05 mm**	**[67]**
Density	**<5 g cm^{-3}**	**[67]**
Stack volume	**<1.1 kW^{-1}**	**[67]**
Surface finish	**<50 µm**	**[67]**
Release of contaminating cations	**<8×10^{-7} mol cm^{-2} (metallic during 5000 h)**	**[72]**
Water adsorption for carbon polymer composites	**<0.3%**	**[24]**

1.9.1 Bulk Electrical conductivity

Bulk electrical conductivity is an important parameter in determining the suitability of a material as a bipolar plate. Metals usually have a high bulk electrical conductivity (typically > 1×10^9 S cm^{-1}) [11], and hence this is not an issue. However it is usually an issue for carbon-polymer composites, which contain a significant amount of binder.

1.9.2 Contact Resistance

A significant source of Ohmic losses is due to the contact resistance that exists between the GDL and the bipolar plate. Several factors contribute to the contact resistance, including the extent of the physical contact, presence of passivating layers on the surface and the compressive force between the GDL and the bipolar plate. The level of the physical contact between the GDL and the bipolar plate depends on their nature (how dense, soft and porous) and how flat the samples are. A prime example is of a soft material such as Grafoil ^{TM} [74], which displays a very low contact resistance as the compliance of a soft material can adapt to the roughness in the contacting material.

In the case of metals, it is very difficult to study the passive layers of oxides and hydroxides that form on metallic surfaces as they are very thin and hence the exact mechanisms of charge transport across them is not known. The oxide layer formation of alloys such as steel have properties that are dependent on their composition, on the electrolyte and electrode potential that they are held [72]. The resistance measured is therefore considered literally as the contact resistance of the system. This is inclusive of the stainless steel and the passive film, rather than ohmic resistance of the passive film itself. The contact resistance, rather an inherent property of the passive film, instead represents the nature of the contact accompanied by the formation of the passive film. [75].

Ex-situ methods are available for approximating the interfacial contact resistance of a given bipolar plate and GDL material using the set up shown in Figure 11 (a) and (b) [11]. In the first set-up (Figure 11 (a)), copper plates are used to hold the arrangement together while under compression by some controlled means. A constant current is passed between the copper plates and the voltage drop between the two samples is measured. Using Ohm's law, and knowledge of the sample's area, the combined resistance of the GDL sheets and the contact resistance at each of the sample interface with the GDL can be determined.

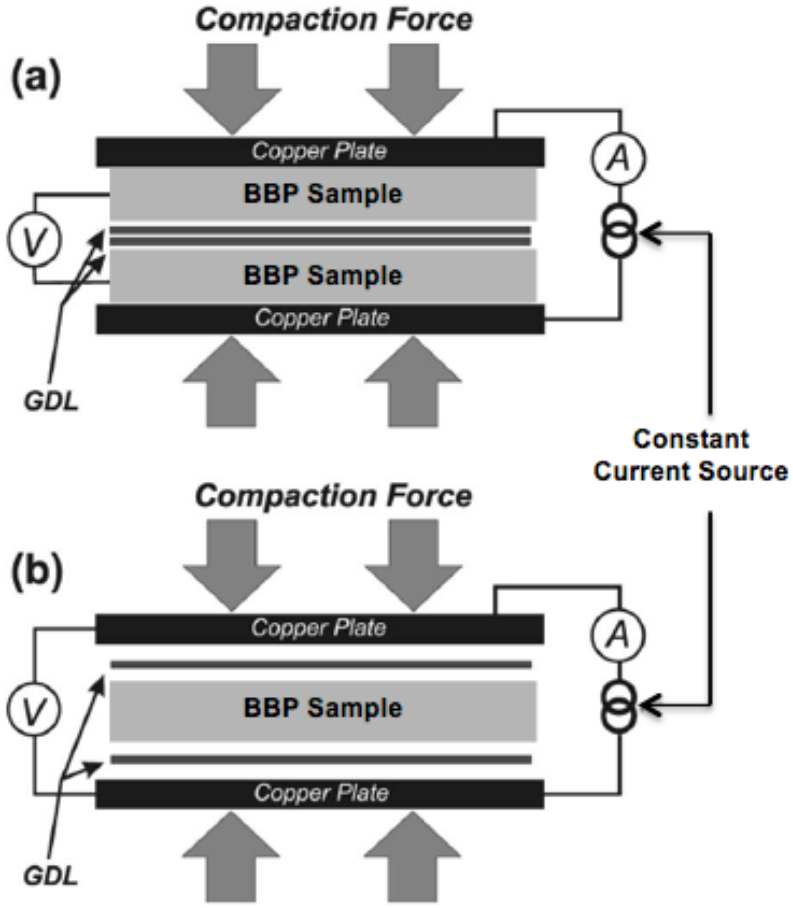

Figure 11: Ex-situ method of measuring interfacial contact resistance of a bipolar plate and GDL material using (a) two bipolar plate samples, (b) a single bipolar plate sample [11].

The second method (Figure 11 (b)) is performed and calculated in a similar way but has the advantage of only acquiring a single sample piece [24, 36]. However, since these measurements do not account for operating conditions and ageing effects, this means that they only provide a guide to the contact resistance existing within a real fuel cell. In-situ methods have also been developed in which gold voltage probes are reinserted at different points within a working cell [72, 76].

Landis and *Turner* [80], have developed a method for measuring bipolar plate conductivity by taking a dimensionally well-defined sample and making contact with it using two sharp pointed electrodes that are a defined distance apart and a constant current is passed through the material. Separate electrodes measure the potential difference established across the material, with the conductivity derived from the current, voltage

and dimensions of the sample. *Canningham et al.* [81] published details of making through-plane conductivity measurements with specific attention given to calibration methods and deconvolution of bulk resistance and other resistances.

Table 4: Contact resistance between different BBP materials under varying compaction pressures.

BPP material	GDL	Clamping pressure (MPa)	Resistance ($m\Omega\ cm^2$)	Ref.
Au-coated Ni	Carbon paper	0.1 -2.1	~20 -2	[77]
Fe-based alloy	Carbon paper	0.1 -2.1	~1000 - 100	[77]
Ni-based alloy	Carbon paper	0.1 -2.1	~100 -5	[77]
Graphite (Cathode)	E-TEK ELAT®	3	10	[72]
Graphite (Cathode)	E-TEK ELAT®	0.4	13	[72]
SS (1.3974) (Cathode)	E-TEK ELAT®	3	10	[72]
SS (1.3974) (Cathode)	E-TEK ELAT®	0.4	50	[72]
SS (316)	E-TEK ELAT®	0.4 - 0.8	~260 -170	[78]
SS (316) High Pt coating	E-TEK ELAT®	0.4 -0.8	~18 -15	[78]
SS (316)	CARBEL®	0.5 -3	120 -30	[79]
Poco® Graphite	CARBEL®	0.5 -3	~30 -10	[39]
Titanium	CARBEL®	0.5 -3	>100 -25	[39]
Steel (316,3 17L, 904L, 349™)	Toray™	0.1 -1.8	1400 -100	[36]
Ferritic steel (AISI 446)	Toray™	0.1 -1.8	1050 -175	[37]

The technique has the advantage of determining the effect of different operating conditions at the anode and cathode on the contact resistance. It was found that the contact resistance at the cathode (~20 mΩ cm^2) was significantly higher than that at the anode (~5 mΩ cm^2) for a given compression force. This is due to the oxide layer that is formed in the air environment in the cathode, whereas it may be reduced to leave bare steel in the hydrogen environment of the anode.

1.9.3 Corrosion Resistance

The internal environment of a PEMFC is warm, moist (up to 100% relative humidity), low pH (as low as *pH* 1), exposed to oxidising and reducing environments and operated at varying electrical potentials [11]. If the electrolyte is acidic as in the PEFC environment (anode *p*H 4.29, and cathode *p*H 4.66) [42], then the oxide layer may dissolve, exposing the underlying metal. This initially occurs only at localised points where owing to some discontinuity in the metal, i.e. the presence of inclusions or a grain boundary, dissolution will be more likely than elsewhere.

This creates a challenging environment for the application of metallic bipolar plates in terms of corrosion resistance and chemical compatibility. This issue is further complicated by the fact that when the fuel cell is not functioning, it is not possible in practice to eliminate water from within the fuel cell; hence the corrosion process is on going. As a result, corrosion should be considered over a period representative of the stack lifetime (in the order of 10 yrs.) and not just the operating lifetime (typically 5000 h).

In order to properly characterise the corrosion process a combination of tests are required as the environments of the anode and cathode are significantly different and this cannot be simulated in a single experiment.

Corrosion studies should be ideally performed in the fuel or oxidant environment in which the bipolar plate will operate, as well as a reproduction of the conditions present with a fuel cell. The presence of halides such as fluoride ions, have to be taken in consideration when

conducting BPP corrosion tests since they promote corrosion. Assuming perfluorinated ionomers are used as the membrane, fluoride ions will typically be present (around 1 ppm level) as a consequence of leaching out of perfluorinated polymer membrane [11]. Accelerated studies are typically utilised to provide an insight into the corrosion rates expected with the lifetime of the BPP; Table 5 shows some of the conditions used to simulate PEMFC's internal environment during accelerated tests.

Table 5: Simulated fuel cell environments used for corrosion studies of different BPP materials

Materials	Conditions	Ref.
Stainless steel alloys	1 M H_2SO_4 +2ppm F^- 70˚C, Purged with H_2 (Anode) and Air (Cathode)	[36, 37]
Stainless steel alloys	H_2SO_4 and NA_2SO_4, pH 4.8, Room temperature, no reactant gas	[75]
A1 and coated A1	0.5 M H_2SO_4, Room temperature	[53]
Stainless steel & coatings (TiN)	0.1 M K_2SO_4, pH1, 80˚C	[82]
Carbon-carbon composite	0.001 N H_2SO_4 + 2ppmF^-, 80˚C, N_2 purge	[22]
Stainless steel ASTM G5 standard	0.5 M H_2SO_4, Room temperature	[32]

1.10 Corrosion rate methodologies

The assessment of corrosion rate methodologies of BPPs has been comprehensively reviewed by *Shores* and *Deluga* [83], methodologies including mass loss measurements, linear polarization resistance, voltammetry polarization, electrolysis and half-cell tests are all discussed.

Other analytical methods such as electrochemical impedance spectroscopy [84], X-ray photoemission spectroscopy depth profiling [37], electron spectroscopy for chemical analysis and Auger electron spectroscopy depth profiling [32], have all been used to study BPP corrosion and surfaces.

1.10.1 Pourbaix diagrams

Pourbaix diagrams (E_H-*p*H-diagrams) are one of the most widely used applications of thermodynamics for estimating corrosion behaviour of different metals in aqueous solutions. The diagrams are used extensively in electrochemistry and electrochemical engineering, finding applications in the study of fuel cells, batteries, electroplating, extractive metallurgy, etc. They are used to determine the limits of stability of a metal in aqueous solution depending on the pH and electrode potential and the relative position of the boundary for oxidation and reduction of water [85]. Predicting the conditions under which corrosion is thermodynamically likely / unlikely to happen is a powerful tool when designing systems that avoid corrosion based on the potential and *pH* conditions.

Pourbaix diagrams present the potential (E_H) of a metal electrode referenced to the standard hydrogen electrode based on the Nernst equation, against the *p*H of the aqueous solution in which corrosion is taking place [85]. The corrosion rates and types depend on the chemical conditions in the aqueous solution. The E_H-*p*H-diagrams may be used in several ways, for example, to: [86]

- Find *p*H, potential and temperature regions, which prevent corrosion.
- Find out which compounds are the corrosion reaction products.
- Find immune materials, which can be used as protective coatings.
- Find a metal that will corrode sacrificially instead of the constructive material. For example, a galvanized the zinc layer on a steel surface.

The boundaries between the areas on an E_H-*p*H-diagram of a corrosion process represent the chemical reactions that define the equilibrium between the adjoining stable chemical species. The exact boundary position depends on the activity of soluble bearing ions [87]. The orientation of the lines indicates the nature of the reactions that take place:

- Horizontal lines – reactions that involve only the transfer of electrons and are independent of *p*H.
- Vertical lines – represent strict chemical reactions that involve H^+ and OH^- ions but are independent of E_H.
- Diagonal lines (positive or negative slope) – reactions that involve electrons, H^+ and OH^- ions.

However, it has to be noted that this only provides a basis for a first approximation of the thermodynamically stable species of the metal and gives no information about corrosion rates [88].

1.10.2 Potentials and polarization

Corrosion reactions involve the transfer of electrons and ions between the metal and the solution, whereby the rates (equivalent to electric currents) depend on the potential difference between the metal and the electrolyte (test solution). The rate at which corrosion occurs is determined by the equilibrium between opposing electrochemical reactions; anodic reaction (metal is oxidized, releasing electrons into the metal) and cathodic reaction (solution species O_2 or H^+ is reduced, removing electrons from the metal).

The rates of anodic reactions increase as the potential of the metal becomes more positive, consequently decreasing the rates of cathodic reactions. As the potential of the metal becomes more negative, the converse effect on the reaction rates occurs. The corrosion behaviour can thus be understood from the relationships between the potential of a metal and the currents flowing (equivalent to rates of the corrosion reactions). The relationships between potential and current may be

determined through polarisation curves as shown schematically in Figure 12.

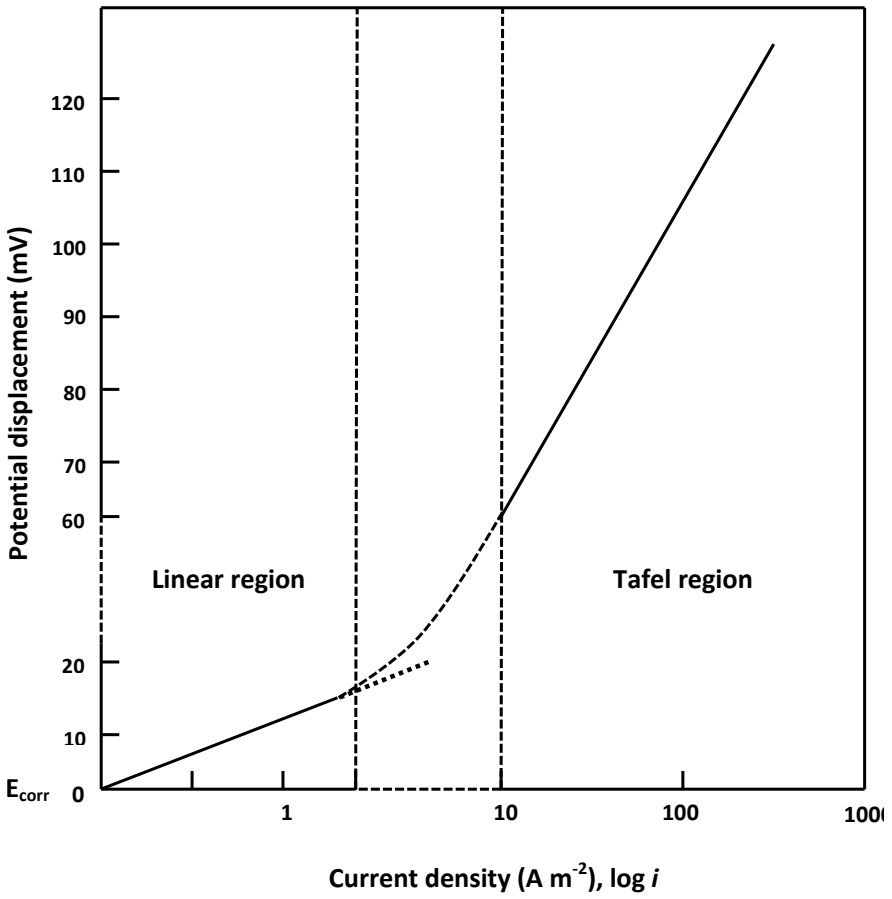

Figure 12: Schematic polarization curve for a corroding metal [89]

The thermodynamic tendency of a metal to corrosion can be determined by measuring its free energy from a standard measurement. The hydrogen reference electrode (HRE) is designated 0.00 V when at 25 °C and 1 atmosphere (atm) hydrogen fugacity and unit activity [85]. The electromotive series developed from this can be used to relate the half-cell reaction of a metal to the HRE. The deviation of a half-cell reaction from the HRE gives an indication of the strength of the driving force of corrosion, however, a large driving force does not necessarily imply a high corrosion rate; the reaction kinetics determine the corrosion rate.

The reference electrode, which ideally has a fixed potential regardless of the environment to which it is exposed, is chosen to give a stable and

reproducible potential in the solution. This means any changes of potential are attributed solely to the electrode under study and not the reference electrode. The commonly used in the laboratory is the saturated calomel electrode (SCE), which has a potential of +0.24 V_{HRE} and consists of mercury covered with a paste of mercurous chloride and mercury in a chloride solution. The potential depends on the concentration of chloride ions and a saturated solution of potassium chloride is used to maintain a constant chloride concentration (Metal / test solution / KCl (saturated), Hg_2Cl_2 (solid) / Hg). Contact between the test solution and the saturated potassium chloride solution of the calomel electrode is usually made through a porous ceramic plug, which minimises the mutual contamination of the two solutions.

1.10.3 Polarization behaviour of corroding metals

Polarization is the resulting electrode potential produced by a net current flow. In an acid solution the potential of the corroding metal (corrosion potential) is determined by the equilibrium between opposing electrochemical reactions. It is the potential at which the total rates of all the anodic reaction (dissolution of a metal) and cathodic reactions (reduction of hydrogen) are equal and is denoted by the symbol E_{corr}. The current density at E_{corr}, which is a measure of the corrosion rate, is called the "corrosion current density" and is denoted by the symbol i_{corr}. The potential E is initially a linear function of the current density, i (the current per unit area) when the potential of the corroding metal is displaced slightly, either by galvanostatic or potentiostatic polarisation from the corrosion potential E_{corr}. This departure from equilibrium at the interface can be described mathematically by the Butler-Volmer equation (Equation 9) [90].

$$i = i_0 \left[\exp\left[\frac{(1-\alpha)}{RT} \eta F \right] - \exp\left[\frac{-\alpha \eta F}{RT} \right] \right]$$

Equation 9

Where:

η is the overpotential, E-E_r

i_0 is the equilibrium exchange current density

α is the charge transfer coefficient ($\alpha_a + \alpha_c$=1)

The magnitude of this displacement is referred to as the overpotential, expressed as η and is the measured deviation in potential assuming that the equilibrium potential is zero. The linear relationship holds for a potential displacement of up to about ±10 mV [87] with a slope of dE/di proportional to the rate of corrosion expressed as the equivalent corrosion current density i_{corr}, i.e.

$$i_{corr} = \left[\frac{\beta_a \beta_c}{2.3\ (\beta_a + \beta_c)}\right] \frac{dE}{di}$$

Equation 10

The quantity $\beta_a\ \beta_c/2.3(\beta_a + \beta_c)$ is a constant (B), known as the Stern-Geary coefficient; which is measured experimentally or estimated [91], which yields:

$$R_p = \frac{B}{i_{corr}} = \frac{dE}{di}$$

Equation 11

$$i_{corr} = {}^{B}/_{R_p}$$

Equation 12

Where:

β_a and β_c anodic and cathodic Tafel slopes, respectively.

B Stern-Geary constant can be determined empirically or can be calculated from β_a and β_c the slopes of the anodic and cathodic Tafel.

R_p true polarisation resistance (di/dE)

Polarisation resistance measurements provide a valuable means of rapidly determining the instantaneous rate of corrosion of a metal. Weight loss measurements, or electrochemical data, can be used to determine the value of the constant *B*. As the overpotential of the metal is increased (±10 mV of E_{corr}), the polarisation curve increasingly deviates from the linear relationship between potential and current until a region is reached in which the potential exhibits a linear dependence on the logarithm of the current density, as shown in Figure 13. This electrode potential shift i.e. $E<E_r$ (the rate of the anodic reaction is suppressed from i_{corr} to i_a) or $E>E_r$ (similarly increasing the cathodic reduction reaction from i_{corr} to i_c) leads to the occurrence of a single electrochemical reaction on the metal surface. This is an indication that the displacement of potential is sufficiently large that one reaction overwhelms the other and current density is then represented by [89]:

For $E- E_r <<0$

$$i_c = i_0 \exp\left[\frac{\alpha\eta F}{RT}\right]$$

Equation 13

And for $E- E_r >>0$

$$i_a = i_0 \exp\left[\frac{(1-\alpha)\eta F}{RT}\right]$$

Equation 14

The relationship between the observed potential (*E*) and current density (*i*) can therefore be given as:

$$E - E_r = i_o + b\log i$$

Equation 15

Where:

$E-E_r$ overpotential (difference between the measured potential and the reversible potential).

i_o exchange current density (current density of the opposing reactions at the reversible potential).

b is the slope *dE/d log i* of the polarisation curve (termed the Tafel slope and is related to the kinetics of the corrosion reaction).

For the cathodic reactions of hydrogen ion reduction or oxygen reduction, the value of *b* is generally about 120 mV. For metal dissolution reactions from active surfaces, values of *b* are generally smaller and in the range 30 to 70 mV [89].

The anodic dissolution of a metal and the cathodic reduction of hydrogen ions in acid solution along with the juxtaposition of the anodic polarization curves are shown schematically in Figure 13. The relationship of the polarisation curves to the reversible potentials and exchange current densities of the metal dissolution and hydrogen ion reduction reactions is also shown. The value of the corrosion current density (i_{corr}) is determined through the extrapolation of the observed Tafel regions of the polarisation curves with the corrosion potential (E_{corr}) intercept. The values of the polarisation curve relative to the reversible potentials (which represent the extreme values, which the potentials of the anodic and cathodic areas can reach) and exchange currents of the reactions, can be determined through further extrapolation, as shown in Figure 13.

The combined cathodic and anodic reaction of hydrogen and iron (for example) where iron is corroding in acidic solution with both the half-cell reactions occurring spontaneously, is illustrated in Figure 13 [92]. At the high values of η, where Equation 13 and Equation 14 are valid, activation polarisation is no longer the controlling mechanism of polarisation. Rather polarization becomes mass transport dependent and is termed concentration polarization.

As the electrode reaction increases under activation control, the diffusion layer becomes depleted in ions available for the reaction, thereby producing a concentration gradient across it. The ability to supply ions from the bulk solution to the electrode becomes rate-limiting as the concentration gradient increases making the concentration polarisation the

rate-limiting step [89]. The concentration gradient produced across the diffusion layer by the reaction of the ions at the electrode surface is what creates this phenomenon.

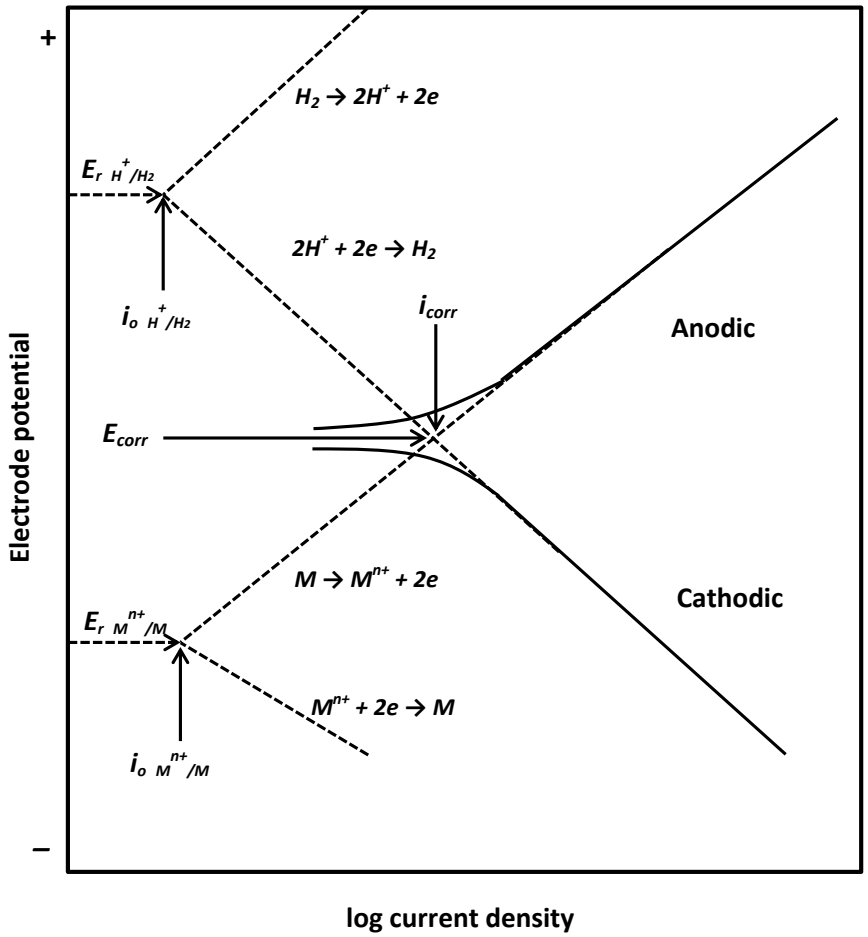

Figure 13: Development of corrosion potential (E_{corr}) and corrosion current (i_{corr}) from the combination of the two equilibrium electrodes [89].

The cathodic reduction of hydrogen ions or oxygen molecules, where these species must be adsorbed on the metal surface in order to react, is a good example of this phenomenon. In the Tafel region, the rate of reduction of hydrogen ions and oxygen molecules increases, as the potential of the metal is made increasingly negative. In turn the hydrogen ions or oxygen molecules are transported from the bulk solution up to the metal / solution interface (transport occurs by the processes of diffusion and convection, and in the case of hydrogen ions, electromigration). As the potential of the

metal is made even more negative, the rate of reduction may increase to such an extent that it exceeds the rate of transport of the reducible species to the metal surface. At which point the cathodic current density attains a limiting value (limiting diffusion current density), whereby the rate of transport of the reducible species controls the rate of reduction and is independent of potential. Two factors that lead to an increase of the limiting diffusion current density and its magnitude are:

- Increasing concentration of the reducible species.
- Increasing movement of the solution.

The rate of reduction of water to produce hydrogen increases as the potential becomes even more negative, until it exceeds the diffusion-limited rates of reduction of hydrogen ion or oxygen. The observed current density then increases due to the reduction of water. In this potential region the diffusion limited currents of hydrogen ions or oxygen reduction, continue to contribute to the total observed currents. The corrosion current becomes equal to the limiting diffusion currents, if in the region of the limiting diffusion currents the anodic polarisation curve intersects the cathodic polarisation curves.

Another important consideration in the polarization behaviour of electrodes is the *IR* drop, as an ohmic potential drop exists through the electrolyte and any oxide films that are present. The contribution of *IR* drop to polarization is equal to the product of the current and circuit resistance; of which the major contributors are formation of oxide films and low conductivity through the solution. The contributors of polarization resistance that can be measured at the corrosion potential, E_{corr} are [93]:

- The ohmic resistance (*IR*) drop R_{Ω}
- The true polarisation resistance, R_p

The total resistance is therefore be defined as:

$$R_T = R_\Omega + R_P$$

Equation 16

1.10.4 Passivation

In many metals the corrosion rate decrease above some critical potential, E_p, despite a high driving force for corrosion (i.e. high anodic polarization); this phenomenon is known as *passivity. Wagner* [94] offered an extension to this definition, the essence of which is: "A metal is passive if, on increasing the electrode potential towards more noble values, the rate of an anodic dissolution in a given environment under steady state conditions becomes less than the rate at some less noble potential".

Passivation is caused by a formation of a thin, protective, hydrated oxide, corrosion-product surface film that acts as a barrier to the anodic dissolution reaction [95]. A convenient way of understanding this phenomenon is by considering the potential–current density diagram of metal, as shown in Figure 14.

In this example anodic dissolution occurs at an ever-increasing rate until a critical current density (i_{crit}), is reached. At this point a substantial drop in corrosion current occurs to the passive current density (i_p), where the measured current ceases to increase with applied potential, at a potential known as the primary passivation potential (E_{pp}). The most negative limit/potential of stability of the passive state is the Flade potential (E_F), which is generally close to the critical passivation potential and depends on the composition of the solution. This behaviour is due to the reaction of the metal surface with water to form an oxide, e.g.

$$xM + yH_2O \rightarrow M_xO_y + 2yH^+ + 2ye^-$$

Equation 17

$$E_{rM_xO_y/M} = E^0{}_{M_xO_y/M} + \frac{RT}{F} ln\alpha_{H^+}$$

Equation 18

The formation of the passivating oxide film is observed to initiate near the peak B of the polarisation curve AB at the point where the i_{crit} is observed. A thin oxide film gradually spreads over until the surface is completely covered. At this point the current due to metal ions leaving the metal decreases gradually, consequently reducing the passage of metal ions through the oxide film. Therefore protecting the metal against corrosion by a passivating oxide film.

The i_{crit} gives a measure of the ease of passivation; the smaller the current, the easier it is to attain the critical passivation potential. The oxide film thickness increases to an equilibrium value until when the metal surface is completely covered; at this point the current becomes independent of potential. The passive current density i_{p}, which may depend on the anion content of the solution, passing through the passivating film is a measure of the protectiveness of the film.

The passive current density remains reasonably constant, as the potential of a metal in the passive state is made more positive until ultimately the current begins to increase with potential. The increase in anodic current (as along DE) is typically associated with localised breakdown of the passivating oxide film by anions (i.e. chloride ions), which leads to exposure of the underlying metal at weak points, grain boundaries, dislocations or inclusions in the metal. Further dissolution leads to the formation of pits, with the initiation occurring at a critical potential called the critical breakdown or pitting potential (E_b). The value of E_b depends on the ratios of the solution concentrations of inhibitive anions (which stabilise the passivating oxide film) and aggressive anions (which break down the oxide film). The breakdown of the film by the anions is inhibited with possibly no critical breakdown potential observed (as along DF), when the ratio of inhibitive to aggressive anions is high enough. The breakdown potential is observed to become more negative, as the ratio of inhibitive to aggressive anions decreases [89].

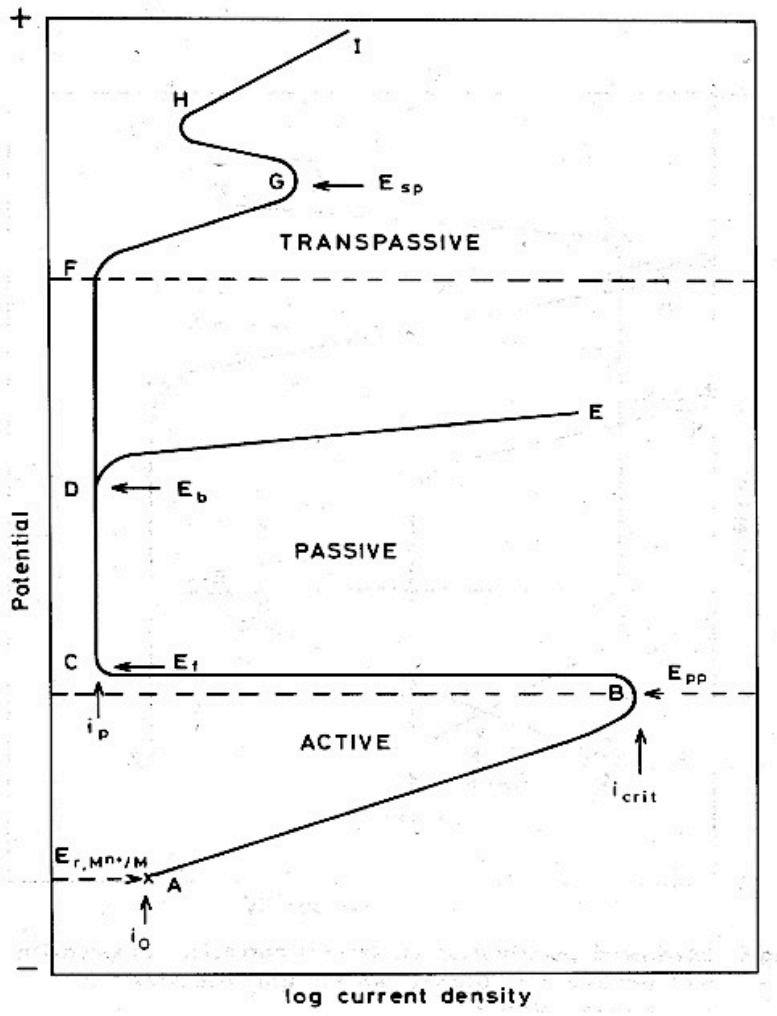

Figure 14: A schematic anodic polarization curve for a metal showing polarization behaviour [89].

An increase in anodic current with positive displacement is observed for some metals (such as along FG), if the composition of the solution is such that breakdown of the film by aggressive anions does not occur. This allows the oxidation of the metal to occur, which yields a soluble ion as in chromium containing alloys, such as stainless steels the chromium may be oxidised to form soluble dichromate ions. An important corrosion reaction that only occurs in strongly oxidising solutions, such as concentrated nitric acid is known as transpassive dissolution.

$$2Cr + 7H_2O \rightarrow Cr_2O_7^{2-} + 14H^+ + 12e^-$$

Equation 19

The rate of transpassive dissolution may decrease as the potential is increased in the positive direction, due to the onset of secondary passivity at G, where the potential range is associated with mass transport control and is characterized by a constant current density independent of the voltage applied. Further increase in potential leads to the anodic current increasing with potential along HI due to the evolution of oxygen as the breakdown of water occurs, as shown in Equation 20.

$$2H_2O \rightarrow O_2 + 4H^+ + 4e^-$$

Equation 20

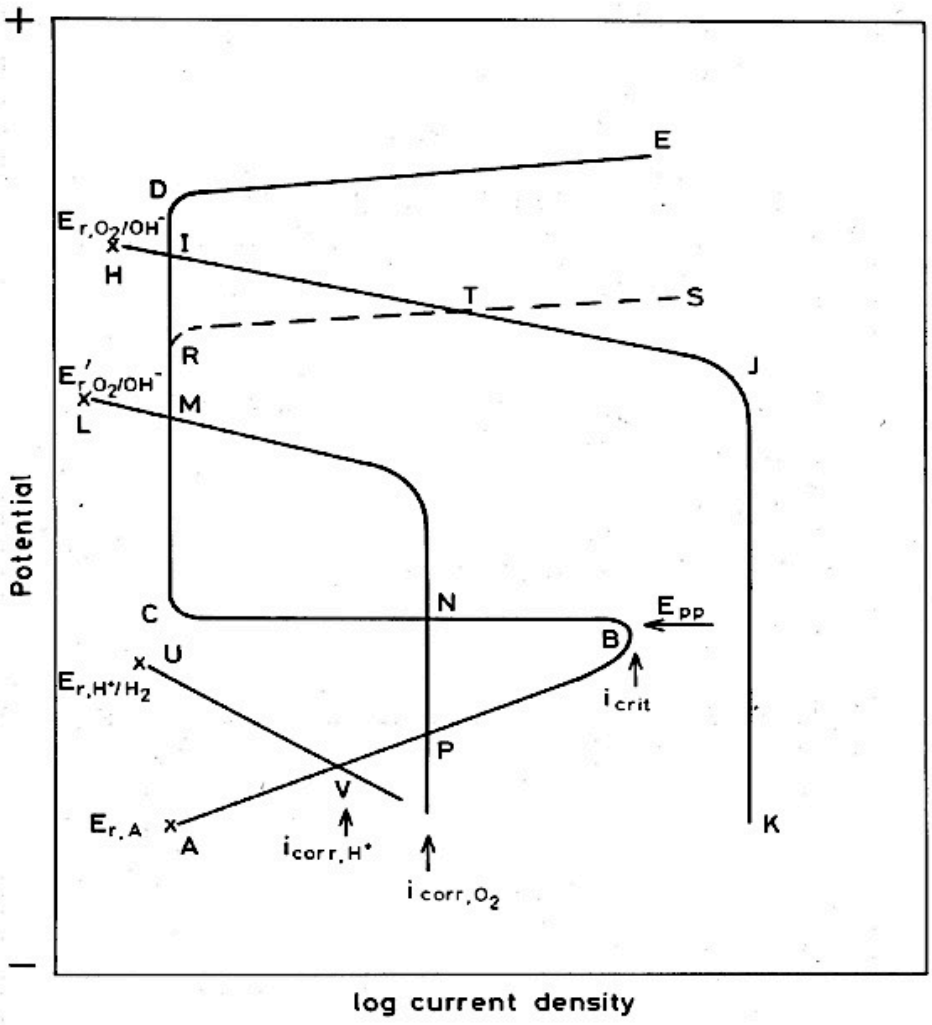

Figure 15: Schematic polarization curve for corrosion, passivation and passive film breakdown for stainless steels in dilute acid solutions [89].

An important aspect of corrosion protection is the formation of a passivating oxide film on metal surfaces. Anodic and cathodic polarisation curves of a system are utilised to determine where passivation is possible such as for stainless steel in dilute acid, as illustrated schematically in Figure 15.

The reduction of hydrogen ions at the cathode may occur in solutions that are oxygen free. In this case a cathodic polarisation curve UV that intersects with the anodic polarisation curve ABCDE at V, is observed. Passivation is not observed in this system as the reversible potential U, for the hydrogen ion/hydrogen equilibrium is more negative than the critical passivation potential B. The presence of dissolved oxygen, polarising metals into the passive region is possible. Dissolved oxygen is a more powerful oxidising agent than the hydrogen ion as the standard electrode potential for the oxygen/hydroxyl ion equilibrium (Equation 21), is 1.24 V more positive than that of the hydrogen ion/hydrogen equilibrium (Equation 22).

$$E_{r,O_2/OH^-} = E^0{}_{O_2/OH^-} + \frac{RT}{F}\ln\frac{a^4_{OH^-}}{p_{O_2}}$$

Equation 21

$$E_{r,H^{n+}/H_2} = E^0{}_{H^{n+}/H_2} + \frac{RT}{F}\ln\frac{p^{1/2}_{H_2}}{a_{H^+}}$$

Equation 22

However, in order to induce transition from the active to the passive state the reduction of oxygen must occur with such a high current that the limiting diffusion current density is greater than the i_{crit}. Thus the cathodic polarisation curve will be HIJK, intersecting the anodic polarisation curve at I; providing a stable corrosion potential in the passive region. The polarisation curve will be according to LMNP if only a small quantity of oxygen is present. The polarisation curves intersect at P if the steel is initially in the active state, as the reduction of oxygen cannot provide

sufficient current to bring the potential of the metal to the critical passivation potential. Therefore corrosion proceeds with the corresponding corrosion current. On the other hand, the polarisation curves intersect at M if the metal is already in the passive state, as the quantity of oxygen can maintain this state.

1.10.5 Corrosion of Stainless Steel Bipolar Plates

A state of immunity exists if the thermodynamically stable form of iron is the metal, hence the metal cannot corrode. Polarising a corroding metal cathodically (the process of cathodic protection) can bring it into the state of immunity by making its potential more negative such that it falls within the immunity zone. It is also possible for a protective oxide film to form on the metal surface, if the thermodynamically most stable state of iron is an oxide so that the iron is in the passive state.

In order to increase the range of protection and improve corrosion behaviour, alloying of metals through addition of chromium, which is well known for its good corrosion properties, is common practice. The reason for this is due to one of its solid reaction products, which acts as a protective barrier between the metal and the environment in oxidizing conditions through the formation of Cr_2O_3. The passive oxide film is self-healing and prevents further surface corrosion, blocking corrosion spreading in the metal's internal structure. The oxide typically grows by diffusion of cations from the metal to the oxide / solution interface via cation vacancies. [96].

The use of corrosion resistant alloys containing chromium, such as stainless steels, means an understanding of the limits for the good corrosion resistance is important. The Pourbaix diagrams for the principal alloying elements in stainless steels (Cr, Ni and Mo) are therefore particularly useful for studying the corrosion behaviour of many corrosion resistant alloys. Nickel is considered a relatively noble metal which is far more noble than Fe [97] or Cr [96], while molybdenum has a beneficial effect on it

encourages fine grain structure and improves tensile strength and yield point.

Although the stability of the metal in the corrosive environment is dependent on the thermodynamic and properties, insight into the kinetics of the electrochemical reaction occurring at the substrate of an alloy surface is only attained through the study of the potential-current density relationship. The corrosion potential gives a relative thermodynamic "ranking" of a metal or alloy in a given environment. In general, a more positive corrosion potential means that the metal can be expected to be more resistant to corrosion in that particular electrolyte than one with a more negative corrosion potential. However, ranking corrosion resistance based on corrosion potential is not very reliable. Therefore, other methods are used to determine actual or likely corrosion behavior. Stainless steels can exhibit active or noble potentials depending on whether they incur corrosion or are in a passive state depending on the environment and other factors.

The selection of a stainless steels (SS) type for bipolar plate applications largely depends on the Cr, Ni, and Mo content of the material as the nature of alloying elements strongly influence the composition of the passive film formed on the metal surface which in turn affects its overall corrosion resistance [36]. The pitting resistance equivalent, (PRE= %Cr + 3.3 x %Mo + 30 x %N) has been identified as a means of ranking and selecting different stainless steels for bipolar plates [77].

Early work by *Davies et al.* [39] on three types of stainless steel bipolar plates, namely, 310L, 316L, and 904L, reported that 904L performed the best while 316L exhibited the worst performance in an environment similar to that of a PEM fuel cell. The thickness of the passive film on the surface of various stainless steel bipolar plates was also later investigated using Auger Electron Spectroscopy (AES), due to its influence on the corrosion. It was reported that the thickness of the passive layer often varies between 3 to 5 nm, decreasing with the alloying element content [79].

Wang and Northwood [98], reported the influence of oxygen and hydrogen containing environments on the corrosion behaviour of 316L SS with regards to; Intergranular corrosion (localised corrosion in the vicinity of the grain boundaries) and pitting corrosion (localized corrosion by which cavities or "holes" are produced). In the simulated cathodes 316L SS bipolar plates showed a greater corrosion resistance, which was attributed to the cathodic protection ability of the oxygen-containing environments. In addition, potentiostatic tests after 5000 h of operation reported metal ion concentrations of about 25 and 42 ppm at the anode and cathode, respectively. It was concluded that such levels of ion concentrations can adversely affect the membrane as corrosion takes place in both anode and cathode environments and the application of a protective coating was necessary as confirmed by *Ma et al.* [82].

Kim et al. [75] investigated 11 stainless steel alloys (encompassing austenitic, ferritic and duplex stainless steels) exposed to sulphuric acid solution employed to simulate PEM fuel cell environment. They showed that change in transpassive transition behaviour of the stainless steels from that of iron to that of chromium occurred with an increase in the *Pitting Resistance Equivalent Number* (PREN), which is a theoretical way of comparing the pitting corrosion resistance of various types of stainless steels, based on their chemical compositions. They also demonstrated that the charge required to remove the passive film is greater for stainless steels with high PREN.

Iversen [99] investigated the corrosion behaviour of twelve austenitic, duplex and high molybdenum stainless steels for bipolar plate applications. The austenitic grade 904L and the duplex grade S32205 were the two candidates selected on the basis of their suitability with regard to corrosion resistance and contact resistance. Due to increase of contact resistance with time conventional grades such as 316L were found to be unsuitable. Furthermore, a suitable combination of manganese and molybdenum

additions to produce a high pitting resistant and electrically conductive stainless steel passive layer was suggested.

Wang et al. [36] also compared the electrochemical behaviour of 316L, 317L, 349 and 904L stainless steel grades in simulating fuel cell anode and cathode environments. The results pointed towards the following performance order 349 >904L > 317L > 316L which correlated the Cr content with the corrosion of the material; showing that the higher the Cr content the higher the corrosion resistance.

The corrosion behaviour of 310 and 304 stainless steels in an acidic electrolyte simulating the operative conditions of PEM fuel cells has also been studied by *Kumagai et al.* [100]. They found that corrosion products appeared on the cathode side bipolar plate for the type 304 SS. In contrast, traces of corrosion were barely detected for type 310 SS according to potentiodynamic polarization curves. This result was ascribed to the formation of a stable passive film on the metal surface. *Pozio et al*. [101] conducted potentiodynamic polarization tests with 304 and 316L stainless steels in simulating PEM fuel cell electrolyte. The corrosion current densities of both materials were found to be higher than the U.S DoE target of 1 μA cm^{-2} [73], while the interfacial contact resistance was also unsuitable for bipolar plate applications.

Shanian and Savadogo [46] on the other hand come to a conflicting conclusion as they ranked twelve different metallic materials as candidates for bipolar plates; five austenitic stainless steels (304, 310, 316, 316L and 317L), four ferritic grades (434, 436, 444 and 446), gold coated aluminium, nitride coated titanium and a nickel-based alloy. The selection criteria were based on mechanical, thermal and electrical properties, corrosion resistance, hydrogen permeability, cost and recyclability. They concluded that the two most suitable materials for bipolar plates according to the methodology adopted, were the austenitic stainless steels 316L and 316, respectively. However, the two main drawbacks of uncoated stainless steels when exposed to the fuel cell environment, i.e., increase of

interfacial contact resistance and the release of metal ions (that poison the membrane) were not considered by the selection process, producing a misleading conclusion.

Literature findings generally conclude that non-coated stainless steels almost always lack corrosion resistance leading to an increasingly poor performance in the fuel cell environment when used as bipolar plates. Therefore it is usually critical that some surface modification method or protective coating be applied on stainless steels in order to improve their performance against corrosion [82, 84].

1.11 Interfacial Contact Resistance (ICR)

The term interfacial contact resistance as applied to the bipolar plate often means the summation of all the resistances between the metallic substrate and the adjacent fuel cell component, typically a carbon based GDL [83]. Although stainless steel is a candidate material for bipolar plates as it permits plates to be as thin as possible and improve on the volumetric and gravimetric power density at reasonable cost, it is generally agreed that stainless steels are prone to chemical attack in the PEM fuel cell environment. Their corrosion products may poison the catalysts in the polymeric membrane and the oxide layer grown on the metal surface increases the interfacial contact resistance between contacting gas diffusion layers and bipolar plates decreasing the power output of the fuel cell [102]. These effects have a dramatic outcome on PEMFC stack efficiency, cost and consequently offset the advantages of metallic bipolar plates; such as their high electrical conductivity. In comparison to the industry standard, graphite, ICR increase results in a power loss in the order of 2 - 5% per each additional 25 mV cm^{-2} [72], while if the stack resistance increases from 0.05 Ω cm^{-2} to 0.2 Ω cm^{-2} , the price of a PEMFC stack (per kW) is estimated to be three times higher [103].

The direct measurement of conductivity of a passive film, in the course of electrochemical testing on different stainless steel samples, provide far

higher values than the values that are generally observed under working fuel cell conditions [75]. In contrast, the substantial surface conductivity degradation of different stainless steels observed in a PEMFC environment cannot be explained by all the data on contact resistance developed so far [39, 79]. It is clear that the performance of a PEMFC system can be significantly improved if the contact losses can be minimized.

The first studies that identified Fe-based alloys as potential materials for BPP's were by *Hornung and Kappelt* [77], they identified the ICR of metallic bipolar plates as the main criterion of material suitability. ICR measurements by *Davies et al.* identified a general trend whereby an increase in Ni and Cr content of stainless steel alloys lead to lower ICR due to the formation of thinner passive films. *Silva et al.* [104] also compared the ICR of 304, 310 and 316L stainless steels with those of a nitride-coated stainless steel specimen (SS 304/F). They concluded that the stainless steels were unsuitable because of an excessive amount of non-conductive oxide (e.g. [Fe + Cr] > 69% and Ni < 24%) that leads to high contact resistance values. The nitride-coated stainless steel specimen (SS304/F) presented a lower contact resistance value with respect to that of the best uncoated 904L stainless steel due to the presence of a low [Fe + Cr] amount. Wan *et al*. also investigated the applicability of different austenitic stainless steel compositions for bipolar plates by simulating the chemical environment of PEMFC. Similarly it was concluded that decreasing contact resistance and corrosion current were observed with increasing Cr content. The performance generally increased in the order 349^{TM} > 904L > 317L > 316L. The report is encouraging for the application of high chromium steels for bipolar plate applications.

1.11.1 Factors Influencing ICR

1.11.1.1 Surface oxide composition

The criterion to select stainless steels for bipolar plate applications sharply depends on the chemical composition of the material as the nature and content of alloying elements strongly influence the composition of the

passive film formed. The strong influence of the oxide film composition on the electrical conductivity of passive layer has been demonstrated previously by *Silva et al.* [104]. They studied the corrosion and ICR of 304, 310 and 316L stainless steels and four different nickel-based alloys regarding their suitability to operate in a PEM fuel cell environment. The surface oxide is a consequence of the alloying elements of the alloy and in a fuel cell environment this could lead to a thickening of the oxide, which in turn increases the contact resistance. *Davies et al.* [79] tested three different non-coated austenitic stainless steels, namely, 316, 310 and 904L grades. The properties of the alloy and passive film after the cells had been run for over 3000 h, without significant performance degradation and the surface resistance for each remained the same with the lowest ICR presented by 904L which has the highest chromium and nickel contents. *Kim et al.* [75] have investigated the contact resistance of eleven different alloys exposed to sulphuric acid solution to simulate PEM fuel cell environment. Chromium and molybdenum contents were found to be decisive for decreasing the contact resistance of stainless steels passive films formed at room temperature. However, it has to be noted that the corrosion rate of stainless steel in sulphuric acid increases as temperature increases [105] which may affect the passive layer composition and, hence, contact resistance.

Furthermore, the contact resistance between BPP and GDL can be effectively diminish through texturing the surface and depositing Cr-rich coatings such as chromium nitride (CrN), using physical vapour deposition (PVD) on the BPP [101, 102, 106]. *Wu* [60] and *Feng* [107] increased the surface Cr content by coating or implantation to improve the bipolar plate surface performance. The processed specimens verified the significant improvement in corrosion resistance and ICR. The results of the above works confirmed that Cr content plays a very important role in stainless steel used as metallic bipolar plates and are in accordance with this research project.

1.11.1.2 Surface roughness

Kraytsberg et al. [102] demonstrated that the ICR is nearly independent of the surface roughness for ground finishes down to the samples grinded with 16 µm emery paper, while samples with a smoother surface finish (i.e. treated with 8 µm , 6.5 µm emery paper and with 1 µm diamond powder) showed a substantially higher contact resistance. It is intuitively clear that if contact members are pressed one toward another, the contact resistance drops as pressure increases. The effect transpires as each contact spot increases the contact area under the load on account of material deformation and the amount of contacting spots increases because of dropping of contacting member separation. This increase in contact area results in diminishing contact pressure, (because the load, which is being applied in consideration to maintain a constant force per unit geometric area, is unchanged) in the areas of actual contact (*Am*).

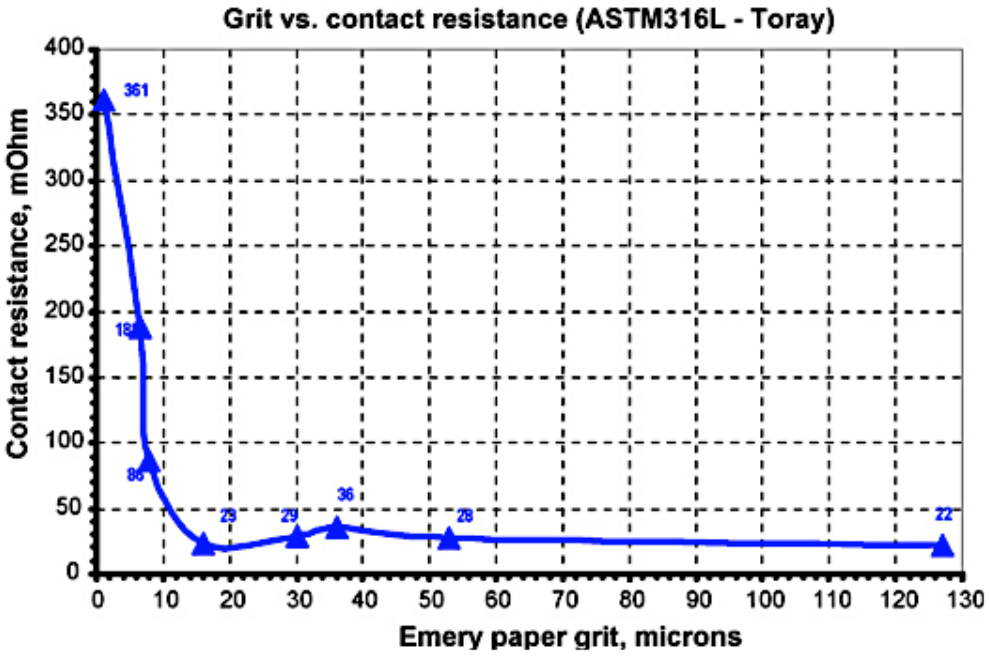

Figure 16: Surface roughness vs. contact resistance values obtained from ASTM316L stainless steel surface (treated with different grades of emery paper) in contract with TORAY paper [102].

Kraytsberg et al. [102] demonstrated that the decrease of the pressure is proportional to the increase of *A*m; whereas the dependence of contact

resistance *versus* pressure has a nonlinear and a very steep character. As a result, the decrease of the specific contact conductivity cannot be compensated by increasing the contact area and the overall resistance is expected to increase as can be seen in Figure 16 [102].

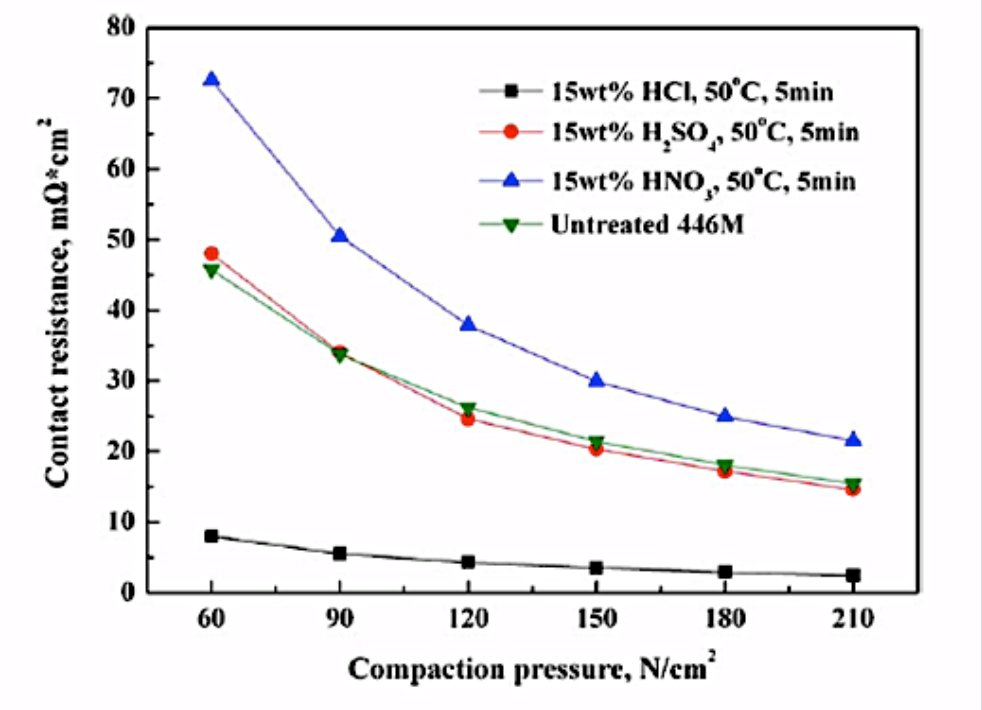

Figure 17: Interfacial contact resistance measured after various chemical treatments for 446M [108].

1.11.2 Theory of contact resistance

In this section due attention is given to the microscopic topography of a bipolar plate–gas diffusion layer interface in order to rationalise all these findings. It is commonly accepted that contact resistance is governed by the surface topography of the contacting pair. The voltage drop across the interface is considered to be a feature of the topographies of the contacting surfaces asperities which decrease the actual area in contact and hence the current which flows only through the contact asperities, as shown in Figure 18 [102].

Earlier models typically assumed the sizes of the actual contact asperities from experimental or theoretical points and then, assuming the asperities

being sufficiently widely spaced to be treated as resistances in parallel within a “macroscopic contact area” [102].

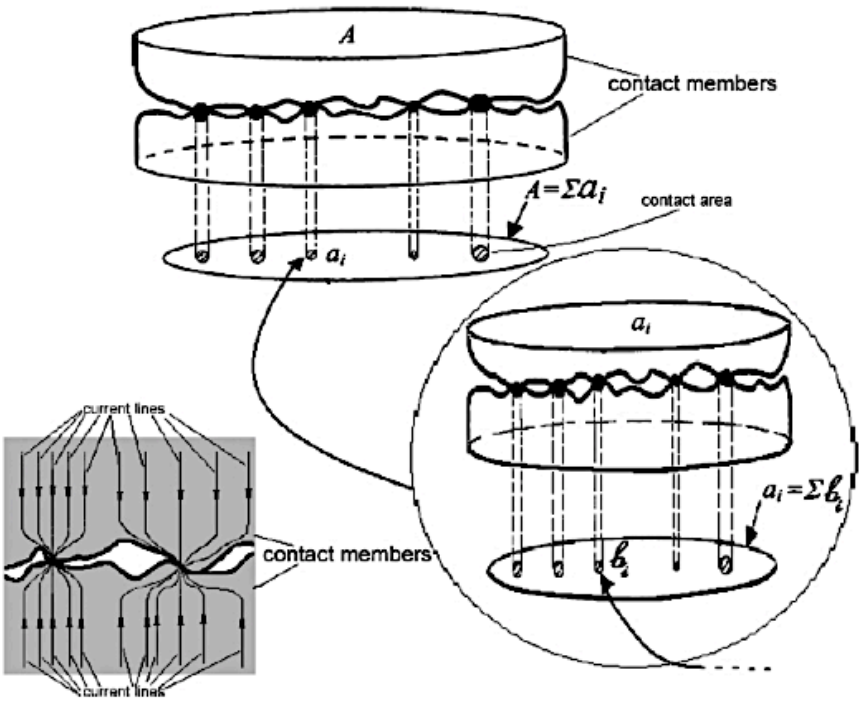

Figure 18: Schematic of real contact spots in case of normal contact surfaces (top and right) and a current restriction (left) [102].

Surface roughness is a multi-scale phenomenon; advances in surface measurement show that a single contact appearing on one scale may be resolved as a cluster of smaller contacts on the next smaller scale (Figure 18). However, contact resistance originates from current constriction in contact asperities and depends on the topography of the surfaces of the contacting members. Moreover, this proposition does not change even though the advanced contact resistance models are using such considerably sophisticated fractal geometry related concepts as fractal roughness and fractal dimension [109].

1.12 Surface treatment of Stainless steel

As mentioned earlier, metallic bipolar plates have many advantages over other materials; however, the issue of corrosion is key as it can lead to increased cell resistances and membrane degradation.

In this work a new and more subtle application of an electropolishing surface treatment method is investigated as a pre-treatment method to help form a more stable and robust surface with a higher surface Cr content which features a reduced corrosion rate and a significant decrease of the interfacial contact resistance.

1.12.1 Electropolishing

Electropolishing is defined in ASTM as the improvement of surface finish of a metal effected by making it anodic in an appropriate solution [110]. It entails the dissolution of metal from the surface to produce a uniquely advantageous surface finish compared to the cutting, tearing and smearing action of abrasives and cutting tools, which always distort the surface. It may be used in lieu of abrasive fine polishing in microstructural preparation [111]. Electropolishing process has been used as a surface treatment (polishing, brightening, etching etc.) for a variety of metallic materials and alloys, like stainless steel; which passivates to a greater extent than does any other passivation treatment. For example electropolished steel parts have been stored at 60 - 70% relative humidity for six months without visible rust [112]. It is a method for achieving new surface qualities that are outstanding in many applications while ensuring that cost saving and technical improvements are realised. This leads to a decrease in the corrosion current density due to the formation of a passive surface film enriched with chromium, resisting corrosion when there is no coating, while providing greater heat reflectivity and better emissivity.

In the literature it is common to distinguish anodic levelling or smoothing from anodic brightening. The former refers to the elimination of surface roughness of height > 1 µm the latter to the elimination of surface

roughness <1 µm comparable to the wave length of light [113]. The distinction however, is a simplification because there is no simple relationship between profile height measured for example by means of a mechanical testing device and brightness determined by measuring the specular reflectance [114]. The remarkable improvement in corrosion resistance of electropolished surfaces of austenitic stainless steels is caused by several interconnecting events occurring during the electropolishing process. These include;

- The removal of the solid (Beilby) layer that consists of inclusions of matertenistic phase, foreign material, pre-existing oxides (created by forming) and machining or abrasive polishing [12, 14].
- By creating a new corrosion resistant layer that is enriched in chromium oxide due to the anomalous co-dissolution of austenitic stainless steel.
- Equipotentialize the grain boundaries of metallic materials [25].

The dissolution of metal ions at the anode and deposition of these released metal ions on the cathode is generalised reaction that occurs during electropolishing. The surface processes that are characterised by the process are smoothing which occurs at the macroscopic level (dictated by the thickness of the viscous layer formed on the anode before it undergoes electropolishing) and brightening which occurs at the microscopic level (dictated by the formation of a thin oxide layer on the anode during electropolishing) [115]. Electropolishing is normally carried out in a bath composed of one or more concentrated acid media and the polishing process is thought to involve the formation of a viscous layer at the metal surface which is further emphasised by the employing moderators and viscosity improvers such as glycerol [111, 116, 117]. The addition of glycerol provides strong hydrogen bonds due to its three OH groups, which dominate the behaviour of adsorbed shielding molecules, resulting in the formation of a larger and more compact cluster layer. This action

suppresses the influence of the metal microstructure, leading to a smooth surface [118].

The work piece typically is immersed in an aqueous acidic electrolyte solution and a DC current is delivered to the anode via a rectifier. Polarisation then occurs at the site of the anode where metal ions dissolve (oxygen gas may evolve depending on the potential), while, hydrogen gas is formed at the cathode [119]. The metal dissolution process during electropolishing can be quantified using Faraday's Law of Electrolysis, as shown in Equation 23 [120], which indicates that process current (I) and treatment time (t) are the two variable that affect the total material loss during electropolishing.

$$W_{loss} = \frac{ItM}{nF}$$

Equation 23

Where;

W total material weight loss

n valence of the metal ion

M molecular weight of the anode

The rate of electropolishing is greatly dependent on the tendency for the metal ions to dissolve from the anode, consequently the higher the current, the more readily the metal ions dissolve from the anode. At high current densities, the mass transport rate of metal ions is what determines the anodic dissolution of the metal ions.

The efficiency of the electropolishing treatment can be determined by calculating the current efficiency of the process. Current efficiency at the anode may be defined as the ratio of current that results in metal dissolution to the total current passed by all the anodic reactions, e.g. oxygen evolution.

1.12.2 Electropolishing mechanisms

In the literature three possible transport mechanisms have been proposed for the process of electropolishing, these are:

- The salt precipitation mechanism, which involves rate-limiting diffusion of the dissolving metal from the anode into the bulk. At the limiting current a thin salt film is present on the anode and the surface concentration of the dissolved metal is equal to the saturation concentration. To maintain electro-neutrality, electrolyte anions accumulate in the anodic diffusion layer [116].
- The acceptor mechanism, which involves rate limiting diffusion of acceptor anions which are consumed at the anode by formation of complexes [116].
- The preferential adsorption of shielding molecules, which involves the rate limiting diffusion of water from the bulk to the anode where it is consumed by formation of hydrated metal ions [116].

However, on account of the presence of other species resulting from dissociation or association reactions, and because of viscosity changes at the actual concentration profiles at the anode are unquestionably more complex than those presented in literature [116]. Grimm *et al* [121], proposed a duplex salt film model, according to the salt film mechanism in an attempt to characterize the role of compact and porous layers in the frequency response of complicated precipitated films. *Matlosz et al.* [122] on the other hand proposed the adsorbate acceptor model based on the concept of acceptor mechanism, which examined the influences of adsorbed intermediates and the transport of acceptor molecules on the electropolishing behaviour in the absence of salt films.

Conversely electropolishing cannot reasonably be explained by the mechanisms above alone, an integration of the above concepts with an additional viewpoint by *Lin et al* [123], which considers the molecular

interactions among the strongly adsorbed molecules formed on the electrode surface, as shown in Figure 19 and Figure 20, where:

1. Layer A indicates the bulk polishing solution containing acceptors (i.e., water molecules which can coordinate to metal ions), acids, and glycerol.
2. Layer B is considered as a relatively compact film mainly consisting of the preferential adsorption molecules, including acceptors (mechanism for the preferential adsorption of shielding molecules [124])
3. Layer C is a salt solution formed by electrolyte and metal ions diffusing from layers B and D, respectively
4. Layer D is attributed to the accumulation of metal ions generated by the dissolution of metal or alloy substrates (layer E), which may be precipitated as a compact metal salt film in the salt film mechanism [116, 121] or as a metal oxide film [123].

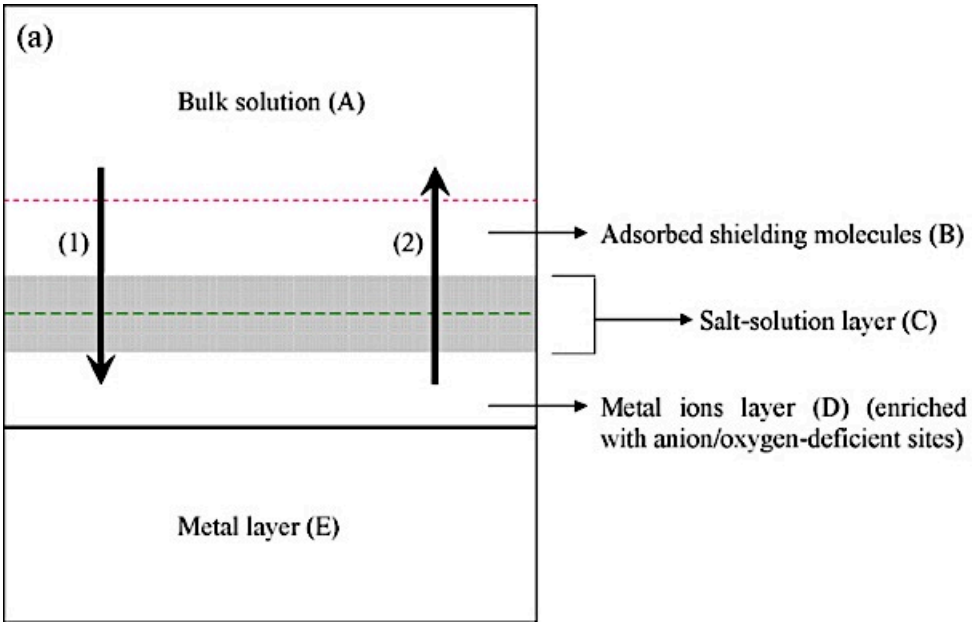

Figure 19: Schematic model for the anodic dissolution with arrows (1) moving in the direction of the acceptor and (2) the moving direction of metal ions [123].

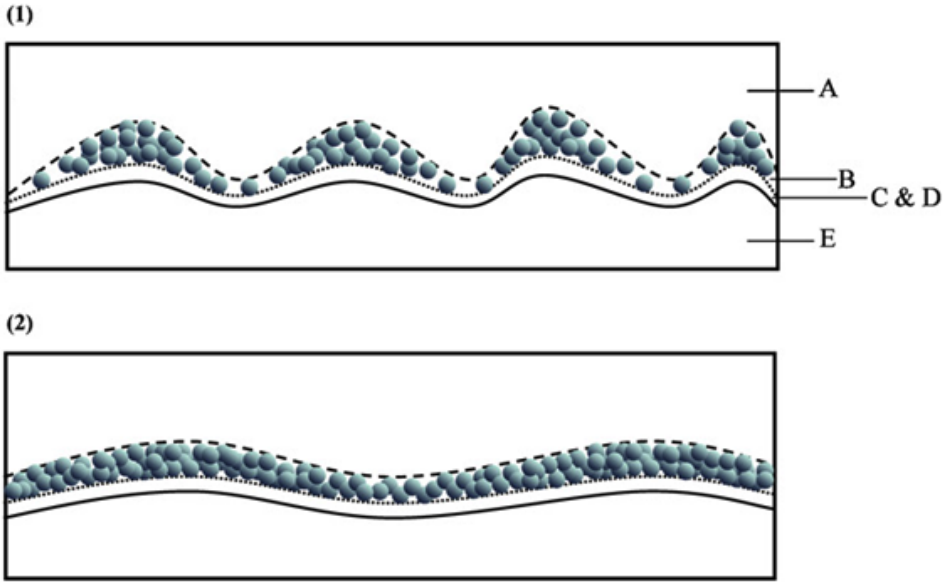

Figure 20: Schematic diagram of the microstructure transformation of an adsorbed shielding molecule layer on SS anodized at a constant current density; (1) weak and (2) strong molecular aggregates and clusters of the adsorbed molecules on the electrode surface [123].

In addition, the role glycerol plays has to be taken into consideration to, as it enhances the hindering effect on the diffusion of acceptors and metal ions (hydrated metal ions or complex ones) toward and away from the anode. This is due to the fact that glycerol comprises of large molecules with poly special functional groups (three OH groups, leading to strong hydrogen bonding between each other) may be concentrated to form a polymeric structure or aggregates in layer B [123].

As seen in Figure 20, in stage (1), the molecular interaction forces among all adsorbed species are so weak that molecule aggregation is not obvious. This layer will shield the anode surface with small clusters in the suitable current density region, whereby an obvious difference in dissolution rates between shielded and less-shielded portions is observed, resulting in a rough surface. However, if the intermolecular interactions become strong enough to form molecular aggregates and clusters (i.e. by increasing the glycerol concentration or reducing the bath temperature), a smoother surface may be obtained. The microstructure of the shielding film is then transformed into stage (2), whereby a very smooth surface in the

micrometre scale is obtained, as the shielding film is compact enough to extend its coverage on the whole surface so that the species will dissolve uniformly from the anode surface [118].

1.13 The anode potential and current density relationship

When an increasing overpotential from a potentiometric circuit is applied across the cell, the anode potential, the cathode potential, and the voltage drop across the cell will be related to the current density. The *I-V* curve can be used to determine whether the temperature and electrolyte combination results in a current plateau where the process current density is independent of potential, providing better control over the rate of electropolishing. The *I-V* curve can be used to provide basic information to apply to a specific case. The current plateau in this region is typically associated with the formation of a viscous layer near the electrode surface that controls the rate of dissolution of the anode by controlling the rate at which the products of anodic dissolution can diffuse away [14]. Changes in the surface condition during treatment can be related to specific sections of the curves. As seen in Figure 21 under potentiostatic conditions, the anodic polarisation curves show a well defined limiting current plateau which can be attributed to a diffusion-controlled process due to a viscous film formed on the surface of the anode [125].

The various parts of the curve (Figure 21) can be distinguished as follows;

- Region A-B: unstable anodic film starts to form where etching occurs characterized by an exponential increase in current until a certain voltage, V_B.
- Region B-C: super-saturation of the salt forming (in case of the salt viscous film mechanism of electropolishing), the film then equilibrates to the saturation level resulting in a drop of the current density to the limiting current density value.
- Region C-D: increase in voltage leads to a competition between the thickening viscous film and the increasing transport rate of

anions to the surface. It becomes increasingly difficult for the anions to reach the surface because of the thickening viscous layer, which lead to a current plateau due to mass transport control and typically observed in stainless steel bearing chromium and nickel in acid electrolyte [6, 20].

- Region D-E: gas evolution with pitting (anodic film dissolves).

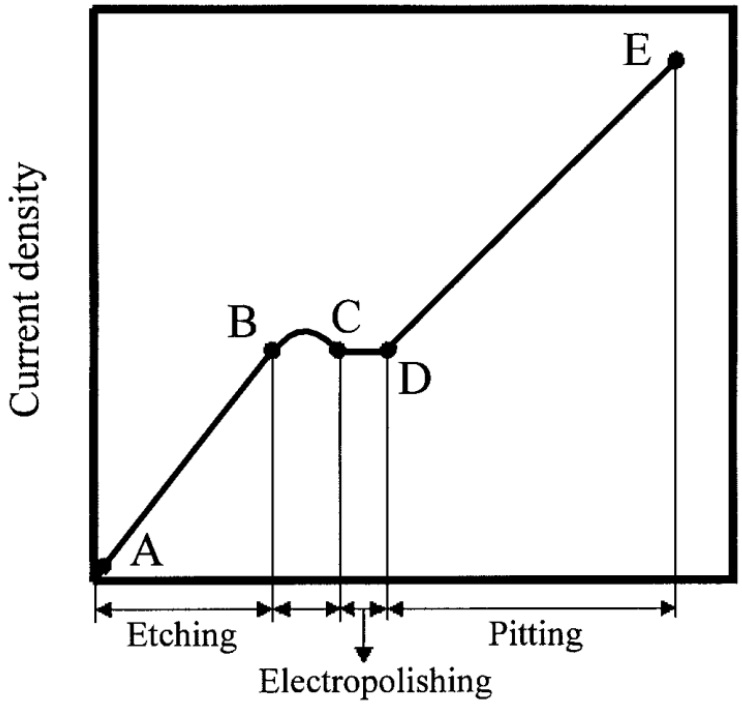

Figure 21: An ideal characteristic *I-V* curve for the determination of the process current and association voltage [126]

Electropolishing in the current on the current plateau region has been shown by *Lee* and *Lai* to lead to surface enrichment of Cr in stainless steel [125]. *Lee* also showed that surface roughness decreases proportionally with an increase in current density. However, it is clear that there is only partial passivity in the current plateau region since the metal still dissolves at an appreciable rate. Under such conditions of partial passivity, it is not surprising that the values of the voltage and current density for any given portion of the curves may vary, depending upon the manner in which the voltage is applied to the cell (although the form of the curves stays the same) [125].

1.14 Effects of electropolishing parameters

The exact mechanism of electrolytic polishing or (electropolishing) has not been established in any specific case, even though it is widely used in industry and in research; however, a general explanation has been developed. In an electrolytic cell, the metal to be electropolished forms the anode and irregularities on the surface are removed by the continued dissolution of the metal leading to the surface becoming smooth and bright. This behaviour is a special case of more regular anodic phenomena, for it is found that, depending on the condition of operation and the solution used, a metal anode can be etched, polished, preferentially passivated, or completely passivated. In order to ensure the desired surface finish is achieved the factors affecting them are explored here.

1.14.1 Bath temperature

As the limiting current density is considered to be proportional to the thickness of the concentration boundary layer affecting dissolution, forced convection helps decrease the thickness of the concentration boundary layer and thereby increases the limiting current [127]. Moreover, agitation further impedes excessive local heating due to the passage of current through the high resistance layers on the anode and maintains a more uniform temperature in the cell.

Murali et al. [115], showed that when the temperature was reduced below ambient temperature, the current density decreased and consequently the effects of the polishing and smoothing action on the surface was limited which resulted in relatively higher surface roughness than test specimens that were electropolished at higher current densities.

Use of high temperatures could also be disadvantageous as it decreases the viscosity of the bath making it more difficult to maintain the viscous layer on the anode; which is critical in diffusion control of the dissolution process, as suggested by *Feliu et al.* [127]. Moreover, *Lin et al.* [118], has shown how with decreasing bath temperature (i.e. minor thermal motion),

the molecular attractive force will dominate the behaviour of absorbed shielding molecules, resulting in suppression of the influence of the metal microstructure, leading to a more uniform dissolution. Thus, an optimum temperature of operation has to be chosen to minimise the power requirement without impairing the finish. Moreover, to avoid the complete destruction of the viscous layer and prevent the attainment of the ideal electropolishing conditions, excessive agitation must be avoided.

1.14.2 Time of treatment

The electrolysis treatment time is one of two variables in Faraday's Law of electrolysis required to determine the total material removed from the work piece. As the treatment time increases the amount of material removed from the anode surface increases and consequently the average surface roughness decreases as demonstrated by *Lee* [126]. He demonstrated how as the polishing time increased from 0 to 400 s, protuberances and damaged layers were removed and the microstructures of the 316L stainless steel were revealed and the average surface roughness decreased with increasing in the polishing time [126].

Another more notable study that characterised the relationship between surface roughness and electropolishing time was conducted by *Lee* and *Lai* [125]. Electropolishing of 316L was conducted in co-acid & glycerine mixture at 60˚C, a current density of 0.09 A cm^{-2}, cathode distance of 7 mm and at polishing times of 3, 5 & 10 min. The initial average surface roughness was 0.1 µm; after 3 min of polishing time it had increased to 0.110 µm, after 5 min polishing time it had decreased to 0.33 µm and after 10 min polishing time it had decreased to 0.033 µm [125]. Furthermore, *Lin* [118] also demonstrated that the surface of 304 SS treated in a bath containing 25% glycerol at 70 ˚C is rougher than that anodised in the same solution at 30 ˚C and concluded that as the bath temperature and treatment time reduced so did the surface roughness.

However, one has to note that the optimum conditions to produce a desired finish will vary depending on the metal, its initial surface finish as

well as the electrolyte used. As electropolishing times are usually in the order of minutes, an approximate general rule is that the treatment time is inversely proportional to the current density applied. [128]

1.14.3 Acid concentration

Acid concentration has a direct effect not only on the surface finish but also on the process voltage range and region of the current plateau associated with electropolishing as demonstrated by *Murali et al.* [115]. Whereby electropolishing of Al-7 Si-0.3Mg, in 5, 10, 20, 30 and 40% (v/v) of Perchloric acid demonstrated that as the acid concentration increased to 30% (v/v), a wider process voltage range was obtained from 4-20.5 V. When the concentration was increased to 40% (v/v), while maintaining the bath temperature, the width of the current plateau region decreased and the current density decreased from 30 to 15 mA cm^{-2}. Co-acid mixture ratios have also been shown by to have a significant effect in achieving a desired finish. *Ponto et al.* [129] demonstrated the significance of concentration range of the co-acid mixture of H_3PO_4-H_2SO_4 in the electropolishing of stainless steel. *Kang* and *Lee* [130] also electropolished 316L stainless steel with H_3PO_4 - H_2SO_4 + glycerol and water (34:47:19 wt%) to achieve an average surface roughness of 1.4 nm compared to average surface roughness of 116.4 nm of the unpolished specimen. It is clear that more than one acid mixture can be used for electropolishing, highlighting the versatility of the process.

1.14.4 Agitation of the electrolyte

There is a tendency for the reaction products to accumulate around the electrodes during electrolysis under steady-state conditions. In some cases agitation is desirable to remove some of the reaction products and maintain the viscous layer at the optimum thickness for polishing, particularly when diffusion or convection cannot supply sufficient fresh electrolyte to the anode.

Moreover, agitation further impedes excessive local heating due to the passage of current through the high resistance layers on the anode and

maintains a more uniform temperature in the cell. *Hryniewicz et al*. [131] highlight this further in results obtained showing a need to introduce forced convection (stirring of the electrolyte) during electropolishing process in view of getting higher efficiency. However, as demonstrated by *Ponto et al.* [129], to avoid the complete destruction of the viscous layer and prevent the attainment of the ideal electropolishing conditions as demonstrated by excessive agitation must also be avoided.

1.14.5 Surface finish

The potential transients under galvanic control can be used as an indicator to distinguish whether brightening or etching is taking place during anodization treatments in a particular electrolyte. An example demonstrated by *Neergat et. al.* is shown in Figure 22, in electrolyte solution of saturated $LiNO_3$ at current densities of 0.2, 0.4, 0.63 and 0.75 A cm^{-2} [132].

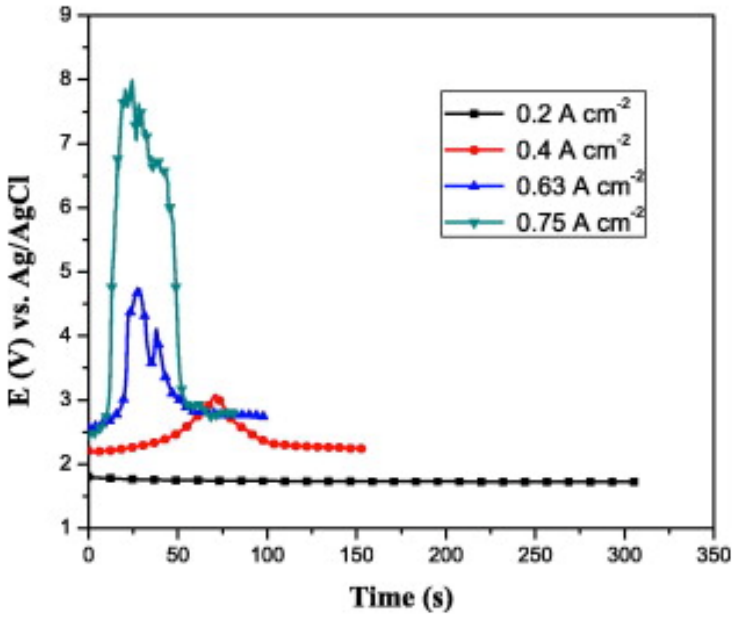

Figure 22: Galvanostatic transients in saturated $LiNO_3$ electrolyte at 0.2, 0.4, 0.63 and 0.75 A cm^{-2} [132].

At low current density (0.2 A cm^{-2}), the dissolution voltage remains constant since the kinetic resistance for metal dissolution into the film is

less than the potential drop required to drive the ions through the film, dissolution occurs uniformly, independent of variations in surface energy and the whole electrode is etched. It is commonly performed on stainless steel at conditions of 0.05 A cm^{-2} in 0.5 M Na_2SO_4 under alkaline conditions [133]. While 0.4 A cm^{-2}, a slight peak is formed that corresponds to brightening of approximately 50% of the electrode surface. A more sustainable potential rise occurs earlier when the current density is increased to 0.75 A cm^{-2}, and the entire electrode surface is brightened [132].

1.15 Project objectives

This project aims to develop a low cost substrate surface treatment for treatment of relatively inexpensive stainless steel components to be utilised as bipolar plates in PEM fuel cells. Electropolishing techniques are to be employed in order to achieve desired reduction in ICR as well as corrosion current densities. The surface treatment resembles that of anodic treatment, whereby the potential of a metal is moved into a passive region when it shifts to an electropositive positive direction after direct current is applied. It differs from anodizing in that the purpose of anodizing is to grow a thick, protective oxide layer on the surface of a material rather than etch/polish. Etching which is typically characterised by a matte finish and shallow pitting free of preferential weld zone attack [134]. Understanding the mechanisms of electropolishing as well the anode *I-V* relationship in order to optimise the treatment processes

The surface treatment specifics entails treating a surface of the stainless steel with an electric current while contacted by an acidic electrolyte, under conditions that reduce the interfacial resistances. The viscosity of the acid electrolyte, which is selected in conjunction with other condition, plays a vital role in the surface finish of metallic BPPs. Furthermore the treatment is carried out with the stainless steel as the anode through the application of a dc current.

Although a low current is desirable in order to ensure a high current efficiency, reducing hydrogen production and the flammability hazard [132], use of dilute electrolytes could also help reduce this risk. The use of sulphate-containing electrolytes (i.e. H_2SO_4) is preferred for stainless steel dissolution; as many reducing agents which produce sulphate anions, are available to convert Cr^{6+} to Cr^{3+} [134]. Furthermore, the use of a dilute sulphate electrolyte at low current densities has been shown to bring about improved surface qualities [132]. As the rate determining process during electropolishing is diffusion of product ions away from the surface and the properties of this diffusion layer are affected by its viscosity, which can be used as a means of controlling the process. The addition of a viscosity enhancing agent typically a polyol, e.g. glycerol (propane-1,2,3-triol) is to be utilised to investigate its effects on the polishing film may be.

The two main advantages of the process are: firstly, to remove the solid (Beilby) layer that consists of inclusions of matertenistic phase, foreign material, pre-existing oxides created by forming, machining or abrasive polishing [116, 128]. Secondly, to create a new corrosion resistant layer that is enriched in chromium oxide due to the anomalous co-dissolution of austenitic stainless steel. Third is to equipotentialize the grain boundaries of metallic materials [135].

In order to both understand and determine whether the treatment technique has met its objectives, in-situ technique such as;

- Potentidynamic scans of the working electrode potential and a measurement of the resulting current, to determine corrosion current densities by Tafel plot and polarisation resistance methods
- Galvanostatic scans where a constant current value is maintained to undertake the anodization technique, whereby the current is held

These techniques allied with ex-situ surface analysis techniques (ToF SIMS & SEM) are to be utilised to investigate the effects of the variable utilised in

the anodization treatment in attaining a surface enriched in Cr content with aim of reducing the corrosion and more importantly the contact resistance of relatively inexpensive stainless steel.

2 Methodology and Experimental

2.1 DC Electrochemical methods

There are several electroanalytical techniques available depending on what aspect of the activities at the interface one desires to explore. Potentiometric measurements which are made at zero current conditions provide a powerful tool for measurement of thermodynamic properties of interfacial processes [136]. Steady state polarization curves provide the general kinetic information of the charge transfer process.

The electrode process can sometimes become time dependent when measurements are made at very short intervals of time. Transient techniques such as chronopotentiometry, chronoamperometry and chronocoulometry and the double pulse analogues of these techniques are employed for the study of fast interfacial processes [95]. Linear sweep and cyclic voltammetry techniques are the two most widely used DC transient techniques in electrochemistry, which involve measuring either the potential or current for an electrochemical corrosion reaction and interpreting it in terms of corrosion rate. The corrosion rate measured via these methods is usually applicable to the specimen's natural corrosion potential (E_{corr}), and will be applied in this research project.

The principal focus will be on tests that are intended to simulate the corrosion conditions within the PEM fuel cell stack, where the environment is comprised of a solution and an imposed electrochemical potential derived from the operation of the fuel cell. This will be done as short-term out-of-stack corrosion tests via polarization techniques, as a comparative screening of candidate stainless steel alloys as well as a means of collecting corrosion current density to determine the alloy's decay rate.

2.1.1 Potential measurements

Potential measurements are useful when determining the thermodynamic state of a metal immersed in an environment. The information obtained from potential measurements together with other information based on knowledge of polarization behaviour can be used to determine the corrosion rate of a metal [137]. The bipolar plate in a stack is usually held at a potential imposed on it by the operation of the fuel cell. This potential will be the adjacent electrode potential modified by an ohmic (*IR*) drop due to the contact resistance which is kept low to optimize overall stack performance [72]. Hence the potential of the bipolar plate is to a good approximation the same as that of the adjacent electrode. However, at open circuit the bipolar plates will establish an E_{corr} determined by its local chemical environment. Consequently, the corrosion reactions on the bipolar plate will operate at different potentials as determined by the fuel cell electrodes, and hence corrosion rates will vary as the stack operating potentials are varied [138].

2.1.2 Linear Polarization

The corrosion behaviour of metals is related to its polarisation behaviour and therefore electrochemical polarization techniques of a metal in a given environment can provide a rapid means of determining its corrosion behaviour [137]. Polarization techniques (i.e. polarization curves) are still very useful in defining alloy-environment combinations and provide a direct measure of the extent of passivity, i.e. onset of passivation, the breakdown of passivation and the relative ease of passivation and related to the metals pitting and crevice susceptibility [137]. This information in conjunction with the anodic and cathodic operating potential range of a PEM fuel cell can be used as an indicator of whether or not the alloy being tested will suffer from corrosion. Polarization curves can also be used in conjunction with Pourbaix diagrams.

2.1.3 Polarization resistance

Polarisation resistance is a technique whereby the sample is polarised by an overpotential of a few mV positive and negative (±10 mV) of its E_{corr} [87]. The polarization resistance behaviour of a metal in an environment is reflected in a linear plot of potential vs. current density, which along with the Tafel parameters can be used to determine the corrosion rate of the metal. When the Tafel linear regions are very short the corrosion current densities can be estimated using a three-point method of extrapolating the anodic and cathodic tafel line to the point of intersection of E_{corr} [138]. This technique has the advantage that it is easy to apply and the overpotentials are small enough to preserve the corrosion process at the natural corrosion potential. The disadvantage for application to the bipolar plate is that it measures i_{corr} at the natural corrosion potential, but the bipolar plate in an operating stack will spend much of its time at an imposed potential that may be far from its natural corrosion potential [83].

2.1.3.1 Cyclic Voltammetry and Linear Sweep Techniques

In electrochemical experiments a simple linear potential waveform often used is where the potential of the working electrode is continuously changed as a linear function of time. This results in the occurrence of oxidation and reduction reactions of an electroactive species in solution (Faradaic reactions); possibly absorption of species according to the potential, and a capacitive current due to the double-layer charging [137]. The simplest technique that uses this waveform is linear sweep voltammetry in which the potential range is scanned in one direction while registering the current. A more commonly used variation of the technique is cyclic voltammetry (CV), in which the direction of the potential is reversed at the end of the first scan resulting in a waveform. This has the advantage that the product of the electron transfer reaction that occurred in the forward scan can be probed again in the reverse scan. In addition, a further voltage excursion takes place to more negative (more reducing) values.

2.2 AC Methods

There are also a host of transient techniques based on superimposing an AC transient signal on a DC base signal using a frequency response analyser (FRA). The FRA uses the frequency response of an impedance signal at each DC potential to provide detailed information on the interfacial processes occurring. In contrast to linear sweep and potential step methods, where the system is perturbed far from equilibrium, EIS applies a small ac voltage or current perturbation / signal (of known amplitude and frequency) to the cell, and the amplitude and phase of the resulting signal are measured as a function of frequency. This may be repeated through a wide range of frequencies (i.e., large frequency spectrum) [96]. The impedance is the measure of the ability of the system to impede the flow of electrical current. EIS is a powerful technique, which can resolve various polarisation losses in a short time without perturbing the system under control.

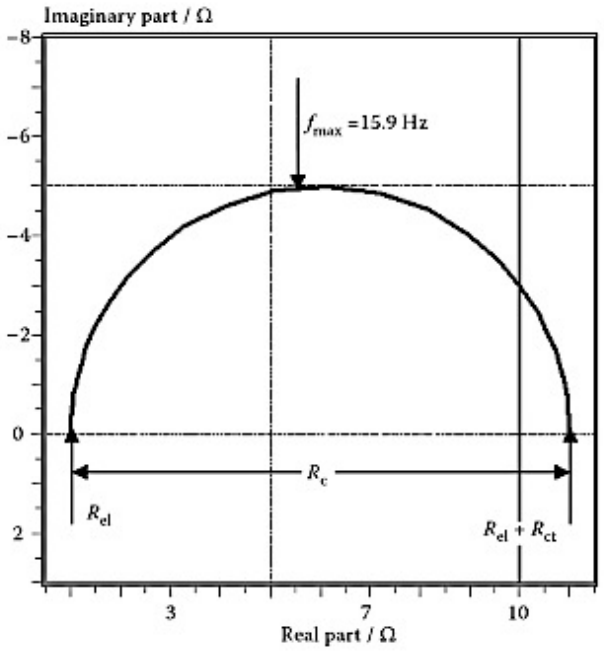

Figure 23: Nyquist plot for the impedance spectra simulated in the frequency range from 10 mHz to 10kHz [139].

The impedance spectra can is plotted as a Nyquist plot (Figure 23), which is an arc, where the frequency increases (right to left). The high frequency arc

represents the double-layer capacitance, the effective charge transfer resistance and the ohmic resistance. The ohmic resistance is given by the real part of the high frequency end of the high frequency arc; it reflects the ohmic losses including the membrane resistance together with the GDL, bipolar plate, and contact resistances [97, 140].

2.3 Electrochemical Test Equipment

This section looks at the hardware used to perform the desired electrochemical tests as well as the limitations of the equipment and the proper methods for utilising the equipment.

2.3.1 Potentiostat

The external circuit used throughout this research project is a potentiostat; the AUTOLAB potentiostat/galvanostat series (model PGSTAT302N).

2.3.2 Electrochemical cells

The electrochemical cell usually consists of a vessel that can be sealed to prevent air entering the solution with inlet and outlet ports to allow the saturation of the solution with an inert gas, either nitrogen (N_2) or argon (Ar). The removal of oxygen (O_2) is usually necessary to prevent currents due to the reduction of O_2 interfering with the response of the system under study [141]. In a cell used for electroanalytical measurements e.g. linear sweep voltammetry (LSV) and cyclic voltammetry (CV) there are always three electrodes, working, counter and reference electrode due to the difficulties arising from concurrent measurement of current and potential [137].

The working electrode is the electrode at which the electrochemical phenomena (reduction or oxidation) being investigated are taking place and the potential here is monitored and controlled very accurately with respect to the RE via the potentiostat, which is in turn controlled via a computer.

Electrochemical tests generally require a reference electrode that is compatible with the solution composition and temperature. A reference electrode is the electrode whose potential is constant enough that it can be taken as the reference standard against which the potentials of the other electrodes present in the cell can be measured [85]. When a suitable reference electrode is used the potential of the working electrode can be controlled reproducibly and any changes in the measured potential during the test can be related to the changes in the working electrode potential. Until recently the HRE was not the most convenient or durable of electrodes as it required configuring the platinum plate and bubbling mechanism within an electrode body, which is not trivial. However, the Hydroflex^{TM} HRE (Gaskatel, Germany) has an internal replaceable cartridge that continuously generates a low volume hydrogen flow that passes through a platinized gas diffusion electrode, resulting in a compact reference electrode without the need for a separate hydrogen source. The HRE is preferable to the SCE or Ag/AgCl reference electrodes as it does not require regular calibration and has no source of contamination (i.e. chloride ions) [142].

The counter electrode serves as a source or sink for electrons so that current can be passed from the external circuit (Potentiostat) through the cell. The solution for the tests being carried out is particularly aggressive and hence platinum has been selected as the counter electrode as it is one of very few materials inert enough to prevent contamination of the solution. The size of electrode depends on the material being used and it has been suggested that a platinum electrode with a flag configuration area of 320 mm (12.5 × 12.5 × 0.25 mm) is sufficient for a wide range of applications [137].

The two electrochemical cells developed in-house for this research project are; Corrosion cell (Avesta cell) and Electropolishing cell.

2.3.2.1 Corrosion cell

Figure 24 shows a schematic diagram of the Avesta electrochemical cell developed for this research project with the relevant electrodes in place. The Avesta cell is an electrochemical cell designed to avoid microcrevice corrosion formed between the working electrode and the gasket at the bottom aperture of the cell. This is achieved by the placement of a filter paper ring between the sample and the gasket, which is flooded by distilled water to dilute the solution in the crevice and thereby reduces its aggressivity. The cell is typically utilised for pitting corrosion testing and although that is not particularly the case here, the cell design still holds other advantages for generalised corrosion testing.

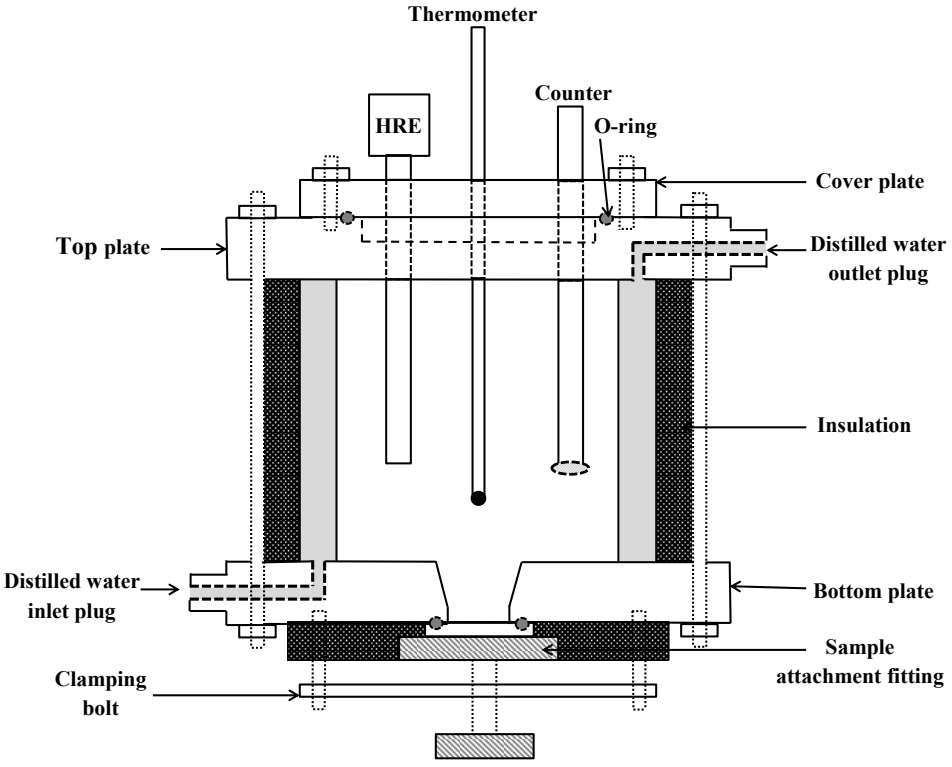

Figure 24: Schematic diagram of the Avesta electrochemical cell used for corrosion studies.

Similar to most corrosion electrochemical cells, the Avesta cell consists of three electrodes (working, reference and counter) and an electrolyte solution (350 ml) that provides the ionic electrical conductivity between the three electrodes. The placement of the working electrode at the

bottom of the cell eliminates the use of epoxy resins; typically used for samples placed directly into the vessel in order to establish a predetermined surface area. Temperature control was achieved by an insulated water jacket connected to an isothermal circulated water bath and monitored with a mercury thermometer in direct contact with the electrolyte solution.

2.3.2.2 Electropolishing cell

The electropolishing cell shown in Figure 25 consists of two electrodes (a working and counter electrode) and an electrolyte solution. The anodised coupon samples, which were the working electrodes, were immersed at the centre of a cylindrical cell containing 350 ml of electrolyte solution. A reference electrode is not particularly necessary as the anodization treatment is galvanostatic method.

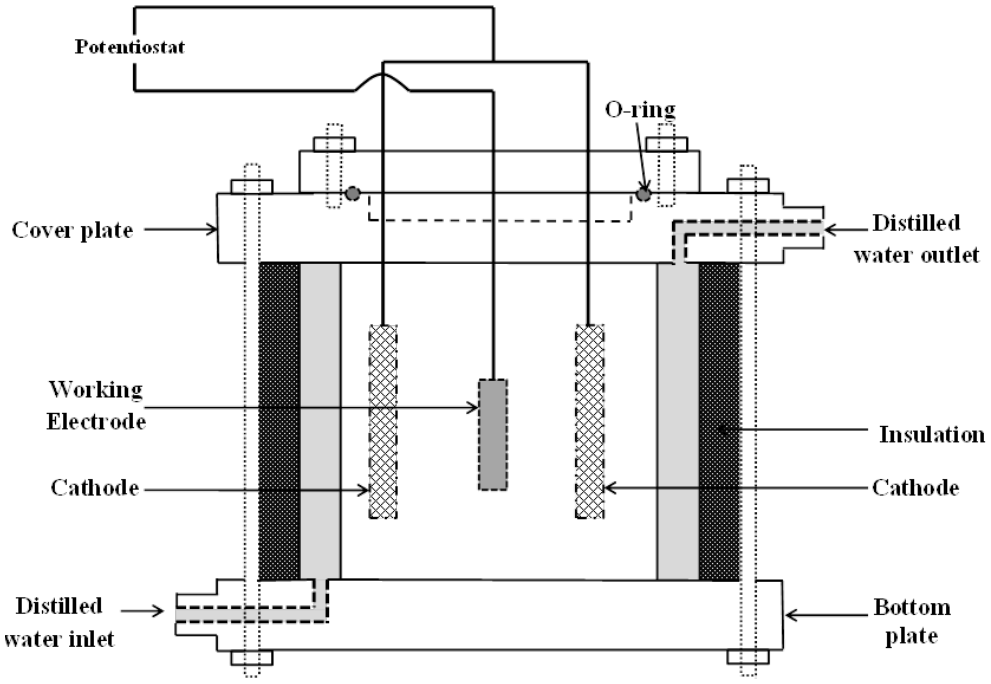

Figure 25: Schematic diagram of electropolishing cell.

Temperature control was achieved by an insulated water jacket connected to an isothermal circulated water bath and monitored with a mercury thermometer in direct contact with the electrolyte solution. The counter

electrode was composed of two platinum coated titanium mesh sheets (50 × 50 × 1 mm), positioned a distance of 10 mm from the working electrode sample.

2.4 Corrosion in simulated fuel cell environment

The repeatability of electrochemical techniques depends highly on ensuring proper preparation techniques are implemented. Here some of the techniques used to ensure repeatable results are described.

2.4.1 Specimen preparation

Electrochemical tests usually utilise a small, well-defined test specimen (working electrode) surface area of which factors such as the surface finish and mounting technique are critical. What this generally means is that the surface finish should be smooth enough to obtain a uniform surface finish and not so smooth that repeatability is difficult, as demonstrated by *El-Naggar* [143]. Surfaces that are extremely smooth, as achieved by electrolytic or mechanical polishing, are not desirable as they respond differently in the environment than a practical surface. A surface roughness that corresponds to 400 to 600 grit (~30-40 microns) silicon carbide grinding paper finish is commonly is used in corrosion testing [137]. The specimen is degreased by immersion in acetone for 1-3 min under an ultrasonic cleaner, followed by rinsing with distilled water, to remove any grit and loose particles from the surface. The two primary objectives of the surface finish here are:

- To ensure that the surface will respond in electrochemical test in a manner similar to the commercially produced material in the service of interest (as a bipolar plate).
- Represent a convenient procedure that is practical enough to eliminate procedures difficult to reproduce.

The mounting of the specimen is also crucial in obtaining high quality repeatable results. Two important considerations in the mounting procedure are:

- Crevices are not created during the mounting of the specimen.
- The mounting material used is inert in the environment being tested.

2.4.2 Aqueous solutions

In order to ensure that the corrosion tests on the specimens will be representative of performance in the PEM fuel cell it is important that the test environment adequately simulate the environment at the surface of the bipolar plate. This means, the solution composition, pH and temperature must be controlled. In order to meet the high purity demands of the electrochemical tests to be conducted, ultra-high purity water has to be used in preparing the acid solution. To achieve this high level of purity the PURELAB UHQ II (18.2 MΩ, Millipore) system was used which utilises five purification technologies - reverse osmosis, adsorption, deionisation, micro-filtration and photo-oxidation radiation to achieve water with a 18 MΩ level of purity.

In order to simulate an environment typical of the prolonged operation of a PEM fuel cell, solutions containing Cl^-, SO_4^{2-} and F^- ions need to be employed. The presence of SO_4^{2-} and F^- ions in the fuel cell is mainly due to the degradation of Nafion [144]. The *p*H of the water withdrawn from a PEM fuel cell operating with H_2 / air is typically, *p*H 1-4 at the beginning of operation, as a result of leaching excess acid from the membrane [83].

To ensure that the corrosion tests carried out on the specimens will simulate the aggressive conditions experienced within a PEFC (possible direct contact with electrolyte membrane) and acted as an accelerated test environment, all electrochemical experiments were conducted in 1 M H_2SO_4 + 2 ppm F^- ions [145] at 70 ˚C in an Avesta electrochemical cell shown in Figure 24. The electrolyte solutions were prepared from analytical grade sulphuric acid 95-97% (EMSURE® ISO, UK) and ultrapure

water (18.2 MΩ, Millipore) with F- ions added from Sodium fluoride anhydrous powder, 99.99% trace metals (SIGMA-ALDRICH). Viscosity enhancing agent, glycerine / glycerol, 99.5% (Mistral Lab Chemicals, U.K) was added to the sulphuric acid in the described contents in order to explore its effects.

2.4.2.1 Electropolishing solution

The electrolyte solutions were prepared from analytical grade sulphuric acid 95-97% (EMSURE® ISO, UK) and ultrapure water (18.2 MΩ, Millipore). Viscosity enhancing agent, glycerine / glycerol, 99.5% (Mistral Lab Chemicals, UK) was added to the sulphuric acid at a range of concentrations (0.25, 0.5 and 1 M) in order to explore its effects.

2.4.3 Aeration and Deaeration

There are three primary factors, which need to be evaluated when deciding to either aerate or deaerate the test solution. These are [137]:

- The test being performed.
- The operating parameters being simulated.
- The desire to maximise the range of oxidizing conditions over which polarization is being measured.

When polarization behaviour is being determined over a range of oxidizing conditions, i.e. potentiostatic polarization tests, it is important to increase the range over which the data is being collected. Moreover, the most reducing condition for a particular environment is established when the test solution is deaerated. This is due to lack of oxygen, which provides an additional reduction reaction during anodic polarization tests. Therefore the corrosion potential of the metal will be more negative, hence increasing the potential range over which the data is collected. The deaeration process is usually undertaken with either argon or high purity nitrogen gas [137]. Prior to running the experiment, the electrolyte was de-aerated by bubbling in nitrogen for 1 hrs. Deaeration was maintain

throughout the experiment with nitrogen gas was continuously fed into the corrosion cell to maintain a blanket of nitrogen on top of the electrolyte.

2.5 Materials

Austenitic, or 300 series, stainless steels represent compositional modifications of the classic 18/8 (18% Cr-8% Ni) stainless steel. They comprise the largest category of stainless steel, accounting for about 70% of all production [38]. The austenitic class offers the most resistance to corrosion in the stainless group, owing to its substantial nickel content and higher levels of chromium, which give it an austenitic structure at all temperatures from the cryogenic region to the melting point of the alloy. Some important compositional modification of the 300 series of austenitc steels that improve corrosion resistance are:[40]

- Addition of molybdenum/ molybdenum plus nitrogen to improve pitting and crevice corrosion resistance.
- Lowering the carbon content or stabilising with either titanium or niobium plus tantalum to reduce intergranular corrosion in welded material.
- Addition of nickel and chromium to improve high temperature oxidation resistance and strength.

Austenitic stainless steels are extensively employed in a broad range of applications due to their relatively low cost and good corrosion resistance. The four chosen stainless steel samples utilized for the preliminary studies were chosen on the basis that: 316 SS is widespread in the design of metallic devices exposed to stringent conditions, 304 SS is regarded as a stamping grade, while 904L and 310 SS, although a bit more expensive, were chosen to enable the study of bulk composition impact on ICR and corrosion resistance, and its influence on passive film composition. A comparison of the bulk elementary composition (w.t %), of 904L, 310, 304

and 316 SS are shown in Table 6. Coupons (25 × 25 × 0.5 mm) were cut from sheets of stainless steel as listed in Table 7, with supplier details.

Table 6: Bulk elemental composition (w.t %) of stainless steel (Supplier data)

Element	904L SS	310 SS	304 SS	316 SS
C	0.02	0.25	0.00045	0.00019
Cr	20.05	25	18.11	16.87
Ni	24.91	22	8.03	10
Mo	4.18	-	-	2.02
Mn	1.49	2	1.05	1.38
Si	0.17	1.5	0.042	0.0046
P	0.02	0.45	-	0.00004
S	0.03	0.3	-	0.00003
Cu	1.45	-	-	-
N	0.082	-	-	0.00054
Ti	-	-	-	0.00017
Co	-	-	-	0.021
Fe	Balance	Balance	Balance	Balance

Table 7: Stainless steel sample supplier details and dimensions

Sample	Supplier	Dimensions
904L SS	Intelligent Energy, UK	60 × 30 × 0.5 mm
310 SS	Intelligent Energy, UK	60 × 30 × 0.5 mm
304 SS	Goodfellows, UK	300 × 300 × 0.5 mm
316 SS	Goodfellows, UK	300 × 300 × 0.5 mm

2.6 Interfacial Contact Resistance

Tests were conducted to establish the relationship of the compression pressure versus contact resistance. Because of the 'sandwich' layered structure, the surface characteristics, and the surface passive (oxide) film may affect the contact resistance between the bipolar plate and the MEA.

The apparatus schematic shown in (Figure 26) was used to perform this measurement, based on that described by *Wang et al.* [36] and *Davies et al.* [79]. The method utilises two pieces of GDL (Toray TGPH090) [36], the materials and compression properties of which have been well characterised by *Mason et al.* [146] and *El-kharouf et al.* [147]. This three-layer assembly is then placed between two gold-coated copper plates and a compaction pressure is applied using a hydraulic air ram (series C95SB50-150, SMC, UK) and measured using an integrated load cell (LCM304-2KN, Omega UK). Electrical resistance measurements were carried out using a potentiostat and a frequency response analyser (PGSTAT302N with FRA2, Metrohm Autolab, The Netherlands) in the frequency range 1-100 kHz and amplitude of 15 mV. The high frequency intercept with the real axis was chosen to represent the ohmic resistance of the system, which is dominated by the contact resistance between components.

In order to correct for the contact resistance between the GDL and the gold-coated copper plates, a calibration in which the two layers of carbon paper are sandwiched between the gold-coated copper plates made in order to correct for the interfacial contact resistance between copper plate and carbon paper ($R_{C/Cu}$). Deducting the total contact resistance from the calibration data and halving the result gives the interfacial contact resistance for the carbon paper / stainless steel ($R_{C/SS}$) interface (assuming the surfaces are identical and homogeneous).

The interfacial contact resistance is the calculated according to:

$$R_{ss} = \left(R_{C/SS} - R_{C/Cu}\right)/2$$

Equation 24

Where;

$R_{C/Cu}$ two carbon paper / copper plate interfaces.

$R_{C/SS}$ two carbon paper / surface film of stainless steel interfaces

R_{SS} surface film of stainless steel interfaces

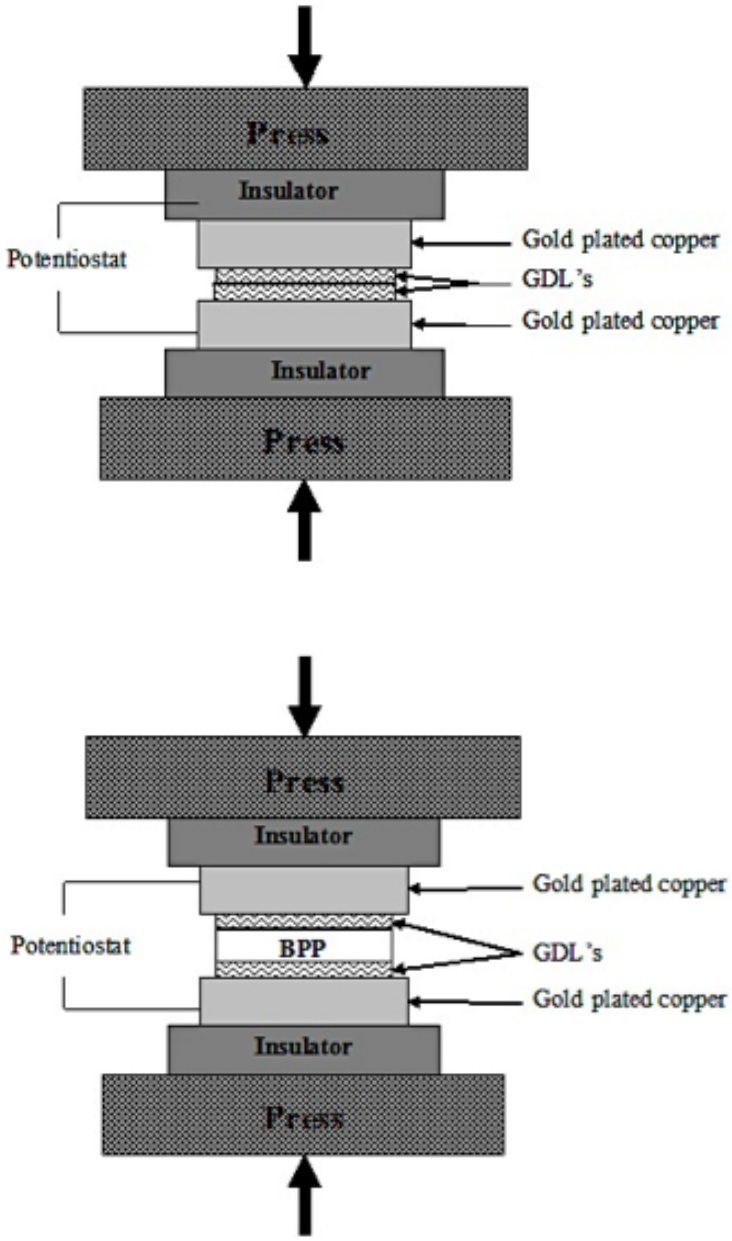

Figure 26: Illustration of rig used to perform interfacial contact resistance measurements. (Top) arrangement for measuring contact resistance with steel sample, and (Bottom) arrangement to determine contact resistance between GDL and gold plated copper

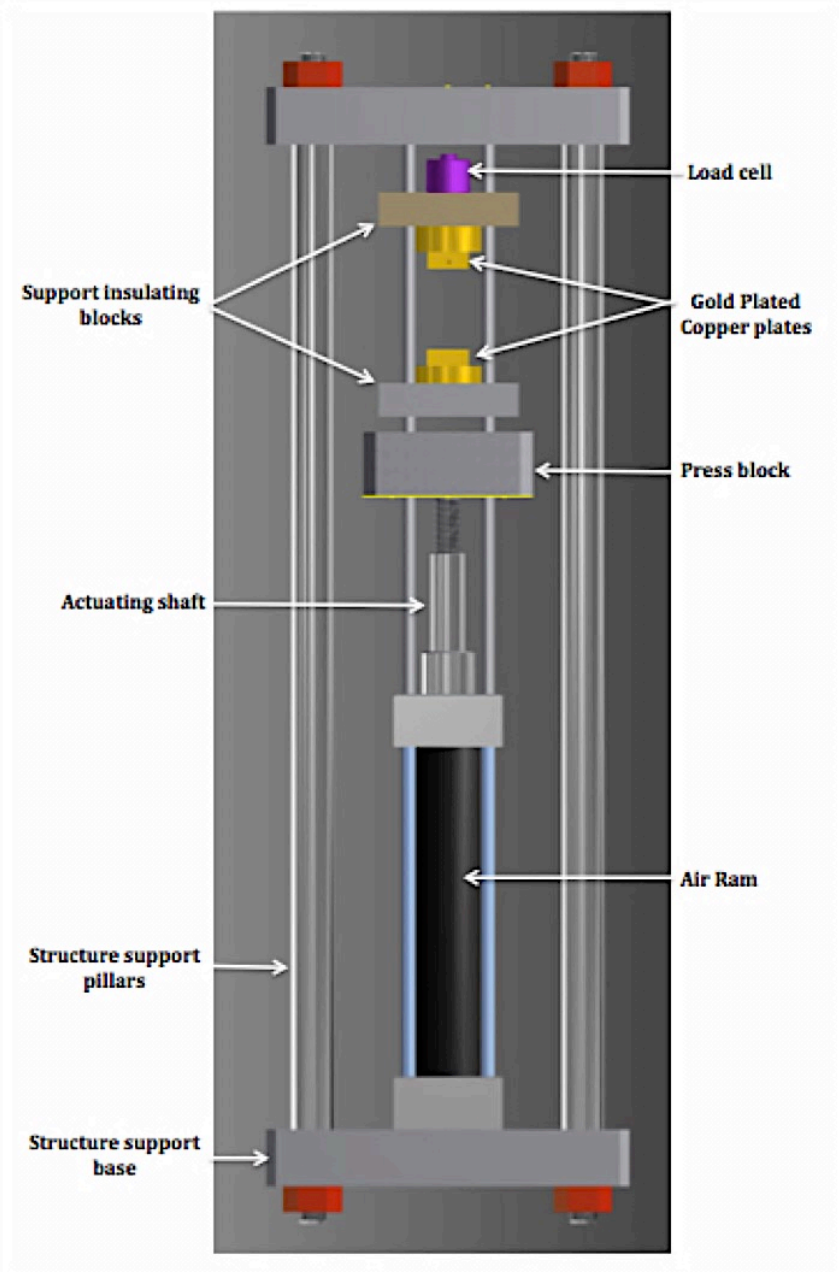

Figure 27: Computer aided design (CAD) image of ICR compression rig.

2.6.1 Surface characterisation post treatment

Surface analysis techniques are useful tools in the characterisation of nano-scale surface differences on the electropolished specimens. Surface composition and surface roughness (*Ra*) measurements provide important information on surface chemistry of the oxide layer, which is critical in the determining corrosion resistance.

2.6.2 Focused Ion Beam Secondary Ion Mass Spectrometry (FIB-SIMS)

Time-of-flight secondary ion mass spectrometry (ToF-SIMS) was carried out using an IONTOF ToF-SIMS V instrument (ION-TOF GmbH, Germany). The mass spectra were collected using a 25 keV Bi^+ analytical ion beam in high current bunched mode to obtain high mass resolution. Positive secondary ions were collected, using a primary beam current of ~1 pA (at a 100 μs cycle time). The analytical area was 200 × 200 μm collecting 256 × 256 pixels. Each analysis was performed with a dose of 5×10^{12} ions cm^{-2}, well within the static SIMS regime.

2.6.3 SEM

Scanning electron microscopy (SEM) was conducted using a Zeiss Supra 40 field emission scanning electron microscope at a beam voltage of 15 kV and a scan rate in the range 6.4-25.6 μs. Analysis was made within a scan size of approximately 1.6 mm^2 (400 ×400 μm) at an image magnification of ×900 and ×1500.

2.6.4 AFM

Surface morphology was characterized using a Park XE-100 atomic force microscope (AFM) in contact-mode. Imaging of the samples was carried out at 0.75 Hz, with scan sizes of 10, 50 and 90 μm at set point 1.24 nN, providing '3D' rendering with a line scan on each sample and an image of the surface roughness (R_a) for each sample using a NSC14 Cr-Au tip.

2.7 Calculations

2.7.1 Tafel line (Extrapolation)

Although it is preferable that both branches exhibit Tafel behavior, concentration polarization (where the rate of a reaction is controlled by the rate at which reactants arrive at the metal surface) may occur toward the tail end of the Tafel regions. This can consequently lead to Tafel regions that are not well defined; hence, determining the corrosion rate (i_{corr}) by

the intersection of the anodic and cathodic Tafel slope will lead to erroneous values. *McCafferty* [91], reported that the corrosion rate can be determined by Tafel extrapolation of either the cathodic or the anodic polarization curve alone. If only one polarization curve is used it is generally the cathodic curve, which usually produces a longer and more well-defined Tafel region (as is our case here). This is because on the cathode, concentration polarization is typically observed at higher currents, when diffusion of oxygen or hydrogen ion is not fast enough to sustain the kinetically controlled rate. As the cathodic polarization curves exhibit wide and well-defined Tafel regions, accurate estimation of i_{corr} was established by extrapolation of the cathodic Tafel slopes back to the corresponding values of E_{corr}. The linear portions should extend over about one decade on the $\log i$ (current) axis as reported by *Flitt and Schweinsberg* [148] for accurate estimation of corrosion rate by the Tafel method.

In the case where the mass transport effects on the cathodic Tafel line come in to play within the linear region of the Tafel plot, a correction for mass transport effects was implemented. The Tafel law can be corrected for transport effects, (Equation 25) by enlarging the region of the voltammetric curve that can be utilized in Tafel plots [95]. Determining the corrosion rate (i_{corr}) is therefore achieved by extrapolation of the mass transport corrected cathodic Tafel slope to the intersection of the E_{corr} line.

$$E = -ln\left[\frac{1}{i_c} - \frac{1}{i_{lc}}\right]$$

Equation 25

Where,

i_{Lc} the limiting current density.

i_c cathodic current density

Anodic polarization may sometimes produce concentration effects, due to passivation, the accumulation of dissolved cations near the electrode

surface as well as roughening of the surface. The concentration effects are then manifested as a deviation from the linear anodic Tafel region at high anodic overpotentials. Based on the principles of the mixed potential theory of uniform corrosion and superposition of the partial *I-V* curves for each of the partial half-cell reactions [149]. Hence, for the dissolution of iron in acid solutions, at equilibrium the total cathodic reaction rate is equal to the total anodic reaction rate:

$$Fe \rightarrow Fe^{2+} + 2e^{-}$$

Equation 26

$$2H^{+} + 2e^{-} \rightarrow H_2$$

Equation 27

$$\left(\left|\vec{i_H}\right| + \left|\vec{i_{Fe}}\right|\right) = \left(\vec{i_H} + \vec{i_{Fe}}\right)$$

Equation 28

Where, the forward arrow refers to the cathodic direction. Thus, $\left|\vec{i_H}\right|$ refers to the rate of the reduction reaction, Equation 27. From Equation 28 the anodic current density i_a is calculated. [91]

$$\vec{i_{net}} = \left(\vec{i_{Fe}} + \vec{i_H}\right) - \left(\left|\vec{i_H}\right| + \left|\vec{i_{Fe}}\right|\right)$$

Equation 29

Or simply;

$$\vec{i_{net}}(net\,\mathrm{exp}erimental) = i_a - \left|i_c\right|$$

Equation 30

Where

$\left|i_c\right|$ cathodic current density

The Tafel slope of the cathodic polarization curve is then first extended to electrode potentials below the corrosion potential. The anodic current density i_a is thus the sum of the experimentally observed anodic current density and the extrapolated cathodic current density.

2.7.2 Current Efficiency calculations

The range of reactions that can occur at the anode during the electrodissolution of stainless steel metals, include oxygen evolution and chromium reoxidation (following reduction at the cathode). Hydrogen evolution at the cathode is the primary reaction, with side reactions including chromium and sulphate reduction. According to Faraday's law the current efficiency (η_P) (Equation 31) can be defined as the ratio between the charge used to form the product (*P*) and the total charge passed (according to the approach presented by Sánchez-Sánchez et al. [150]). The molar mass is calculated from the bulk elemental composition (w.t %) of stainless steel.

$$\eta_P = \frac{\frac{m_P}{M_P}\frac{\nu_e}{\nu_P}F}{Q}$$

Equation 31

$$m_P(mm\ cm^{-2}) = \frac{\eta_P\ I(A)\ t(min)}{S(cm^2)}\left[\frac{1C}{1A\ s}\frac{g(ss\ dissolved)}{C\ to\ dissolve\ 1g}\frac{60s}{1min}\frac{1000mg}{g}\right]$$

Equation 32

Table 8: Calculation of the charge required to dissolve 1g of 3166,assuming valency of Fe=3, Cr=6 and Ni=2.

	wt%, g	*MW* g/g mol^{-1}	M_P (x10^{-2}) g mol^{-1}	*g-equiv/ g mol*	*g-equiv* (x10^{-2})	Q C
Fe	68.66	56	1.23	3	3.68	3549
Cr	16.87	52	32.4	6	1.95	1878
Ni	10	58.7	17	2	0.341	329
			Total charge to dissolve 1g of 316 SS =			5756

$$m_P(mm\ cm^{-2}) = 10.42\frac{\eta_P\ I(A)\ t(min)}{S(cm^2)}$$

Equation 33

Where:

m_P	mass of product generated / lost
M_P	molar mass in (g mol^{-1})
MW	molecular weight
Q	charge passed (C)
S	surface area
v_e and v_P	stoichiometric ratios of electrons and product.

The current efficiency calculations are based on the amount of charge required to dissolve 1 g of the stainless steel (Table 8) and assume the highest solution valency state for each metal species (Fe, Cr and Ni) in the calculation. Values lower than unity (or 100%, when expressed as a percentage) imply the generation of by-products different from *P*, either electrolysis of the solvent or supporting electrolyte. In this case the current efficiency, represents the ratio of charge that oxidizes the electrode (Equation 34 to Equation 36) to the total charge that is passed by the reactions in Equation 34 to Equation 38. The number of coulombs to dissolve 1 g of 316 SS is calculated assuming that Equation 34 to Equation 36 are applicable and the composition of the 316 SS, with the chemical composition: Cr (16.87%), Ni (10%), C (190 ppm), Mn (1.38%), Si (4600 ppm), P (40 ppm), S (30 ppm) Mo (2.02%) and Fe (matrix). Once the total mass change is known current efficiency can be calculated by rearranging to get Equation 33.

At the anode:

$$Fe + 3H_2O \rightarrow Fe(OH)_3 + 3H^+ + 3e^-$$

Equation 34

$$Cr + 4H_2O \rightarrow CrO_4^{-2} + 8H^+ + 6e^-$$

Equation 35

$$Ni + 2H_2O \rightarrow Ni(OH)_2 + 2H^+ + 2e^-$$

Equation 36

With side reactions:

$$2H_2O \rightarrow O_2 + 4H^+ + 4e^-$$

Equation 37

$$Cr(OH)_3 + H_2O \rightarrow CrO_4^{-2} + 5H^+ + 3e^-$$

Equation 38

At the cathode:

$$2H^+ + 2e^- \rightarrow H_2$$

Equation 39

With side reactions:

$$CrO_4^{-2} + 5H^+ + 3e^- \rightarrow Cr(OH)_3 + H_2O$$

Equation 40

$$SO_4^{2-} + 4H^+ + 2e^- \rightarrow SO_2 + 2H_2O$$

Equation 41

3 Results

3.1 Characterization of untreated stainless steel

Various techniques were utilised in the study:

1. Thermodynamic modelling
2. Polarization curves
3. Linear polarization resistance (LPR)
4. Contact resistance measurements

3.1.1 Thermodynamic modelling

Thermodynamic data for the reactions involving the metal, its ions, and its oxides can be usefully presented as a potential-*p*H diagram. These diagrams are used for estimating corrosion behaviour of different metals in aqueous solutions. HSC Chemistry software (H-Enthalpy, S-Entropy, C-Heat capacity), (Outotec, Finland, HSC Chemistry v.6.12), was used to perform Gibbs free energy minimization calculations and to provide insight into the limits of stability of the stainless steel alloying elements (Fe, Cr, Ni and Mn) in aqueous solution depending on the *p*H and electrode potential and the relative position of the boundary for oxidation and reduction of water.

The highlighted numbered regions within the E_h-*p*H diagrams are representative of:

- The corrosive region: the most stable form is the metal cation or any non-protective anion (corrosion will occur until the metal is consumed)
- The immune region: corrosion is thermodynamically impossible
- The passive region: an insoluble protective layer (hydroxide or oxide layer) is the most stable form; initial corrosion will occur until a protective layer is formed.

The *p*H of water withdrawn from a PEM fuel cell operating with H_2/air is typically *p*H 1-4 at the beginning of operation, presumably as a result of leaching excess acid from the membrane or ion leaching. After sometime of operation the water is essentially pure at a *p*H of 6-7 [138]; therefore, stability fields that lie below *p*H< 6 will be the main regions of focus.

3.1.1.1 Iron (Fe)

Figure 28 is an example of the E_H-*p*H-diagram for iron in aqueous solutions in which no complex ions are formed and the oxides of iron are the only stable solid phases, calculated for 1M concentration of dissolved iron at PEM fuel cell operating temperature of 70 °C. The boundaries between the areas on the diagrams represent the chemical reactions that define the equilibrium between the adjoining stable chemical species, with the boundary position depending on the activity of soluble bearing ions.

The diagram shows the zones of thermodynamic stability of the various ions (in solution) and the solid oxides of iron in relation to the standard reversible potentials of the H^+/H_2 or O_2/OH^- reactions, indicated as dashed lines. Iron will corrode to produce ions only if the potential–*p*H condition is such that the thermodynamically stable form of iron is an ion in solution i.e. Fe^{2+}, Fe^{3+} or $HFeO_2^-$.

The Pourbaix diagrams of Fe at 70 °C, highly oxidizing and acidic conditions are represented at the upper left hand corner represents conditions that are, conditions under which the higher valence state of iron (Fe^{3+}) is the more stable form. This is the stability region of the Fe^{3+} ion; however, in reality the stable form is the hydrated ion $Fe(H_2O)_6^{3+}$ (aq) [97]. As the acidity decreases i.e. 1 > *p*H > 6; the stable ion Fe^{3+} is ultimately replaced by haematite (Fe_2O_3), with no valency change as a new stability field is entered. With increasing temperature, a slight shift of the boundary represented by the vertical line between the two stability fields representing equilibrium between Fe^{3+}/ Fe_2O_3 with no valency change is observed.

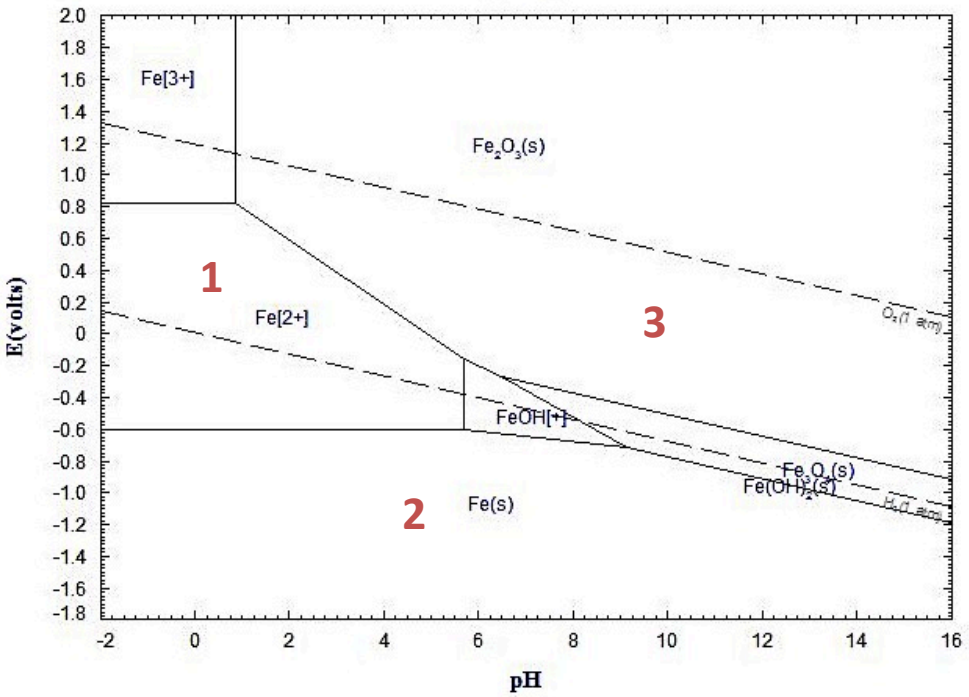

Figure 28: Potential-pH equilibrium diagram for the iron-water system at 70 ˚C (solid substances considered are only; Fe, Fe_3O_4 and Fe_2O_3)

The Pourbaix diagram of Fe upper left hand corner represents conditions that are highly oxidizing and acidic, conditions under which the higher valence state of iron (Fe^{3+}) is the more stable form. This is the stability region of the Fe^{3+} ion; however, in reality the stable form is the hydrated ion $\mathrm{Fe(H_2O)_6^{3+}}\ (aq)$ [97]. As the acidity decreases i.e. 1 > *p*H > 6; the stable ion Fe^{3+} is ultimately replaced by haematite (Fe_2O_3), with no valency change as a new stability field is entered. With increasing temperature, a slight shift of the boundary represented by the vertical line between the two stability fields representing equilibrium between Fe^{3+}/ Fe_2O_3 with no valency change is observed.

As the oxidising power decreases from the left hand corner of the diagrams (i.e. as the potential of the ordinate decreases), more reducing conditions are approached and ultimately the lower valence state, ferrous ions (Fe^{2+}) becomes the stable species represented by the half reaction (Equation 42) which confirms no change in acidity.

$$Fe^{3+} + e^{-} \rightarrow Fe^{2+}$$

Equation 42

Further reduction in the oxidizing potential leads to the Fe^{2+} ion being replaced by the more stable metal Fe. The horizontal boundary here that separates the two stability fields is representative of the OCP and is independent of *p*H. With increasing temperature this boundary shifts towards more oxidizing conditions, which consequently mean an increase in the OCP towards the noble direction with respect to the concentration. While increasing the *p*H from the upper part of the Fe^{2+} field of stability, results in a change of oxidation state, in the lower part of Fe^{2+} field of stability, Fe^{2+} gives way to the formation of the hydroxide as represented by Equation 43, where no change in oxidation state occurs.

$$Fe^{2+} + H_2O \rightarrow FeOH^{+} + H^{+}$$

Equation 43

In basic solutions with pH>6, the main aqueous species is $FeOH^{+}$ with the thermodynamically stable haematite oxide (Fe_2O_3) and magnetite oxide (Fe_3O_4).

3.1.1.2 Chromium (Cr)

Figure 29 is an example of the E_h-*p*H-diagram for chromium in aqueous solutions at at 70 °C. The dissolved species of chromium, which represent corrosion, are Cr^{2+} and Cr^{3+} together with its four-hydrolysis steps. Chromium corrodes in acidic solutions to form Cr^{2+}, which is unstable and can oxidize further to three or six valence forms. Depending on *p*H, temperature, and concentration, Cr^{3+} species can be either aqueous complexes or a solid compound (Cr_2O_3), which represents passivity. Though not shown in Figure 29, in the pH range 6 > *p*H > 2, $HCrO_4^-$ and dichromate ion $Cr_2O_7^{2-}$ (orange-reddish colour in solution) coexist [88]. In basic solutions with *p*H > 6, the main aqueous species is the tetrahedral ion CrO_4^{2-} that causes a yellowish color to the solution. At *p*H < 1 the main

solute species is H_2CrO_4. Equilibria among protonated species may be represented in the form:

$$H^+ + CrO_4^{2-} \leftrightarrow HCrO_4^-$$

Equation 44

$$Cr^{3+} + e^- \rightarrow Cr^{2+}$$

Equation 45

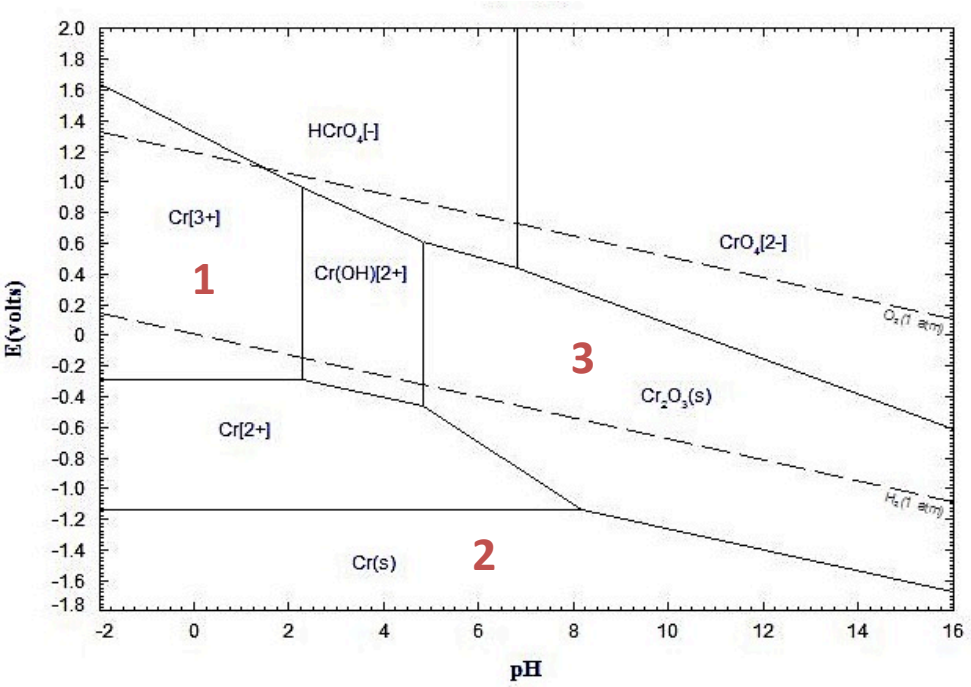

Figure 29: Potential-pH equilibrium diagram for the chromium-water system at 70 °C, considering anhydrous Cr_2O_3 (in chloride free solution)

The corrosion area at alkaline *p*H and the *p*H-independent corrosion area at high potentials increase with temperature. The reason for this behaviour is related to the temperature dependence of the ionic product of water. Secondly, the concentration of dissolved chromium species changes also the size of the different stability areas. The immunity and passivity areas increase with increasing concentration, while the corrosion areas decrease.

3.1.1.3 Nickel (Ni)

Figure 30 is an example of the E_h-*p*H-diagram for nickel in aqueous solutions at 70 °C. The immunity area of nickel is part in common with the stability area of water, which means that nickel cannot reduce water in this area. However, the corrosion resistance of nickel is highly dependent on *p*H and oxidation agents. As seen in Figure 30, nickel corrodes mainly in acid to neutral solutions by predominance of the ions Ni^{2+} and $NiOH^{+}$, while in non-complexing, neutral to strongly alkaline solutions free from oxidizing agents, nickel should not corrode.

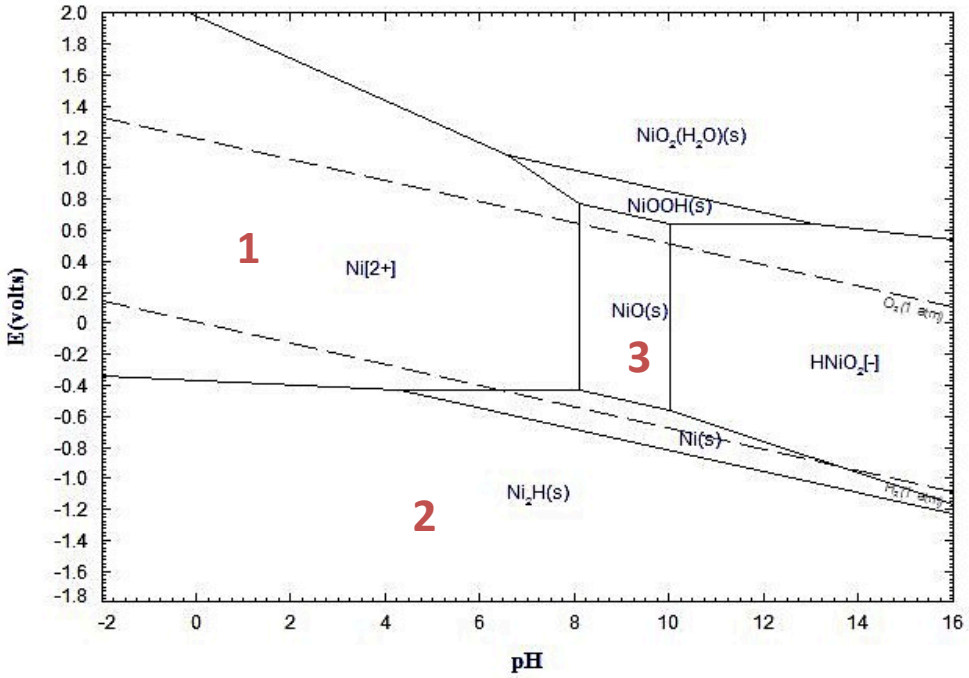

Figure 30: Potential-pH equilibrium diagram for the nickel-water system at 70 °C

3.2 Corrosion behaviour of stainless steels

3.2.1.1 Polarization curve

Figure 31 to Figure 34 depicts the potentiodynamic polarization curves of four prominent stainless steel alloys, 904, 310, 304 and 316 SS, tested at different temperatures (60, 70 and 80°C). The corrosion systems only partially exhibit the limiting current density at high cathodic current

densities. While the anodic branches of the polarization curves do not show the typical passivation behaviour exhibited in the Tafel region.

The corrosion potential, E_{corr} of each alloy was therefore determined from the point of convergence of the cathodic/anodic Tafel lines with E_{corr}, where equilibrium between the forward and backward reactions is established. Figure 35 demonstrates the trend of each alloy with respect to temperature and lists the actual E_{corr} values with respect to a HRE. The cathodic Tafel regions are observed to be far more well- defined for all the tested alloys, compared to the anodic domain. Accordingly, determination of the corrosion rate (i_{corr}) by intersection of anodic and cathodic Tafel lines at the corrosion potential will lead to erroneous values. Corrosion rates were therefore estimated using the cathodic portion of the polarization curves only. As the cathodic polarization curves exhibit wide and well-defined Tafel regions, accurate estimation of i_{corr} was established by extrapolation of the cathodic Tafel lines back to the corresponding values of E_{corr}. The anodic current density i_a is thus the sum of the experimentally observed anodic current density and the extrapolated cathodic current density as shown for 904L SS, 304 SS, 304 SS and 316 SS in Figure 36 to Figure 47. The E_{corr} and i_{corr} values for all the four alloys studied (904L SS, 310 SS, 304 SS and 316 SS) across the temperature range 60 - 80 °C are shown in Table 9.

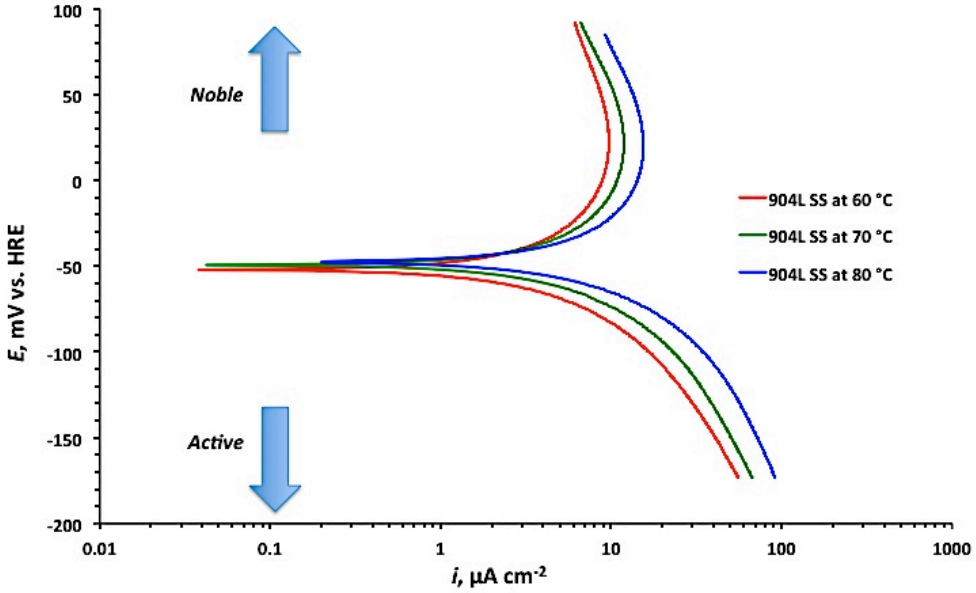

Figure 31: Tafel plots of 904L SS in 0.5M H_2SO_4, de-aerated with N_2 in the PEM fuel cell operating temperature range at a scan rate of 1 mV s^{-1}.

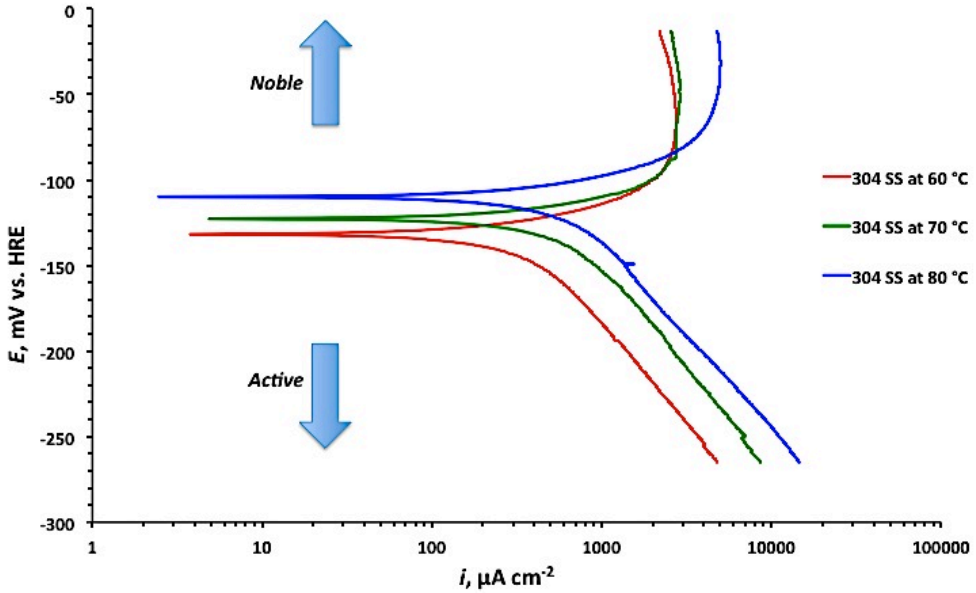

Figure 32: Tafel plots of 310 SS in 0.5M H_2SO_4, de-aerated with N_2 in the PEM Fuel cell operating temperature range at a scan rate of 1 mV s^{-1}.

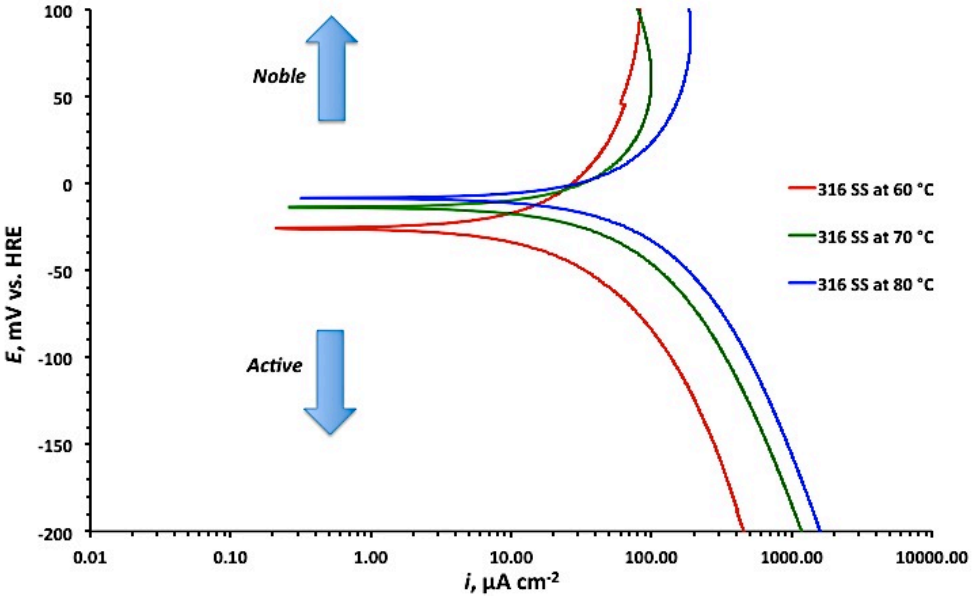

Figure 33: Tafel plots of 316 SS in 0.5M H_2SO_4, de-aerated with N_2 in the PEM Fuel cell operating temperature range at a scan rate of 1 mV s^{-1}.

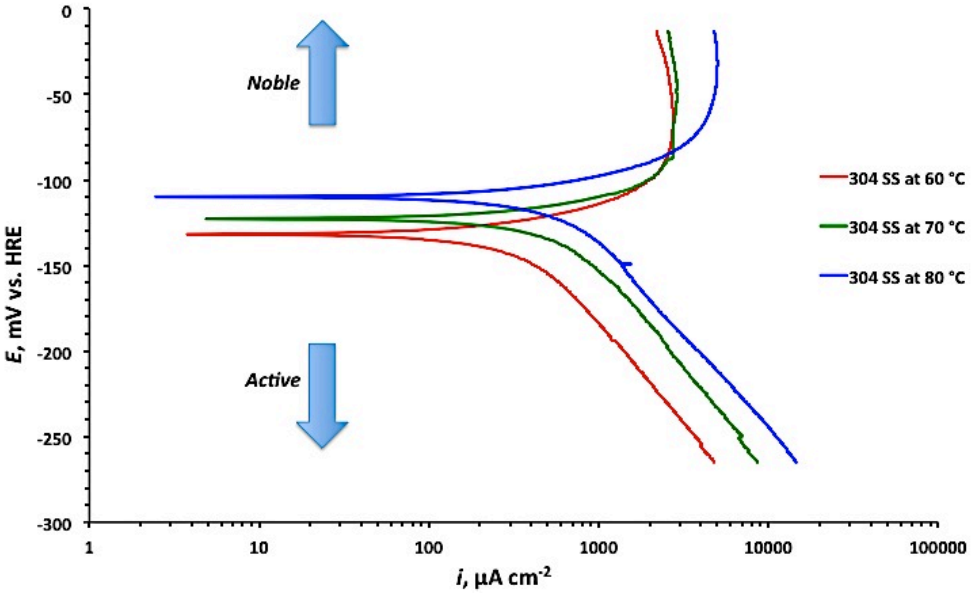

Figure 34: Tafel plots of 316 SS in 0.5M H_2SO_4, de-aerated with N_2 in the PEM Fuel cell operating temperature range at a scan rate of 1 mV s^{-1}.

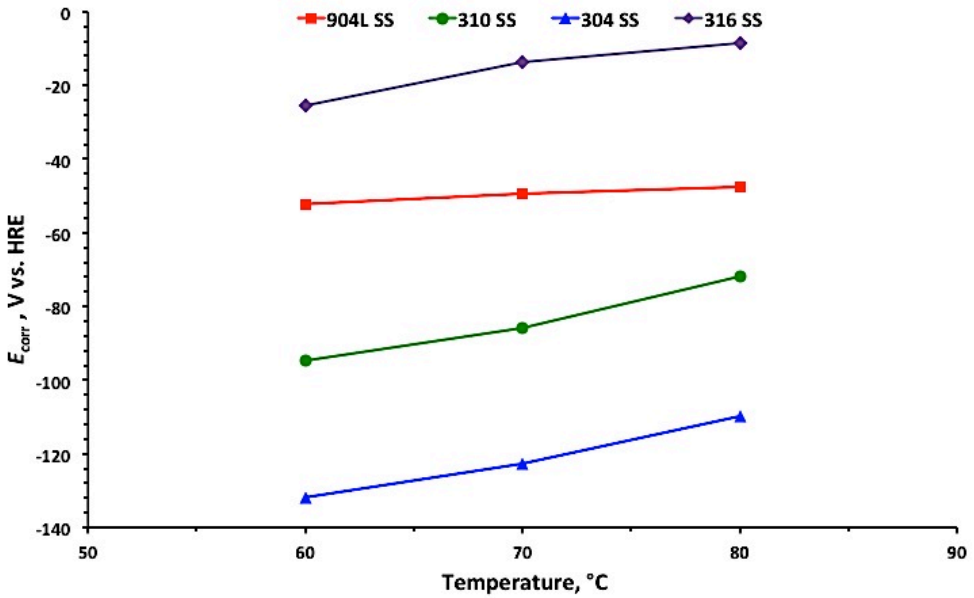

Figure 35: Dependence of E_{corr} of 904, 304 & 316 SS, alloys on temperature in 0.5M H_2SO_4, de-aerated with N_2.

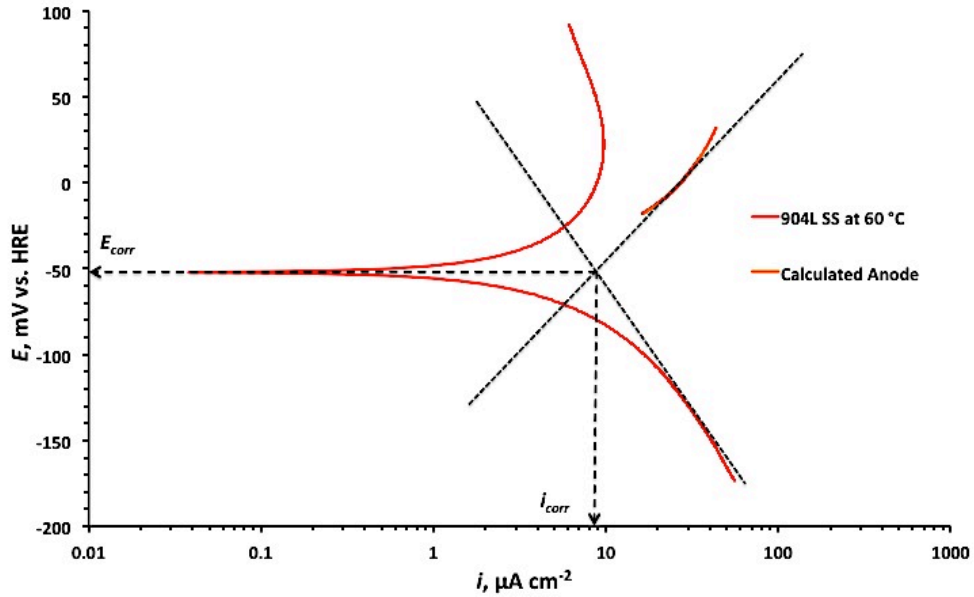

Figure 36: Tafel plot extrapolation of 904L SS in 0.5M H_2SO_4 at 60°C, de-aerated with N_2 at a scan rate of 1 mV s^{-1}.

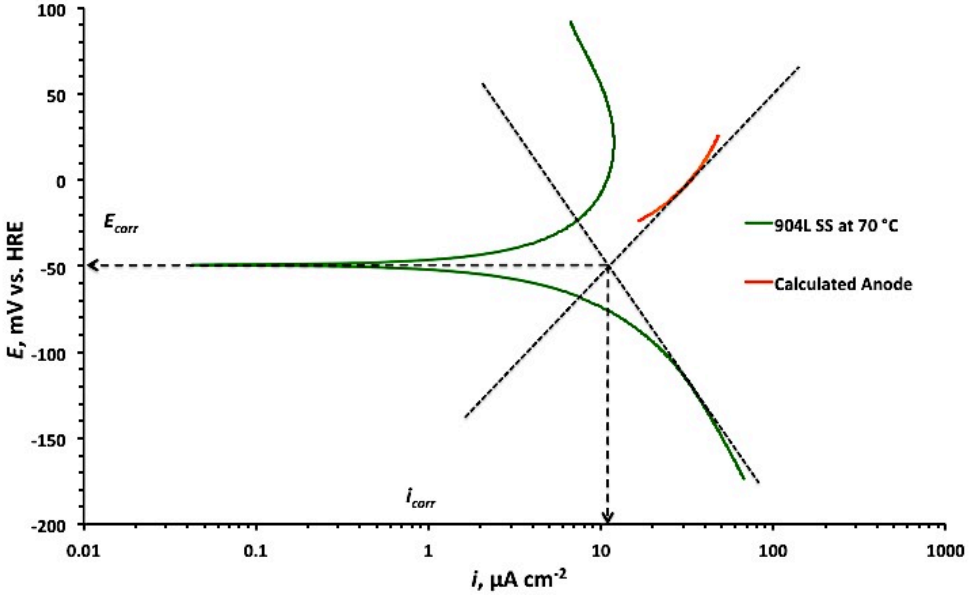

Figure 37: Tafel plot extrapolation of 904L SS in 0.5M H_2SO_4 at 70°C, de-aerated with N_2 at a scan rate of 1 mV s^{-1}.

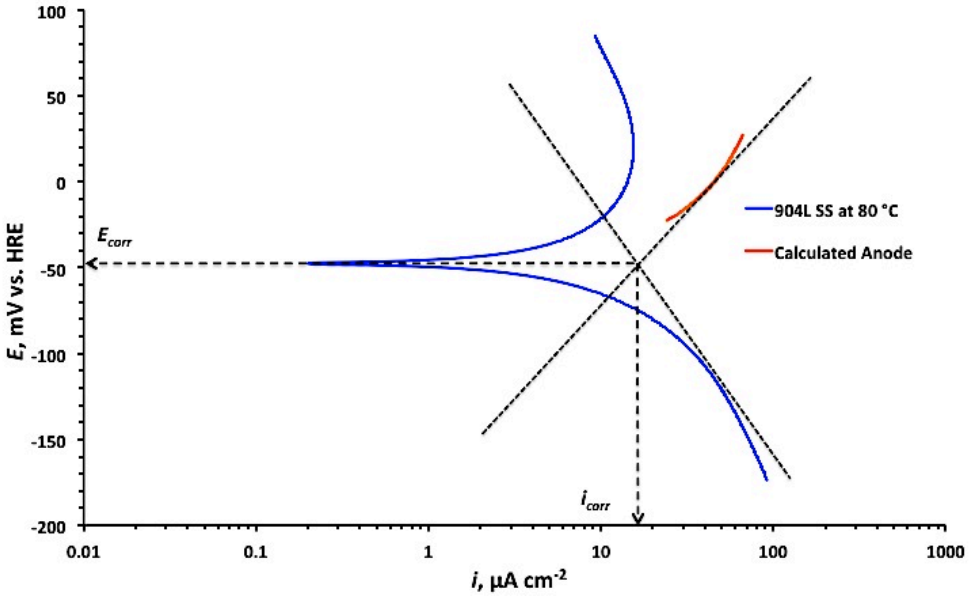

Figure 38: Tafel plot extrapolation of 904L SS in 0.5M H_2SO_4 at 80°C, de-aerated with N_2 at a scan rate of 1 mV s^{-1}.

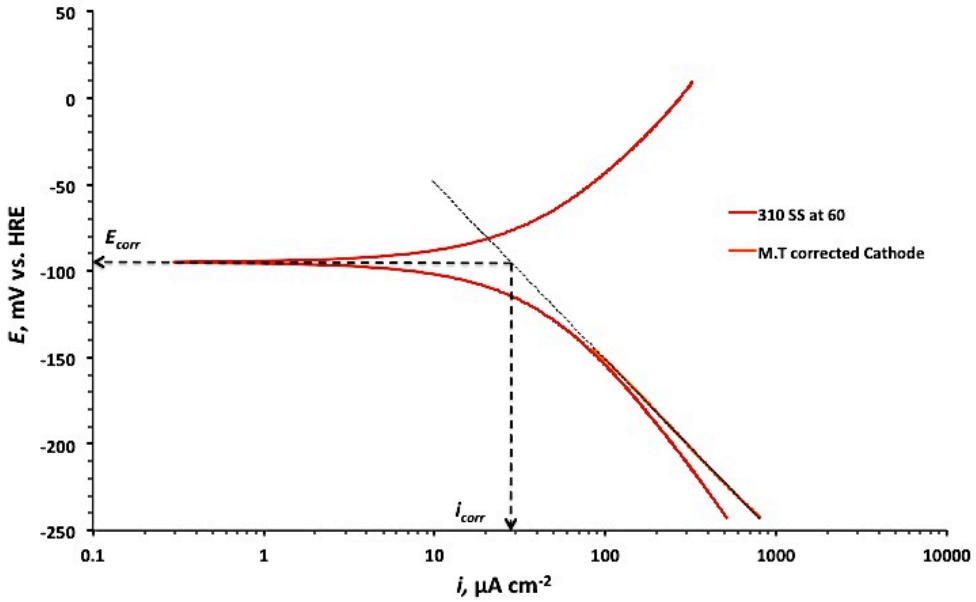

Figure 39: Tafel plot extrapolation of 310 SS in 0.5M H_2SO_4 at 60°C, de-aerated with N_2 at a scan rate of 1 mV s^{-1}.

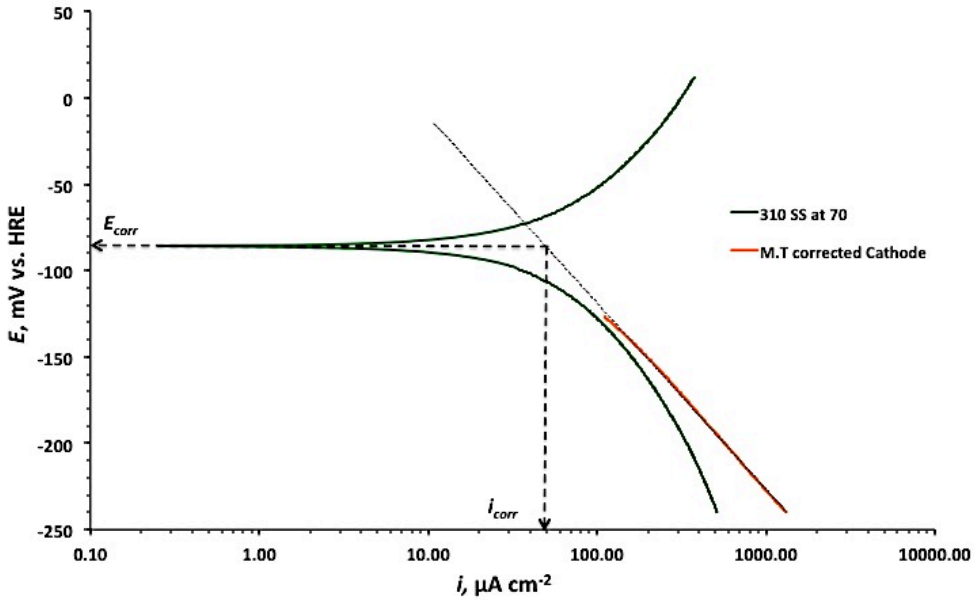

Figure 40: Tafel plot extrapolation of 310 SS in 0.5M H_2SO_4 at 70°C, de-aerated with N_2 at a scan rate of 1 mV s^{-1}.

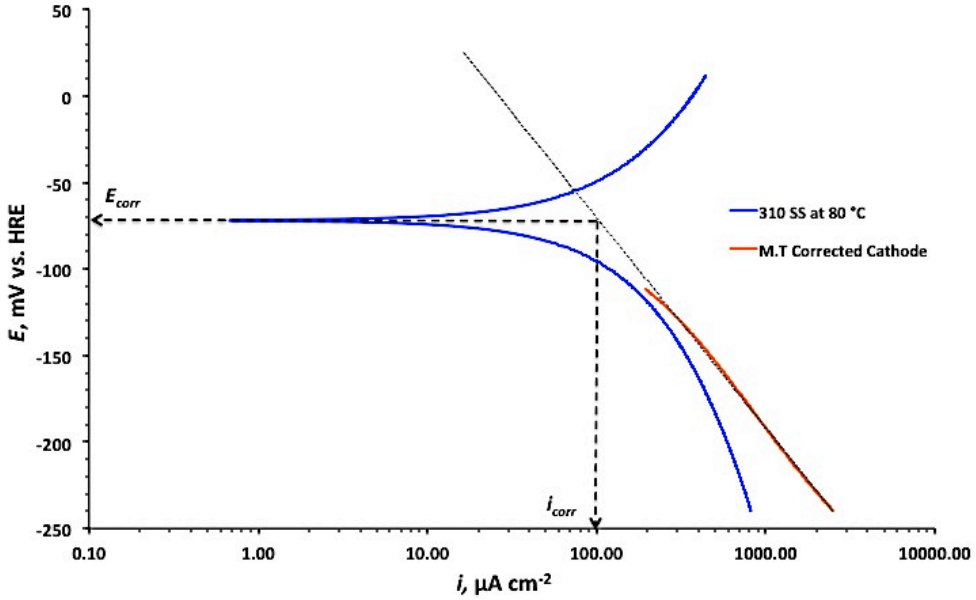

Figure 41: Tafel plot extrapolation of 310 SS in 0.5M H_2SO_4 at 80°C, de-aerated with N_2 at a scan rate of 1 mV s^{-1}.

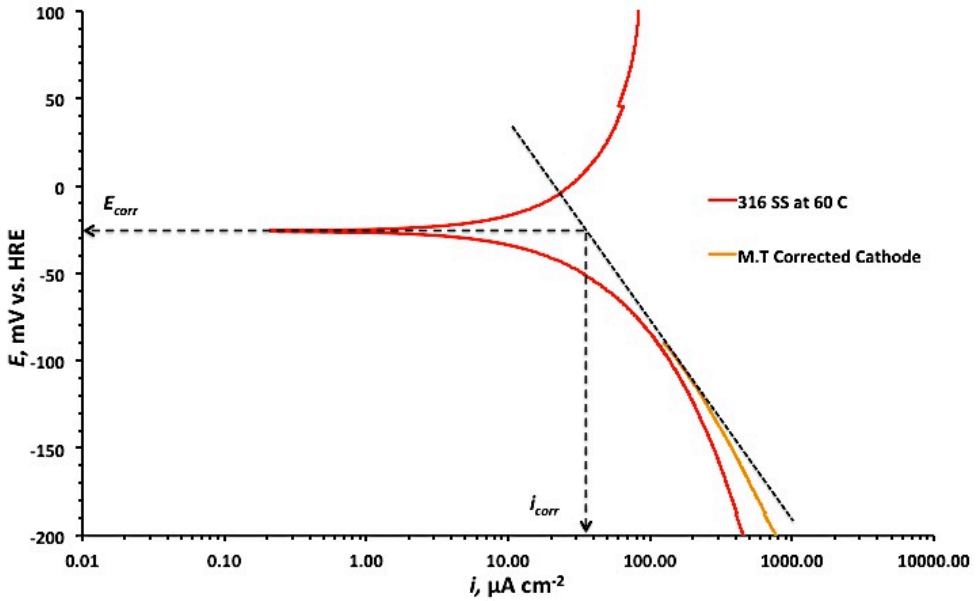

Figure 42: Tafel plot extrapolation of 316 SS in 0.5M H_2SO_4 at 60 °C, de-aerated with N_2 at a scan rate of 1 mV s^{-1}.

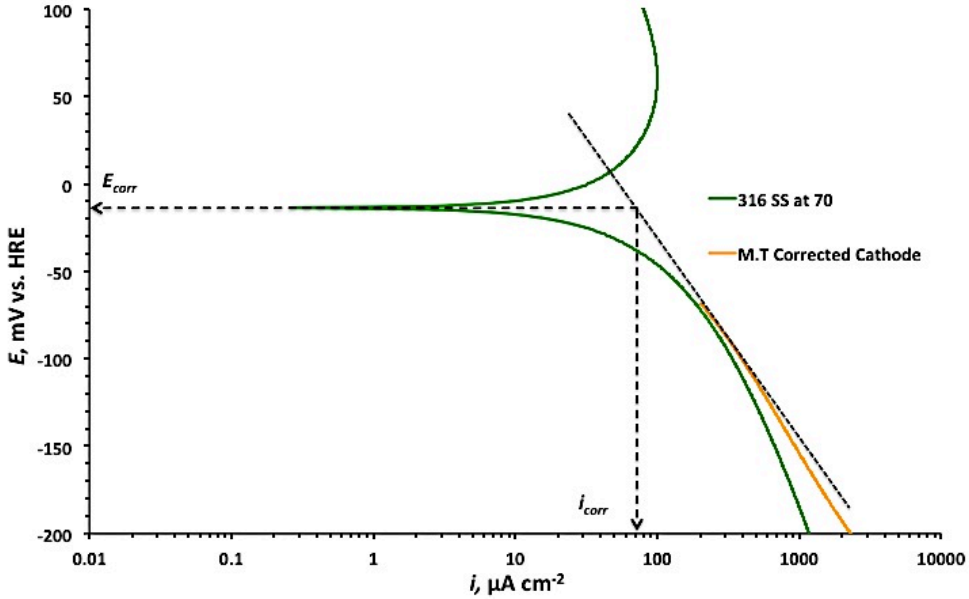

Figure 43: Tafel plot extrapolation of 316 SS in 0.5M H_2SO_4 at 70°C, de-aerated with N_2 at a scan rate of 1 mV s^{-1}.

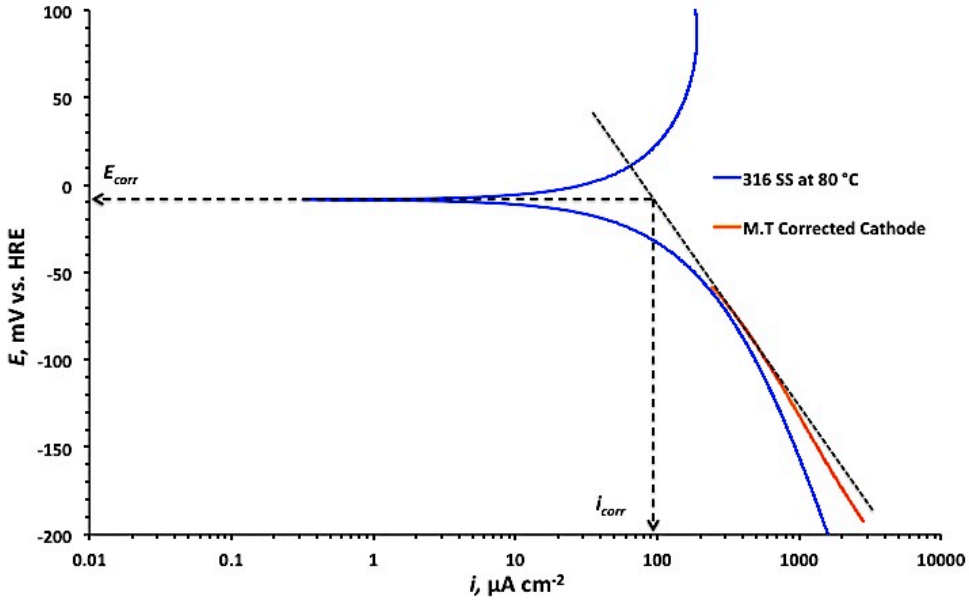

Figure 44: Tafel plot extrapolation of 316 SS in 0.5M H_2SO_4 at 80°C, de-aerated with N_2 at a scan rate of 1 mV s^{-1}.

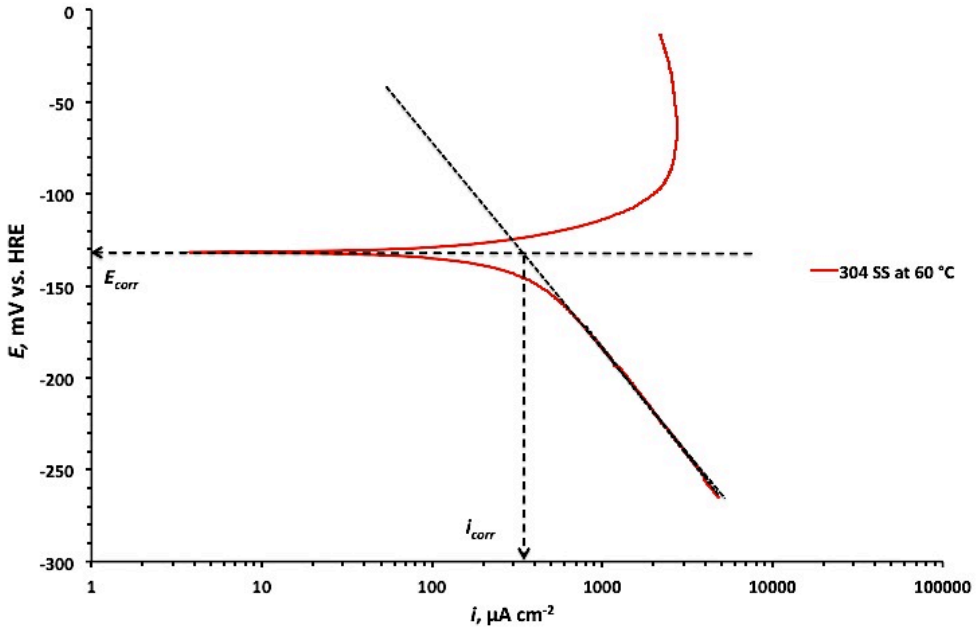

Figure 45: Tafel plot extrapolation of 304 SS in 0.5M H_2SO_4 at 60°C, de-aerated with N_2 at a scan rate of 1 mV s^{-1}.

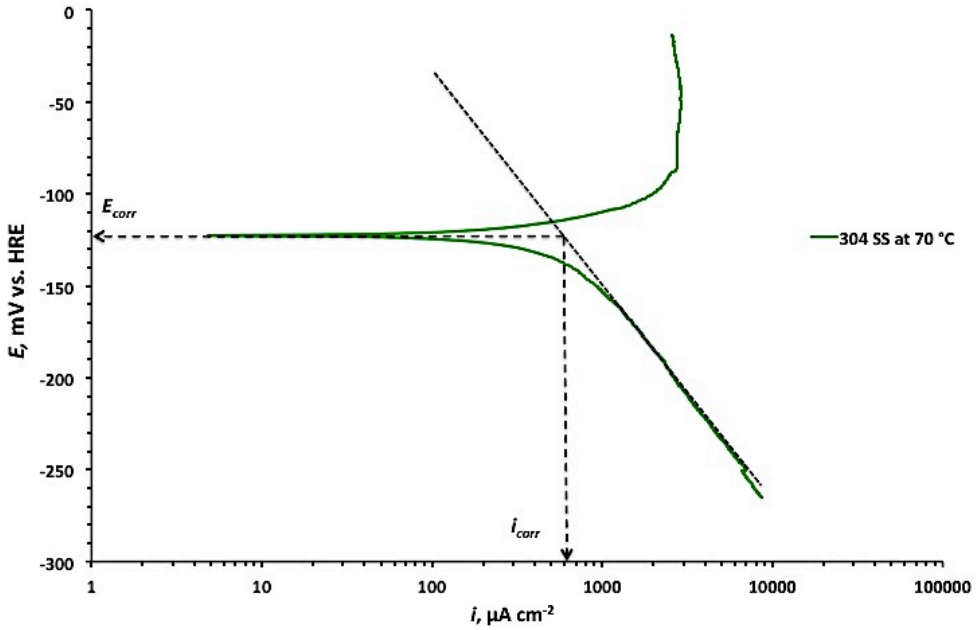

Figure 46: Tafel plot extrapolation of 304 SS in 0.5M H_2SO_4 at 70°C, de-aerated with N_2 at a scan rate of 1 mV s^{-1}.

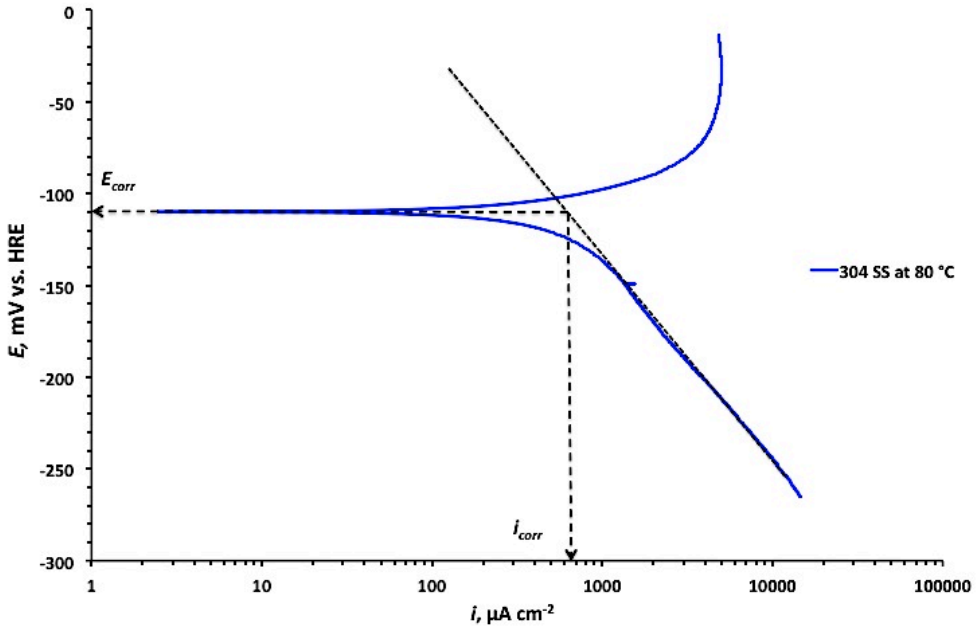

Figure 47: Tafel plot extrapolation of 304 SS in 0.5M H_2SO_4 at 80°C, de-aerated with N_2 at a scan rate of 1 mV s^{-1}.

Table 9: Corrosion current densities of tested stainless steel alloys determined by Tafel plot extrapolation method at 60, 70 and 80 °C.

	Temp, °C	E_{corr}, mV_{HRE}	i_{corr}, µA cm^{-2} (Tafel)
	60	-52.2	8
904L SS	70	-49.4	12
	80	-47.6	17
	60	-94.8	28
310 SS	70	-85.7	50
	80	-72	100
	60	-25.6	50
316 SS	70	-13.6	84
	80	-8.4	101
	60	-131.8	330
304 SS	70	-122.7	620
	80	-109.9	670

3.2.1.2 Linear Polarisation Resistance (LPR)

Another technique of measuring i_{corr} that is based on the theoretical and practical demonstration that at potentials close to E_{corr} the relationship between potential and applied current is approximately linear. The inverse of this slope can be related to i_{corr} by following Equation 11 [91] in section 1.10.3. For stainless steel the suggested value for the Stern–Geary coefficient is 26 mV [151]. Table 10 summarizes the current density values determine via Tafel plot extrapolation and LPR method with R_p values.

Table 10: Comparison of corrosion current densities of 910L, 310, 304 and 316 stainless steel alloys determined by Tafel plot extrapolation method and LPR method at 60, 70 and 80 °C in 0.5 M H_2S0_4

	Temp, °C	R_p, Ω cm^{-2}	i_{corr}, µA cm^{-2} LPR	i_{corr}, µA cm^{-2} Tafel
	60	3.730	7	8
904L SS	70	2.813	9	12
	80	2.027	13	17
	60	0.692	38	28
310 SS	70	0.360	72	50
	80	0.234	111	100
	60	0.835	31	50
316 SS	70	0.389	67	84
	80	0.274	95	101
	60	0.031	831	330
304 SS	70	0.019	1368	620
	80	0.018	1429	670

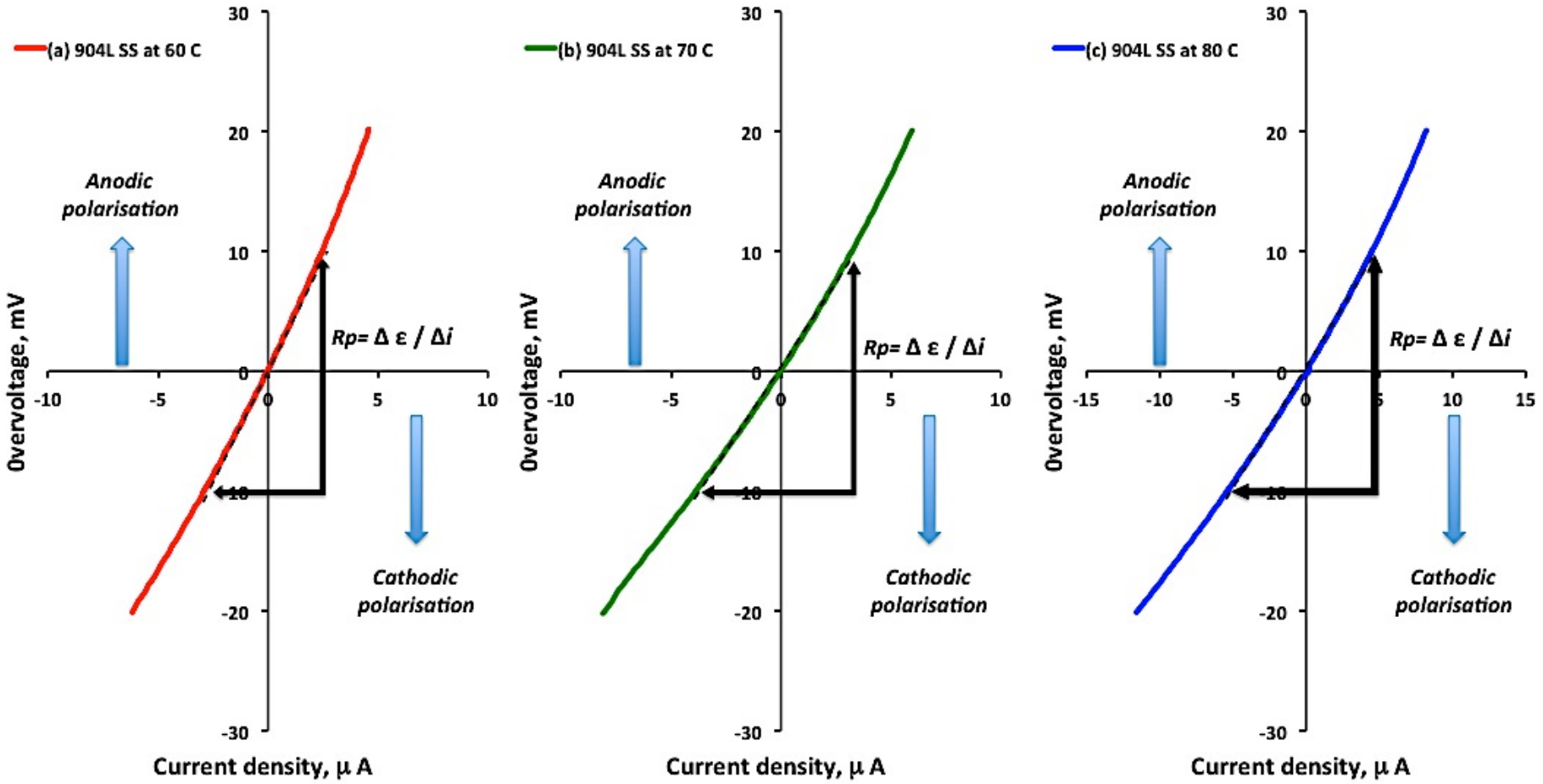

Figure 48: LPR Polarization curve obtained by potentiodynamic polarization (± 10 mV/*E*corr, 0.1 mV/s) for 904L SS in 0.5 M H_2SO_4 at (a) 60 ° C (b) 70 ° C and (c) 80 ° C.

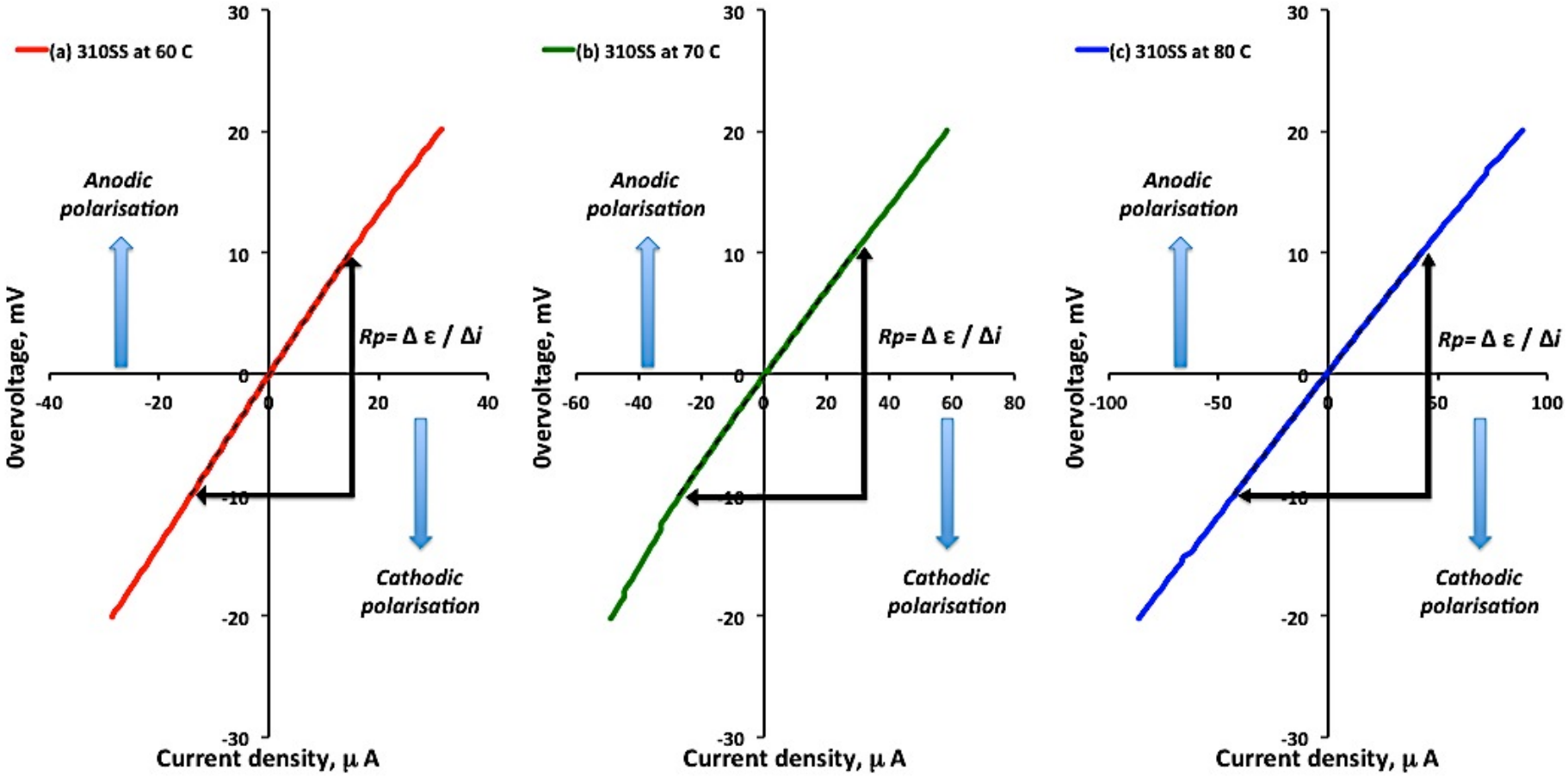

Figure 49: LPR Polarization curve obtained by potentiodynamic polarization (±10 mV/Ecorr, 0.1 mV/s) for 310 SS in 0.5 M H_2SO_4 at (a) 60 ° C (b) 70 ° C and (c) 80 ° C.

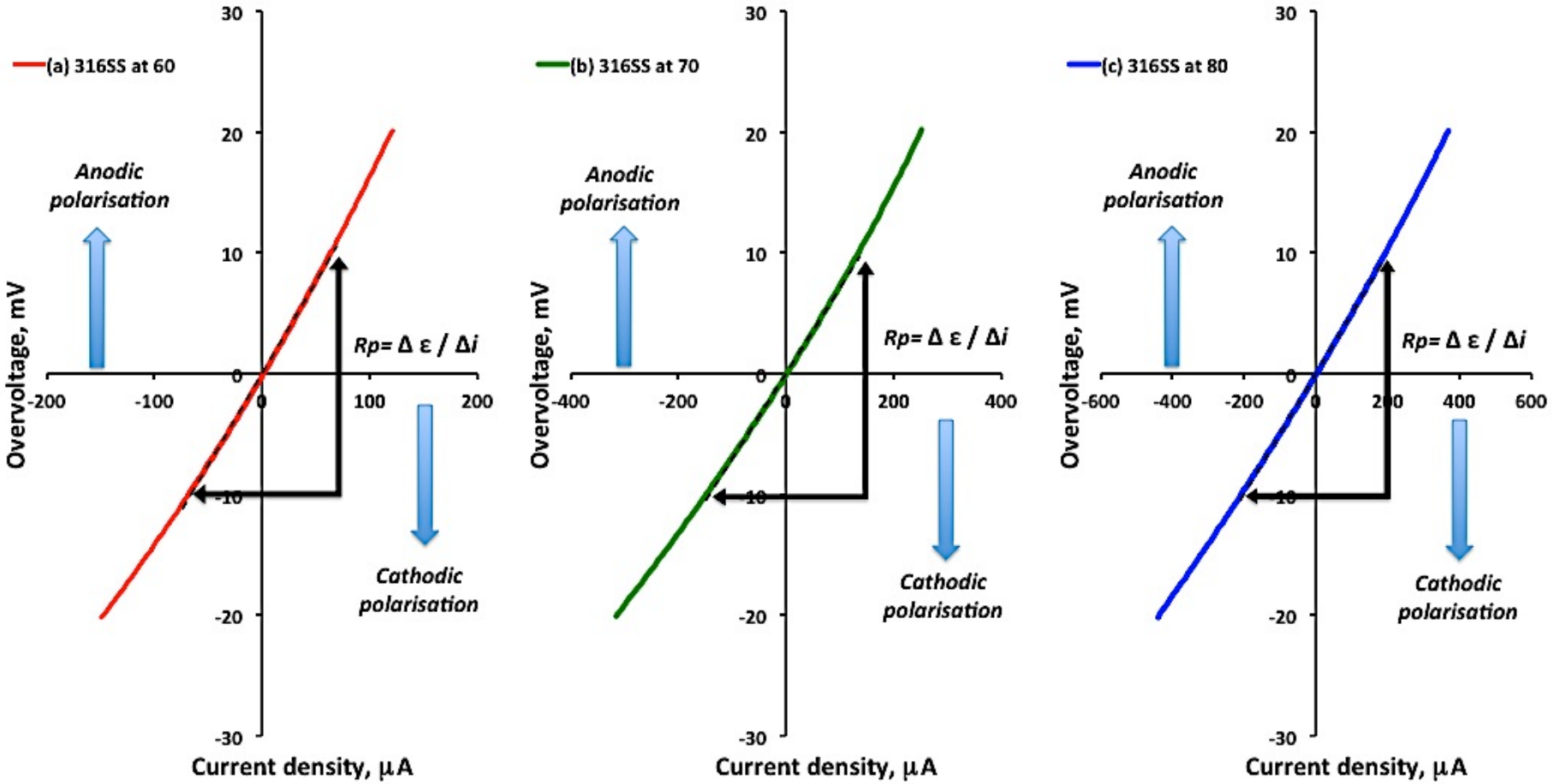

Figure 50: LPR Polarization curve obtained by potentiodynamic polarization (± 10 mV/Ecorr, 0.1 mV/s) for 304 SS in 0.5 M H_2SO_4 at (a) 60 ° C (b) 70 ° C and (c) 80 ° C.

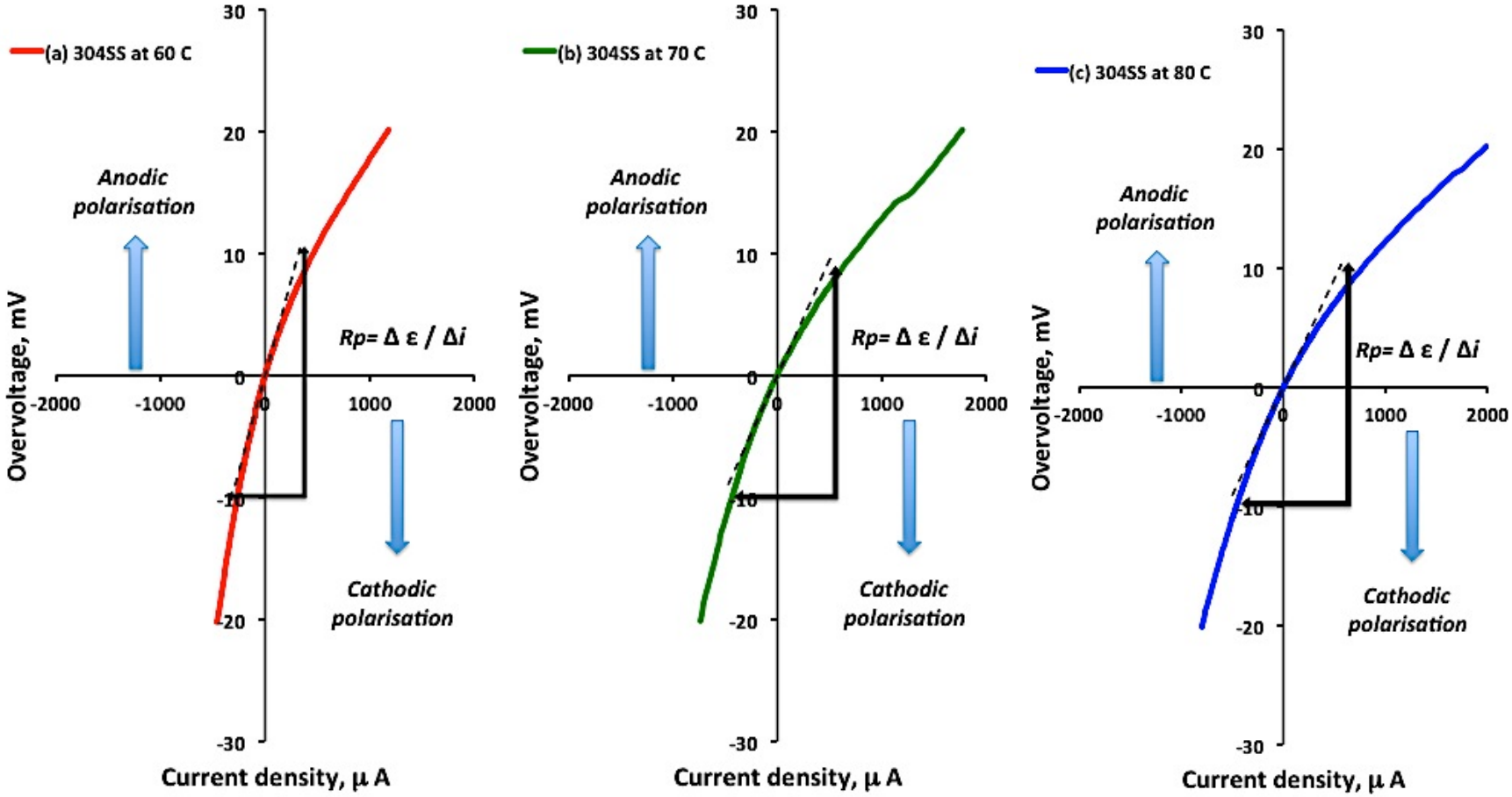

Figure 51: LPR Polarization curve obtained by potentiodynamic polarization (±10 mV/Ecorr, 0.1 mV/s) for 304 SS in 0.5 M H_2SO_4 at (a) 60 ° C (b) 70 ° C and (c) 80 ° C.

3.2.2 Electrical Contact Resistance

The interfacial contact resistance between pristine samples of the different stainless steels and the carbon paper was investigated at different compaction forces. Only one interfacial contact resistance of the carbon paper / surface film for stainless steel formed in air is plotted (Figure 52) since both sides of the steel samples were cleaned and dried in the same manner allowing the same surface film formed in air on the either stainless steels to form.

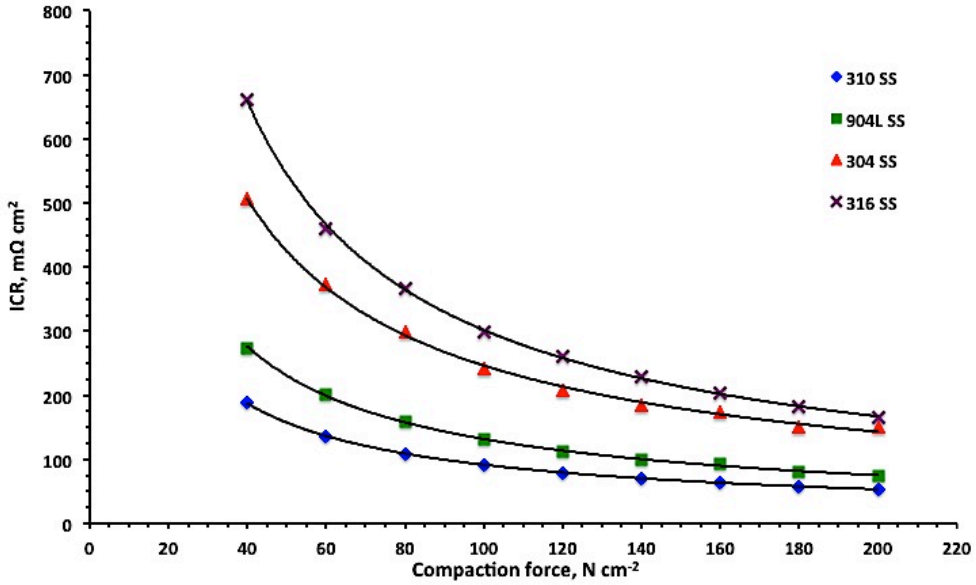

Figure 52: Comparison of ICR as a function of compaction force for 310 SS, 904L SS, 304 SS & 316 SS

From Figure 52 it can be seen that the ICR values of all samples initially decrease quickly under low compaction force; where a low compaction force mainly influences the ICR. This is due to fact that the contact points between the testing sample and the carbon paper increase as the compaction force increases. On the other hand, under higher compaction forces, the ICR decreases gradually and finally approach a plateau where

the compaction force / contact points is no longer the main influence on the ICR.

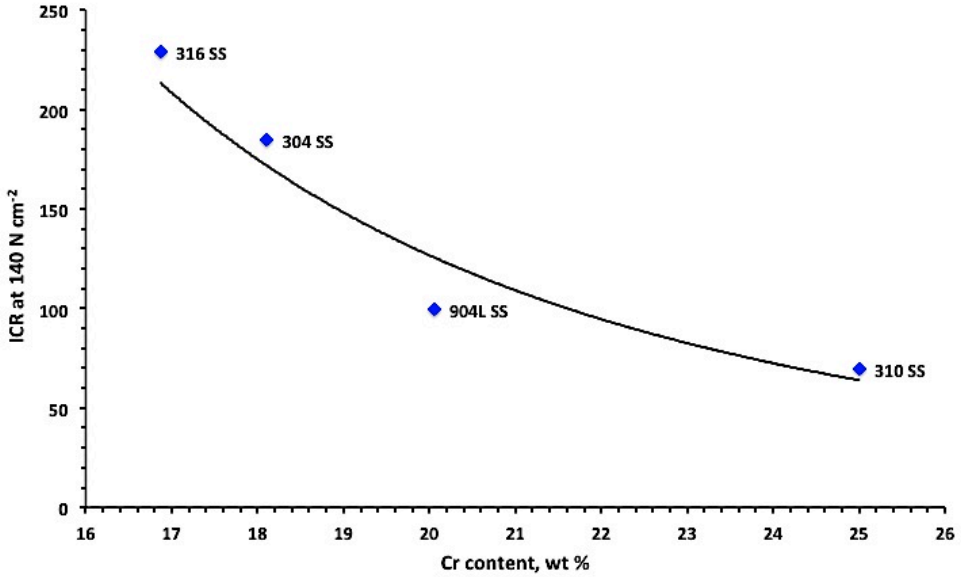

Figure 53: Interfacial contact resistance for 310 SS, 904L SS, 304 SS and 316 SS at the DOE recommended compaction force of 140 N cm^{-2}

3.2.3 Discussion

The E_{corr} values for all the four alloys studied (904L SS, 310 SS, 304 SS and 316 SS) across the temperature range 60 - 80 °C are shown in Figure 35. The highest E_{corr} values are exhibited by 316 SS across the whole temperature range of study (-8.4 mV_{HRE}, at 80 °C), with the most negative OCP value at the same temperature was that of 304 SS (-131.8 mV_{HRE}, at 60 °C). The OCP value of the four stainless steel alloys, 904L SS, 310 SS, 316 and 304 SS respectively, shifted towards more positive values (noble direction) as temperature increased from 60 to 80 °C. A positive linear correlation is observed with increase in temperature as observed in Figure 35.

This shift towards noble/active direction for the tested alloys becomes more pronounced with increasing temperature of the electrolyte solution, from 60 - 80 °C for lower alloyed SS. The average ennoblement of the corrosion potential was in the order of, 1.14 mV/ °C for 310 SS > 1.10 mV/ °C for 304 SS > 0.86 mV/ °C for 316 SS > 0.23 mV/ °C for 904L SS as seen in Figure 35. This shows a clear distinction between E_{corr} shift and the more noble behaviour of the highly alloyed SS and qualitatively, this behaviour correlated well with the actual corrosion performance of the alloys.

The results for stainless steels with differing levels of alloying elements have shown that the passivation behaviour depends strongly on the content of Cr, Ni and Mo. Corrosion potentials and other properties of steels depend also on the concentration of other additives appearing either as intentionally added, e.g. Cu, Mn, C, N, or present as impurities in the steel. *Wilde and Green* [51] found that content of Mn and S is detrimental for the resistance of 304 steels against corrosion, shifting corrosion potential up to ~-201 mV_{HRE}, while the most positive corrosion potential of low impurity content 304 steels have corrosion potential of about -49 mV_{HRE}. In all cases the presence of Cu and Mo was found to be beneficial.

Corrosion potentials of pure constituents of stainless steels in deaerated sulphuric acid solutions at *pH* ~ 1 are in the following range;

- Pure Fe has corrosion potential at about – 259 mV_{HRE} [49].
- Active dissolution corrosion potential of Cr is about -499 mV_{HRE}, while the corrosion potential of passive Cr is about -159 mV_{HRE} [13], and controlled by the *Wagner–Traud* mechanism with cathodic hydrogen evolution reaction on the passive surface of Cr.
- Corrosion potential of Ni is about -211 mV_{HRE} [152].

The corrosion potentials of the four different stainless steels alloys will obviously not only be within the potential range of mainly of Fe, Cr and Ni but also depend upon the electrochemical properties and behaviour of these components, while the other alloying components can change the corrosion potential of stainless steel only to some extent in the direction corresponding to their nobility.

The corrosion behaviour of the alloys tested was determined by either of the two methods; Tafel extrapolation or LPR, with both demonstrating similar trends of increase in current density with respect to temperature for all the stainless steel alloys tested. As seen in Figure 31 to Figure 34, in all cases, the cathodic branches of the polarization curves display a typical Tafel behaviour, which makes it possible to make an accurate evaluation of the cathodic Tafel slope (β_c) as well as corrosion currents (i_{corr}) by the Tafel extrapolation method. In contrast, the anodic polarization curves do not display the expected log / linear Tafel behaviour over the complete applied potential range. An inflection is quite clear in the anodic branches, which could be attributed to passivation and pitting, which makes it impossible to make an accurate evaluation of the anodic Tafel slopes (β_a) [148], [8], [34]. It has also been noted that the curvature of the anodic branches may be attributed to the deposition of the corrosion products or impurities in the steel (e.g., Fe_3C) to form a non-passive surface film [87].

The LPR method was also utilised here for comparison in order to validate of corrosion rates measured by the latter. The LPR method is generally considered a non-destructive way of estimating the instantaneous corrosion rate of a metal as only a small perturbation is applied from E_{corr} in order to determine the corrosion current density. Moreover, this method of estimating the rate of corrosion is not very sensitive to the exact values of β_a and β_c, contrary to the Tafel extrapolation method. Figure 48 to

Figure 51 show the LPR plots from which the R_p values were determined at 60, 70 and 80°C for the 904L SS, 310 SS, 316 SS and 304 SS.

Analysis of the current densities (Table 10) across the tested temperate range (60 - 70°C) for both methods demonstrated a trend decreasing current densities following the order; 904L SS < 310 SS < 316 SS < 304 SS. The Tafel extrapolation method general demonstrated similar current densities to the LPR method for 904L SS, 310 SS, and 316 SS. However, much higher current densities are observed for 304 SS under the LPR method, compared to the Tafel extrapolation method. As observed in Figure 51 the linear polarization curves for 304 SS are considerably non-linear, which confuses the determination of the polarization resistance value to a certain extent. The non-linearity of the polarisation curve may be attributed to the considerable dissimilar values of Tafel slopes which comprises of the charge-transfer controlled oxygen reduction on the cathodic side and the diffusion controlled corrosion of passivated stainless steel on the anodic side, as mentioned in the introduction.

The variation of current density per temperature decade, which can be used as an indicator of the stability of the oxide layer with increasing temperature, also shows an increasing trend with temperature for all the tested alloys. The Tafel plot extrapolation technique indicated the largest rise per temperature decade for 304 SS, with the following order, 904L SS < 310 SS < 316 SS < 304 SS.

With regards to LPR, it is evident from Figure 48 to Figure 51 that the slopes of the plots increase as the temperature of the electrolyte solution increases. The R_p values were within same order of magnitude for the 300 series SS, while R_p values for 904L SS alloy remained an order of magnitude higher across the temperature range tested. A decrease in R_p values for all tested SS alloys with increase in the electrolyte solution temperature is

noted, and can be attributed to a greater degree of dissolution that of the protective oxide layer of the SS.

The noted difference in performance between the alloys is due to the variation in the alloying composition of the stainless steels which lead to varying properties of the passive oxide film, as demonstrated by *Davies et al*. [79]. The lower corrosion current densities of 904L SS and 310 SS can be attributed to the presence of greater amounts of chromium, nickel and molybdenum that result in a more stable protective oxide layer on the surface of the alloy. The presence of Cr makes these films passive over a greater range of anodic potentials, while the presence of Ni makes them stable. However, the distribution of metal ions in the film is usually different from that in the alloy, with the accumulation of Cr(III) ions in the outer layer and almost total depletion of Ni(II) from the layer [113]. When the passive film is exposed to an aqueous solution, a mixture of iron and chromium oxides, with hydroxide and water-containing compounds is usually located in the outermost region of the film, with chromium oxide enrichment at the metal-film interface [7].

The ICR of 316 SS and 304SS is relatively high in comparison to 310 SS and 904L SS because of the weak conductivity of the passive film formed on the surface. It is also noted that the ICR are similar in trend for both the higher alloy stainless steels (310 SS and 904L SS) and lower alloy stainless steel (304 SS and 316 SS). The thickness of the passive films consisting of chromium, iron and nickel oxides formed on the steel surface has been attributed as the key inhibitors to the electrical conductivity [35, 79]. As seen in Figure 53, which shows evidently the ICR for the different stainless steels at a compaction force of 140 N cm^{-2} (whereby the ICR is of the order of 50 – 250 mΩ cm^{-2}), the interfacial contact resistance decreases with the Cr content of the alloys, with 310 SS showing the lowest interfacial contact

resistance and 316 SS the highest. The ICR between carbon paper and surface film formed in air for different steels, which also translates as the surface conductivity, increases in the order 310 < 904L < 304 < 316. This is in good agreement with results previously observed for the same materials, with ICR value ranging between (50 – 250 mΩ cm^{-2}) [36, 39, 100, 153]. The variation in the interfacial resistance throughout the range of stainless steel sample was most likely due to the composition of the alloys, in particular the passive film, which results from the formation of an insoluble oxide film on the surface. The principal components of this film for stainless steel are iron, nickel and chromium oxides, of which the cumulative properties of these oxides contribute to inhibiting the electrical conductivity [154-156].

A low ICR of a metallic bipolar plate is an important factor that influences the output power of the fuel cell stack and can increase the durability of the fuel cell stack. Although at present unsatisfactory to reach DOE targets, and problematic when exposed to the corrosive environment of a PEM fuel cell, low-cost surface treatment could represent a good compromise between using as-received 316 stainless steel plates and precious metal coated ones.

3.3 Anodization surface treatment

The effects of the process electrochemistry and system variables (H_2SO_4 concentration, glycerol content and convection effects) are explored with the use of polarisation data to investigate the effects under standard conditions, i.e. 25 ° C and 1 atm. The material of choice is 316 SS, which is the most widely studied SS for bipolar plate applications akin to its good corrosion resistance in simulated PEFC environment, low cost and based to the corrosion current density and ICR analysis from section 3.2.

3.3.1 Process electrochemistry

3.3.1.1 Acid concentration

The anode potential, and the voltage drop across the cell are related to the current density as seen in Figure 54 for 316 SS, where by an increasing overpotential from a potentiometric circuit is applied over a wide range of oxidizing conditions in order describe the electrochemical reactions. Three electrolyte concentrations, 0.25, 0.5 and 1 M H_2SO_4 acid electrolyte solutions were utilised in investigating the effect of acid concentration. In all cases, up to around 1200 mV_{HRE} a native passive film exists at the surface of the sample; steady enough so that no primary active/passive peak is observed. Within the passive range, slightly higher current densities are observed as the electrolyte concentration increases in the order of 1M> 0.5> 0.25 M H_2S0_4. The transition from the passive state into the transpassive state at all three electrolyte concentrations takes place at approximately 1200 mV_{HRE}, with similar oxidation currents. The rapid increase in current density with small increase in electrode potential, as a consequence of the breakdown of the passive film, is a clear indication of depassivation and is typically associated with the formation of etched pits. With increasing overpotential the onset of the secondary current plateau is then observed at approximately 1350 mV_{HRE}, as typically observed in stainless steel bearing chromium and nickel in acid electrolyte [121, 157].

The current plateau extends to approximately 1850 mV_{HRE}, and is typically associated with the formation of a viscous layer near the electrode surface. The electrode at this point undergoes a transpassive dissolution process, with metal ions from the surface are transport controlled in aqueous solution whereby oxidation decreases the current flow [121]. Within this polishing regime, the current density plateaus were in the order 1M < 0.5M

< 0.25M H_2SO_4 concentration with current densities in the range of 10 - 70 mA cm^{-2}.

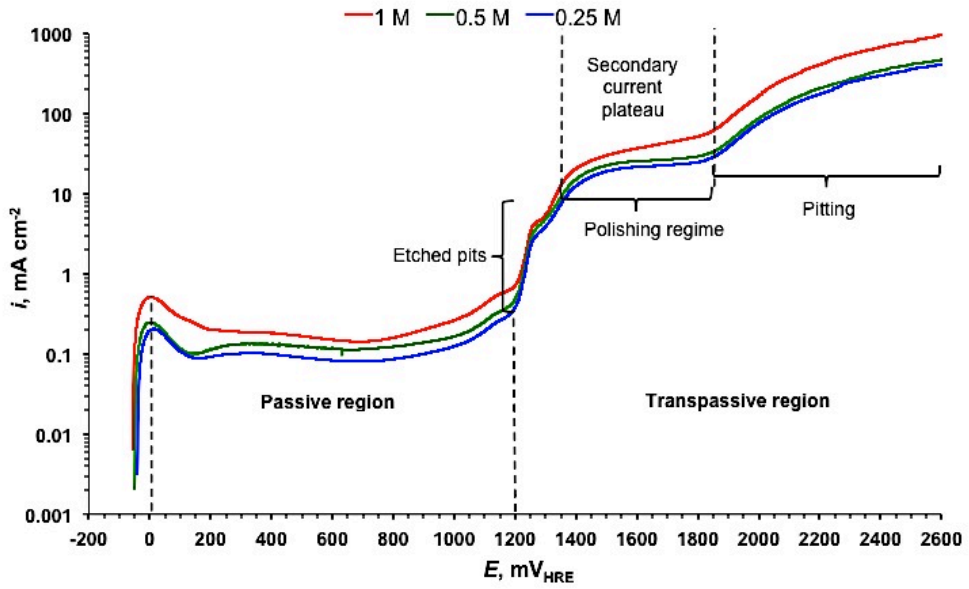

Figure 54: Polarization characteristics (E_{corr} – 2600 mV_{HRE} at 1 mV s^{-1}) obtained on 316 SS showing current profile for passive, active and pitting regimes as a function of sulphuric acid concentration at 25 ° C and 1 atm.

A distinct characteristic difference in the feature of the three electrolyte concentrations investigated, is that in 1 M H_2SO_4 an apparent inclination angle change is observed in the rectilinear part of polarization curve in the polishing regime (1200 – 1850 mV_{HRE}), which may be attributed to oxygen evolution and/or metal oxidation occurring quite rapidly at the highly anodic potentials. In contrast at concentrations of 0.25 and 0.5 M H_2SO_4 uniform current plateaus are observed whereby the formation of a secondary film controls the chemical dissolution through its interface with the electrolyte; thereby defining a potential range independent of the current [158]. While beyond 1900 $mV_{RHE,}$ the current density increases with

increasing overpotential, whereby oxygen evolution occurs with pitting of the surface of the bulk metal.

3.3.1.2 Current Efficiency

The mass change determined by weight loss measurements and current efficiency calculations of the various treatment 316 SS are shown in Table 11 and

Table 12. As seen in Figure 55, mass loss increases as the current density is increased, with an increasing gradient observed with increasing electrolyte concentration. The increase in dissolution at higher current densities is associated with both increased ionic strength and higher field gradients across the passive layer. However as seen in Figure 56, with increased current density the current efficiency reduces, as it is inversely proportional to the current efficiency as shown in Equation 33 in section 2.7.2.

As electrolysis treatment time is one of two variables in Faraday's law of electrolysis required to determine the total material removed from the sample, its effects were also investigated. As seen in Figure 57, the current efficiency decreases with increasing treatment time; more notably at current density of 12.5 mA cm^{-2}, while at 25 mA cm^{-2} & 50 mA cm^{-2}, the current efficiency changes are less noticeable over longer treatment times.

Table 11: Current efficiencies and the associated data for the anodization process of 316 SS under different conditions. All measurements were performed at 25 °C.

Sample No.	H_2SO_4 Conc.	C.D A cm^{-2}	Current mA cm^{-2}	Time min	S.A cm^2	Weight			Current Efficiency %
						Initial g	Final g	Removed mg cm^{-2}	
1	1M	0.0125	12.5	5	11.19	2.493	2.486	0.644	98.8
2	1M	0.025	25	5	11.06	2.434	2.424	0.895	68.6
3	1M	0.05	50	5	11.56	2.526	2.511	1.315	50.5
4	1M	0.1	100	5	11.22	2.476	2.452	2.113	40.5
5	0.5M	0.0125	12.5	5	11.12	2.453	2.446	0.630	96.6
6	0.5M	0.025	25	5	11.23	2.478	2.470	0.668	51.2
7	0.5M	0.05	50	5	11.13	2.487	2.475	1.033	39.6
8	0.5M	0.1	100	5	11.41	2.498	2.479	1.647	31.6
9	0.25M	0.0125	12.5	5	11.85	2.587	2.583	0.321	49.2
10	0.25M	0.025	25	5	11.12	2.442	2.437	0.468	35.9
11	0.25M	0.05	50	5	11.74	2.529	2.520	0.716	27.5
12	0.25M	0.1	100	5	11.16	2.437	2.424	1.174	22.5

Table 12: Current efficiencies as a function of treatment time and current densities 0.5M H_2SO_4 and the associated data for anodization process of 316 SS under different conditions. All measurements were performed at 25 °C.

Sample No.	H_2SO_4 Conc.	C.D Acm^{-2}	C.D $mA\ cm^{-2}$	Time min	S.A cm^2	Weight			Current Efficiency %
						Initial mg	Final mg	Removed mg/cm^2	
1	0.5M	0.0125	12.5	5	11.12	2.453	2.446	0.63	96.6
2	0.5M	0.0125	12.5	10	11.18	2.400	2.387	1.19	91.3
3	0.5M	0.0125	12.5	30	11.37	2.475	2.440	3.07	78.5
4	0.5M	0.0125	12.5	60	10.28	2.460	2.399	5.94	75.9
5	0.5M	0.025	25	5	11.23	2.478	2.470	0.67	51.2
6	0.5M	0.025	25	10	11.36	2.480	2.465	1.31	50.3
7	0.5M	0.025	25	30	11.33	2.504	2.458	4.04	51.7
8	0.5M	0.025	25	60	11.26	2.475	2.386	7.84	50.1
9	0.5M	0.05	50	5	11.13	2.487	2.475	1.03	39.6
10	0.5M	0.05	50	10	11.27	2.518	2.496	2.00	38.3
11	0.5M	0.05	50	30	11.16	2.425	2.359	5.94	38.0
12	0.5M	0.05	50	60	12.00	2.604	2.477	10.61	33.9

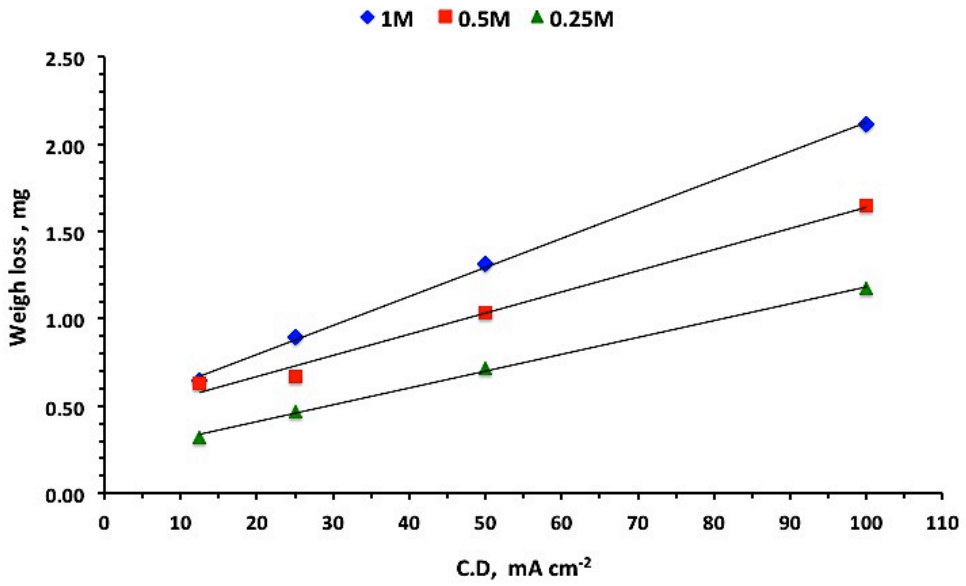

Figure 55: Weight loss for anodization process of 316 SS as a function of Current density (C.D) and H_2SO_4 concentration at 25 ° C and 1 atm, at treatment time of 5 min.

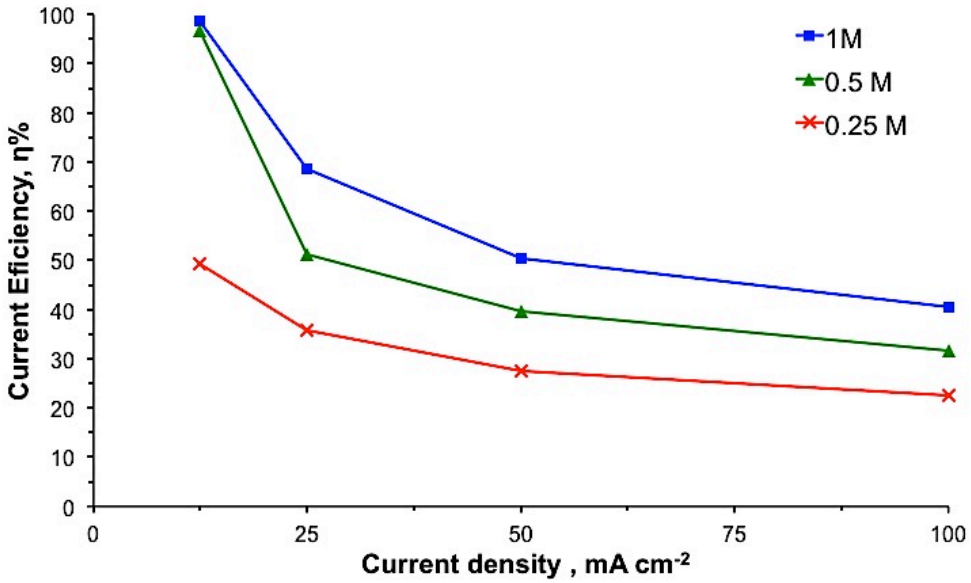

Figure 56: Current efficiency for anodization process of 316 SS as a function of current density and H_2SO_4 concentration at 25 ° C and 1 atm, at treatment time of 5 min.

On account of the uniformity in the current density plateau in the polishing regime, higher current efficiency, as well as the environmental and

economic benefits of utilising a less concentrated solution, 0.5M H_2SO_4 was chosen as the electrolyte concentration in the following investigation of the anodization process. The optimum process variables following were determined based on these findings.

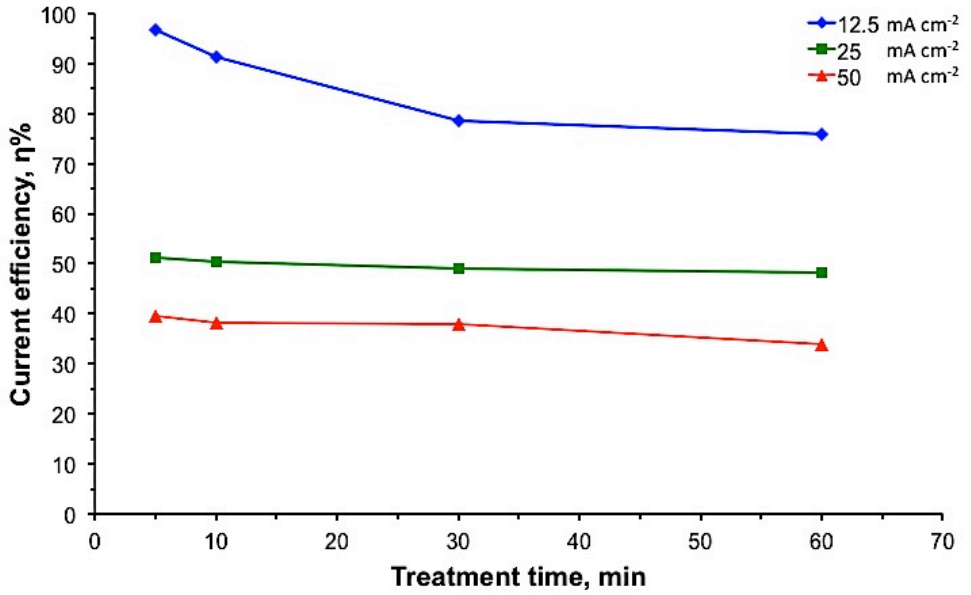

Figure 57: Current efficiency for anodization process of 316 SS as a function of treatment time and current density at room temperature in 0.5 M H_2SO_4

3.3.1.3 Additives –viscosity enhancer

Figure 58 shows the effect of the addition of viscosity enhancing additive, glycerol, in comparison with the standard electrolyte (0.5 M H_2SO_4) with no additives, in v/v ratios of; 100:0 (0%), 90:10 (10%) and 70:30 (30%). The general shapes of all four polarisation curves in the transpassive range are associated with the anodization process are similar, with a secondary current plateau range between 1350 and 1850 mV_{RHE}. The current density within the polishing regime is seen to decrease with increasing v/v ratio of the glycerol additive. Electrolyte solution the current density plateaus were in the order 100:0 < 90:100 < 80:20 < 70:30 with respect to H_2SO_4 to glycerol v/v ratio, with current densities in the range of 20-90 mA cm^{-2}.

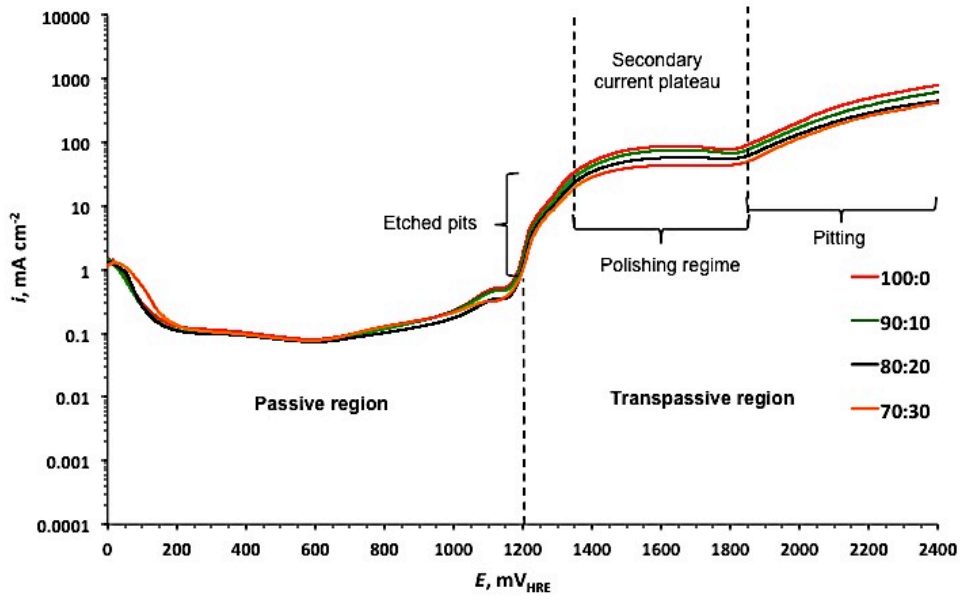

Figure 58: Polarization characteristics (1 mV s^{-1}) obtained on 316SS in 0.5M H_2SO_4 electrolyte showing current profile for passive, active and pitting regimes as a function of v/v% of glycerol

Viscosity enhancing agents have been found to be particularly advantageous when used in conjunction with sulphuric acid as the acidic component in the electrolyte [129]. In the 0.5 M H_2SO_4 with addition of varying glycerol content (0%, 10% and 30% v/v) electrolyte solutions, polarisation data in the region of the secondary current plateau, show that with increasing glycerol v/v content a decrease in the current density is observed. This suggests that the viscosity of the polishing film could be affected by addition of a viscosity enhancing agent, as noted by *Voort et al.* [111].

3.3.1.4 Agitation

As there is a tendency during electropolishing for the reaction products to accumulate around the electrodes during electrolysis under steady state conditions, agitation is some cases can be desirable. It aids in removing some of the reaction products and maintain the viscous layer at the optimum thickness, particularly at low temperatures when diffusion or

convection cannot supply sufficient fresh electrolyte to the anode. Figure 59 to Figure 61 represent polarization curves obtained on 316 SS in three varying electrolyte conditions (0%, 10% and 30% v/v glycerol additive), under three varying conditions with agitation delivered by a magnetic stirrer; when v=0, referred to natural convection (without mixing), when v>0, referring to forced convection with moderate mixing at the relative electrolyte velocity of about 0.1 m s^{-1}, when (v>>0) referred to forced convection with intensive mixing at the relative electrolyte velocity > 0.2 m s^{-1}.

A linear current density scale is chosen to better observe the difference of varying the electrolyte velocities with respect to the electrolyte solution. In each case a similar current density plateau is observed between 1350 mV_{HRE} to 1850 mV_{HRE}, however the general shape varies with electrolyte condition with the current density range observed following the order 0% > 10% > 30%. The effects of agitation are only observed in the 0% electrolyte solution, whereby the current density in the secondary current plateau region increases under conditions of EP (v>0) / (v>>0) forced convection compared to EP (v=0) carried out under natural convection (in still electrolyte). The differences in the current density of the secondary plateau region which is a maximum, with an increase of approximately 8 mA cm^{-2} observed between 1600 – 1700 mV_{HRE} is clearly not significant enough for agitation to be a key contributor to the efficiency of the process. While, under electrolyte conditions with addition of glycerol (0% and 30%) the effects of agitation are not observed and is practically independent of agitation and agitation intensity. Therefore, need to introduce the forced convection is dispensable during EP process in view of getting higher efficiency of electropolishing operation.

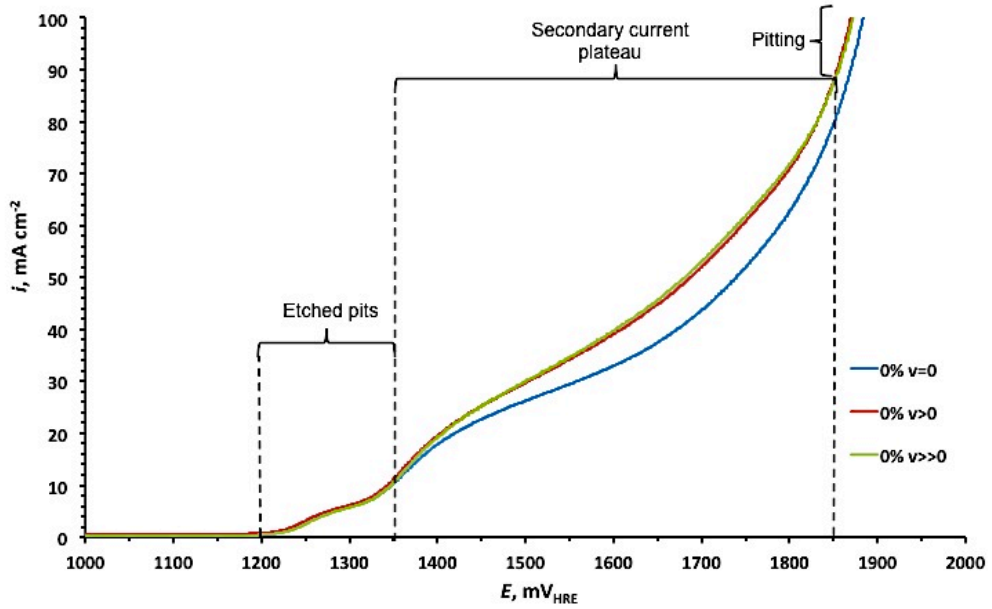

Figure 59: Electropolishing polarization characteristics obtained on 316 SS dependent on convection/stirring conditions in 0.5 M H_2S0_4 with no glycerol additive at temperature of 25 ˚C

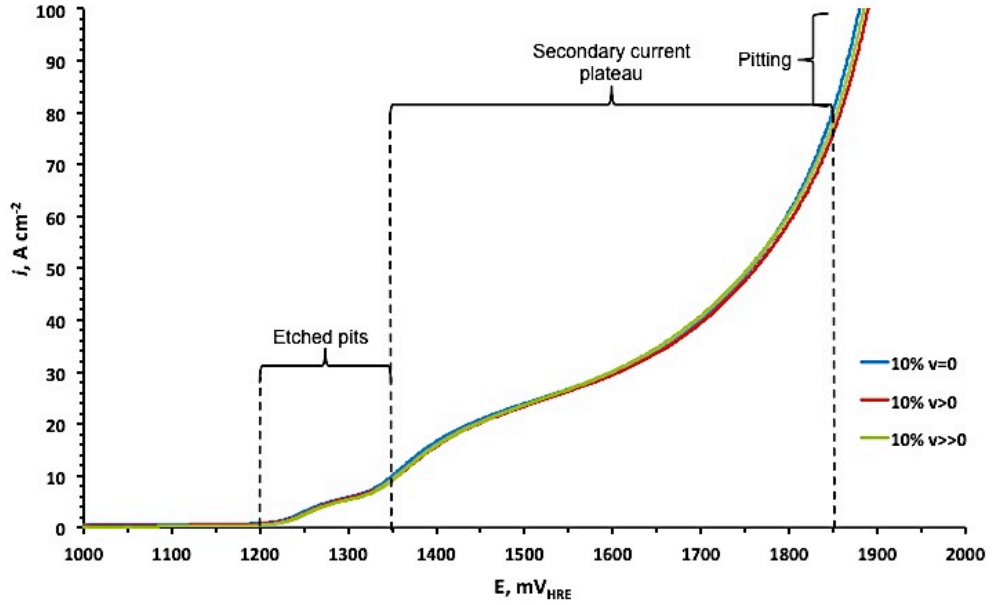

Figure 60: Electropolishing polarization characteristics obtained on 316 SS additive dependent on convection/stirring conditions in 0.5 M H_2S0_4 with 10% v/v glycerol additive at temperature of 25 ˚C

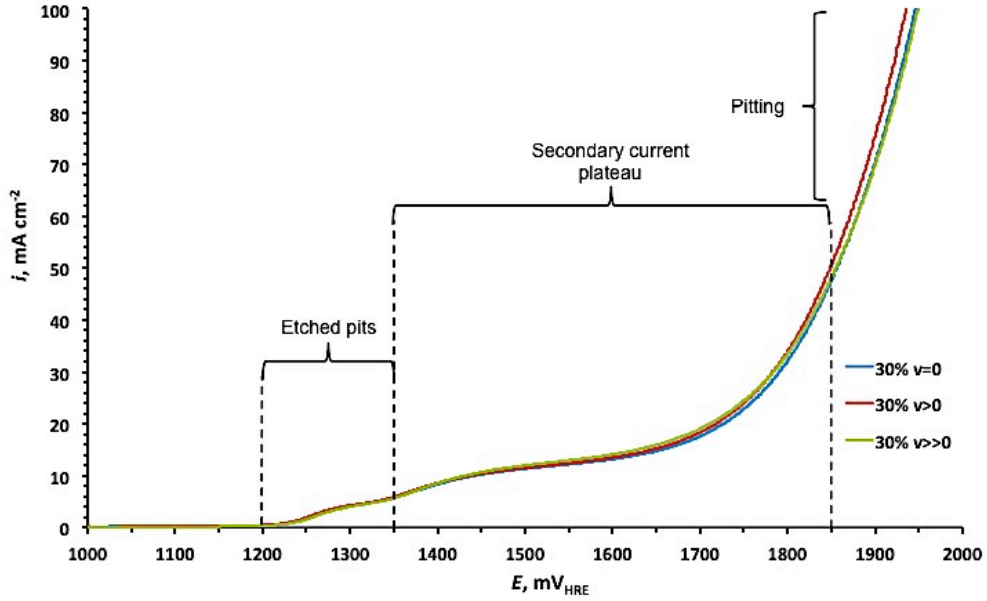

Figure 61: Electropolishing polarization characteristics obtained on 316 SS additive dependent on convection/stirring conditions in 0.5 M H_2S0_4 with 30% v/v glycerol additive at temperature of 25 ˚C

3.3.1.5 Potential transients

An indicator to distinguish whether brightening or etching is taking place during anodization treatments in a particular electrolyte under galvanic control is the potential transient. As seen in Figure 62, the electrode potential transient of 316SS, during anodization treatment in all three electrolyte mixtures investigated, demonstrated a constant dissolution voltage over a treatment time of 1800 s. The initial voltage drop registered is associated with the high potential difference between the 316 SS and the counter electrode prior to immersion into the electrolyte solution. After immersion the potential difference equilibrates within approximate potential range corresponding to the polishing regime associated with the secondary current plateau range between 1400 - 1800 mV_{HRE}.

An increase in the potential difference between the 316SS electrode and the reference electrode (Figure 62), is observed with increasing content of the glycerol additive to the 0.5 M H_2SO_4 electrolyte. The glycerol additive,

which is intended to act as a viscosity-enhancing agent, increases the electrolyte resistance and therefore the potential increases difference required to maintain the desired current density. In 30% v/v glycerol additive electrolyte, the highest potential difference ranging between 1670 - 1620 mV_{RHE} was observed which lies at the higher end of the polishing regime and the initiation of pitting.

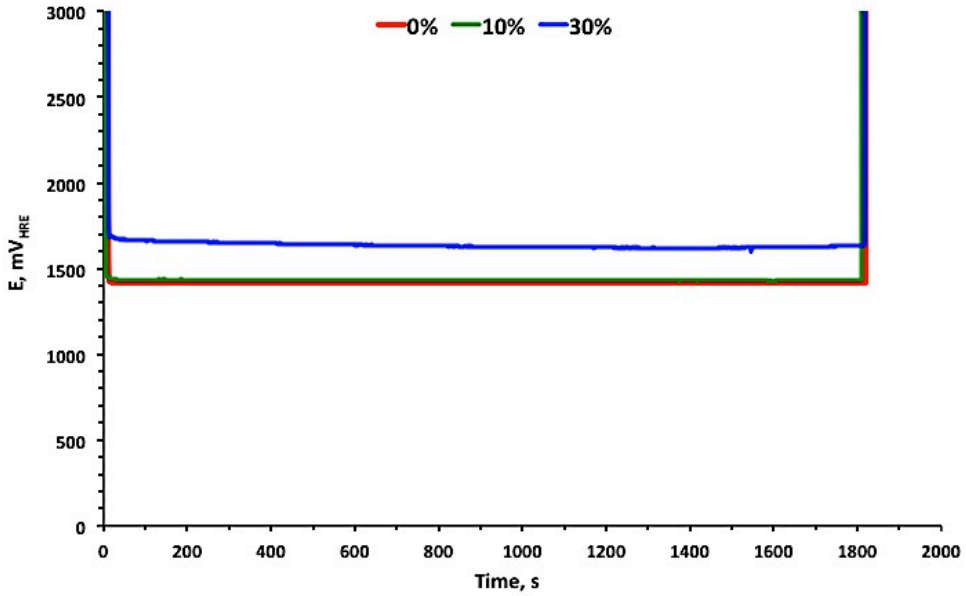

Figure 62: Potential transient of 316 SS in 0.5 M H_2SO_5 with 0%, 10% and 30% glycerol additive at 12.5 mA cm^{-2} at 25 ° C for 1800 s

While in electrolyte solution containing 10% v/v glycerol additive a lower potential difference of ranging between 1440 - 1430 mV_{HRE} was observed and in electrolyte solution with no additive, a potential difference of ranging between 1410 - 1420 mV_{HRE}, which both lie within the polishing regime. In all three electrolyte solutions the potential differences observed fluctuated within a small range, to adapt to the every changing surface electrochemistry of an alloy such as stainless steel. At approximately 1800 s, a sharp increase in potential difference of the 316SS samples in the three

electrolytes is observed, due to the specimen removal from the electrolyte prior to switching the current off.

3.3.2 Surface analysis

3.3.2.1 ToF-SIMS

ToF-SIMS was used to study the near-surface chemical composition of the samples. The near-surface composition has a significant effect on the properties of stainless steel, as surface oxides can have conducting, semi-conducting or insulating properties depending on the stoichiometric composition. This may have a significant effect on the ICR, with decrease in conductivity due to oxides generally considered to follow the trend of: Ni-oxide > Cr-oxide > Fe-oxide [104]. During the ToF-SIMS analysis not all isotopes for the respective elements could be measured due to mass interferences and poor ion yields. The percentages of the isotopes selected and counted were: Cr 97.3%, Fe 97.6%, Ni 71.7% and Mo 54.8%. The counts were then normalised to 100%, i.e. Cr = Counts / 97.3% etc., and recorded in Table 13.

Figure 63 shows the Fe, Cr, Ni and Mo compositions at the near surface of the untreated 316 SS, compared to the various treated samples. It can be seen that the electrochemical treatment leads to an enhancement in the near-surface content of Cr and Ni, while reducing the Fe content significantly and the Mo content slightly in comparison to the untreated 316 SS sample. The effects of the treatment regime are also prominent, with respect to the electrolyte solution (with/without glycerol) and treatment time. As the treatment time increases the amount of material removed from the anode surface increases and consequently the average surface roughness is altered, as demonstrated by Lee [126].

As seen in Table 13, the relative count ratios for all treated samples lay within a limited range: Cr 46-54 %, Fe 41-48%, Ni 4.5-6% and Mo 0.44-0.47%, with minimal changes seen with increases in treatment time and glycerol content.

Table 13: ToF SIMS isotope count (Fe, Cr, Ni and Mo) of untreated 316 SS and treated 316 SS in 0.5 M H_2SO_5 with 0%, 10% and 30% glycerol additive at 12.5 mA cm^{-2} at 25 ° C

	Relative Count Ratio %			
Sample	**Cr**	**Fe**	**Ni**	**Mo**
316SS	**31.32**	**64.41**	**3.24**	**1.03**
0% (5 min)	**60.31**	**34.15**	**4.85**	**0.69**
0% (10 min)	**51.68**	**42.48**	**5.31**	**0.54**
0% (30 min)	**48.51**	**45.80**	**5.03**	**0.66**
10% (5 min)	**55.35**	**38.82**	**5.38**	**0.45**
10% (10 min)	**59.23**	**35.04**	**5.15**	**0.59**
10% (30 min)	**58.99**	**35.29**	**5.25**	**0.47**
30% (5 min)	**57.04**	**36.66**	**5.83**	**0.47**
30% (10 min)	**59.86**	**34.50**	**5.08**	**0.55**
30% (30 min)	**60.16**	**34.38**	**4.81**	**0.65**

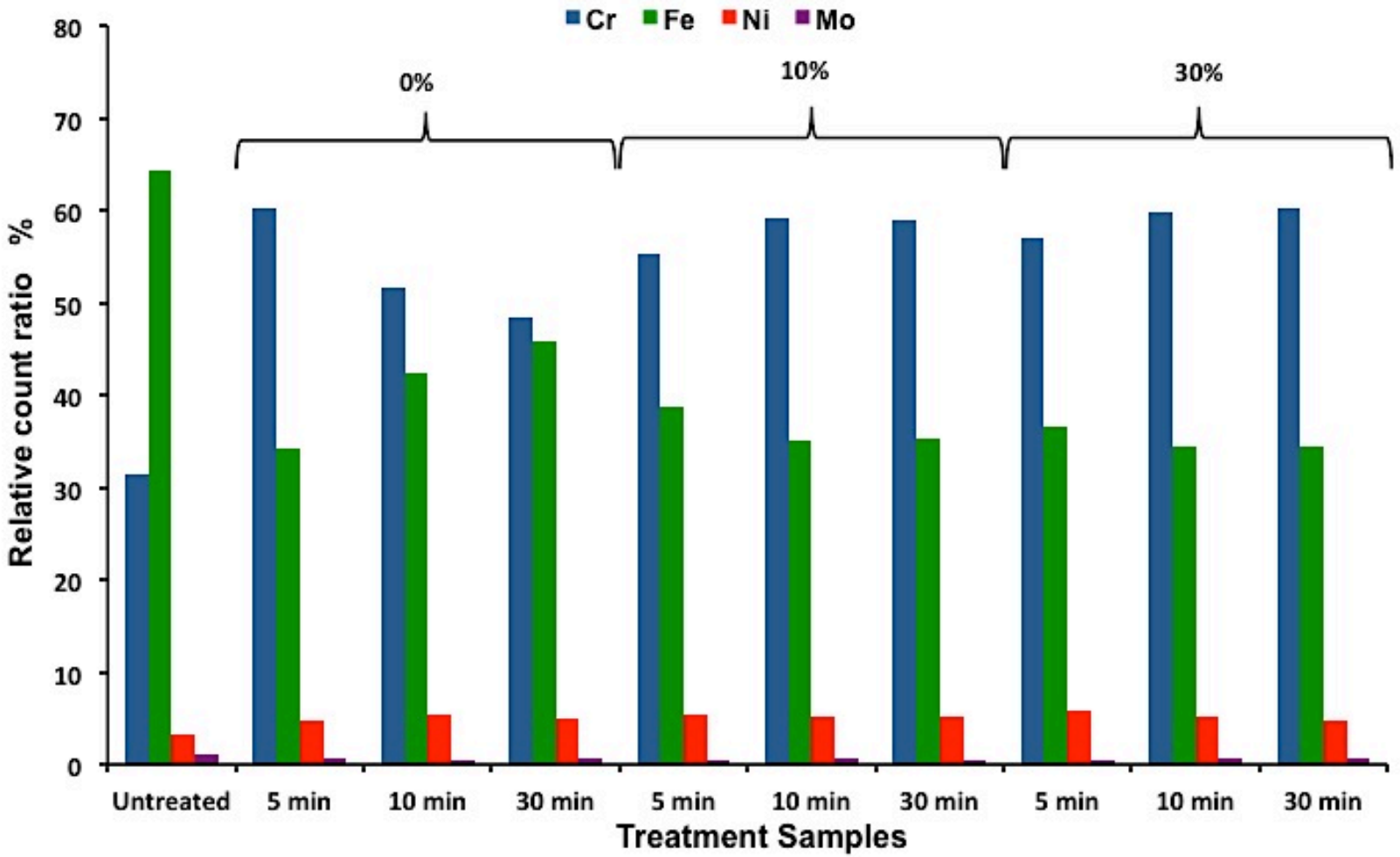

Figure 63: ToF SIMS isotope count (Fe, Cr, Ni and Mo) of untreated 316 SS (1) and treated samples of 316 SS in 0.5 M H_2SO_5 with 0%, 10% and 30% glycerol additive at 12.5 mA cm^{-2} at 25

3.3.2.2 SEM

SEM images of untreated 316 SS and the treated samples 0%, 10& and 30% samples are shown in Figure 64 to Figure 67, moreover, all the images along with the inverse/negative of the images are also shown in Appendix A1. SEM images of the treated samples in comparison to the untreated 316 SS, exhibited general dissolution over the entire surface, with crystallographic etching apparent at treatment times of 5 and 10 minutes and few hemispherical pits observed. The inversed SEM images show that the dissolution effect along the grain boundaries as well as surface pitting, is more evident at longer treatment times. This is because the oxides at the grain boundary are less ordered and therefore more easily dissolved than the more ordered regions within the grains of the metal [159]. At longer treatment times (30 min) grain boundary are not noticeable completely, dissolution process occurs across the whole surface with only shallow pitting, general etching and a few deep pits observed across the whole surface.

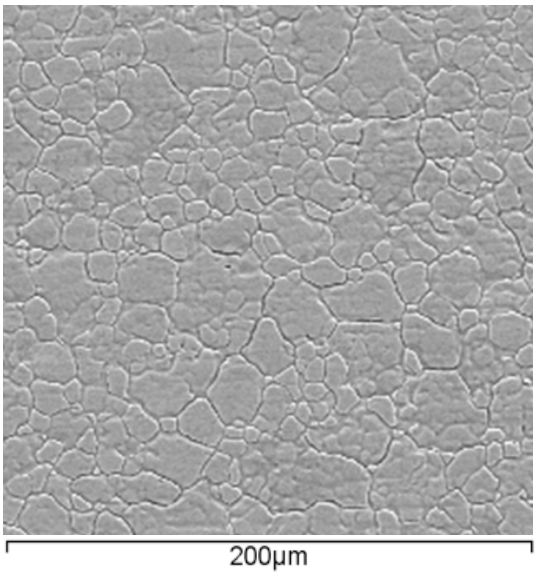

Figure 64: SEM image of untreated 316 SS (left) alongside inverted image (right) at magnification ×900.

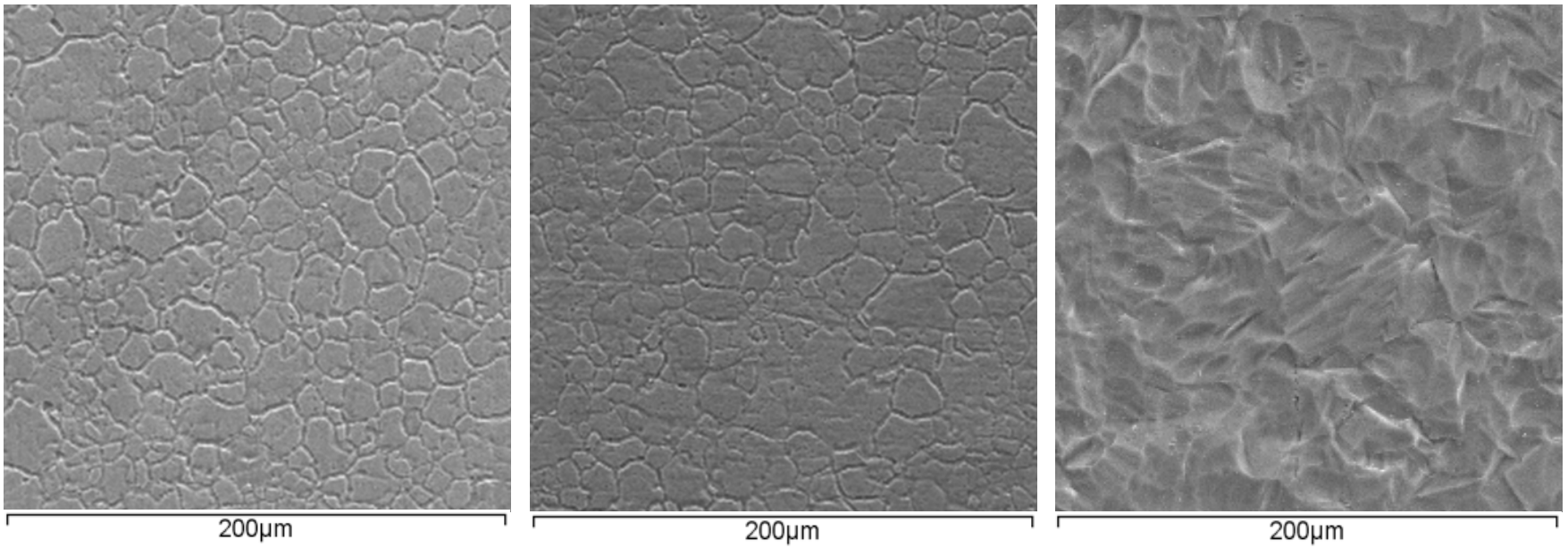

Figure 65: SEM image of treated 316 SS in 0.5 M H_2SO_5 with 0% glycerol additive, 12.5 mA cm^{-2}, 25 ° C, treatment time of 5 min, at magnification ×900, 0% (10 min) at magnification ×900 and 0% (30 min) magnification ×1500, showing general dissolution at grain boundary.

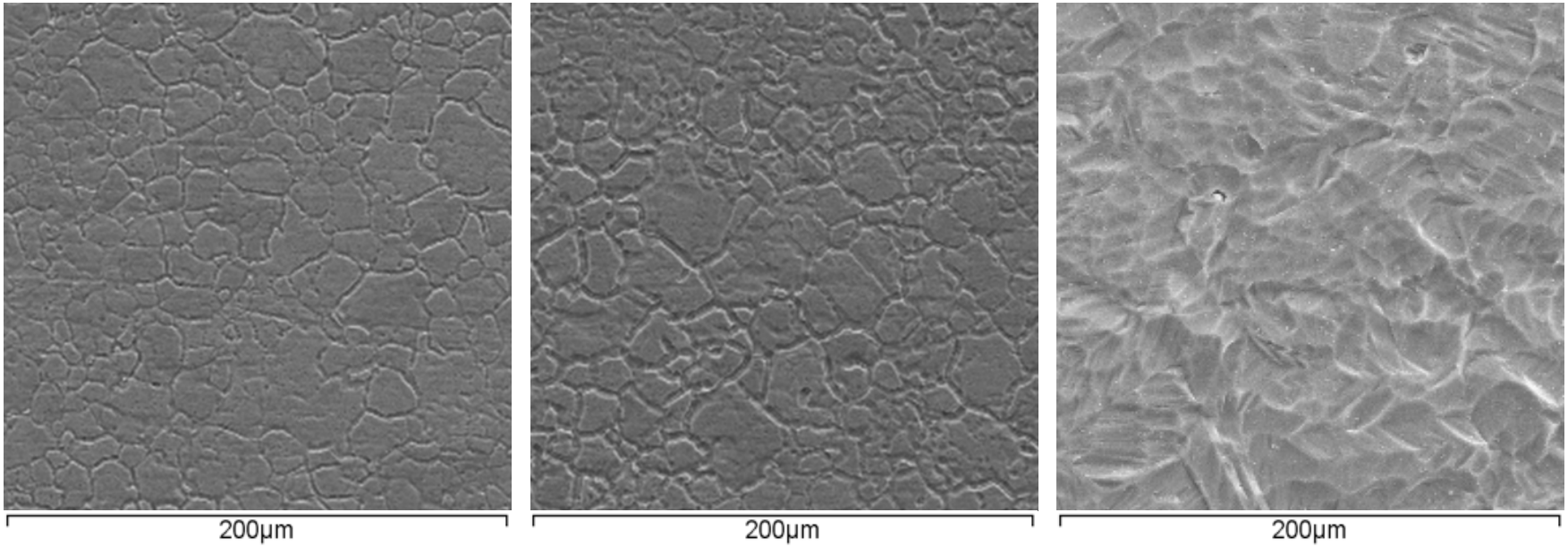

Figure 66: SEM image of treated 316 SS in 0.5 M H_2SO_5 with 10% glycerol additive, 12.5 mA cm^{-2}, 25 ° C, treatment time of 5 min, at magnification ×900, 10% (10 min) at magnification ×900 and 10% (30 min) magnification ×1500, showing general dissolution at grain boundary.

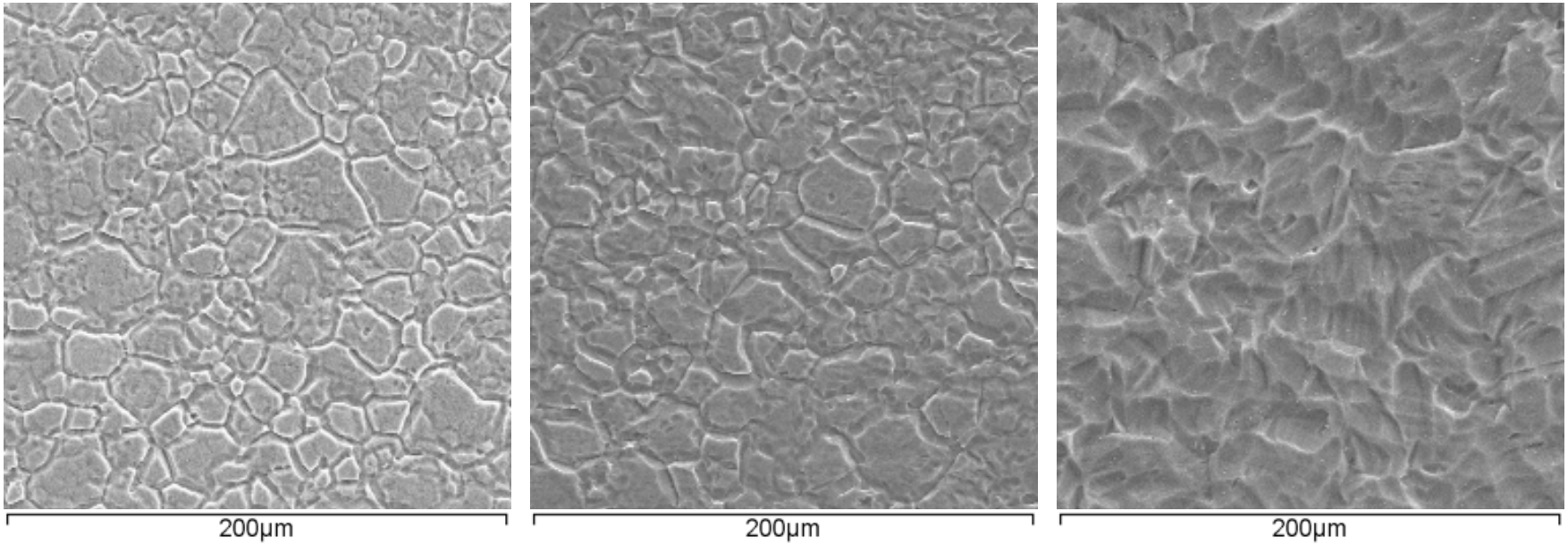

Figure 67: SEM image of treated 316 SS in 0.5 M H_2SO_5 with 30% glycerol additive, 12.5 mA cm^{-2}, 25 ° C, treatment time of 5 min, at magnification ×900, 30% (10 min) at magnification ×900 and 30% (30 min) magnification ×1500, showing general dissolution at grain boundary.

3.3.2.3 AFM

AFM measurements were performed to give a quantitative measure of surface roughness. Table 14 compares the surface roughness of untreated 316 SS with that of all the treated samples (0%, 10% and 30%).

Table 14: Ra measurements of 316 SS and treated 316 SS in 0.5 M H_2SO_5 with 0,10 and 30% glycerol additive, 12.5 mA cm^{-2}, 25 ° C at treatment times of 5, 10 and 30 min

	R_a (nm) at 90 µm scan		
% Additive	**5 min**	**10 min**	**30 min**
0%	74	92	200
10%	71	88	194
30%	119	173	200

Figure 98 to Figure 107 in Appendix A2 show images from the R_a measurement scan for untreated 316 SS and all the treated samples, using contact mode topography line scan at a scan size of 90 µm. The surface roughness of the all treated samples is observed to increase with increasing time. The effect of the addition of viscosity enhancing agent (glycerol), seems to hinder the surface roughness increase at 10% v/v, while at 30% v/v glycerol content the process seems to enhance the surface roughness of the treated samples.

3.3.3 Interfacial contact resistance

Figure 68 to Figure 70 show the relationship between ICR and compaction force (40-200 N cm^{-2}) of the treated samples 0%, 10% and 30%, in comparison with untreated 316 SS. The ICR decreases monotonically with increasing compression for all the samples studied. This trend and the absolute values for untreated 316 SS are similar to those reported by *Wang et al.* [36]. The electrochemically treated samples demonstrate a common trend of lower ICR values compared to the untreated 316 SS sample across

the whole compaction force range for all treatment regimes. The degree of improvement of ICR is dependent on the treatment regime, a combination of electrolyte solution (with/without additive) and treatment time. The dominant factor however seems to be the treatment time, with all treated samples (0%, 10% and 30%), at 5 and 10 min treatment times (Figure 71 to Figure 73) demonstrating similar ICR values and trends with respect to compaction force and the best performance obtained at the longest treatment time (30 min). At the US DoE target compression of ~140 N cm^{-2}, all the treated samples at treatment times of 5 and 10 min, demonstrated ICR values within the approximate range of the DoE ICR target of 20 mΩ cm^2 as shown in Table 15. Samples treated at 30 min, demonstrated ICR values well below the DoE target.

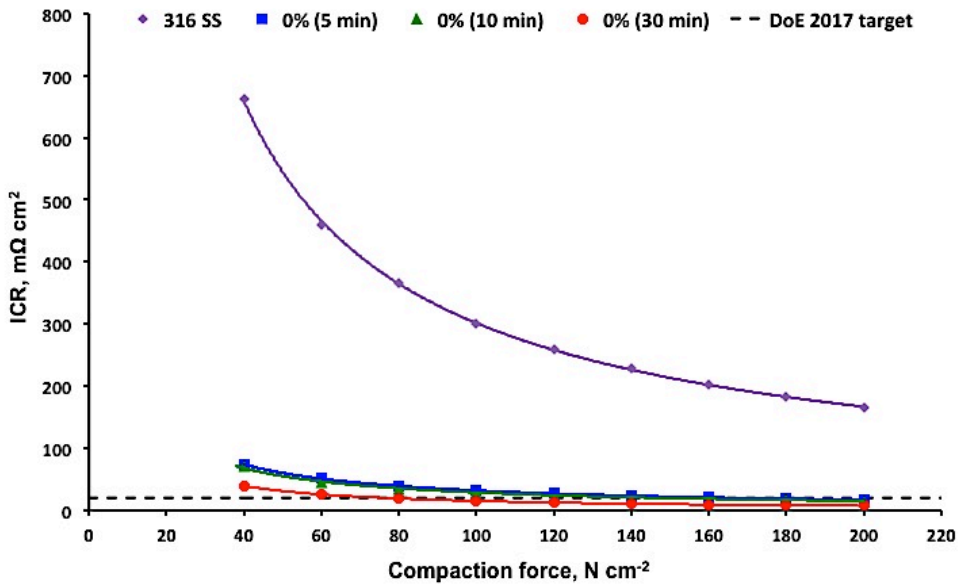

Figure 68: ICR as a function of compaction force for electrochemically treated 316 SS with 100:0 v/v glycerol additive (0%), 12.5 mA cm^{-2}, 25 ° C, at treatment times of 5, 10 and 30 min.

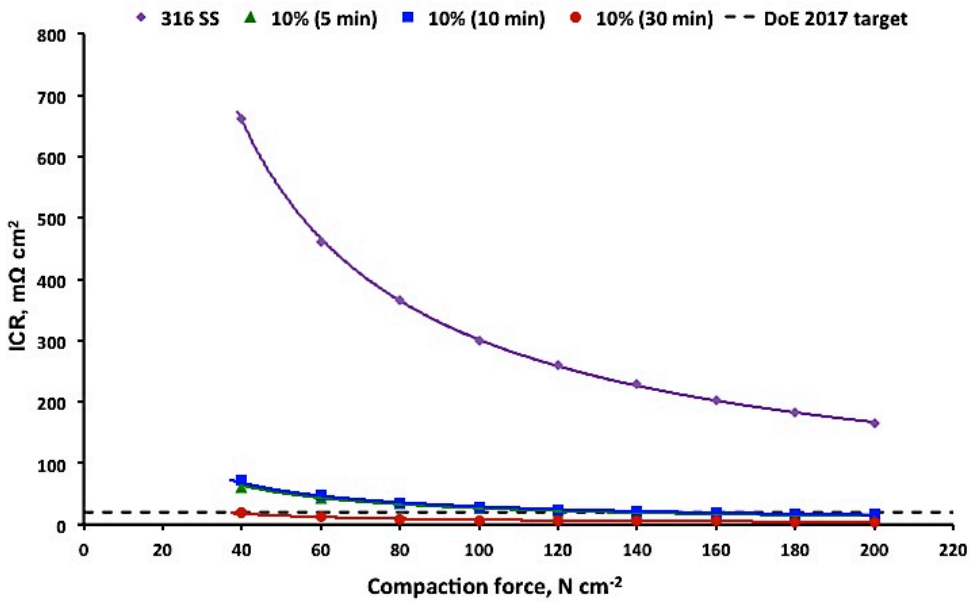

Figure 69: ICR as a function of compaction force for electrochemically treated 316 SS with 90:10 v/v glycerol additive (10%), 12.5 mA cm^{-2}, 25 ° C, at treatment times of 5, 10 and 30 min.

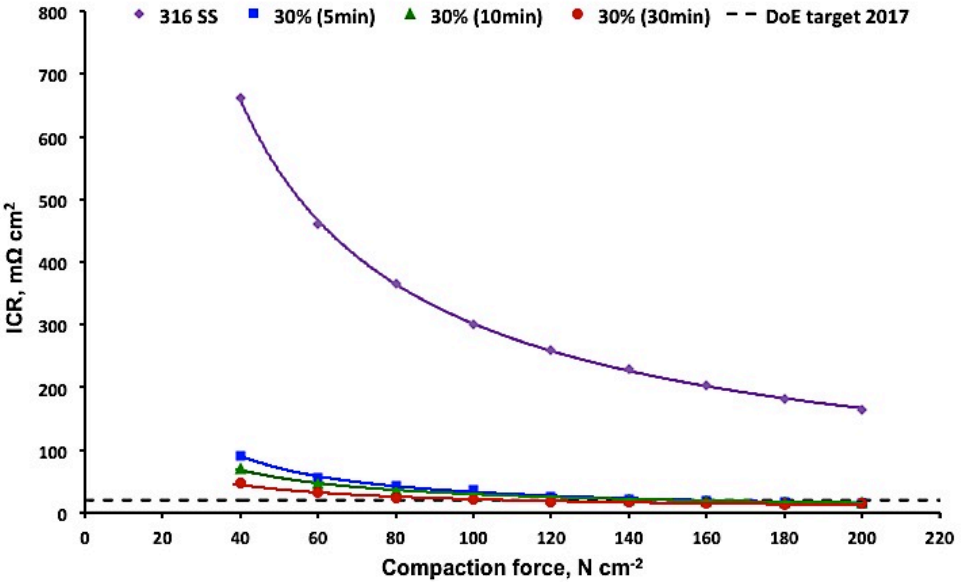

Figure 70: ICR as a function of compaction force for electrochemically treated 316 SS with 70:30 v/v glycerol additive (30%), 12.5 mA cm^{-2}, 25 ° C, at treatment times of 5, 10 and 30 min.

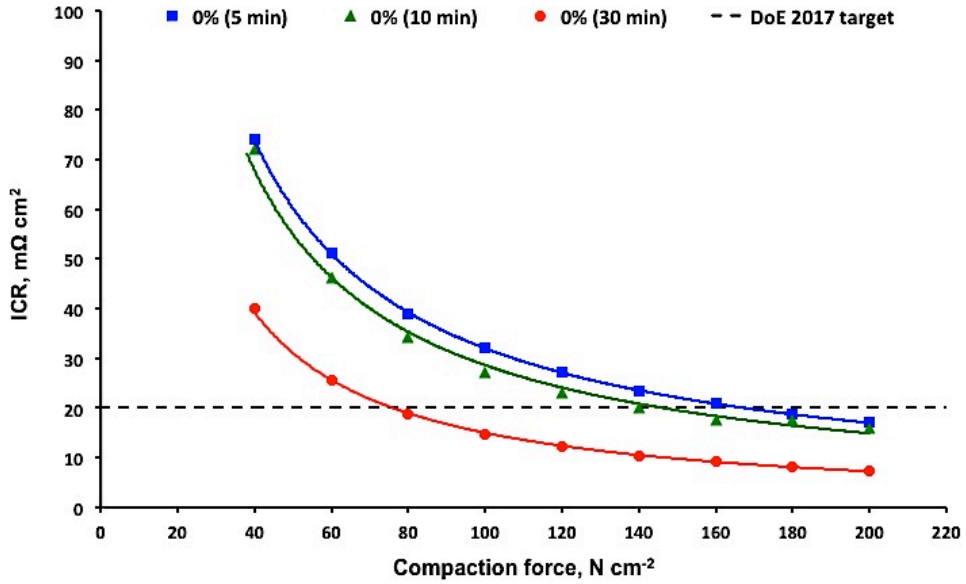

Figure 71: Close up of ICR as a function of compaction force for electrochemically treated 316 SS with 100:0 v/v glycerol additive (0%), 12.5 mA cm^{-2}, 25 ° C, at treatment times of 5, 10 and 30 min.

.

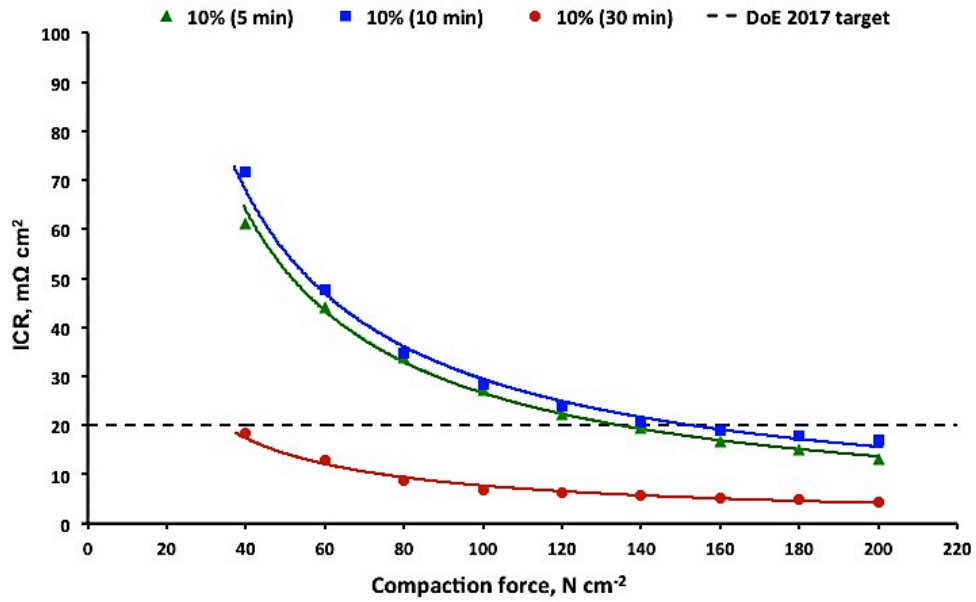

Figure 72: Close up of ICR as a function of compaction force for electrochemically treated 316 SS with 90:10 v/v glycerol additive (10%), 12.5 mA cm^{-2}, 25 ° C, at treatment times of 5, 10 and 30 min.

.

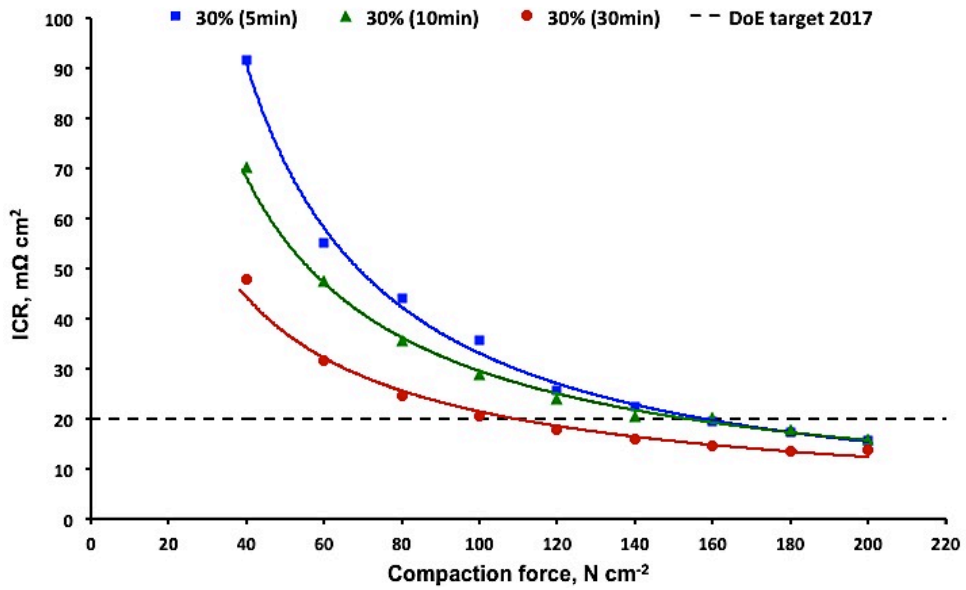

Figure 73: Close up of ICR as a function of compaction force for electrochemically treated 316 SS with 70:30 v/v glycerol additive (30%), 12.5 mA cm^{-2}, 25 ° C, at treatment times of 5, 10 and 30 min.

.

Table 15: ICR values of 316 SS and treated 316 SS in 0.5 M H_2SO_5 with 0,10 and 30% glycerol additive, 12.5 mA cm^{-2}, 25 ° C, treatment times of 5, 10 and 30 min, at the DoE target compression force at 140 N cm^{-2}

	ICR (mΩ cm^2) at 140 N cm^{-2}		
Time (min)	**0%**	**10%**	**30%**
5	23.5	20.5	22.4
10	20.0	19.4	20.4
30	10.4	5.7	15.9

3.3.4 Corrosion in simulated PEFC environment

The potentiodynamic polarisation response for only two treatment electrolyte conditions (0% and 10%) along with that of untreated 316 SS in simulated PEFCs anode and cathode environments is investigated. This is because a prerequisite of the developed substrate treatment is cost and with treatment condition of electrolyte with 30% v/v additive, the ICR

values at compression of 140 N cm^{-2} has demonstrated similar trends to 0% and 10%.

3.3.4.1 Simulated anode environment

In anodic simulated PEM fuel cell conditions (1 M H_2SO_4 +2 ppm F^- ions at 70 ˚C purged with H_2 gas), the polarization curves (Figure 74 and Figure 75) of the treated samples (0% and 10%) in comparison to untreated 316 SS demonstrate lower current densities across the polarization scan range (-200 to 1500 mV_{RHE}). Furthermore the ease of passivation indicated by i_{crit}/E_{pp} is greater for all the treated samples (0% and 10%) in comparison to the standard 316 SS untreated sample.

As seen in Figure 74, the difference in the i_{crit} (~100 - 150 µA cm^{-2}) of the three treated samples 0% (5, 10, 30 min) is marginal, with 0% (5 min) demonstrating the lowest value. In comparison to the untreated 316 SS (~300 µA cm^{-2}), the treated samples also demonstrate lower passive current density (i_p), which provides a measure of the protectiveness of the film with almost similar current densities at these points for all 0% samples and a slightly lower current density for 10% (5min) in comparison with 10% (10 min and 30 min). As the potential range increases the current density decreases to a point that it is approximately independent of the potential. At this point the process may be visualised as a combination of film growth balanced by film dissolution for maintaining an approximately constant or very slowly increasing, film thickness [82].

On the anode (Figure 76 and Figure 77), at high power operation at up to 100 mV_{HRE} [160], the treated samples demonstrate current densities, ranging between 30 - 50 µA cm^{-2} in comparison to the untreated 316 SS at ~105 µA cm^{-2} (Table 16). Nevertheless at 100 mV_{HRE} all the samples (0%, 10% and 316 SS) demonstrate current densities lower than the critical passivation current density (i_{crit}). This indicates the surface of the stainless steel samples should all be passivated forming a protective film while being exposed to potentials in the active potential range.

Lower power operation could conceivably induce much greater corrosion rates on samples if the fuel cell anode potential were able to force the bipolar plate into active corrosion. As long as the current being drawn from the system is lower than the critical passivation current density (i_{crit}) the surface of the stainless steel should be passivated.

The lowest electrode potentials occurs at (or near) the reversible potential for hydrogen oxidation (0 mV_{HRE}), where the electrode does not bias the bipolar plates since there is no current flow through the stack and is only weakly coupled to that of the platinum (Pt) catalyst layer [152]. As seen in Figure 76 and Figure 77, at ~ 0 mV_{HRE} although all the samples (0%, 10% and 316 SS) demonstrate current densities lower than the critical passivation current density (i_{crit}), indicating passivation of the surfaces. The treated samples demonstrated lower current densities in the range of 93 – 109 μA cm^{-2} compared to the untreated 316 SS at 215 μA cm^{-2} (Table 16).

The potential shift at E_{corr} can be used to determine whether the surface treatment process has lead to a surface that is either more active / noble in comparison to the 316 SS. Figure 78 and Figure 79 show a close up of the E_{corr} established by both the treated samples (0% and 10%) in comparison to the untreated 316 SS. The treated samples (0% and 10%), exhibited E_{corr} shifts towards more positive values (noble direction), in comparison to the untreated 316 SS. The shift towards ennoblement of the treated samples was most pronounced for 0% (5 min) and 10% (10 min). A distinctive pattern is not particularly observed with regard to treatment time or electrolyte solution at this point with respect to E_{corr} shifts.

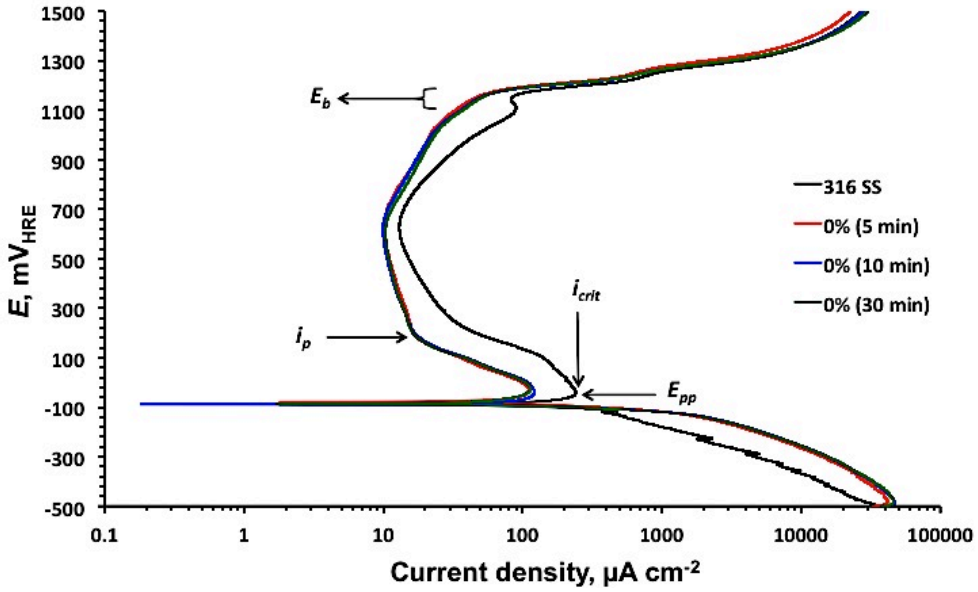

Figure 74: Polarization curves of 0% samples in comparison with 316 SS, in simulated PEFC anode environment (1 M H_2SO_4 +2 ppm F^- ions at 70 ˚C) purged with H_2 gas.

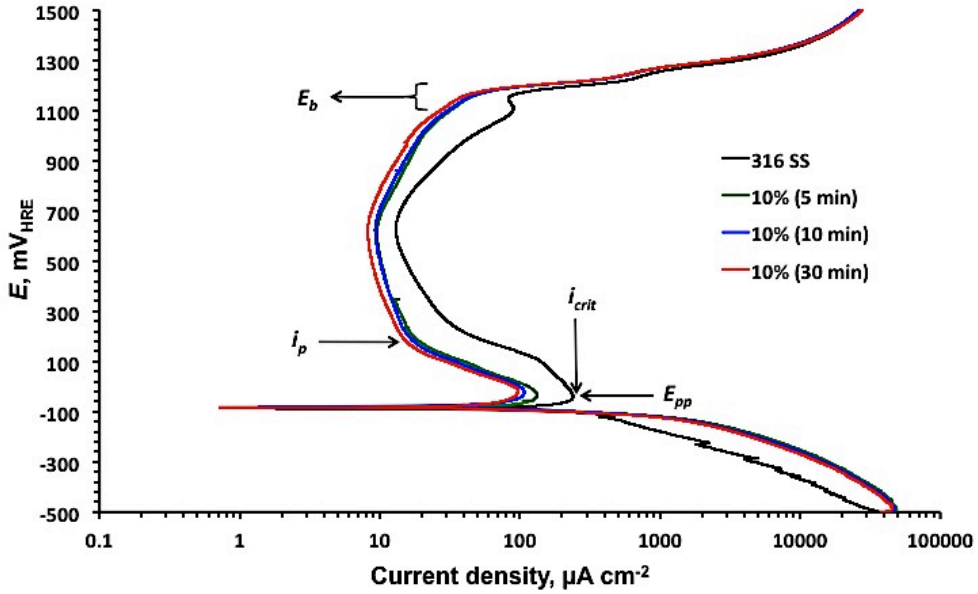

Figure 75: Polarization curves of 10% samples in comparison with 316 SS, in simulated PEFC anode environment (1 M H_2SO_4 +2 ppm F^- ions at 70 ˚C) purged with H_2 gas.

Table 16: Comparison of corrosion current densities at E_{corr}, 0.1 mV_{HRE}, peak (i_{crit}) and passivation (i_p) of anodised treated and untreated 316 stainless steel determined by Tafel plot extrapolation method and LPR method at 70 °C in Anodic PEM fuel cell simulated environment.

	E_{corr} mV_{HRE}	i_{crit}, µAcm^{-2}	i_p, µA cm^{-2}	At E = 0 mV_{HRE} i_{corr}, µA cm^{-2}	At E = 100 mV_{HRE} i_{corr}, µA cm^{-2}
316SS	88.5	242	32.6	215	140
A.T 1 (5 min)	79.8	111	16.1	99	36.2
A.T 1 (10 min)	87.6	121	16.2	109	38.3
A.T 1 (30 min)	86.2	114	15.4	105	39.0
A.T 2 (5 min)	84.4	110	11.9	93.3	30.2
A.T 2 (10 min)	79.8	113	14.3	102	32.6
A.T 2 (30 min)	83.5	98.8	9.6	94.7	31.6

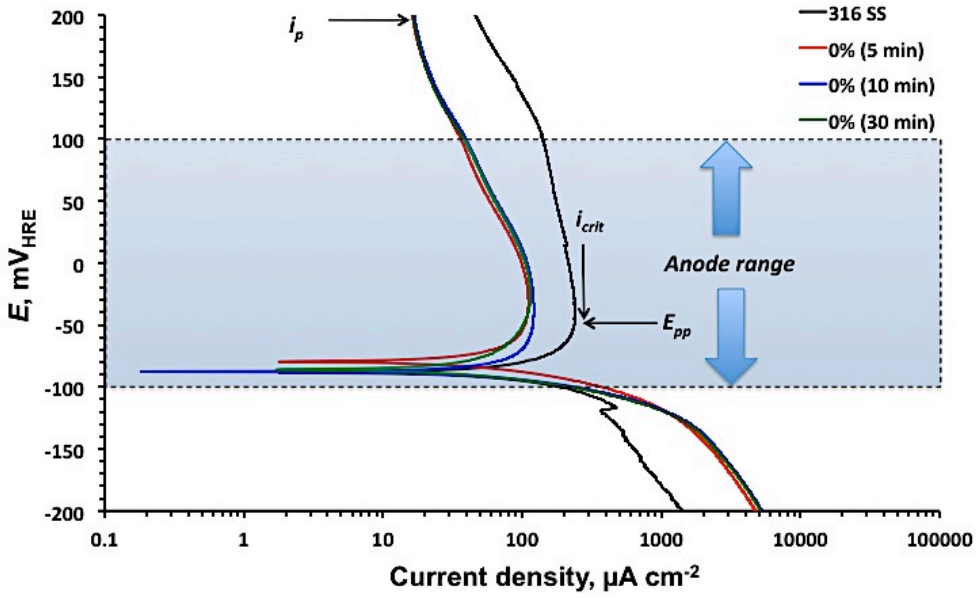

Figure 76: Polarization curve of 0% samples in comparison with 316 SS, showing potential range in simulated PEFC anode environment (1 M H_2SO_4 + 2 ppm F^- ions at 70˚C) purged with H_2.

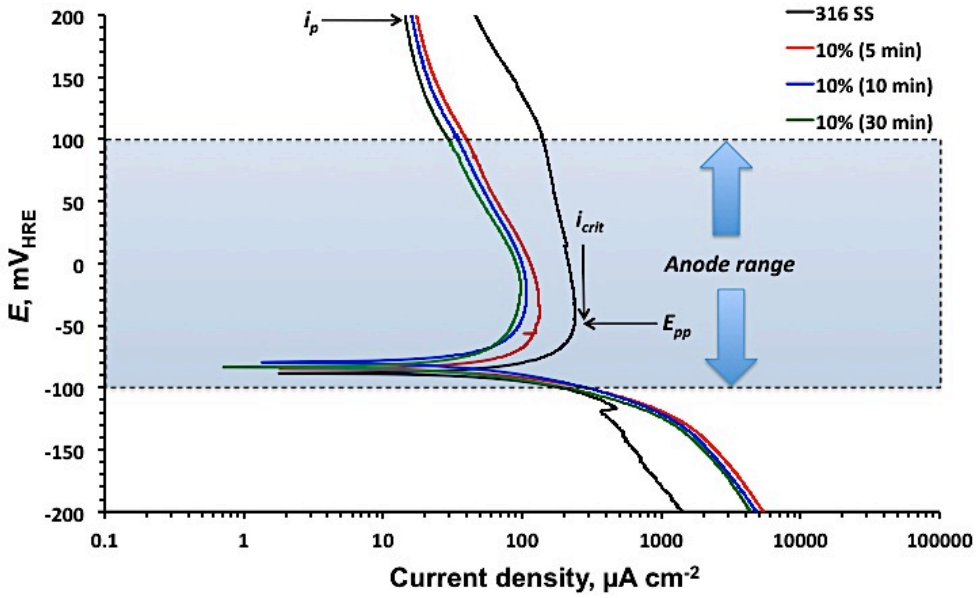

Figure 77: Polarization curve of 10% samples in comparison with 316 SS, showing potential range in simulated PEFC anode environment (1 M H_2SO_4 + 2 ppm F^- ions at 70 ˚C) purged with H_2.

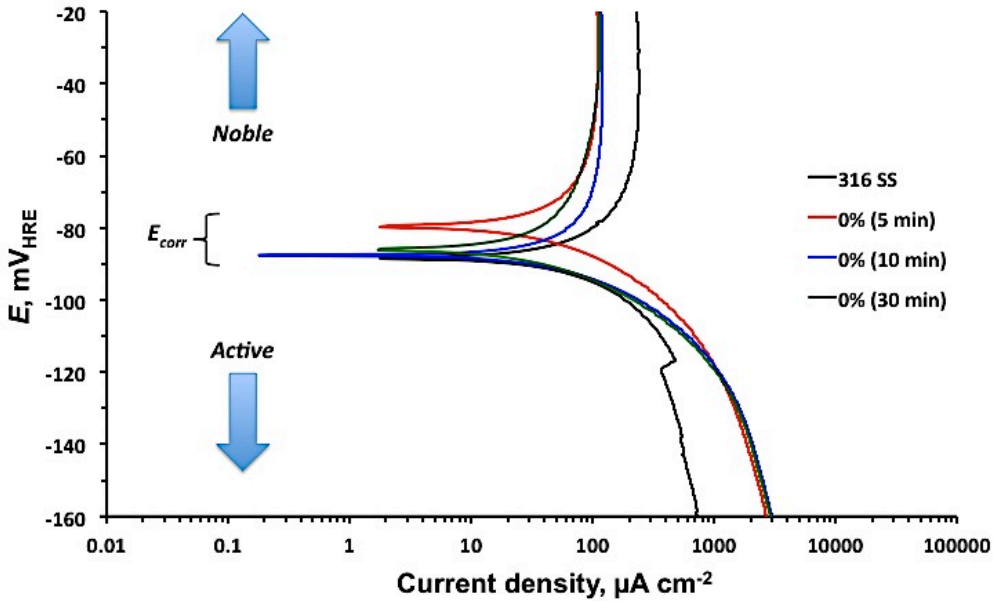

Figure 78: Tafel plots showing OCP shifts of 0% samples in comparison with 316 SS, in simulated PEFC anode environment (1 M H_2SO_4 + 2 ppm F^- ions at 70 ˚C) purged with H_2.

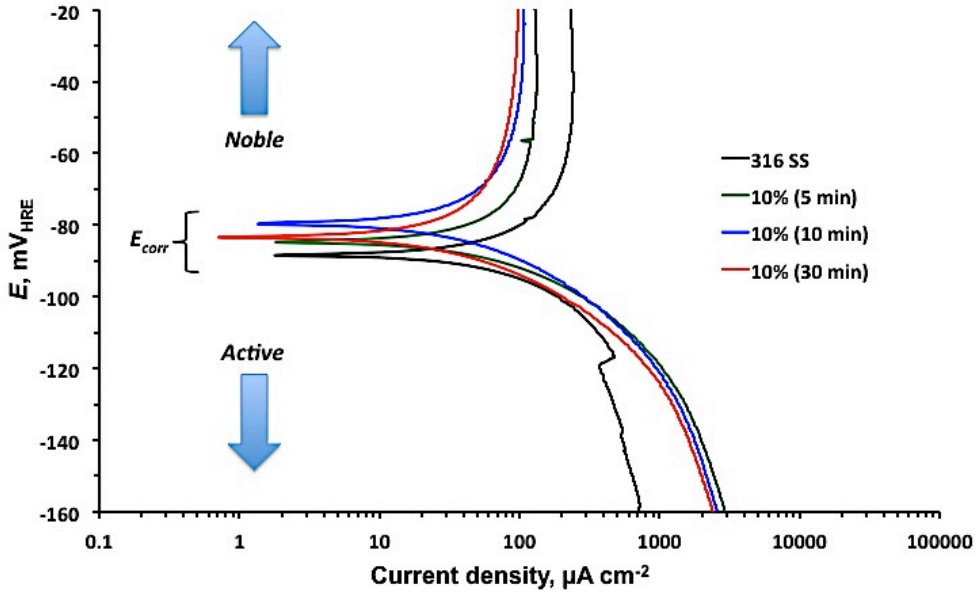

Figure 79: Tafel plots showing OCP shifts of 10% samples in comparison with 316 SS, in simulated PEFC anode environment (1 M H_2SO_4 + 2 ppm F^- ions at 70 ˚C) purged with H_2.

3.3.4.2 Simulated cathode environment

The potentiodynamic polarisation response for two treatment conditions (0% and 10%) along with that of untreated 316 SS in simulated PEM fuel cell cathode environments (1 M H_2SO_4 +2 ppm F^- ions at 70 ˚C purged with Air) is shown in

Figure 80 and Figure 81. As seen in both figures, the polarization curves of samples treated under both conditions (0% and 10%) generally demonstrate lower current densities across the polarization scan range (-200 to 1500 mV_{HRE}). Across the passive range between passive current density (i_p) and the critical breakdown potential (E_b), where the current is not affected by changes in overpotential, the current density of all 0% and 10% treated samples, fluctuate with no distinctive pattern. They do however demonstrate lower current densities than the untreated 316 SS at both points of interest (i_p and E_b).

The region of interest with regards to cathode operating range is typically between 800 – 1200 mV_{HRE}; a close up of this region of the polarisation curves is shown in Figure 82 and Figure 83. As shown, the treated samples demonstrate more positive transpassive corrosion potentials as well as lower current densities compared to the untreated 316 SS sample. At high load cathode operating voltage (800 mV_{HRE}) the corrosion current densities are more or less similar to those of the untreated 3166 SS as shown in Table 17. With 0% samples demonstrating a decreasing trend with regards to treatment time in the order 0% (30 min) < 0% (10 min) < 0% (5 min), while 10% samples demonstrating fluctuating response with regards to treatment time. Moreover, as the potential is made more positive, beyond where the current is reasonably constant until eventually the current begins to increase rapidly with potential and the dissolution of the passive film and transpassivation occurs at the critical pitting potential (E_b) is observed. At cathodic OCP typically (~ 1200 mV_{HRE}), the corrosion current densities of all the treated samples are all lower than the untreated 316 SS, a decreasing trend 0% samples of the order 0% (30 min) < 0% (10 min) <

0% (5 min) is observed, while a fluctuating order is observed for 10% samples of the order 10% (10 min) < 10% (30 min) < 10% (5min). This highlights that the lowest treatment time (5 min) for both 0% and 10% samples demonstrate the best performance.

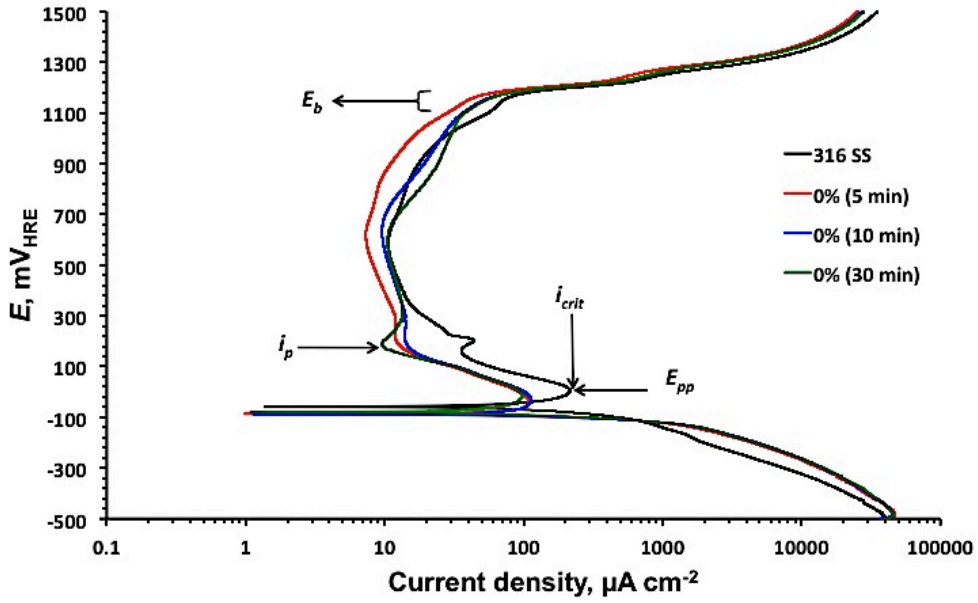

Figure 80: Polarization curve of 0% samples in comparison with 316 SS, in simulated PEFC cathode environment (1 M H_2SO_4 + 2 ppm F^- ions at 70˚C) purged with air.

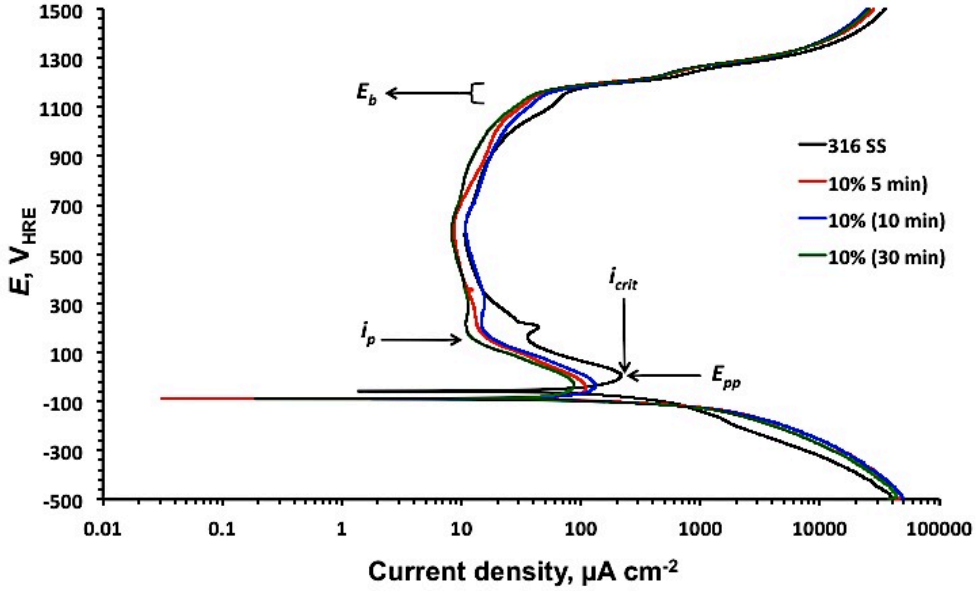

Figure 81: Polarization curve of 10% samples in comparison with 316 SS, in simulated PEFC cathode environment (1 M H_2SO_4 + 2 ppm F^- ions at 70˚C) purged with air.

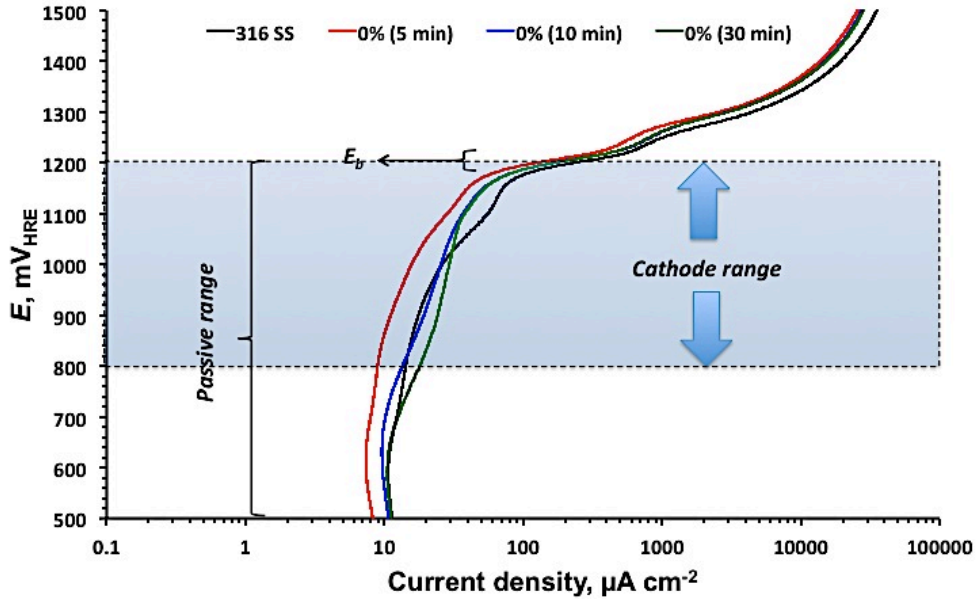

Figure 82: Close up of Cathodic range (800-1200 mV_{HRE}) of the polarization curve of 0% samples in comparison with 316 SS, in simulated PEFC cathode environment (1 M H_2SO_4 + 2 ppm F^- ions at 70˚C) purged with air.

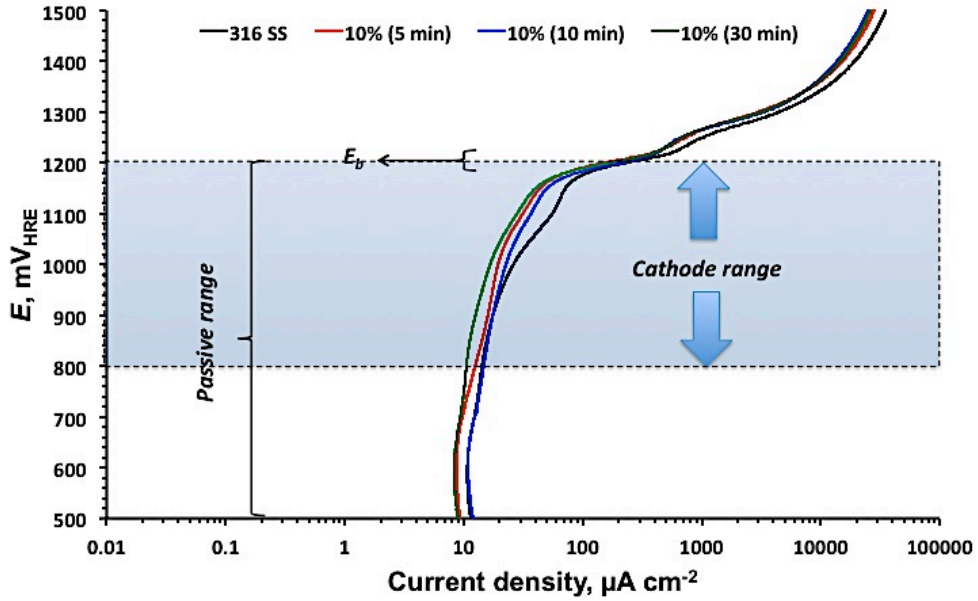

Figure 83: Close up of Cathodic range (800-1200 mV_{HRE}) of the polarization curve of 10% samples in comparison with 316 SS, in simulated PEFC cathode environment (1 M H_2SO_4 + 2 ppm F^- ions at 70˚C) purged with air.

Table 17: Comparison of corrosion current densities of 316 SS and treated 316 SS (Treatment condition: H_2S0_4 + v/v glycerol additive of 0 and 10%, 12.5 mA cm^{-2}, 25 ° C, at 5 and 10 min) in the PEM fuel cell cathode operating potential range (800 mV_{HRE} and 1200 mV_{HRE}) at 70 ˚C in simulated PEM fuel cell cathode environment.

	At E = 800 mV_{HRE}	At E = 1200 mV_{HRE}
	i_{corr}, μA cm^{-2}	i_{corr}, μA cm^{-2}
316 SS	14.24	231.1
0% (5 min)	8.93	122.7
0% (10 min)	13.53	164.1
0% (30 min)	18.0	165.0
10% (5 min)	12.47	151.1
10% (10 min)	14.75	206.4
10% (30 min)	10.53	167.7

3.3.5 Durability

The long-term corrosion behavior of the treated samples and untreated 316 SS in simulated PEMFC anode and cathode environments were studied with potentiostatic and cyclic voltammetry measurements. Potentiostatic studies were carried out at optimum PEM fuel cell operating potentials where the maximum load is applied, corresponding to ~ 100 mV_{HRE} and 800 mV_{HRE} on the anode and cathode respectively. In the anode environment process at 100 mV_{HRE}, the solution is purged with H_2, while in the simulated cathode environment at 800 mV_{HRE}, in the solution is purged with air.

3.3.5.1 Potentiostatic tests

Potentiostatic polarization measurements of treated samples (0% and 10%) and untreated 316 SS for comparison, in simulated anode and cathode environments of 1M H_2SO_4 + 2ppm F^- ions, at 70 ˚C are shown in Figure 84 and Figure 85, respectively. The current stabilization for 316 SS

takes longer in the anode environment than in the cathode environment, due to a lack of oxygen. The treated samples however stabilised more rapidly (within approximately 1500 s) and showed little difference in their stabilisation time in both simulated anode and cathode environments.

As seen in Figure 84, the transient current for untreated 316SS initially decays rapidly below the U.S DoE target, followed by an increase which peaks at ~2 µA cm^{-2} after 3000 s above the US DoE target, which is in agreement with Yang *et al.* [161]. The current density then subsequently decreases across the whole range, finally stabilizing between 2800 - 3000 s at a current density just above the U.S DoE target. On the other hand, the treated samples in the simulated anode environment demonstrated a rapid decay in the transient current followed by a stable current in the range of 0.1 - 0.5 µA cm^{-2}, well below the US DoE target of 1 µA cm^{-2}. Passivation behaviour under simulated cathode conditions is shown in Figure 85, whereby a more rapid transition to a stable current density can be observed with a greater degree of stability associated with the oxidising environment under fuel cell cathode conditions. The untreated 316 SS in simulated fuel cell environment exhibited a transient current of ~1.7 µA cm^{-2}.

3.3.5.2 Accelerated degradation

Conditions during start-up and shut-down can lead to harsher operating conditions with electrode potentials capable of rising to over 1200 mV during these events as reported by Baumgartner et al. [162] . In order to get an understanding of how the materials are likely to perform over the extended operating periods required for practical applications, accelerated testing is necessary. Linear scan voltammetry over the fuel cell operating potential window under simulated conditions provides an indication of material performance and consequently of the passive film durability in applications which experience a high number of start-up and shutdown protocols. On the cathode, the high potentials the bipolar plate is exposed to result in high current densities and potentials that accelerate

degradation. On the anode, the low potentials experienced at OCP, where hydrogen oxidation takes place, bring about concerns over the film stability. The fuel cell anodic region is taken to be between OCP - 100 mVHRE to represent the relatively low overpotential of the hydrogen oxidation reaction. During start / stop processes where possibility of highly induced voltages may occur due to the relatively large overpotential of the oxygen reduction the cathode potential range can extend between 600 - 1200 mVHRE [162]. The anti-corrosion behaviour of the anodised samples in 1 M H2SO4 + 2ppm F^- ions, at 70 ˚C in the fuel cell cathode and anode operating potential range is shown in Figure 86 and Figure 87 respectively.

On the anode side, all treated samples show initial (~ 10 scans) current lower than that of untreated 316 SS. However, only 0% (5 min), 10% (10 min) and 10% (30 min) samples show an initial current density below the US DoE's recommended target of 1 µA cm^{-2}, followed by an incremental rise in current densities up to an equilibrating point of approximately 10 µA cm^{-2} (which is lower than the previous US DoE target of 16 µA cm^{-2}). While 0% 30 min), 10% (5 min) and 10% (10 min) demonstrated initial current densities above the U.S DoE's target (3 - 4 µA cm^{-2}), with a rapid rise in current densities after 10 cyclic scan to an equilibrating point of approximately 45 µA cm^{-2}, similar to that of untreated 316 SS.

On the cathode side, all the treated samples demonstrated current densities lower that the recommended U.S DoE target initially with a steady increase in current density within the range 0.1 - 1 µA cm^{-2}. However, both 0% (10 min) and 0% (30 min) are the only samples that demonstrated current densities above the 1 µA cm^{-2} target after 130 cyclic scans with varied fluctuations beyond this point. The higher current densities observed on the anode side are once again attributed to the absence of O_2 in the deaerated electrolyte solution, of which a critical amount is necessary to prevent corrosion by passivating the surface [163].

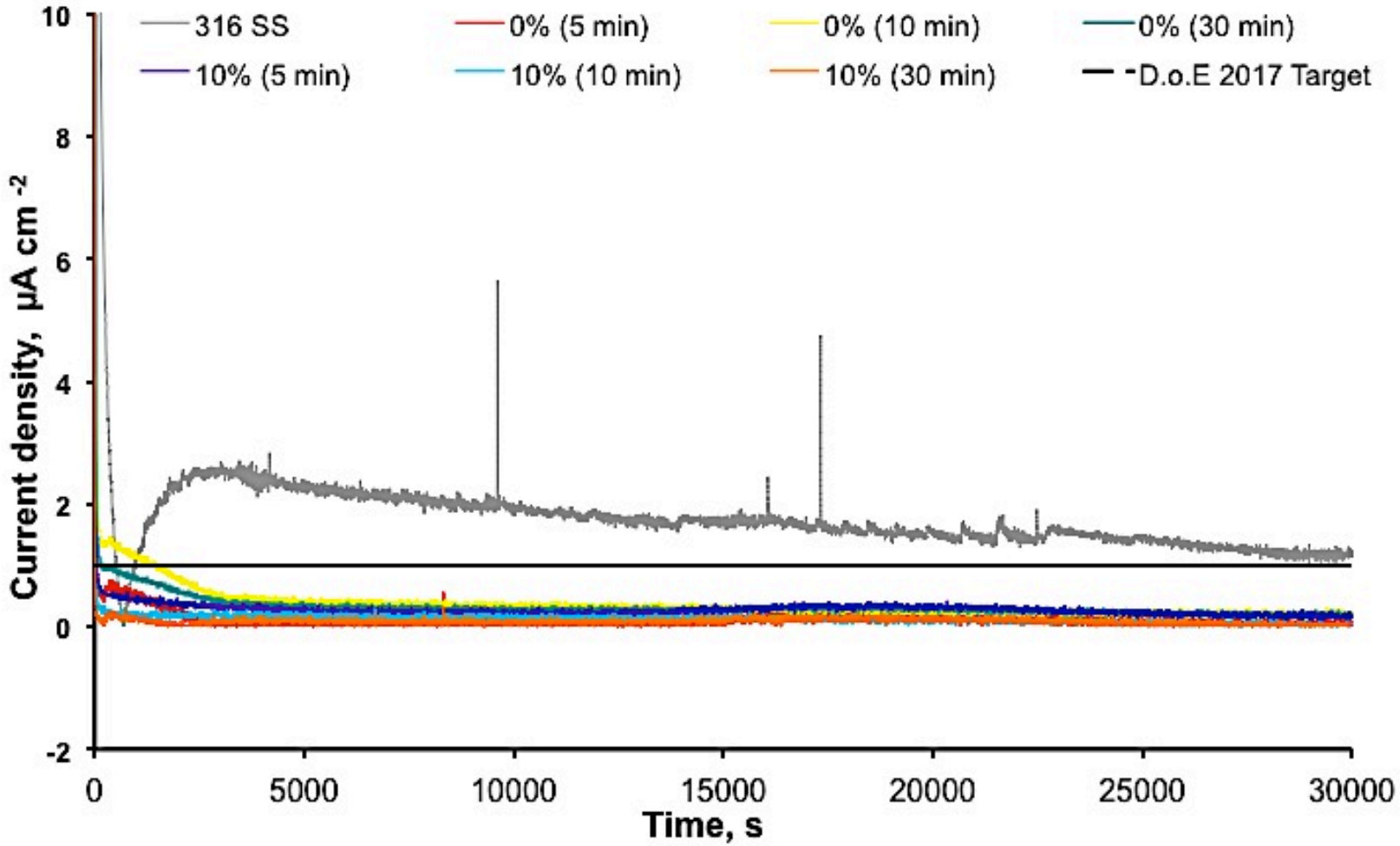

Figure 84: Potentiostatic data at anode operating potential of 100 mV_{HRE} in simulated fuel cell anode conditions (1 M H_2SO_4 + 2 ppm F^- ions), at 70 ˚C purged with H_2.

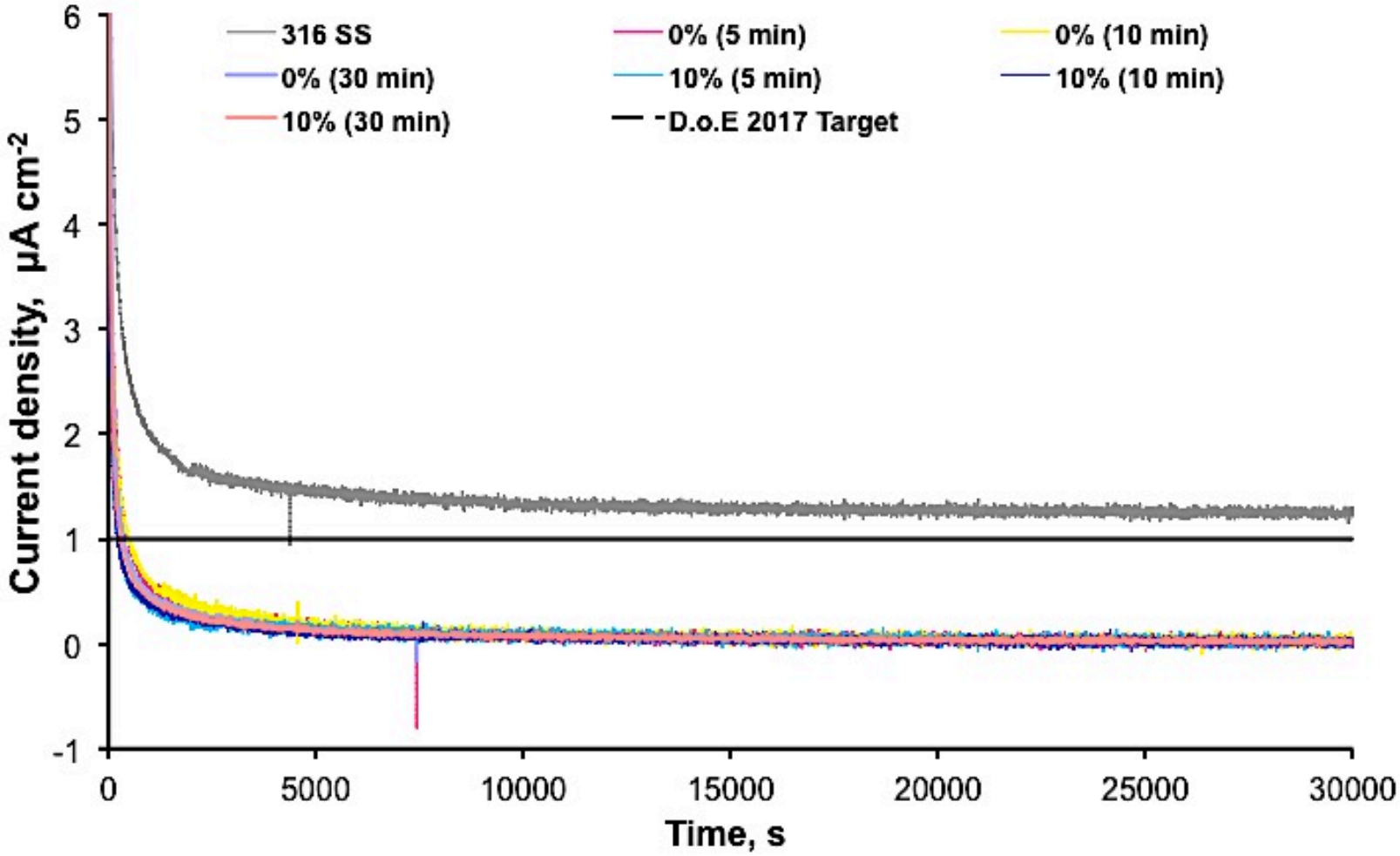

Figure 85: Potentiostatic data at cathode operating potential of 800 mV_{HRE} in simulated fuel cell cathode conditions (1 M H_2SO_4 + 2 ppm F^- ions), at 70 ˚C purged with Air.

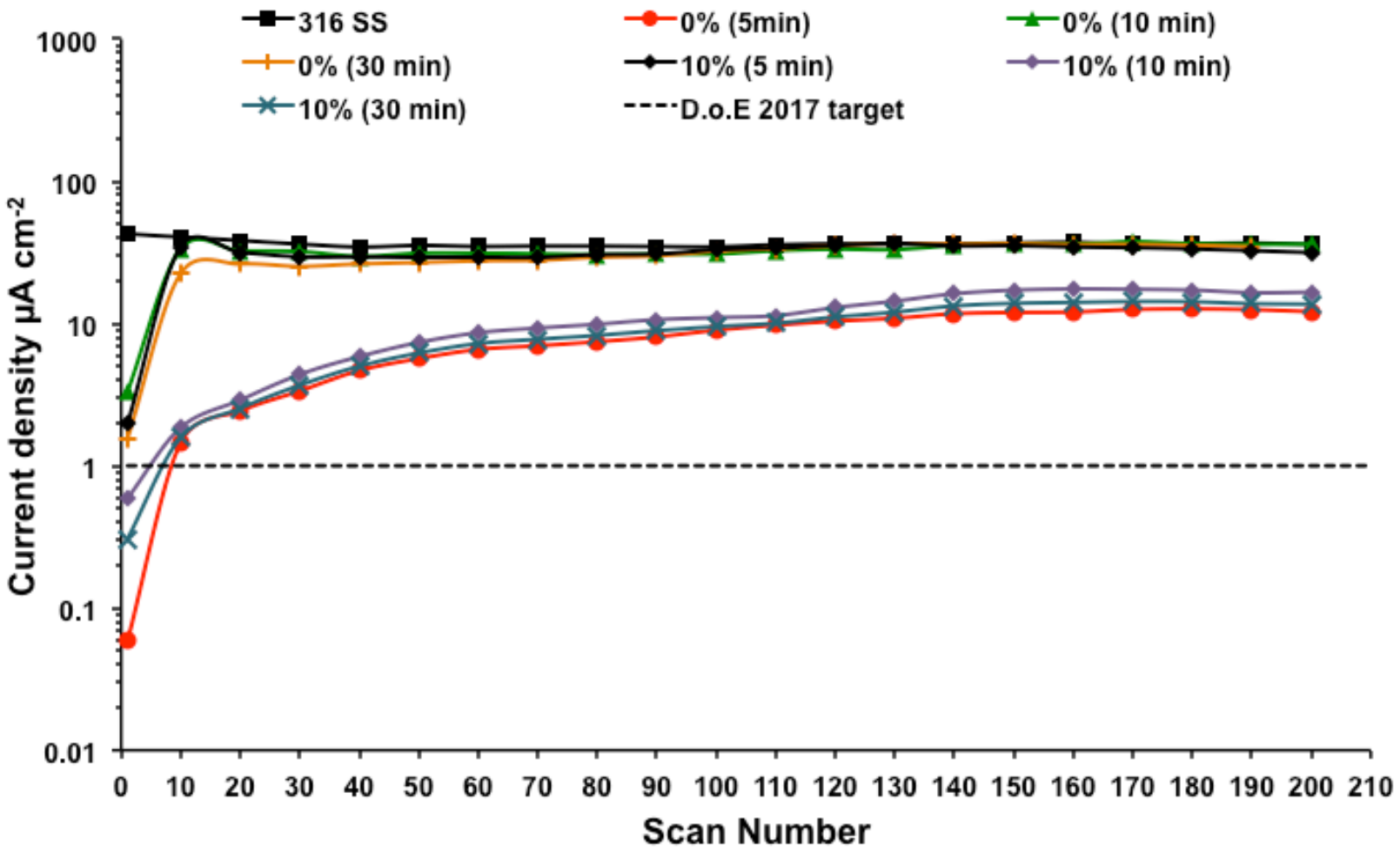

Figure 86: Current density values over 200 scans (scan rate of 1mV cm^{-2}) at anode operating potentials; cyclic scans between OCP – 100 mV_{HRE} in simulated fuel cell anode conditions (1 M H_2SO_4 + 2 ppm F^- ions), at 70 ˚C purged with H_2.

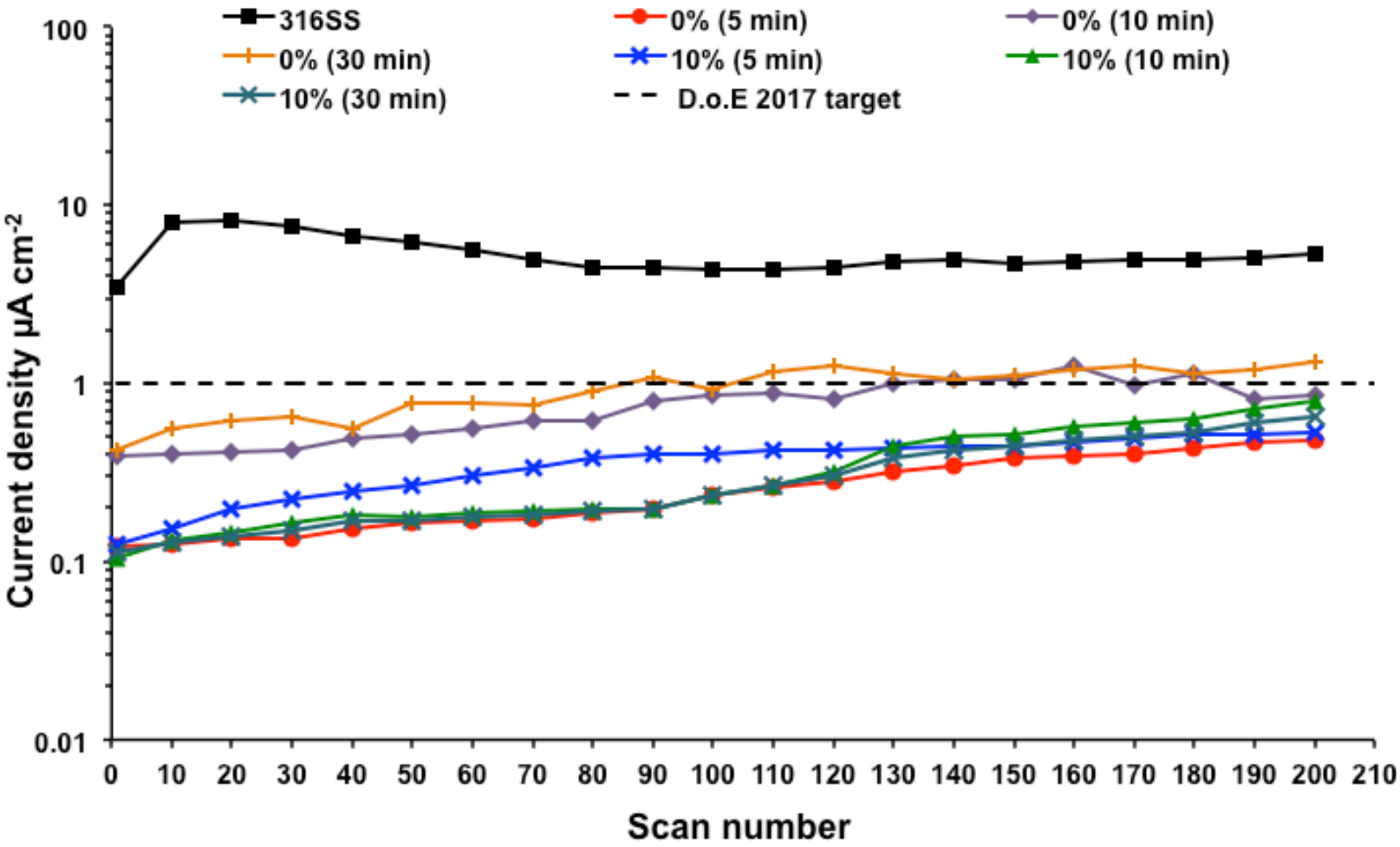

Figure 87: Current density values over 200 scans (scan rate of 1mV cm^{-2}) at cathode operating potentials: cyclic scans between 600-1500 mV_{HRE} in simulated fuel cell cathode conditions of (1M H_2SO_4 + 2 ppm F^- ions), at 70 ˚C purged with air.

3.3.6 Discussion

The surface treatment technique was developed with the aim of improving the surface characteristics of 316 SS with regards to ICR and corrosion characteristics. The process, which adopts electropolishing principles and methodology, focuses on secondary current plateau in the transpassive range that is typically ascribed to a quasi-passivation process whereby oxidation leads to an insoluble layer at the electrode surface.

Polarisation curves of the 316 SS in the dilute acids (0.25, 0.5 and 1 M H_2S0_4) demonstrated a secondary current plateau in the transpassive region, where the electrode undergoes a transpassive dissolution process that is transport controlled in aqueous solution [121]. The formation of a secondary film at this current plateau region controls the chemical dissolution through its interface with the electrolyte; thereby defining a potential range independent of the current [158]. Furthermore, current transient data showed that at low current densities the dissolution voltage remains constant suggesting that etching typically occurs in this region with no brightening effects that are typically indicated by the formation of peaks at higher current densities [24].

Current efficiency calculations showed that a low current is typically desirable in order to ensure a high current efficiency, where the effects of the ionic strength (between 1 M and 0.5 M), doesn't seem to play a key role. However, at higher current density, the effects of the ionic strength of the electrolyte solutions come into play, with higher anion concentrations increasing the rate of attack and thus the metal dissolution. This is in accordance with the ion-replacement model, which suggests that when the oxide matrix is attacked by anions, it exhibits ionic conductivity that results in metal dissolution [164]. The current efficiency of the anodization process is also observed to be dependent on increasing electrolyte concentration, decreasing current density and treatment time. This is because the rate determining process during electropolishing is one of diffusion of product

ions away from the surface; so as the current density and treatment time increase, mass transport effects become more evident, leading to a decrease in the efficiency of the process.

The effects of the anodization process with regards to the near surface enrichment of Cr and Ni ions studied via ToF SIMS, showed an increase in relative count ratios of Cr and Ni for all treated samples. Samples treated without the addition of glycerol to enhance the viscosity of the electrolyte solution demonstrated a decrease in Cr and increase in Fe of the near surface relative count ratios with respect to increasing treatment time. This is possibly due to the fact that as the treatment time increases the amount of material removed from the anode surface increases, and the dissolved content saturates the electrolyte hindering the rate of dissolution and making the process less favourable to the enrichment process beyond a limiting time. Samples treated with the addition of glycerol (10% and 30% v/v) demonstrated a small increase in Cr and small decrease in Fe relative count ratios respectively with treatment time.

The addition of viscosity enhancing agents (i.e. glycerol), has been associated with the formation of a viscous layer at the metal surface, which suppresses the influence of the metal microstructure on the dissolution rate [118]. At high glycerol content (10 - 30% v/v), the near surface count ratios of Cr and Fe are relatively similar with respect to treatment time. This may be due to the fact that glycerol is a large molecule with poly-functional groups (three OH groups, leading to strong hydrogen bonding) which may be concentrated to form aggregates on the surface [123]. Under conditions of high glycerol content and low temperature, i.e. room temperature (25 ˚C), strong intermolecular interactions lead to the formation of a compact shielding layer, which hinders the transportation of dissolved metal ions and acceptors.

The anodization process has demonstrated to be effective in increasing the Cr and Ni near-surface relative count ratio, which is particularly favourable for decreasing surface contact resistance. The near surface, which

essentially forms the passive film, is principally composed of an inner chromium-iron oxide Cr_2FeO_4 region and an outer iron-nickel oxide region. A general trend whereby the interfacial resistivity of stainless steel alloys decreases with increasing Cr and Ni content, has been demonstrated by *Davies et al.* [79]. An increased Mo content of stainless steel has been demonstrated to lead to a decrease in the anodic peak by an order of magnitude [158], and has been considered to be a decisive factor in determining contact resistance with greater Mo content demonstrating much lower ICR [75]. However, the slight reduction in the Mo content between untreated and treated samples implies that Mo is not the reason for improved corrosion and ICR observed here.

Moreover, polished surfaces typically exhibit higher ICR values as they have fewer irregularities, which lowers the surface area an thus density of the contact points between the metal and the carbon fibres [165]. By texturing the surface through the anodization process to alter the morphology and modifying the surface composition, the ICR between BPP and GDL should effectively diminish, which has been demonstrated by others [101, 102, 106]. However it has been noted that in order to decrease the ICR between BPP and GDL, the surface roughness of the BPP must be <1.2 µm, which is equivalent to that of GDL (depending on the GDL structure) [165]. The electrochemically treated samples showed R_a values in the range of 74 - 200 nm, which were significantly lower than the R_a values of a GDL. This in turn means that the surface asperities and surface roughness cannot be attributed as the main contributing factors to the reduction in ICR. However, it supports the conclusion that the key attributing factor here to the significantly low ICR is the presence of a thin passive film associated with a higher Cr and Ni surface content. This is a product of the superficial surface compositions, which seem to have a greater impact on the contact resistance between the treated surface and the GDL, rather than the surface roughness as also demonstrated by *Bai et al.* [166]. This is also in agreement with *Lee et al.* who also suggested improvement of ICR

following electrochemical surface treatment of BPP can be attribute to the minimization of the oxide layer thickness [32, 33].

With regard to corrosion, alloys expected to have a good corrosion resistance as a bipolar plate should ideally exhibit passive behaviour at all fuel cell electrode potentials. Depending upon the mode of operation of a stack the bipolar plate might spend much of its time at an imposed potential that may be far from its natural corrosion potential [138], which depending on the passive characteristics of the surface may induce higher current density and greater degree of dissolution. On the anode side the lowest and highest electrode potentials occur at (or near) reversible potential for hydrogen oxidation (0 mV_{HRE}) and ~ 100 mV_{HRE} respectively. All treated samples under conditions of 0% and 10% v/v glycerol additive to the acid electrolyte (0.5 M H_2SO_4), demonstrated shifts in E_{corr} in favour of towards ennoblement, which for stainless steel is typically correlated with behaviour of alloys with a higher alloy content of Cr and Ni, which is in agreement with the ToF SIMS near surface analysis. At typical anode operating potential (~ 100 mV_{HRE}), all the samples demonstrate current densities lower than the critical passivation current density (i_{crit}). It is observed that this anode potential is in the passive region for all the materials tested, indicating the surface of the stainless steel samples are passivated forming a protective film. Similar observations are also made at (or near) reversible potential for hydrogen oxidation (0 mV_{HRE}). Furthermore, the width of the active peaks of the treated samples within the anodic dissolution range, which is the distance between i_{crit} and i_p, are noted to be narrower compared to that of the untreated 316 SS sample. This in turn means the passivation process for the treated samples takes place over a smaller potential window indicative of a more rapid passivation process.

In the simulated PEFC cathode environment, at 800 mV_{HRE} (typical cathode operating potential) all the tested specimens lie in the passive region. As the potential of a metal is made more positive, the passive current density

(i_p) remains reasonably constant until eventually the current begins to increase with the initiation of transpassivation. The breakdown of the oxide by anions via the initiation of transpassivation, occurs at a critical potential called the critical breakdown potential (E_b) of the passivation process is the imperative parameter; in this case between 1000 and 1200 mV_{RHE}. The formation of peaks are observed in this region which could be attributed to transpassivation due to the formation of high valence chromium [167]. The treated samples all demonstrate more positive transpassive potentials as well as lower current densities to the untreated 316 SS sample. Such decreases in current are due to a greater degree of resistance from localised breakdown of the passivating oxide film by anions, particularly fluoride ions (F^-), which induce localised dissolution of the passivating oxide film at weak points, usually associated with some discontinuity such as a grain boundary, dislocation or inclusion in the metal, leading to exposure of the underlying metal which can dissolve, giving rise to an increase in the anodic current.

The durability of the treated samples in the fuel cell operating potential window demonstrated that the current stabilization for the samples takes longer in the anode environment than in the cathode environment, more noticeably for the untreated 316 SS sample. The longer stabilisation time at the anode is due to the absence of O_2 in the deaerated simulated fuel cell electrolyte solution, of which a critical amount is necessary to prevent corrosion by passivating the surface [163]. The formation of a passive film over the whole surface only occurs when the current becomes relatively constant with respect to time. In the anode environment hydrogen induces the passive film dissolution and the length of time that this process takes is an indication of the formation of a dense passive film [168]. The treated samples reach a constant current density, which is a testament to the coverage of the whole surface by a passive film. On the anode side there is clearly a more concern about the long-term passive film stability.

The decrease in the corrosion current densities can be attributed to a greater degree of resistance from localised breakdown of the passivating oxide film by anions, particularly fluoride ions (F^-). These anions induce localised dissolution of the passivating oxide film at weak points, usually associated with some discontinuity such as a grain boundary, dislocation or inclusion in the metal, leading to exposure of the underlying metal which can dissolve, giving rise to an increase in the corrosion current. Similar results for 304 SS in sulphuric acid solutions were obtained by *Hermas et al.* [105].

Moreover, the reduction in corrosion currents and the more rapid passivation rate for the treated samples can be attributed to the increase in Cr surface content. Chromium oxide in the oxide film prevents further surface corrosion by blocking oxygen diffusion to the steel surface preventing the spread of corrosion into the metal's internal structure, due to very strong bonds formed between the steel and the oxide ions because to the their similar size. Furthermore, chromium has a critical passivating current density hundreds of times less than that of iron and since its OCP is more negative, chromium is much more stable than iron in weak oxidizing mediums. Moreover chromium oxide, which prevents further surface corrosion by blocking oxygen diffusion to the steel surface and blocks corrosion from spreading into the metal's internal structure, due to the similar size of the steel and oxide ions, they bond very strongly and remain attached to the surface. This in turn means that for the treated samples, as a result of their improved electrical characteristics, i.e. high electrical conductivity, the reduction of solution species will occur at the film/solution interface at quite low anode potentials; too low to produce substantial ion transport and consequent the typical film growth consists of a Cr_2FeO_4 spinel oxide with excess Cr [159].

4 Conclusion

The electrochemical treatment was developed with the aim of improving the interfacial contact resistance (ICR) and corrosion properties of relatively inexpensive stainless steel (316 SS) for use as a bipolar plate material in PEFCs. Polarization studies, ICR measurements and surface analysis techniques that include ToF SIMS, SEM and AFM, were employed to establish the following conclusions:

- ICR measurements exhibited significant improvements with values in the range of 6 - 24 mΩ cm^2 at 200 psi (~ 140 N cm^{-2}), within the US Department of Energy 2017 target for metallic bipolar plates of 20 mΩ cm^2 for Interfacial contact resistance.
- Polarisation studies under simulated PEFC environment demonstrated improvements in the corrosion resistance at both anode and cathode operating potentials. Enhanced durability of the passive film was observed with corrosion current densities in the range of 0.1 - 0.5 µA cm^{-2}, lower than the US Department of Energy 2017 target for metallic bipolar plates of 1 µA cm^{-2}.
- ToF SIMS near surface analysis measurements exhibited an increase in relative count ratios of Cr and Ni as a consequence of the surface treatment. With the decrease in ICR and corrosion current density of stainless steel alloys generally attributed to increasing Cr and Ni content.
- The electrochemical treatment is observed to be an etching process with SEM images observed to exhibit general dissolution over the entire surface, with crystallographic etching apparent and few hemispherical pits.
- Previous studies have indicated that increased surface roughness and surface morphology is a cause of reduction in ICR. In this work, AFM data of surface roughness and morphology although

showed increased Ra values; these however, were not significant enough to affect the ICR significantly

- The tuning of variable such as treatment time and addition of glycerol as a viscosity-enhancing agent had some impact on the ICR, with sampled treated at 30 min demonstrated lowest ICR values across the whole compaction range. However, with respect to corrosion current density, it did not result in significant improvements across the treated samples. Furthermore ToF SIMS near surface analysis also demonstrated the variables did not have significant differences in the element count ratios of Cr and Ni.
- The current efficiency calculations demonstrated that shorter treatment times always produced the highest current efficiencies, which will consequently impact the economic costs.
- The improved performance with regards to ICR and corrosion resistance can only therefore be attributed to the formation of a thinner more durable passive film, which was shown to be due to an enriched Cr and Ni composition at the near surface.

The suitability properties of metallic BPPs are determined by key factors such as weight, cost, corrosion resistance, ease of manufacture / processing and contact resistance. Although various metals have been assessed and many qualify in terms of materials properties only a few meet cost targets. Here the main focus has been on iron-based alloys, in particular austenitic stainless steels, because of their low cost. However, due to inherent characteristics the performance of low cost austenitic stainless steel is limited without the use of costly precious metal coatings. The surface treatment technique here is a proposed alternative to improving performance and durability of low cost austenitic stainless steel for use as BPPs in PEMFC's, by increasing the near surface Cr and Ni content leading to improved ICR and corrosion resistance. The use of acid electrolyte with low concentration in conjunction with a low treatment

current density and treatment times, ensure not only costs in order to adhere to cost targets but also safety measures are meet.

5 Future work

Although great strides have been made here to improve the ICR and corrosion resistance of stainless steel bipolar plates considerable amount of work is still required to make fuel cells an alternative power sources in the near future for residential and mobile applications. The application of surface treatment techniques to enhance the properties of low cost stainless steel seems to show promise for application as a bipolar plate material.

Through the application of the principles of electropolishing, effective surface modification method has been applied to an austenitic stainless steel substrate. However, in order to improve the performance, the process optimisation requires to be extended, changing process parameters such acid electrolyte, electrolyte refreshment, operating temperature and imposed current signal (DC versus pulsed current). Investigating the effects of these process parameters can lead to a broader operating window, or to a higher quality of the electrochemically treated surface.

However, a better understanding of the changes in the interfacial contact resistance against time for candidate steels at the operational condition is required in order to provide a greater insight into the phenomena since during fuel cell operation the passive films may thicken with time. This requires the steel samples to be pre-treated potentiostatically in the solution at varying time periods while measuring the current transient, with the total interfacial contact resistance measured following the transient process.

Also out stack corrosion test have been the main concern up to this point, however the disadvantage with direct reference to the application to the bipolar plate is that it measures corrosion rates at accelerated rates in simulated environments which may not be a true response to actual long term performance measures. In order to understand the corrosion mechanism during actual operation of a PEM fuel cells, it is crucial to carry

out in situ testing operate with treated stainless steel bipolar plates. This will help to providing an insight into the tendency for corrosion to occur at certain locations within the bipolar plate, in mapping localised corrosion of the bipolar plate and also in further investigation of the durability of the metallic bipolar plate.

Assessing the effect of corrosion by products on the solid polymer electrolyte membrane conductivity and corresponding fuel cell performance is another important step. In order to study this phenomenon, the conductivity of Nafion membrane under compression while being exposed to Fe ions introduced into the system via a carrier gas (H_2/ air) will require to be measured. The corrosion rate information of the treated stainless steel specimens can be used in determining the amount of Fe ions required for exposure of the membrane. This will hopefully provide an insight into the amount of time the membrane will need to be exposed to Fe ions before its performance degrades to unacceptable levels.

Furthermore, the anodization treatment process may be combined with the deposition of protective coatings further enhancing the bipolar plate performance. Investigating the economics, manufacturability and long-term reliability, is also a significant aspect to be investigated, as ultimately the uptake of the process will depend on cost as well as technological merit.

6 Nomenclature

Am	areas of actual contact
B	Stern-Geary a constant
b	is the slope *dE/d log i* of the polarisation curve (termed the Tafel slope and is related to the kinetics of the corrosion reaction)
E_b	critical breakdown or pitting potential
E_{corr}	corrosion potential
E_{pp}	critical passivation potential
E_r	thermodynamic predicted fuel cell output (V)
$E_r°$	theoretical cell voltage under non-standard conditions
E_r	is the overpotential (difference between the measured potential and the reversible potential)
F	Faradays constant (96,487 C mol^{-1})
i_{corr}	corrosion current density
i_{crit}	critical passivation current density
$\lvert i_c \rvert$	cathodic current density
i_p	passive current density
I	process current
M	molecular weight of the anode
M	atom in metal surface
M^{n+}	ion in solution
m_P	mass of product generated / lost
M_P	molar mass in (g mol^{-1})
ne^-	electrons in metal
n	number of electrons transferred per ion
n	valence of the metal ion/ number of electrons
$[O]$	activity of reactant to be oxidised at equilibrium
$[R]$	activity of reactant to be reduced at equilibrium
R	Gas constant, 8.314 J mol^{-1} K^{-1}

P_{H2}, P_{O2}, P_{H2O}	partial pressures of hydrogen, oxygen and water respectively
r	contact radius of a circular contact
R_p	polarisation resistance
$R_{C/SS}$	interfacial contact resistance sum of carbon paper/stainless steel
$R_{C/PF}$	interface component and a carbon paper/passive film interface component
Q	charge passed (coulombs)
S	surface area
T	absolute temperature
t	polishing time
$v(x)$	slowly varying function of the Knudsen ratio
V	real output of the fuel cell (V)
v_e and v_P	stoichiometric ratios of electrons and product
α	symmetry coefficient
β_a	anodic Tafel slope
β_c	cathodic Tafel slope
ΔG º	standard free energy
η	overpotential, E-E_r
η_{act}	activation losses
η_{ohmic}	ohmic losses
η_{conc}	concentration losses
ϑ	absolute temperature
ρ	bulk resistance (both contacting members are of similar material)
R_Ω	ohmic resistance (IR) drop
W	total material weight loss

7 Appendix A1

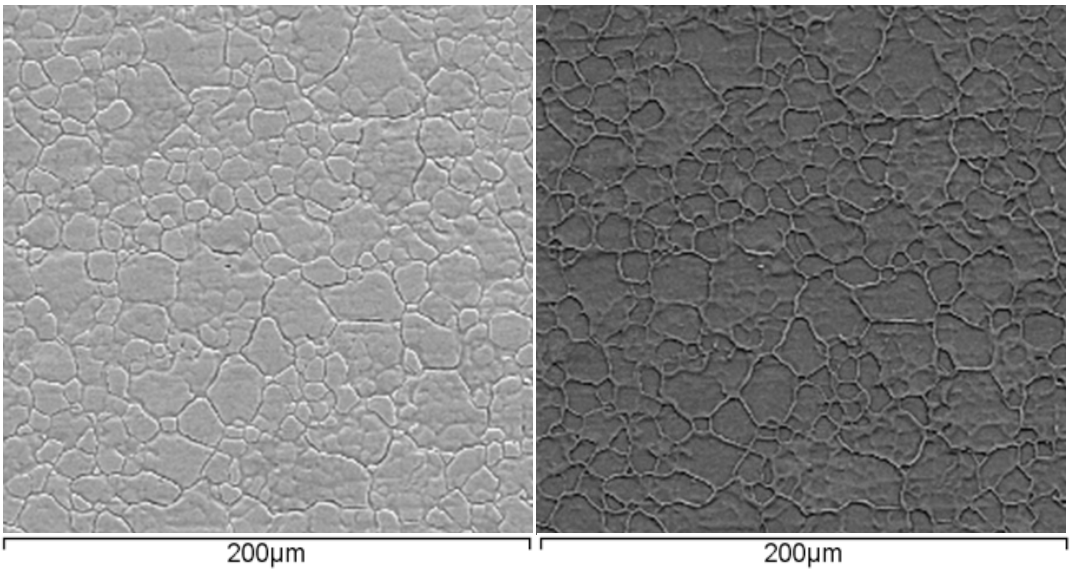

Figure 88: SEM image of untreated 316 SS (left) alongside inverted image (right) at magnification ×900.

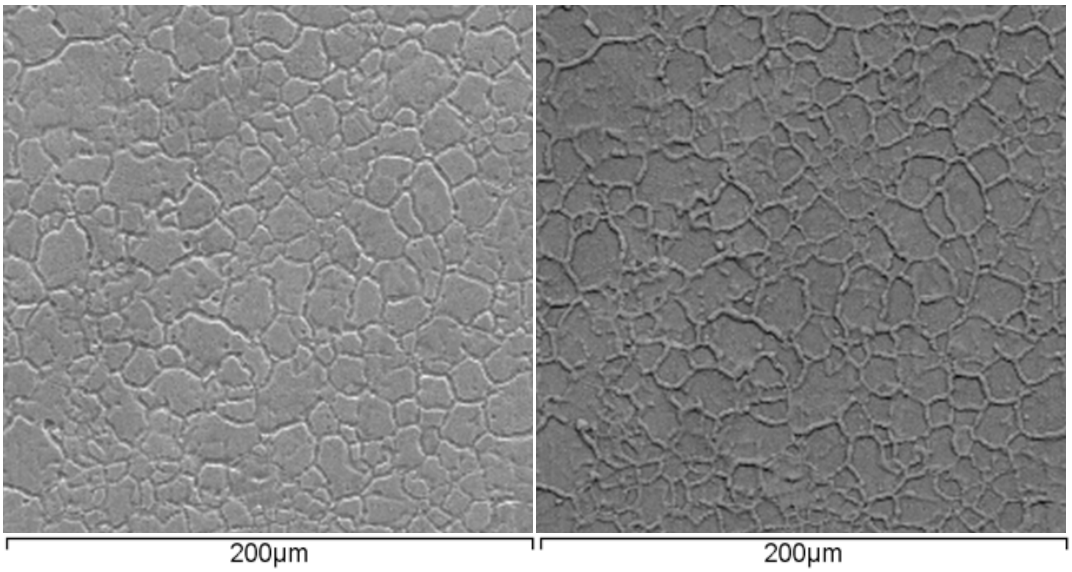

Figure 89: SEM image of 0% (5min) (left) alongside inverted image (right), showing general dissolution at grain boundary at magnification ×900.

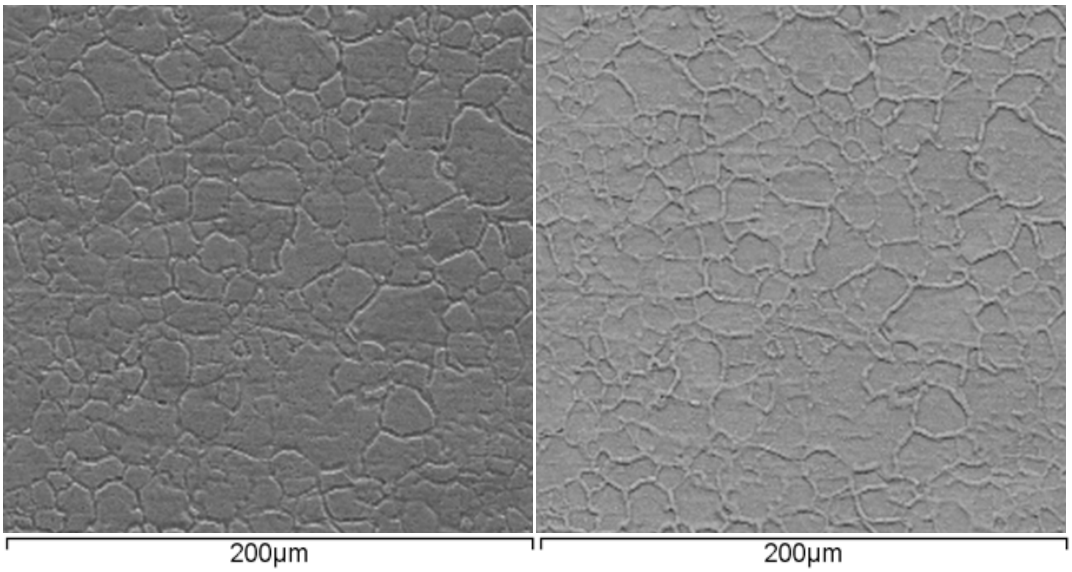

Figure 90: SEM image of 0% (10 min) (left) alongside inverted image (right), showing general dissolution at grain boundary at magnification ×900.

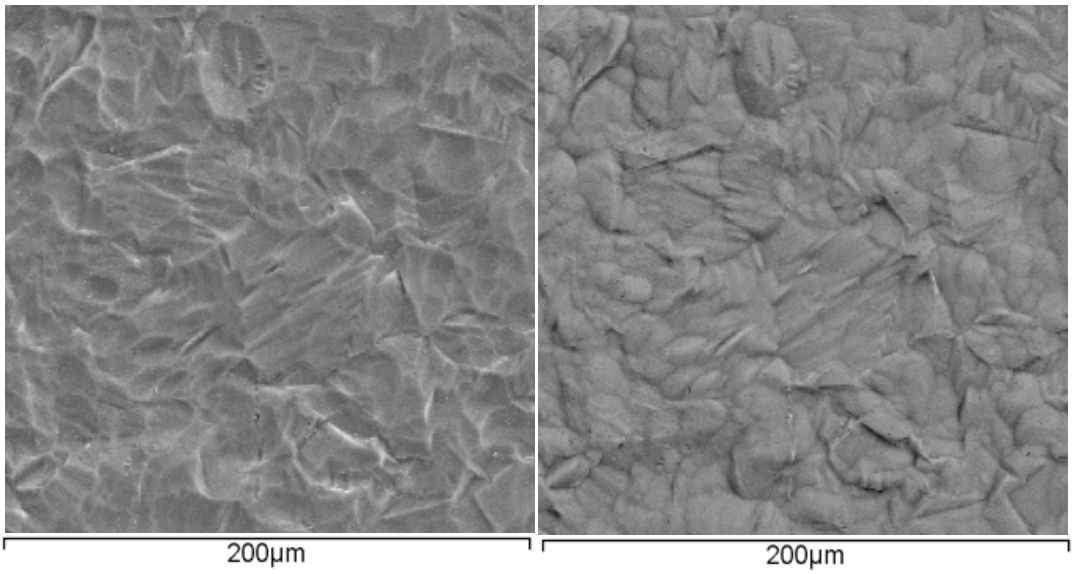

Figure 91: SEM image of 0% (30 min) (left) alongside inverted image (right), showing general etching and some shallow pits at magnification ×1500.

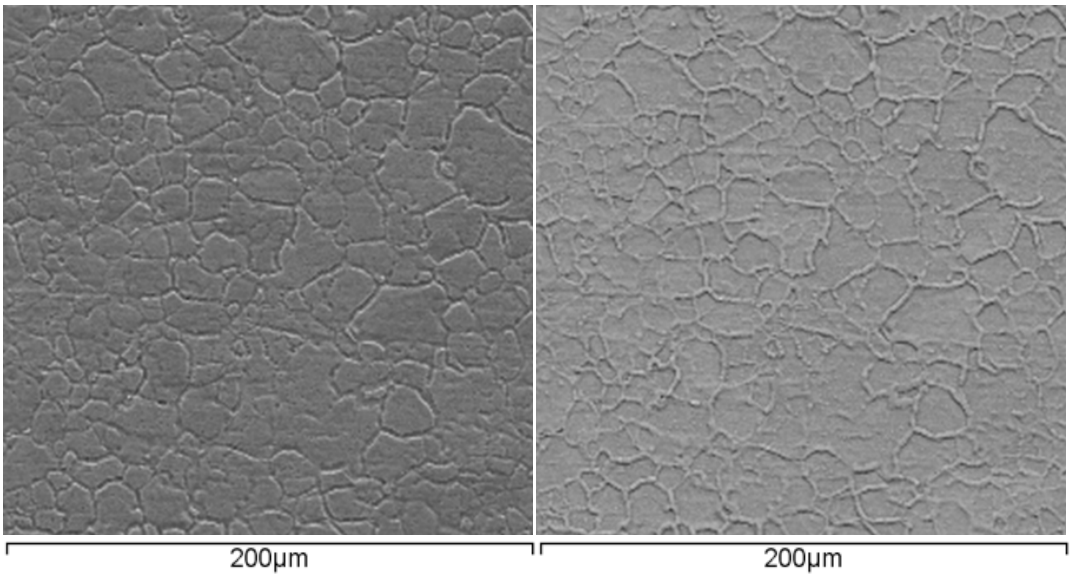

Figure 92: SEM image of 10% (5 min) (left) alongside inverted image (right), showing general dissolution at grain boundary at magnification ×900.

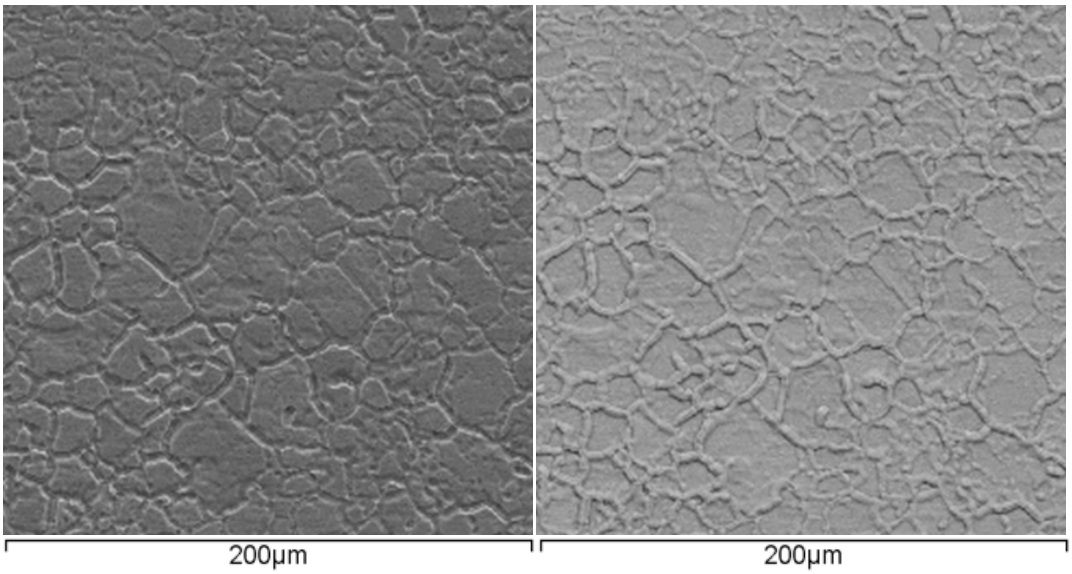

Figure 93: SEM image of 10% (10 min) (left) alongside inverted image (right), showing general dissolution at grain boundary at magnification ×900.

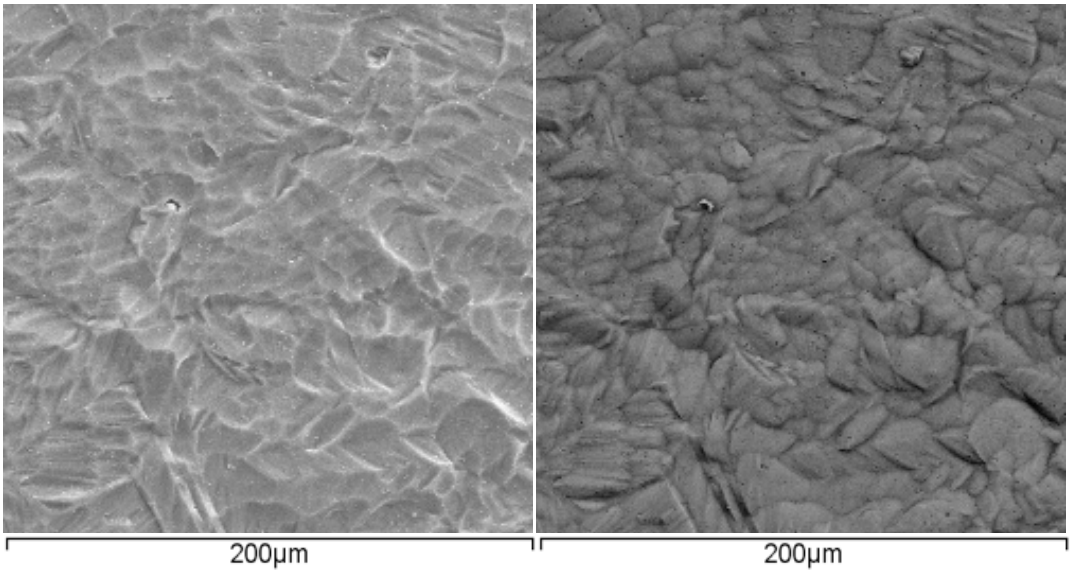

Figure 94: SEM image of 10% (30 min) (left) alongside inverted image (right), showing general dissolution at grain boundary at magnification ×1500.

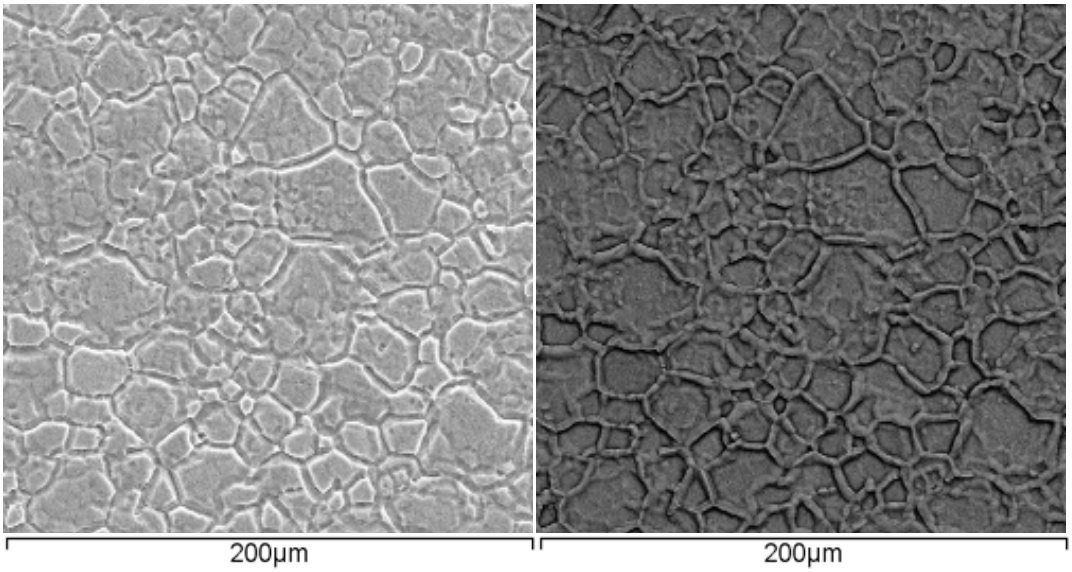

Figure 95: SEM image of 30% (5 min) (left) alongside inverted image (right), showing general dissolution at grain boundary at magnification ×900.

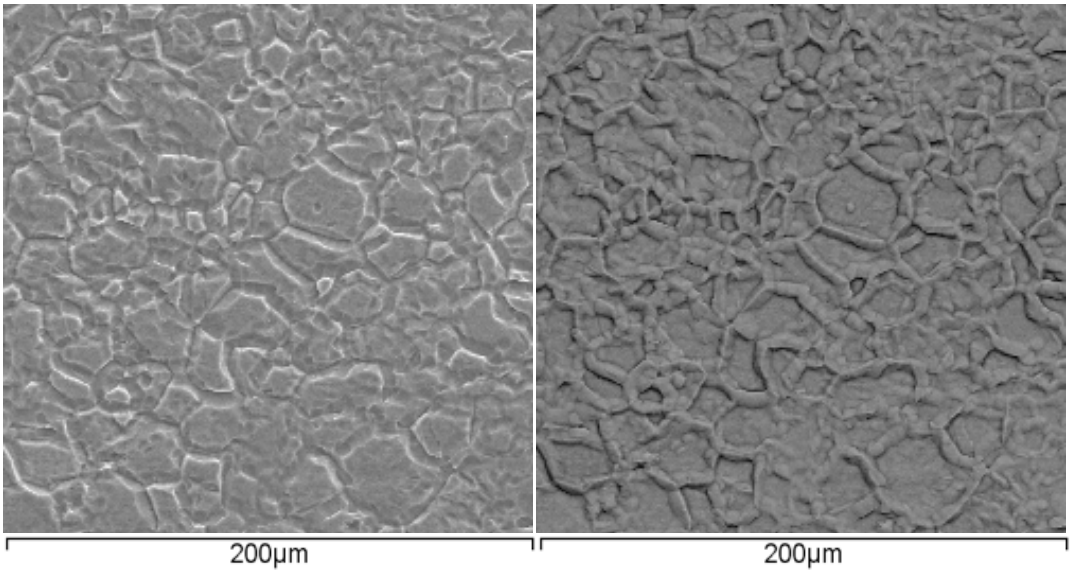

Figure 96: SEM image of 30% (10 min) (left) alongside inverted image (right), showing general dissolution at grain boundary at magnification ×900.

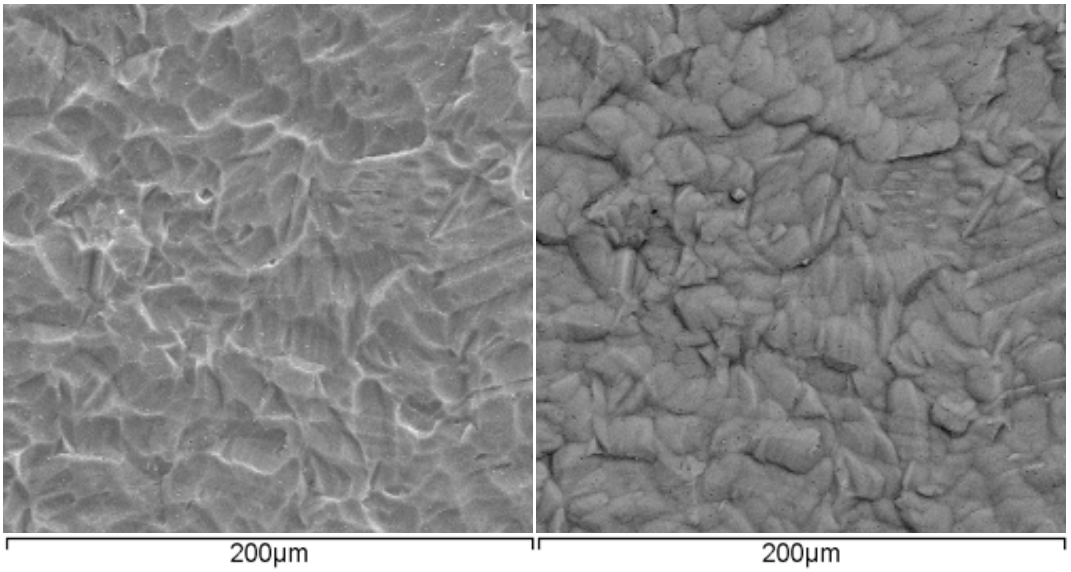

Figure 97: SEM image of 30% (30 min) (left) alongside inverted image (right), showing general dissolution at grain boundary at magnification ×1500.

8 Appendix A2

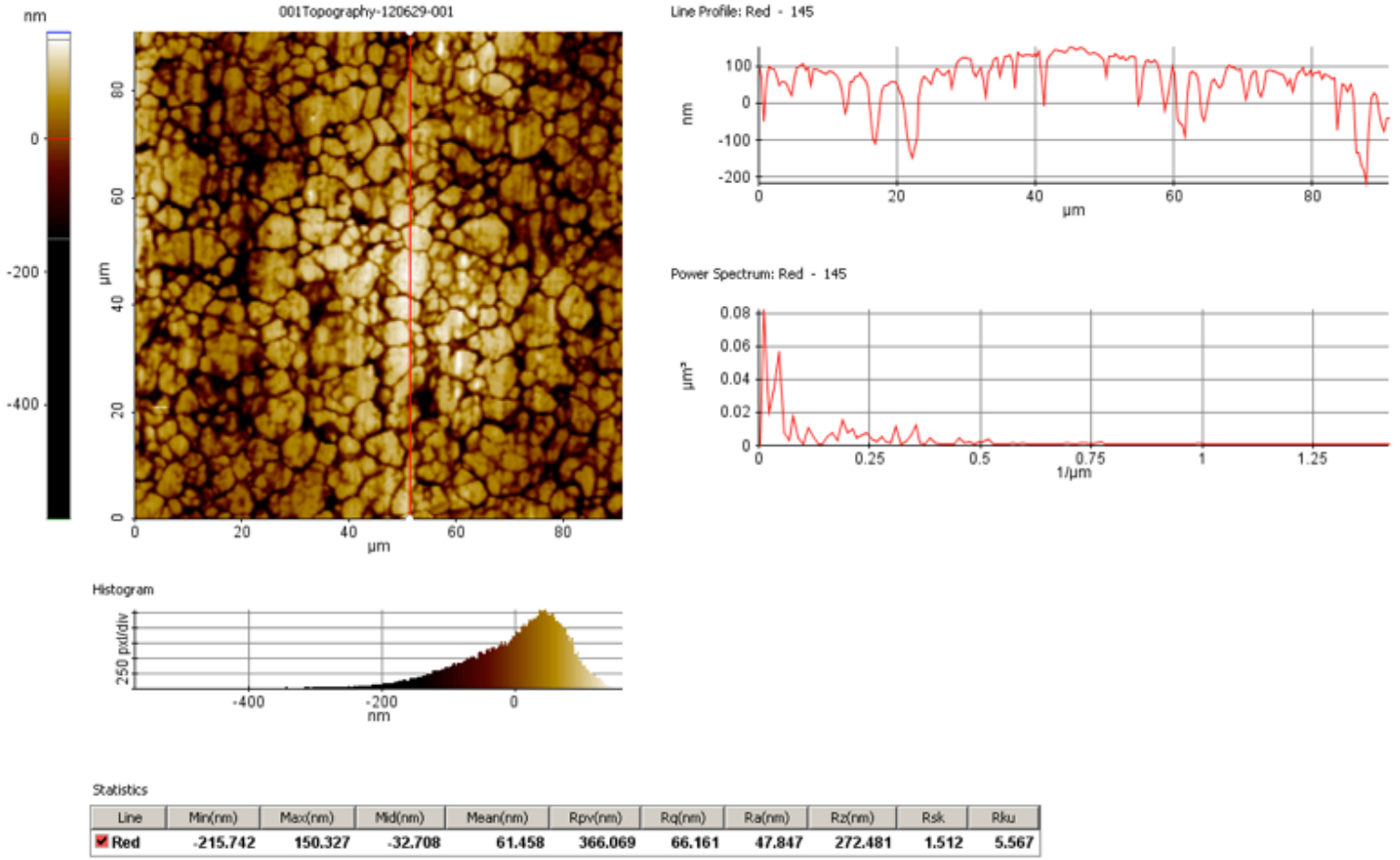

Statistics

Line	Min(nm)	Max(nm)	Mid(nm)	Mean(nm)	Rpv(nm)	Rq(nm)	Ra(nm)	Rz(nm)	Rsk	Rku
Red	-215.742	150.327	-32.708	61.458	366.069	66.161	47.847	272.481	1.512	5.567

Figure 98: Screen image of Ra measurement scan for untreated 316 SS, using AFM contact mode topography line scan at scan size of 90 µm.

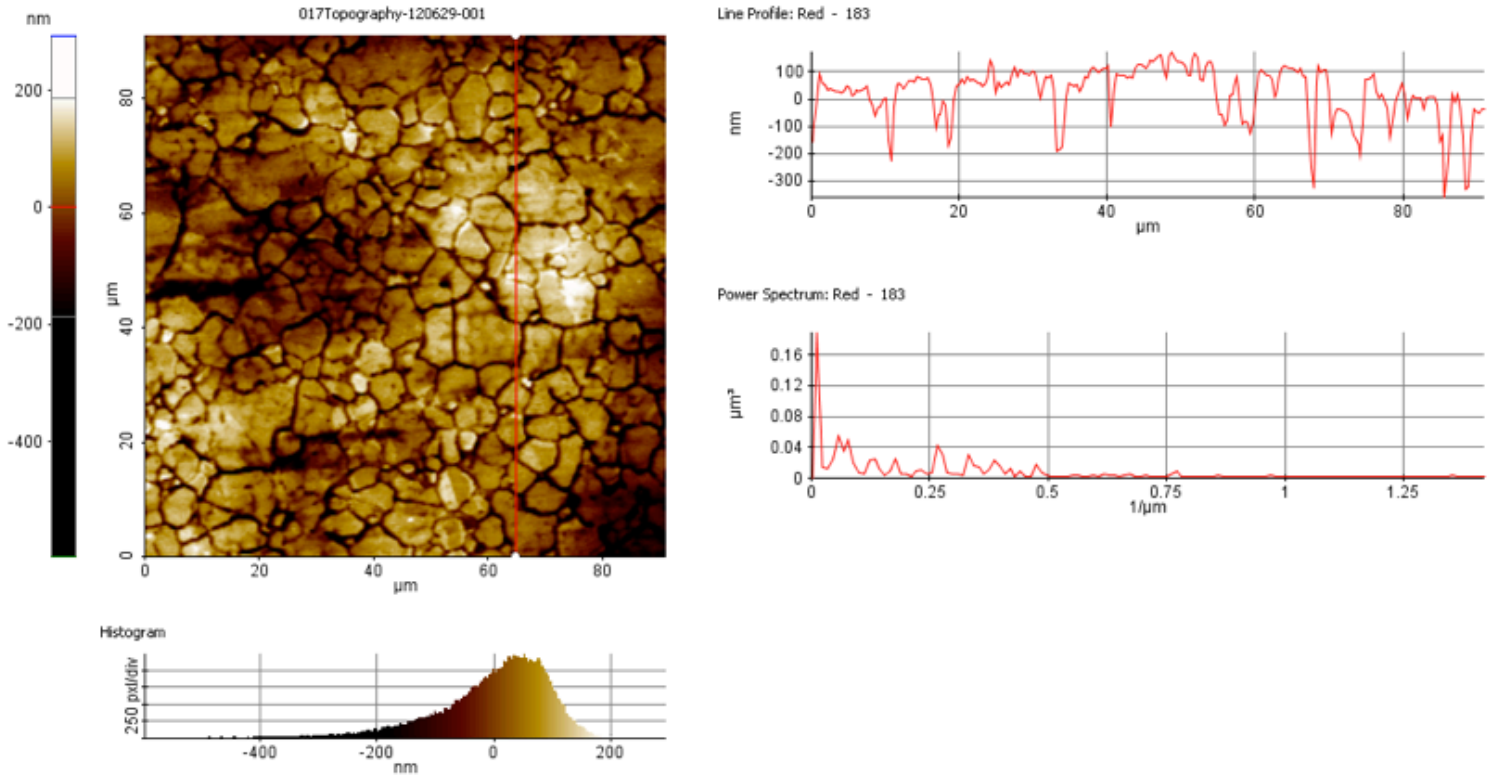

Statistics

Line	Min(µm)	Max(µm)	Mid(µm)	Mean(µm)	Rpv(µm)	Rq(µm)	Ra(µm)	Rz(µm)	Rsk	Rku
Red	-0.360	0.172	-0.094	0.020	0.532	0.097	0.074	0.445	1.329	4.992

Figure 99: Screen image of Ra measurement scan for 0% (5 min), using AFM contact mode topography line scan at scan size of 90 µm.

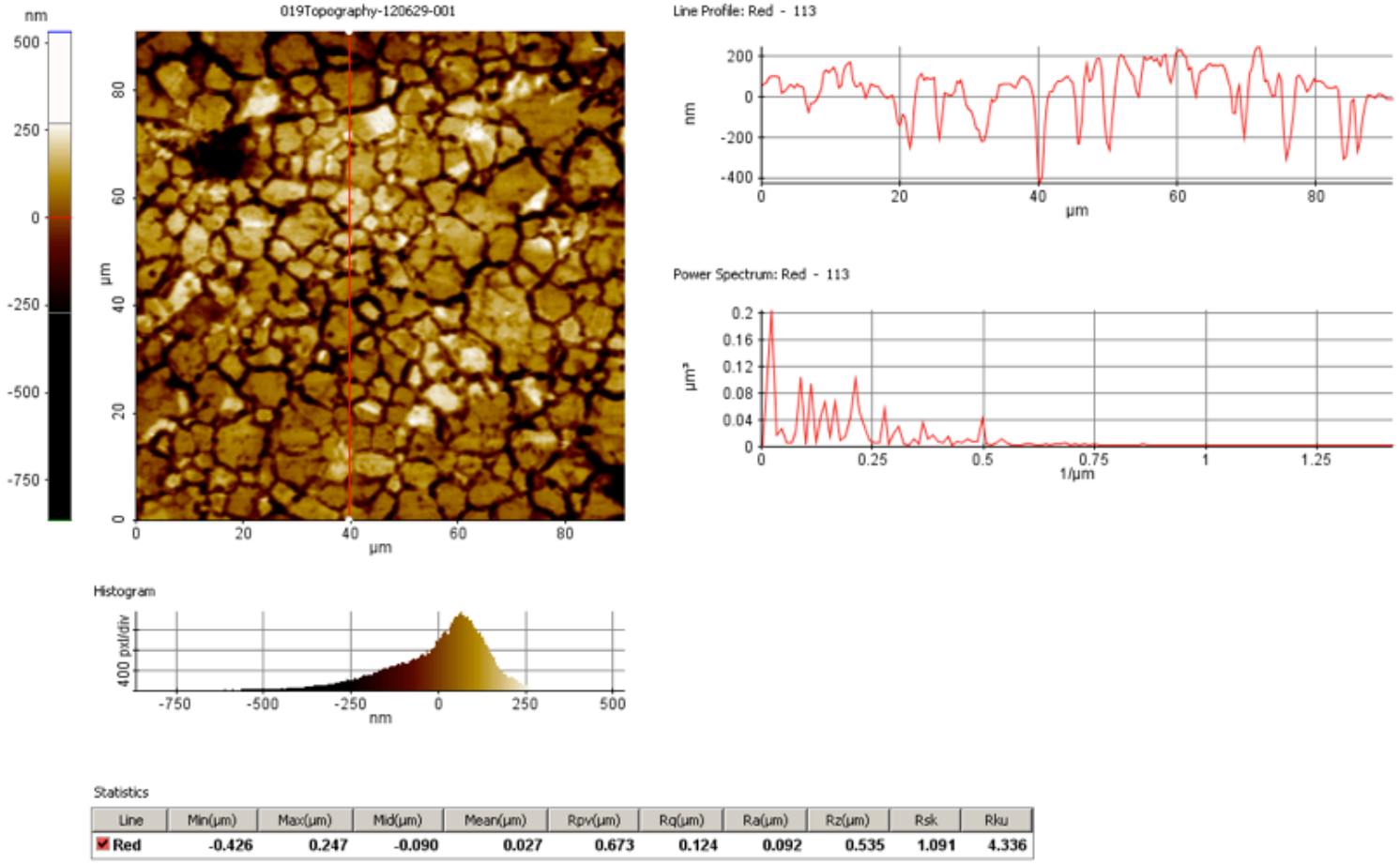

Statistics

Line	Min(µm)	Max(µm)	Mid(µm)	Mean(µm)	Rpv(µm)	Rq(µm)	Ra(µm)	Rz(µm)	Rsk	Rku
Red	-0.426	0.247	-0.090	0.027	0.673	0.124	0.092	0.535	1.091	4.336

Figure 100: Screen image of Ra measurement scan for 0% (10 min), using AFM contact mode topography line scan at scan size of 90 µm.

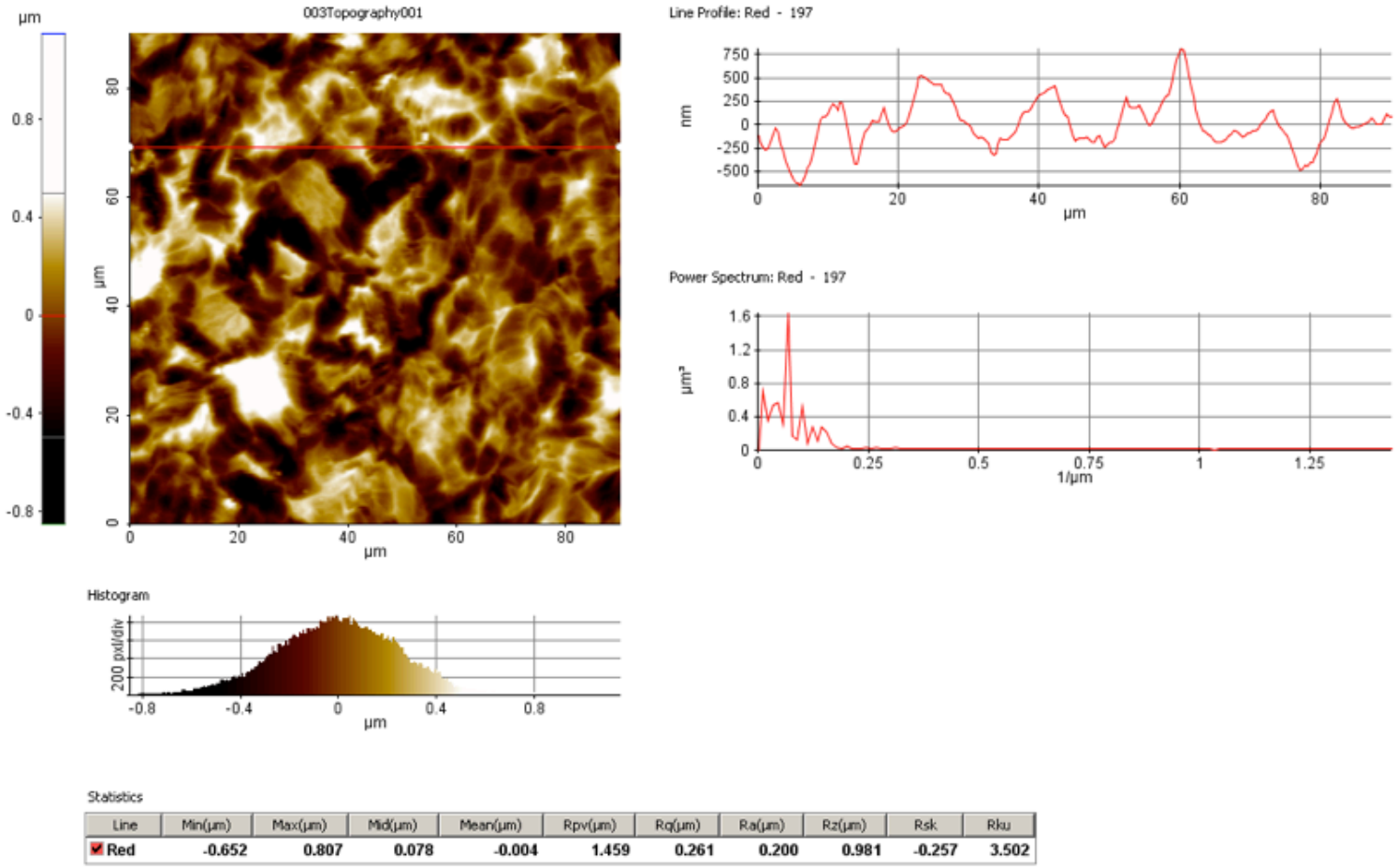

Statistics

Line	Min(µm)	Max(µm)	Mid(µm)	Mean(µm)	Rpv(µm)	Rq(µm)	Ra(µm)	Rz(µm)	Rsk	Rku
☑ Red	-0.652	0.807	0.078	-0.004	1.459	0.261	0.200	0.981	-0.257	3.502

Figure 101: Screen image of Ra measurement scan for 0% (30 min), using AFM contact mode topography line scan at scan size of 90 µm.

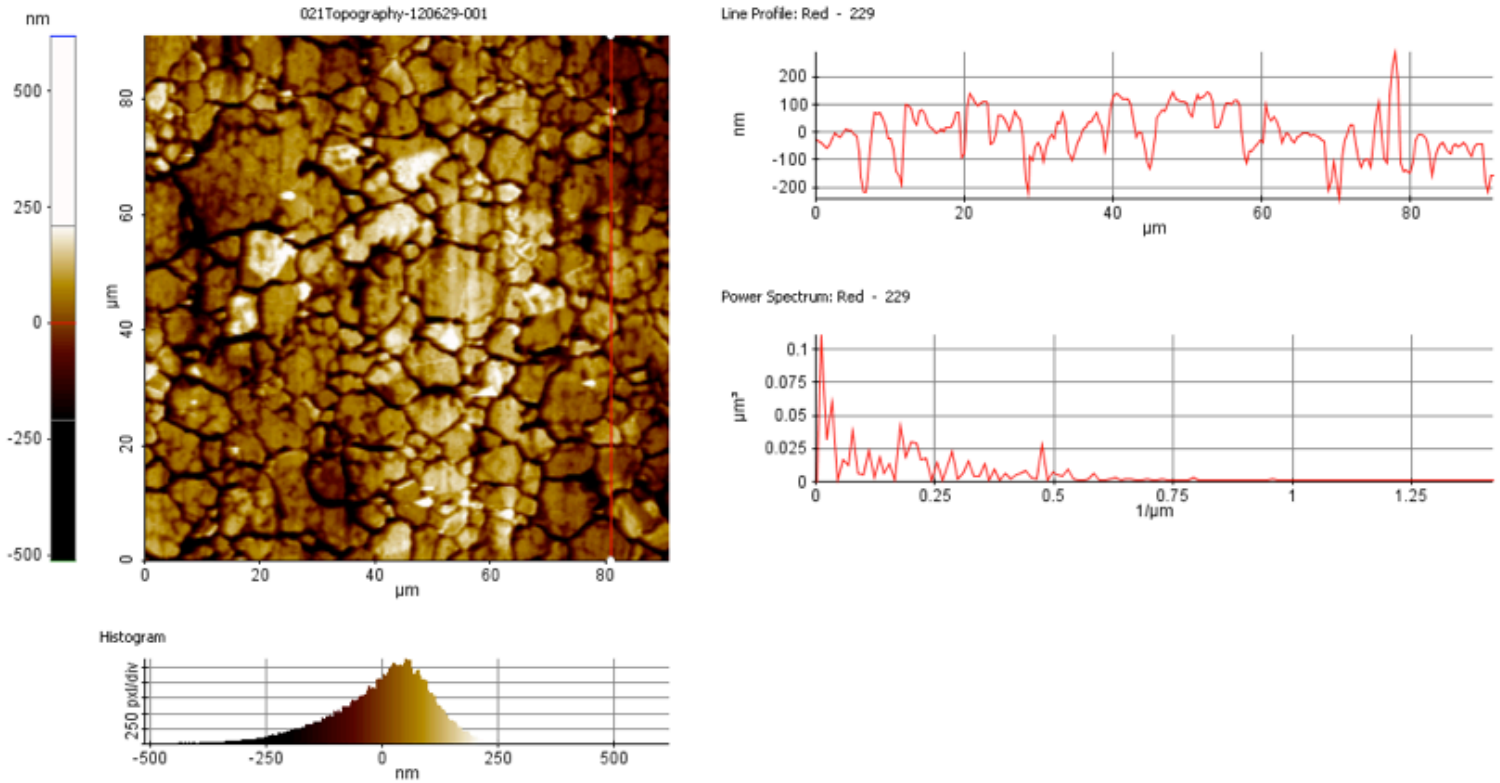

Statistics

Line	Min(nm)	Max(nm)	Mid(nm)	Mean(nm)	Rpv(nm)	Rq(nm)	Ra(nm)	Rz(nm)	Rsk	Rku
Red	-241.261	287.887	23.313	-5.971	529.148	88.888	70.528	393.682	0.096	3.026

Figure 102: Screen image of Ra measurement scan for 10% (5 min), using AFM contact mode topography line scan at scan size of 90 µm.

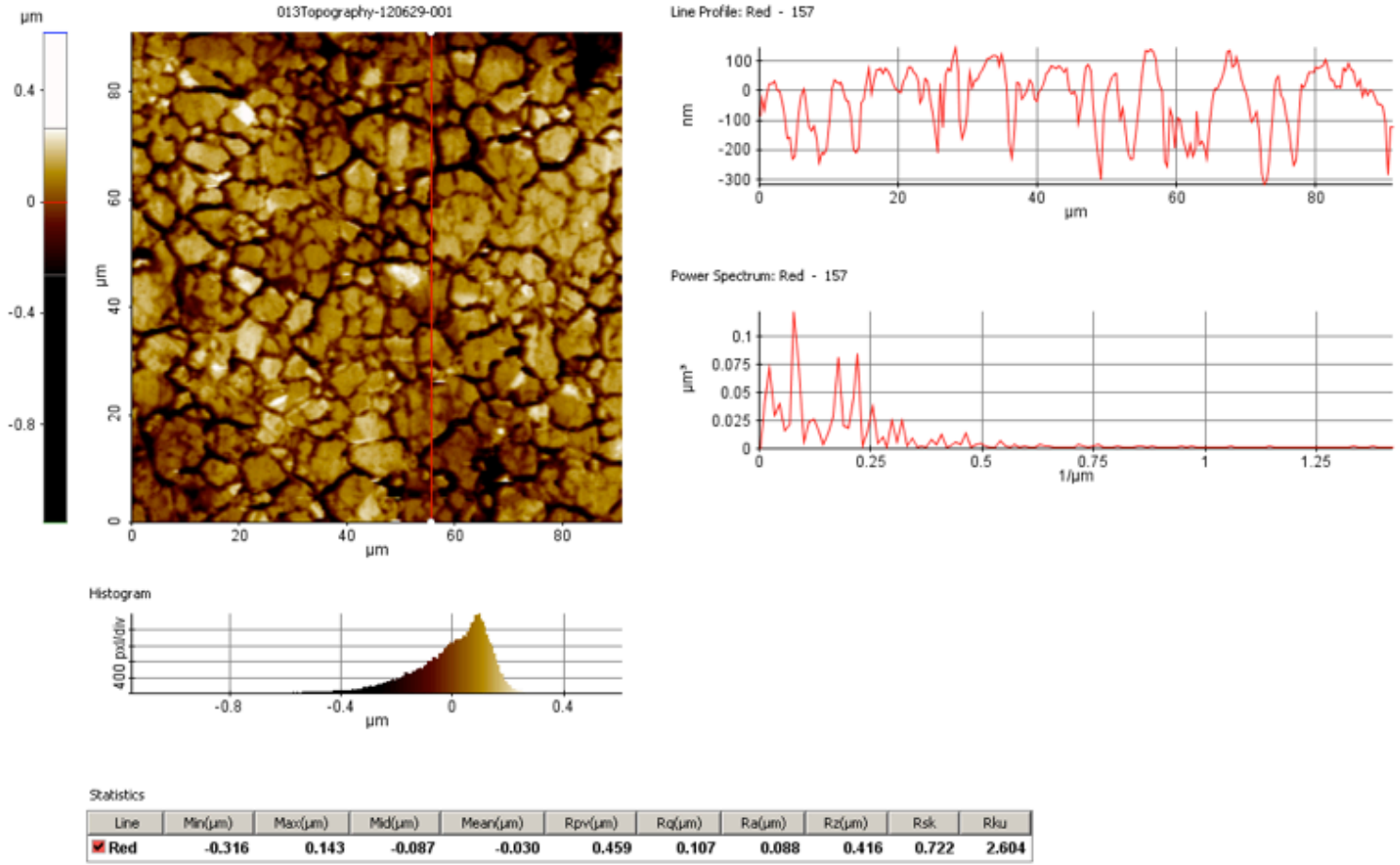

Statistics

Line	Min(µm)	Max(µm)	Mid(µm)	Mean(µm)	Rpv(µm)	Rq(µm)	Ra(µm)	Rz(µm)	Rsk	Rku
Red	-0.316	0.143	-0.087	-0.030	0.459	0.107	0.088	0.416	0.722	2.604

Figure 103: Screen image of Ra measurement scan for 10% (10 min), using AFM contact mode topography line scan at scan size of 90 µm.

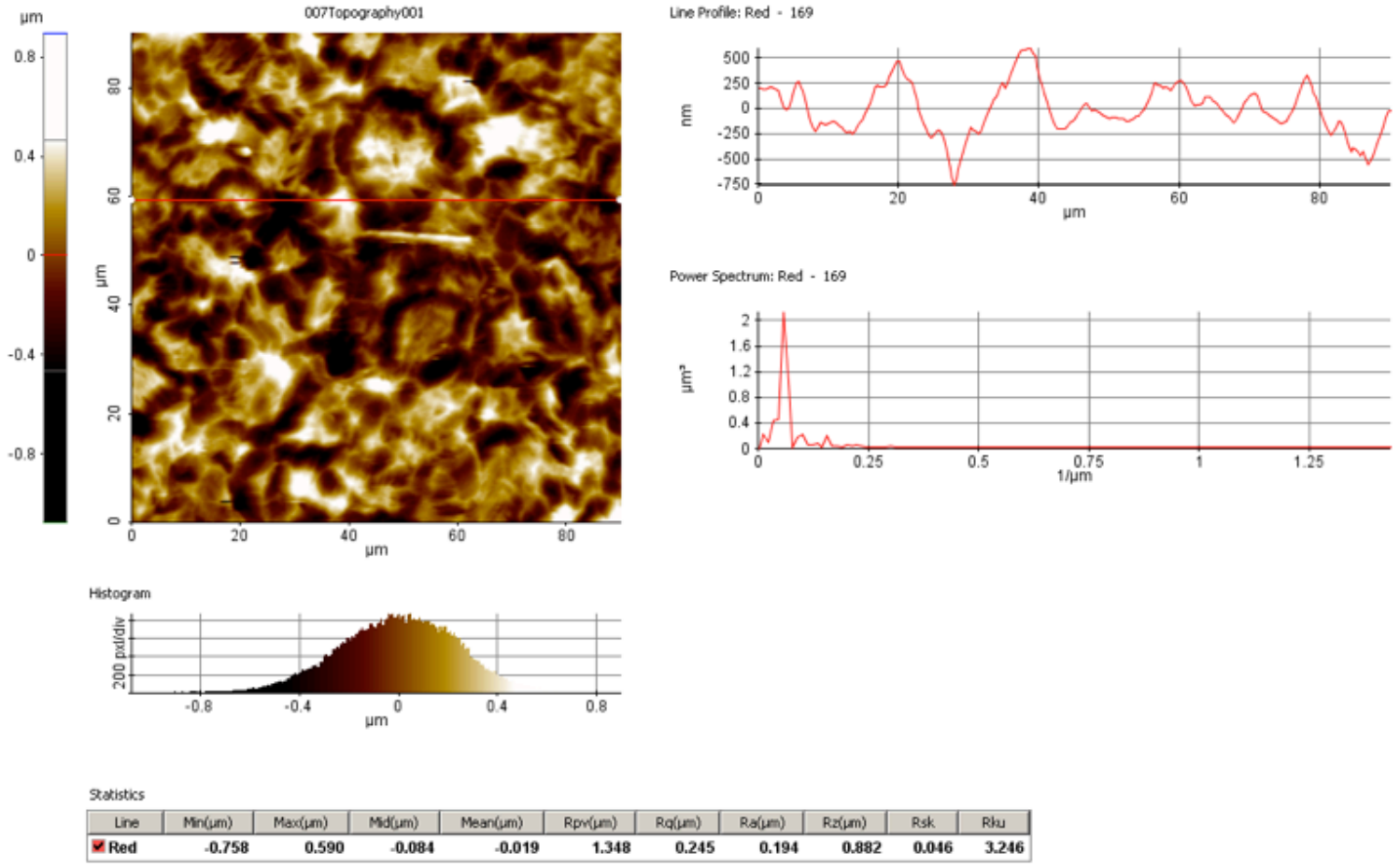

Statistics

Line	Min(µm)	Max(µm)	Mid(µm)	Mean(µm)	Rpv(µm)	Rq(µm)	Ra(µm)	Rz(µm)	Rsk	Rku
Red	-0.758	0.590	-0.084	-0.019	1.348	0.245	0.194	0.882	0.046	3.246

Figure 104: Screen image of Ra measurement scan for 10% (30 min), using AFM contact mode topography line scan at scan size of 90 µm.

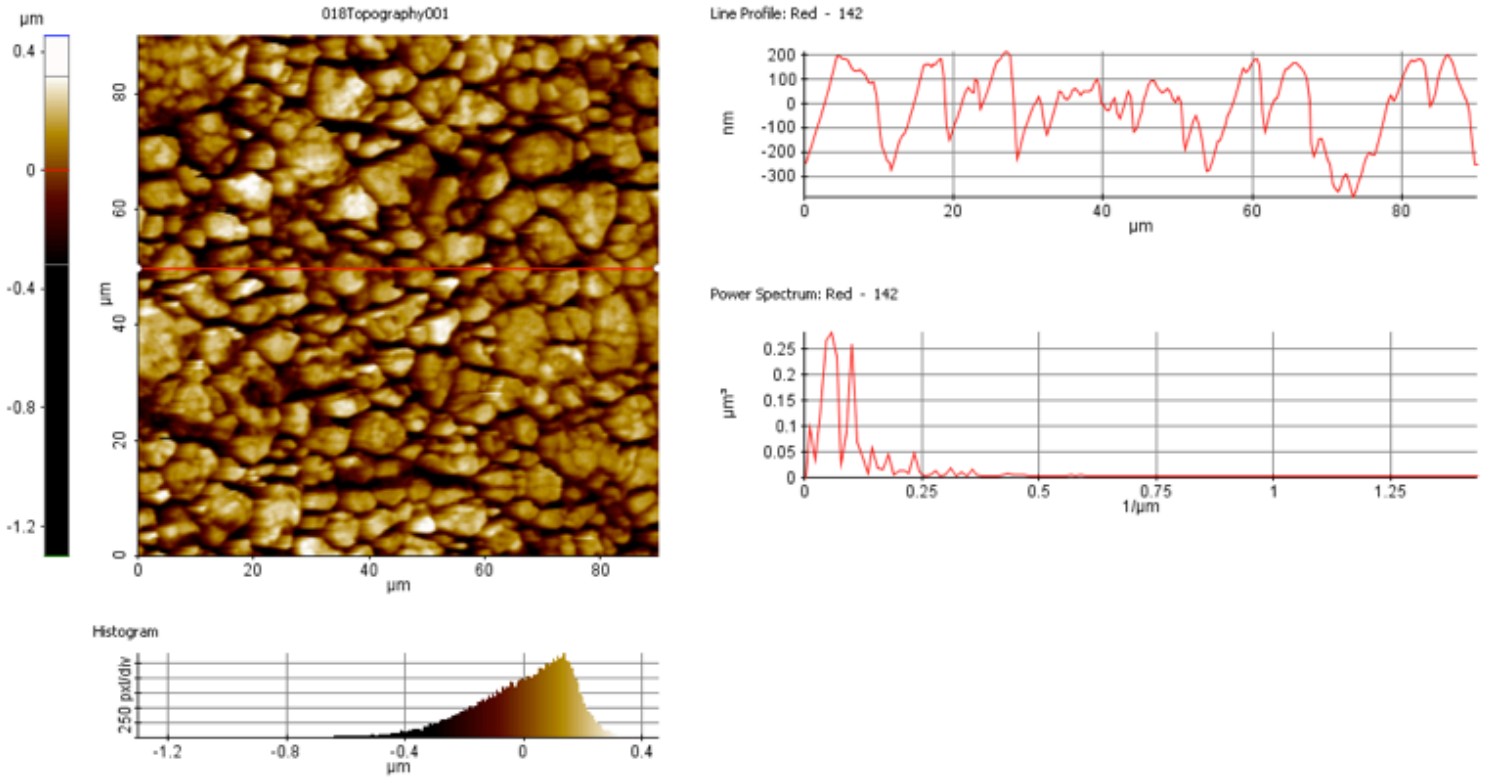

Statistics

Line	Min(µm)	Max(µm)	Mid(µm)	Mean(µm)	Rpv(µm)	Rq(µm)	Ra(µm)	Rz(µm)	Rsk	Rku
Red	-0.385	0.212	-0.086	-0.012	0.597	0.145	0.119	0.503	0.571	2.498

Figure 105: Screen image of Ra measurement scan for 30% (5 min), using AFM contact mode topography line scan at scan size of 90 µm.

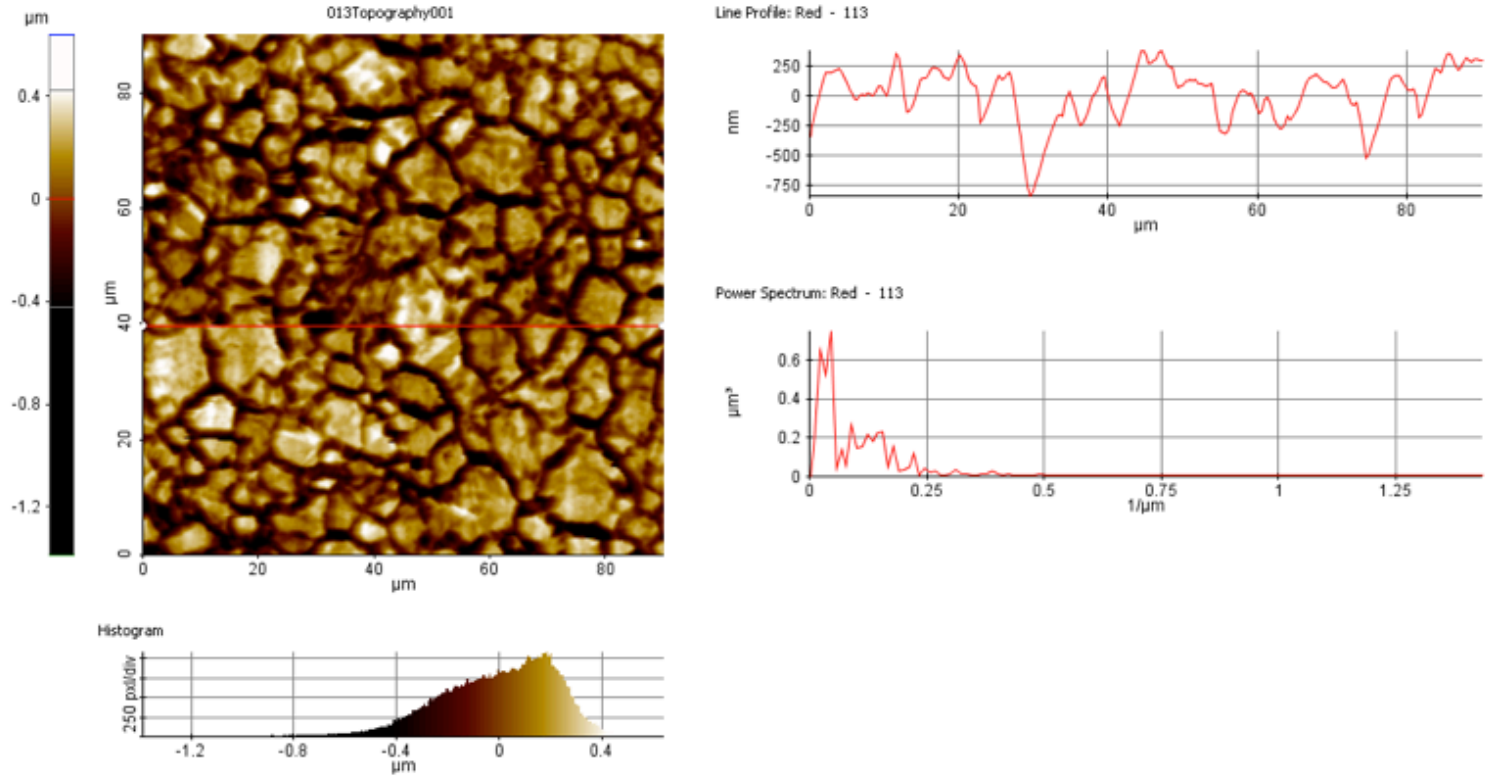

Statistics

Line	Min(µm)	Max(µm)	Mid(µm)	Mean(µm)	Rpv(µm)	Rq(µm)	Ra(µm)	Rz(µm)	Rsk	Rku
Red	-0.836	0.376	-0.230	0.010	1.212	0.224	0.173	0.798	1.062	4.544

Figure 106: Screen image of Ra measurement scan for 30% (10 min), using AFM contact mode topography line scan at scan size of 90 µm.

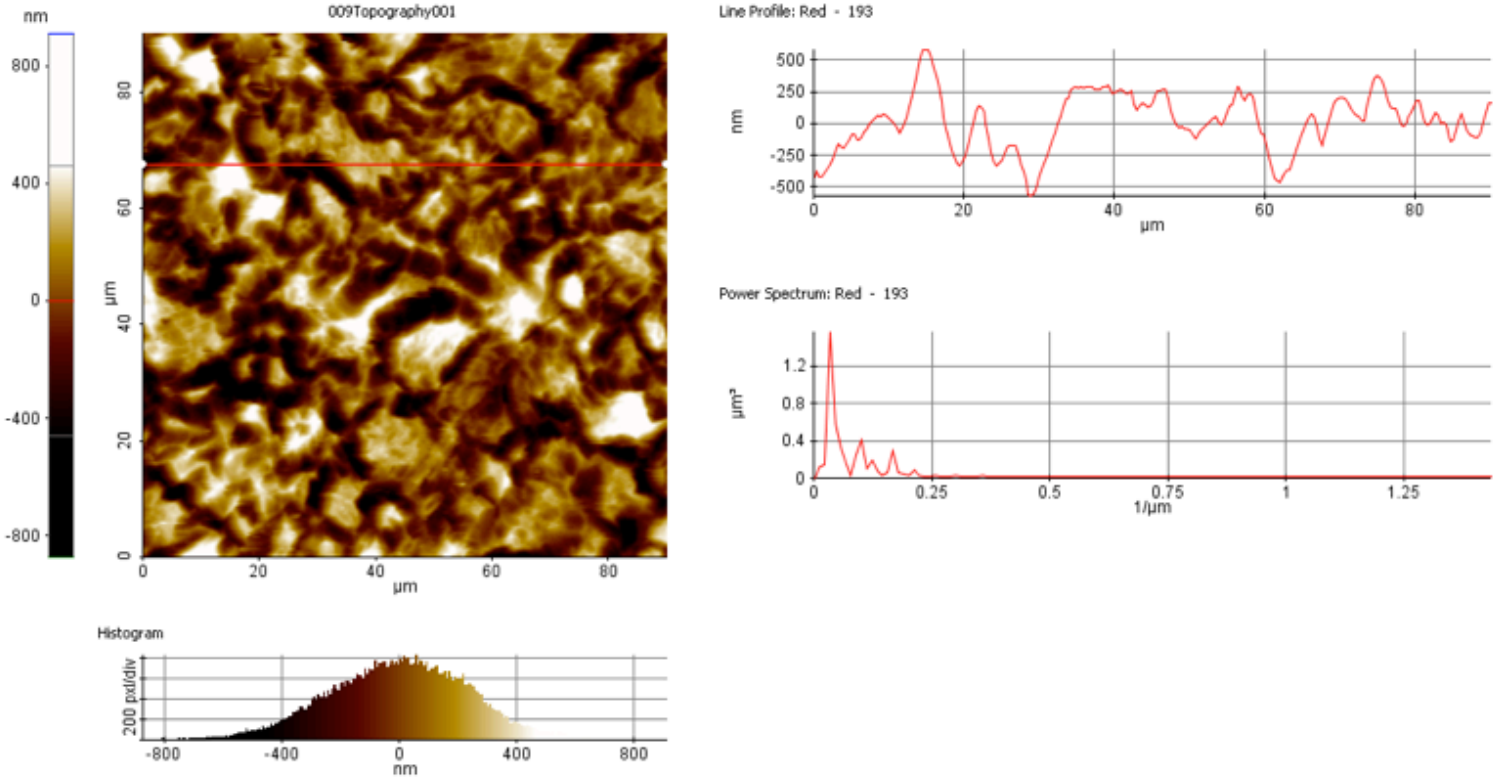

Statistics

Line	Min(nm)	Max(nm)	Mid(nm)	Mean(nm)	Rpv(nm)	Rq(nm)	Ra(nm)	Rz(nm)	Rsk	Rku
Red	-570.828	579.455	4.313	4.757	1150.283	226.871	179.358	790.880	0.233	2.854

Figure 107: Screen image of Ra measurement scan for 30% (30 min), using AFM contact mode topography line scan at scan size of 90 µm.

9 References

[1] X. Li, Principles of Fuel Cells, Taylor & Francis, 2005.
[2] W. Vielstich, Handbook of Fuel Cells, 6 Volume Set, John Wiley & Sons, 2009.
[3] K.S. Jeong, B.S. Oh, Journal of Power Sources, 105 (2002) 58-65.
[4] J. Larminie, A. Dicks, Fuel cell systems explained, 2 ed., J. Wiley, 2003.
[5] F. Energies, in: Future Energies Magazine, 2006.
[6] K.R. Cooper, V. Ramani, J.M. Fenton, H.R. Kunz, Experimental Methods and Data Analyses for Polymer Electrolyte Fuel Cells Scribner Associates, Inc. , 2007.
[7] Z. Jiang1, Z.-J. Jiang2, Carbon Nanotubes Supported Metal Nanoparticles for the Applications in Proton Exchange Membrane Fuel Cells (PEMFCs), 2011.
[8] J.B. Benziger, M.B. Satterfield, W.H.J. Hogarth, J.P. Nehlsen, I.G. Kevrekidis, Journal of Power Sources, 155 (2006) 272-285.
[9] X.-Z. Yuan, C. Song, H. Wang, J. Zhang, Electrochemical Impedance Spectroscopy in PEM Fuel cells; Fundamentals and Applications, Springer London Dordrecht Heidelberg, New York, 2010.
[10] J.S.a.J. Marcinkoski, in, US DoE DoE Fuel Cell Technologies Office, 2013.
[11] D.J.L. Brett, N.P. Brandon, Journal of Fuel Cell Science and Technology, 4 (2007) 29-44.
[12] H. Tsuchiya, O. Kobayashi, International Journal of Hydrogen Energy, 29 (2004) 985-990.
[13] I. Bar-On, R. Kirchain, R. Roth, Journal of Power Sources, 109 (2002) 71-75.
[14] H. Tawfik, Y. Hung, D. Mahajan, Journal of Power Sources, 163 (2007) 755-767.
[15] C.A. Reiser, L. Bregoli, T.W. Patterson, J.S. Yi, J.D. Yang, M.L. Perry, T.D. Jarvi, Electrochemical and Solid-State Letters, 8 (2005) A273-A276.
[16] H.-C. Kuan, C.-C.M. Ma, K.H. Chen, S.-M. Chen, Journal of Power Sources, 134 (2004) 7-17.
[17] V. Mehta, Analysis of Design and Manufacturing of Proton Exchange Membrane Fuel Cells, University of Washington, 2002.
[18] K. RoBberg, V. Trapp, "Graphite Based Bipolar plates", Handbook of Fuel Cells: Fundamentals Technology and Applications, Advances in electrocatalysis, materials, diagnostics and durability, John Wiley & Sons, 2003.

[19] R.A. Mercuri, in, ucar gRAPH-tECH inc. Lakewood Ohio, US, Seven Hills, OH, 2000.
[20] P.L. Hentall, J.B. Lakeman, G.O. Mepsted, P.L. Adcock, J.M. Moore, Journal of Power Sources, 80 (1999) 235-241.
[21] W.J. Lackey, Carbon–Carbon Composites, in: K.H.J.B. Editors-in-Chief: , W.C. Robert, C.F. Merton, I. Bernard, J.K. Edward, M. Subhash, V. Patrick (Eds.) Encyclopedia of Materials: Science and Technology (Second Edition), Elsevier, Oxford, 2001, pp. 952-966.
[22] T.M. Besmann, J.W. Klett, J.J.J. Henry, E. Lara-Curzio, Journal of The Electrochemical Society, 147 (2000) 4083-4086.
[23] Porvair, in, Porvair Fuel Cell Tachnology Inc. , 2004.
[24] E.A. Cho, U.S. Jeon, H.Y. Ha, S.A. Hong, I.H. Oh, Journal of Power Sources, 125 (2004) 178-182.
[25] A. Müller, P. Kauranen, A. von Ganski, B. Hell, Journal of Power Sources, 154 (2006) 467-471.
[26] C. Del Río, M.C. Ojeda, J.L. Acosta, M.J. Escudero, E. Hontañón, L. Daza, Journal of Applied Polymer Science, 83 (2002) 2817-2822.
[27] D. Acierno, A.A. Collyer, Rheology and processing of liquid crystal polymers, Chapman & Hall, 1996.
[28] H. Wolf, M. Willert-Porada, Journal of Power Sources, 153 (2006) 41-46.
[29] N. de las Heras, E.P.L. Roberts, R. Langton, D. R. Hodgson, Energy & Environmental Science, 2 (2009) 206-214.
[30] T. Cheng, Bipolar plates and plate materials, Taylor & Francis, 2009.
[31] S. Karimi, N. Fraser, B. Roberts, F.R. Foulkes, Advances in Materials Science and Engineering, 2012 (2012) 22.
[32] S.-J. Lee, C.-H. Huang, J.-J. Lai, Y.-P. Chen, Journal of Power Sources, 131 (2004) 162-168.
[33] S.-J. Lee, J.-J. Lai, C.-H. Huang, Journal of Power Sources, 145 (2005) 362-368.
[34] H. Li, J. Zhang, K. Fatih, Z. Wang, Y. Tang, Z. Shi, S. Wu, D. Song, J. Zhang, N. Jia, S. Wessel, R. Abouatallah, N. Joos, Journal of Power Sources, 185 (2008) 272-279.
[35] H. Wang, J.A. Turner, Fuel Cells, 10 (2010) 510-519.
[36] H. Wang, M.A. Sweikart, J.A. Turner, Journal of Power Sources, 115 (2003) 243-251.
[37] H. Wang, J.A. Turner, Journal of Power Sources, 128 (2004) 193-200.
[38] M. Applebaum, in, Michelle Applebaum Research 2004.
[39] D.P. Davies, P.L. Adcock, M. Turpin, S.J. Rowen, Journal of Applied Electrochemistry, 30 (2000) 101-105.
[40] A.J. Sedriks, Corrosion of Stainless Steels, 2nd ed., Wiley-Interscience, 1996.

[41] J. Wind, R. Späh, W. Kaiser, G. Böhm, Journal of Power Sources, 105 (2002) 256-260.
[42] N. Aukland, A. Boudina, D.S. Eddy, J.V. Mantese, M.P. Thompson, S.S. Wang, Journal of Materials Research, 19 (2004) 1723-1729.
[43] D.R. Hodgson, B. May, P.L. Adcock, D.P. Davies, Journal of Power Sources, 96 (2001) 233-235.
[44] S. Frangini, A. Masci, Surface and Coatings Technology, 184 (2004) 31-39.
[45] A.S. Woodman, E.B. Anderson, K.D. Jayne, M.C. Kimble, American Electroplaters and Surface Finishers Society, Proceedings AESF SUR/FIN '99 6 (21-24) (1999) 717-725
[46] A. Shanian, O. Savadogo, Journal of Power Sources, 159 (2006) 1095-1104.
[47] V.V. Nikam, R.G. Reddy, Journal of Power Sources, 152 (2005) 146-155.
[48] N. Cunningham, D. Guay, J.P. Dodelet, Y. Meng, A.R. Hlil, A.S. Hay, Journal of The Electrochemical Society, 149 (2002) A905-A911.
[49] Y. Wang, D.O. Northwood, Journal of Power Sources, 163 (2006) 500-508.
[50] S. Joseph, J.C. McClure, R. Chianelli, P. Pich, P.J. Sebastian, International Journal of Hydrogen Energy, 30 (2005) 1339-1344.
[51] M.A.L. García, M.A. Smit, Journal of Power Sources, 158 (2006) 397-402.
[52] M.M. Morshed, B.P. McNamara, D.C. Cameron, M.S.J. Hashmi, Journal of Materials Processing Technology, 141 (2003) 127-131.
[53] S.-J. Lee, C.-H. Huang, Y.-P. Chen, Journal of Materials Processing Technology, 140 (2003) 688-693.
[54] G.Q. Lu, C.Y. Wang, Journal of Power Sources, 144 (2005) 141-145.
[55] P.L. Hentall, J.B. Lakeman, G.O. Mepsted, P.L. Adcock, J.M. Moore, Journal of Power Sources, 80 (1999) 235-241.
[56] M.P. Brady, B. Yang, H. Wang, J.A. Turner, K.L. More, M. Wilson, F. Garzon, JOM, 58 (2006) 50-57.
[57] C. Mitterer, Journal of Solid State Chemistry, 133 (1997) 279-291.
[58] A.B. LaConti, A.E. Griffith, C.C. Cropley, J.A. Kosek, in, US6,083,641, 2000.
[59] Y. Fu, M. Hou, G. Lin, J. Hou, Z. Shao, B. Yi, Journal of Power Sources, 176 (2008) 282-286.
[60] B. Wu, G. Lin, Y. Fu, M. Hou, B. Yi, International Journal of Hydrogen Energy, 35 (2010) 13255-13261.
[61] J. F. D. Lomax, B.D. James, G.N. Baum, C.E. Thomas, in, DIRECTED TECHNOLOGIES, INC., Virginia, US, 1998.
[62] D.J. Brian, in, Direct Technologies Inc., Arlington, US, 2008.
[63] ORN, in, Philadelphia, USA, 2011.

[64] L.G. Marianowski, Progress Report for Fuel Cell Power Systems, Development of a $10/kW Bipolar Seperator, DIANE Publishing, 2000.
[65] F. Energies, in, Future Energies, 2003.
[66] E. Energy, in, Efficient Energy, 2012.
[67] V. Mehta, J.S. Cooper, Journal of Power Sources, 114 (2003) 32-53.
[68] A. Heinzel, F. Mahlendorf, O. Niemzig, C. Kreuz, Journal of Power Sources, 131 (2004) 35-40.
[69] E. Middelman, W. Kout, B. Vogelaar, J. Lenssen, E. de Waal, Journal of Power Sources, 118 (2003) 44-46.
[70] F.N.B. M. Ruge, in: Proceedings of the 1st European PEFC Forum, Lucerne, Switzerland, 2001, pp. 399-308.
[71] L.G. Marianowski, in, Gas Technology Institute, Des Plaines, IL, 2001.
[72] R.C. Makkus, A.H.H. Janssen, F.A. de Bruijn, R.K.A.M. Mallant, Journal of Power Sources, 86 (2000) 274-282.
[73] D. U.S, in, 2011.
[74] J.J. Hwang, H.S. Hwang, Journal of Power Sources, 104 (2002) 24-32.
[75] J.S. Kim, W.H.A. Peelen, K. Hemmes, R.C. Makkus, Corrosion Science, 44 (2002) 635-655.
[76] S. Miachon, P. Aldebert, Journal of Power Sources, 56 (1995) 31-36.
[77] R. Hornung, G. Kappelt, Journal of Power Sources, 72 (1998) 20-21.
[78] J. Ihonen, F. Jaouen, G. Lindbergh, G. Sundholm, Electrochimica Acta, 46 (2001) 2899-2911.
[79] D.P. Davies, P.L. Adcock, M. Turpin, S.J. Rowen, Journal of Power Sources, 86 (2000) 237-242.
[80] L. Landis, J.L. Tucker, in: R&D Magazine Cahners Business Information, 2002.
[81] N. Cunningham, M. Lefèvre, G. Lebrun, J.-P. Dodelet, Journal of Power Sources, 143 (2005) 93-102.
[82] L. Ma, S. Warthesen, D.A. Shores, Journal of New Materials for Electrochemical Systems, 3 (2000) 221-228.
[83] D.A. Shores, G.A. Deluga, "Basic Material Corrosion Issues", Handbook of Fuel cells - *Fundamentals, Technology and Applications*, Wiley, 2003.
[84] M.C. Li, C.L. Zeng, S.Z. Luo, J.N. Shen, H.C. Lin, C.N. Cao, Electrochimica Acta, 48 (2003) 1735-1741.
[85] D.B. Hibbert, Introduction to Electrochemistry, Macmillan, London, 1993.
[86] M. Pourbaix, Atlas of Electrochemical Equilibria in Aqueous Solution, Oxford University Press, 1996.
[87] D.A. Jones, Principles and prevention of corrosion, Prentice Hall, 1996.
[88] K.R.A. TRETHEWEY, J.A. CHAMBERLAIN, Corrosion: For Science and Engineering, Addison-Wesley Longman, Incorporated, 1995.
[89] G. Hinds, in: The electrochemistry of corrosion, NPL, London UK, 2008.

[90] M. Noel, K.I. Vasu, Cyclic Voltammetry and the Frontiers of Electrochemistry,, Oxford & IBH publishing Co. PVT. LTD, New Delhi, 1990.
[91] E. McCafferty, Corrosion Science, 47 (2005) 3202-3215.
[92] J.T. Stock, M.V. Orna, A.C.S.D.o.t.H.o. Chemistry, A.C.S.D.o.A. Chemistry, A.C.S. Meeting, Electrochemistry, past and present, American Chemical Society, 1989.
[93] F. Mansfiel, Corrosion, 1981.
[94] C. Wagner, Corrosion Science, 5 (1965) 751-764.
[95] C.M.A. Brett, A.M.O. Brett, Electrochemistry: Priciples, Methods and Applications, Oxford University Press, 1993.
[96] J. Wu, X.Z. Yuan, H. Wang, M. Blanco, J.J. Martin, J. Zhang, International Journal of Hydrogen Energy, 33 (2008) 1735-1746.
[97] A. Parthasarathy, B. Dave, S. Srinivasan, A. Appleby, C. Martin, Journal of the Electrochemical Society, 139 (1992) 1634-1641.
[98] Y. Wang, D.O. Northwood, Electrochimica Acta, 52 (2007) 6793-6798.
[99] A.K. Iversen, Corrosion Science, 48 (2006) 1036-1058.
[100] M. Kumagai, S.-T. Myung, S. Kuwata, R. Asaishi, H. Yashiro, Electrochimica Acta, 53 (2008) 4205-4212.
[101] A. Pozio, F. Zaza, A. Masci, R.F. Silva, Journal of Power Sources, 179 (2008) 631-639.
[102] A. Kraytsberg, M. Auinat, Y. Ein-Eli, Journal of Power Sources, 164 (2007) 697-703.
[103] P.K. E.J Carlson, J. Sinha, Y. Yang, in, TIAX LLC Cambridge, Massachusetts, 2005.
[104] R.F. Silva, D. Franchi, A. Leone, L. Pilloni, A. Masci, A. Pozio, Electrochimica Acta, 51 (2006) 3592-3598.
[105] A.A. Hermas, M.S. Morad, Corrosion Science, 50 (2008) 2710-2717.
[106] H. Wang, M.P. Brady, G. Teeter, J.A. Turner, Journal of Power Sources, 138 (2004) 86-93.
[107] K. Feng, Y. Shen, D. Liu, P.K. Chu, X. Cai, International Journal of Hydrogen Energy, 35 (2010) 690-700.
[108] K.M. Kim, J.H. Park, J.H. Kim, K.Y. Kim, International Journal of Hydrogen Energy, 36 (2011) 9926-9935.
[109] L. Kogut, K. Komvopoulos, Journal of Applied Physics, 94 (2003) 3153-3162.
[110] ASTM, Annual book of ASTM standards, Philadelphia, PA, 1979.
[111] G.F.V. Voort, ASM Handbook, ASM International, 2004.
[112] L.J. Durney, Electroplating engineering handbook, , Van Nostrand Reinhold, 1984.
[113] K.I. Popov, S.S. Djokić, B.N. Grgur, Fundamental Aspects of Electrometallurgy, Kluwer Academic/Plenum Publishers, 2002.

[114] R. Sard, H. Leidheiser, F. Ogburn, E.S.C. Division, E.S.E. Division, Properties of electrodeposits, their measurement and significance, Corrosion, Electrodeposition, and Electronics Divisions, Electrochemical Society, 1975.
[115] S. Murali, M. Ramachandra, K.S.S. Murthy, K.S. Raman, Materials Characterization, 38 (1997) 273-286.
[116] D. Landolt, Electrochimica Acta, 32 (1987) 1-11.
[117] L.J. Durney, Electroplating engineering handbook, Springer, 1984.
[118] C.-C. Lin, C.-C. Hu, T.-C. Lee, Surface and Coatings Technology, 204 (2009) 448-454.
[119] A. Redman, Electrolytic Polishing and Bright Plating of Metals, Alvin Redman . 1948.
[120] D.R. Askeland, P.P. Fulay, W.J. Wright, The Science and Engineering of Materials, Cengage Learning, 2010.
[121] R.D. Grimm, A.C. West, D. Landolt, Journal of The Electrochemical Society, 139 (1992) 1622-1629.
[122] M. Matlosz, S. Magaino, D. Landolt, Journal of The Electrochemical Society, 141 (1994) 410-418.
[123] C.-C. Lin, C.-C. Hu, Electrochimica Acta, 53 (2008) 3356-3363.
[124] V.V. Yuzhakov, H.C. Chang, A.E. Miller, Physical Review B - Condensed Matter and Materials Physics, 56 (1997) 12608-12624.
[125] S.-J. Lee, J.-J. Lai, Journal of Materials Processing Technology, 140 (2003) 206-210.
[126] E.S. Lee, The International Journal of Advanced Manufacturing Technology, 16 (2000) 591-599.
[127] S. Feliu, J.A. Gonzalez, Corrosion Science, 11 (1971) 307-318.
[128] W J McTegart, The Electrolytic and Chemical Polishing of Metals Pergamon Press, London, 1956.
[129] L. Ponto, M. Datta, D. Landolt, Surface and Coatings Technology, 30 (1987) 265-276.
[130] C.-K. Kang, Y.-S. Lee, Journal of Materials Science: Materials in Medicine, 18 (2007) 1389-1398.
[131] T. Hryniewicz, K. Rokosz, Materials Chemistry and Physics, 122 (2010) 169-174.
[132] M. Neergat, K.R. Weisbrod, Corrosion Science, 53 (2011) 3983-3990.
[133] W. Ye, Y. Li, F. Wang, Electrochimica Acta, 54 (2009) 1339-1349.
[134] K.R. Weisbrod, V.L. Trujillo, H.E. Martinez, in: Other Information: PBD: Dec 1997, 1997, pp. Medium: ED; Size: 32 p.
[135] T. Hryniewicz, R. Rokicki, K. Rokosz, Corrosion, 64 (2008) 660-665.
[136] E.P. Serjeant, Potentiometry and Potentiometric Titration, Interscience, New York, 1984.

[137] N.G. Thompson, J.H. Payer, Corrosion Testing Made Easy: DC Electrochemical Test Methods, NACE International, Houston, Texas, 1998.
[138] G. Rocchini, Corrosion Science, 38 (1996) 1019-1031.
[139] H. Wang, X.Z. Yuan, H. Li, PEM Fuel Cell Diagnostic Tools, Taylor & Francis, 2011.
[140] P. Kurzweil, H.J. Fischle, Journal of Power Sources, 127 (2004) 331-340.
[141] P.A. Christensen, A. Hamnett, Techniques and mechanisms in Electrochemistry, Chapman and Hall, London, 1994.
[142] D.T. Sawyer, A. Sobkowiak, J.L. Roberts, Electrochemistry for Chemists, Wiley, 1995.
[143] M.M. El-Naggar, Journal of Applied Electrochemistry, 34 (2004) 911-918.
[144] M.F. McGuire, Stainless Steels for Design Engineers, ASM International, 2008.
[145] D.P.W. H H Voss, in, United States, 1995.
[146] T.J. Mason, J. Millichamp, T.P. Neville, A. El-kharouf, B.G. Pollet, D.J.L. Brett, Journal of Power Sources, 219 (2012) 52-59.
[147] A. El-kharouf, T.J. Mason, D.J.L. Brett, B.G. Pollet, Journal of Power Sources, 218 (2012) 393-404.
[148] H.J. Flitt, D.P. Schweinsberg, Corrosion Science, 47 (2005) 3034-3052.
[149] C. Wagner, W. Traud, Journal of Applied Electrochemistry and Physical Chemistry, 44 (1938) 391-402.
[150] C.M. Sánchez-Sánchez, E. Expósito, J. Solla-Gullón, V. García-García, V. Montiel, A. Aldaz, Journal of Chemical Education, 80 (2003) 529.
[151] G. Guo, E. University of Kansas. Civil, A. Engineering, Laboratory and Field Tests of Multiple Corrosion Protection Systems for Reinforced Concrete Bridge Components and 2205 Pickled Stainless Steel, University of Kansas, 2006.
[152] NPL, in, 2014.
[153] W. Jin, K. Feng, Z. Li, X. Cai, L. Yu, D. Zhou, Journal of Power Sources, 196 (2011) 10032-10037.
[154] I. Olefjord, L. Wegrelius, Corrosion Science, 31 (1990) 89-98.
[155] N. Ramasubramanian, N. Preocanin, R.D. Davidson, Journal of the Electrochemical Society, 132 (1985) 793-798.
[156] G. Lorang, M. Da Cunha Belo, A.M.P. Simoes, M.G.S. Ferreira, Journal of the Electrochemical Society, 141 (1994) 3347-3356.
[157] R. Kirchheim, B. Heine, H. Fischmeister, S. Hofmann, H. Knote, U. Stolz, Corrosion Science, 29 (1989) 899-917.
[158] M. Bojinov, I. Betova, R. Raicheff, Journal of Electroanalytical Chemistry, 430 (1997) 169-178.

[159] T.P. Hoar, D.C. Mears, G.P. Rothwell, Corrosion Science, 5 (1965) 279-289.
[160] W. Yoon, X. Huang, P. Fazzino, K.L. Reifsnider, M.A. Akkaoui, Journal of Power Sources, 179 (2008) 265-273.
[161] Y. Yang, L.-j. Guo, H. Liu, International Journal of Hydrogen Energy, 36 (2011) 1654-1663.
[162] W.R. Baumgartner, P. Parz, S.D. Fraser, E. Wallnöfer, V. Hacker, Journal of Power Sources, 182 (2008) 413-421.
[163] B.S. Covino Jr, M. Rosen, T.J. Driscoll, T.C. Murphy, C.R. Molock, Corrosion Science, 26 (1986) 95-107.
[164] K.W. Mao, M.A. Laboda, J.P. Hoare, Journal of the Electrochemical Society, 119 (1972) 419-&.
[165] J. André, L. Antoni, J.-P. Petit, E. De Vito, A. Montani, International Journal of Hydrogen Energy, 34 (2009) 3125-3133.
[166] C.-Y. Bai, M.-D. Ger, M.-S. Wu, International Journal of Hydrogen Energy, 34 (2009) 6778-6789.
[167] A. Fattah-alhosseini, A. Saatchi, M.A. Golozar, K. Raeissi, Electrochimica Acta, 54 (2009) 3645-3650.
[168] J. Wang, J. Sun, S. Li, Z. Wen, S. Ji, International Journal of Hydrogen Energy, 37 (2012) 1140-1144.